Vitrification of historic and future high level nuclear wastes within alkali borosilicate glasses

Andrew James Connelly
M.Eng.

A Thesis submitted to the Department of Engineering Materials
at the University of Sheffield in partial fulfilment of
the requirement for the Degree of Doctor of Philosophy.

February 2008

The
University
Of
Sheffield.

Abstract

The disposal of highly radioactive and toxic wastes generated by the nuclear industry is one of the biggest challenges facing the world today. Currently, in the UK there is a large legacy waste holding which has been accumulating since nuclear energy was first harnessed during World War 2. Processing of this waste with a view to final disposal is a complex and difficult task. This work investigates one aspect of that process, namely turning this waste into glass (or vitrification).

This work uses multiple techniques including x-ray absorption spectroscopy, magic angle spinning nuclear magnetic resonance and molecular dynamic simulations, to investigate the structural role of ZrO_2 and UO_3 within the alkali borosilicate glass used in the UK for waste immobilisation. The effect of these additions on the bulk glass structure and selected glass properties are also explored.

In waste glasses Zr occurs as a 6 co-ordinated Zr ion surrounded by Si, B, Na and Li. The effect of ZrO_2 additions on the bulk glass structure and properties is highly complex. The addition of ZrO_2 appears to be characterised by a non-linearity in the trends of certain physical and structural parameters. At low levels of ZrO_2 the level of leaching from the glasses and the co-ordination of B increase. However, with higher ZrO_2 contents this trend is reversed. It is believed that the increase in B co-ordination destabilises the glass network and so increases leaching from the glass.

Work with Molecular Dynamic (MD) computer simulation of glasses showed the applicability of this approach to nuclear waste glasses and its ability to accurately reproduce changes in glass structure with changing compositions. The possibilities for solubility limit prediction using MD are also shown.

In waste glasses UO_3 is shown to exist as the uranyl $(UO^2)^{2+}$ species bound to the glass network. Addition of UO_3 to glasses decreases the co-ordination of B requiring 2 moles of alkali oxide to charge compensate its presence within the glass network. This indicates that U acts as an intermediate. Limited leach tests show that the presence of UO_3 within the glasses destabilises the formation of a gel layer.

Atomyriades

Nature, it seems is the popular name
for milliards and milliards and milliards
of particles playing their infinite game
of billiards and billiards and billiards.

Piet Hein

"A poet once said, 'The whole universe is in a glass of wine.' We will probably never know in what sense he meant that, for poets do not write to be understood. But it is true that if we look at a glass of wine closely enough we see the entire universe. There are the things of physics: the twisting liquid which evaporates depending on the wind and weather, the reflections in the glass, and our imagination adds the atoms. The glass is a distillation of the earth's rocks, and in its composition we see the secrets of the universe's age, and the evolution of stars. What strange array of chemicals are in the wine? How did they come to be?... If our small minds, for some convenience, divide this glass of wine, this universe, into parts - physics, biology, geology, astronomy, psychology, and so on – remember that nature does not know it! So let us put it all back together, not forgetting ultimately what it is for. Let it give us one more final pleasure: drink it and forget it all!"

R. Feynman
The Feynman Lectures on Physics
Vol. 1, 1977

Acknowledgements

Firstly, a big thank you to my supervisors Dr. Neil Hyatt, Dr. Karl Travis, Dr. Russell Hand and Dr. Ewan Maddrell, without whom none of this would have been possible. Thank you for your enthusiastic support, and for putting up with my insistent questioning.

I must also thank all the people who have helped me in achieving this piece of work. A big thank you to Dr. Diane Holland and Dr. Ben Parkinson at the University of Warwick for running MAS-NMR experiments and providing lots of advice and useful discussions. A big thank you as well to Dr. David Apperley at the EPSRC MAS-NMR service at the University of Durham for being so understanding about putting radioactive glass in his MAS-NMR spectrometer. Thank you also to Bob Billsborrow at the SRS for his beam line, which produced some great XAS results. Thank you to Oliver Hannant and Dr. Sue Forder and Sheffield Hallam University for the Mössbauer work. Thank you to Paul Bingham for many enthusiastic and interesting conversations on everything glassy.

Thank you to Ian "Killer" Watts and Dean Hemlock for some great times glass melting, to Mouldy for mending everything I broke, and Bev Lane for running all the DTA experiments. A big thank you to Andy Brown at the University of Leeds for producing such beautiful images of the active glasses. Also, thank you to Tim Brewer, Lin Marvin and Nick Marsh at the University of Leicester for ICP and XRF analysis. Thanks also goes to the EPSRC and Nexia Solutions Ltd. for funding this project.

Thank you to all the guys in the ISL, particularly Ollie, James, Lyubka, Gillian, Laura and everyone else for keeping me sane and putting up with my alternate enthusiasms and stresses.

A huge thank you goes to all my friends, particularly Lisa for believing in me and being great, Jo for keeping me sane and being a great friend, Nev for never dropping me and always being up for an adventure, Nat, Harry, and everyone else.

Finally, thank you to all my family without whose support and love over the years I wouldn't have been able to get this far and certainly would never have been able to finish. A special thank you to Mum and Dad for always being there when I needed them. I dedicate this to you.

Table of Contents

1 Introduction

The first commercial nuclear reactor for the generation of electricity was commissioned in the UK in 1956 and, by 2006, ca. 22 % of the UK's electrical energy came from nuclear power (19% generated in the UK, 3% was imported from France (AUA 2007)). The legacy of over 50 years of nuclear electricity production and military uses is the challenge of nuclear waste disposal. The most problematic form this waste takes is so called High Level Waste (HLW). This waste consists of highly toxic and radioactive elements and is produced during the reprocessing of commercial spent fuels. HLW is also a bi-product of nuclear weapons production and naval propulsion programmes; this legacy has become a major political and scientific challenge.

HLW must be dealt with in such a way to prevent, or significantly delay, toxic and radioactive material entering the biosphere. Waste immobilisation, as this process is called, is a complex and multifaceted problem with many different types of waste and disposal methods (Wilson 1996). The generally accepted route for disposal of HLW is as follows:

1. Immobilisation of waste within a durable glass or ceramic wasteform;
2. Sealing of this wasteform within a metal canister (e.g. stainless steel);
3. Transport and disposal of sealed wasteform into a repository, usually underground;
4. Backfill and eventual sealing of repository.

The repository concept is designed to prevent (or significantly delay) water contact with the wasteform. If water penetrates the repository barriers the wasteform also prevents, or significantly delays, leaching of radionuclides and their dispersal to the far-field and biosphere. This project deals with the composition and properties of a glass wasteform for the immobilisation of historic and possible future HLW streams.

The historic waste examined is that stored on the Sellafield site in Highly Active Storage Tanks (HAST). These waste streams date from as early as the 1950s and are rich in U, Cr, Fe, Al and Mg. The long lived radioactive nature and toxicity of U make immobilisation of this element a priority. Aspects of a possible glass to immobilise this waste were examined including structure, redox, and durability.

The future wastes are those from alternative advanced reprocessing techniques. In the UK and France, nuclear fuel rods are reprocessed using the PUREX process: fuel cladding is first mechanically removed, the spent nuclear fuel is then dissolved in concentrated nitric acid, and the useful U and Pu are subsequently separated from the fission products by solvent extraction. The HLW arising from this process, comprising the fission products and minor actinides, is vitrified in a sodium lithium borosilicate glass matrix.

Alternative dissolution techniques for processing irradiated nuclear fuel can involve significant amounts of fuel assembly components being taken into solution. This leads to waste streams in which zirconium, iron, chromium and nickel account for 60-70 wt% on an oxide basis as well as fission products and non-recycled actinides (Maddrell 2001). The low solubility and refractory nature of zirconium oxide within borosilicate glasses means that economic vitrification in the standard glass compositions is a challenging task.

This work aims to characterize the structural role of Zr in alkali borosilicate glass and investigate alternative borosilicate compositions for the vitrification of this high Zr waste stream.

These project strands are brought together by the methodologies used and an effort to understand, through careful experiment and computer simulation, some of the fundamental science of nuclear waste glasses. This is done though the use of simplified compositions to look at the effect of individual elements (primarily U and Zr) and their structural role within, and effects upon, the nuclear waste glass network.

1.1 Glossary

^{IV}B and ^{III}B – 3 and 4 co-ordinated boron

BO – Bridging Oxygens

Dell-Bray model – Model describing the

DTA – Differential Thermal Analysis

EDS – Energy Dispersive Spectroscopy

EXAFS – Extended X-ray Absorption Fine Structure

$g(r)$ – partial distribution function

HLW – High Level Waste

K – $[SiO_2]/[B_2O_3]$

MAS-NMR – Magic Angle Spinning – Nuclear Magnetic Resonance

MD – Molecular dynamics

NBO – Non Bridging Oxygens

Q^n – Number of BO to a Si atom where Q^4 indicates a Si with 4 BO, Q^3 indicates a Si atom with 3 BO and one NBO etc.

R – $[R_2O]/[B_2O_3]$

R_2O – Alkali oxide (e.g. Na_2O)

T_f – fictive temperature

T_g – glass transition temperature

T_X – temperature of crystallisation

TEM – Transmission Electron Microscopy

v_{iO} – valence

XANES – X-ray Absorption Near Edge Structure

XRD – X-Ray Diffraction

σ – standard deviation

1.2 Publications and conferences from thesis

1.2.1 Refereed Papers in Primary Journals – Submitted

A. J. Connelly, N. C. Hyatt, K. P. Travis, R. J. Hand, R. J. Short, E. Maddrell, J. M. Charnock, The structural role of Zr within alkali borosilicate glasses for nuclear waste immobilisation, European Journal of Glass Science and Technology, 2007.

1.2.2 Contributions to conferences and meetings – Posters

A. J. Connelly*, N. C. Hyatt, K. P. Travis, R. J. Hand, E. R. Maddrell, Structural aspects of uranium in borosilicate glasses, Proceedings of the 21st International Congress on Glass, Strasbourg, France, July 2007.

1.2.3 Contributions to conferences and meetings – Talks

A. J. Connelly*, N. C. Hyatt, K. P. Travis, R. J. Hand, E. R. Maddrell, Vitrification of high zirconia nuclear waste streams: An EXAFS study, 4th Radioactive Waste Immobilisation Network meeting, 2005.

A. J. Connelly*, N. C. Hyatt, K. P. Travis, R. J. Hand, R. J. Short, E. Maddrell, J. M. Charnock, The structural role of Zr within alkali borosilicate glasses for nuclear waste immobilisation, 8th European society of glass conference, 2006.

A. J. Connelly*, N. C. Hyatt, K. P. Travis, R. J. Hand, E. R. Maddrell, Vitrification of high zirconia nuclear waste streams: An EXAFS study, Universities' Nuclear Technology Forum, 2006.

A. J. Connelly*, K. P. Travis, N. C. Hyatt, R. J. Hand, E. R. Maddrell, Modelling the structure of alkali borosilicate glasses with molecular dynamics, Society of Glass Technology Annual Conference, 2007.

2 Literature Review

2.1 Introduction to nuclear energy

Nuclear energy provides 25-30 % of the worlds energy needs and this figure may grow in the near future in response to international efforts to reduce future carbon emissions. In the UK approximately 19 % of our electrical energy is supplied from nuclear power. Almost all of the global nuclear energy is supplied by the U-fuel cycle; alongside electricity, this cycle produces radioactive waste (Wilson 1996, Aus 2007).

2.1.1 The nuclear reaction

Within a nuclear reactor (**Figure 2.2**), atoms of certain heavy elemental isotopes (e.g. U, Pu) are split into two or more daughter nuclei (fission). Splitting is caused by neutron absorption to form an unstable nucleus, this in turn fissions and produces large amounts of energy as heat. The majority of reactors use ^{235}U for which there are many possible reaction routes e.g.

$$^{235}_{92}U + ^{0}_{1}n \rightarrow ^{94}_{40}Zr + ^{139}_{57}La + 197 \text{ MeV} \qquad \textbf{Equation 2.1}$$

The range of fission products covers about a third of the periodic table (from around copper to the mid-lanthanides). The most common are clustered into two groups due to higher probability of asymmetric fission (see **Figure 2.1**). The reaction also produces neutrons which go on to cause other fission reactions (the chain reaction). The energy produced[1] is used to heat a fluid medium (e.g. water) which ultimately creates steam to drive a turbine (as in many fossil fuel electricity plants).

[1] The energy is produced according to the Special Theory of Relativity ($E = mc^2$). The energy in comes from a mass loss. However all neutrons and protons are conserved so the mass loss comes from a change in the overall binding energy of the atoms. Binding energy is the difference between the cumulative mass of the neutrons and protons and the actual mass of an atom.

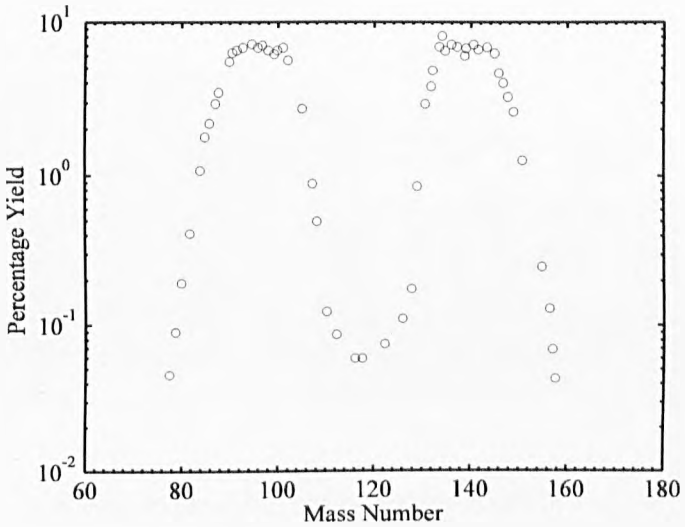

Figure 2.1: Fission products of U^{235} for slow (thermal)neutrons. Shows yield against mass number of atoms produced with the unsymmetrical distribution of daughter nuclei, after Uwaterloo (2007).

The nuclear chain reaction can only occur if neutrons of certain energies are available. The majority of reactors make use of thermal neutrons. These have been slowed (*via* elastic scattering with a material of low atomic number – a moderator) to achieve thermal equilibrium with their surroundings. The moderated neutrons are more efficiently captured by ^{235}U and ^{239}Pu nuclei causing nuclear fission. The Boiling Water Reactor (BWR), Pressurised Water Reactor (PWR) and Advanced Gas cooled Reactor (AGR) are all thermal reactors (i.e. they all make use of thermal neutrons). **Figure 2.2** shows a schematic of a PWR reactor.

Other types of reactor (outside the scope of this work) use fast neutrons, these Fast Breeder Reactors (FBR) do not use moderators, generating power from Pu fission while simultaneously transmuting ^{238}U to Pu in, or around, the fuel (Pu breeding). In this way FBRs can generate more than 50 times as much energy per kilogram of U ore than can a thermal system alone, and they are virtually self-sufficient in fuel. There has been limited uptake of this technology due to the large expense of new build and concerns about Pu proliferation.

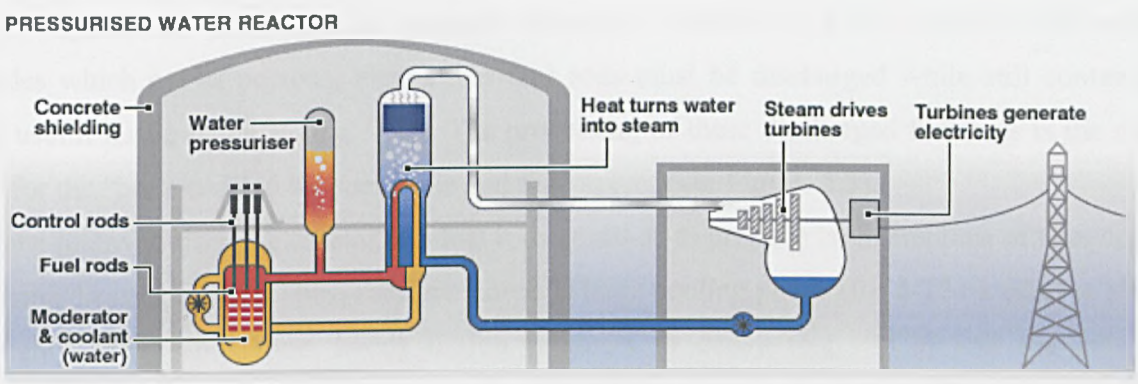

- **Fuel rods** – Uranium oxide (UO_2) arranged in tubes to form fuel rods. The rods are arranged into fuel assemblies in the reactor core.
- **Moderator** – This material slows down fast the neutrons released from fission (in PWR reactors water is used, alternative reactor types may use graphite, or heavy water).
- **Control rods** – Used to control fission process, made from a neutron absorbing material so can be raised or lowered to decrease or increase level of fission.
- **Coolant and steam generator** – liquid or gas (in PWR water is used, alternative reactor types may use CO_2 or liquid sodium) is used to remove heat from the core and to convert water to steam.
- **Pressure vessel or pressure tubes** – Either a robust steel vessel containing the reactor core and moderator, or a series of tubes holding the fuel and conveying the coolant through the moderator.
- **Containment** – The structure surrounding the core is usually concrete to protect those outside from the effects of radiation or any malfunction.

Figure 2.2: Layout of Pressurized Water Reactor with discussion in more general terms (Wilson 1996, BBC 2007).

2.1.2 Fuel rods

The majority of fuel rods are produced with ^{235}U as the main fissionable species, however, natural U contains only 0.72 at% ^{235}U. In order to reduce the cost per unit of energy produced, natural U is usually enriched to 3.5-5.0 % ^{235}U so as to allow a sustained reaction in a smaller core.

Whilst a fuel rod is in a reactor it is constantly being bombarded with neutrons and undergoing

fission. Thus, the proportion of ^{235}U and the structural integrity of the fuel rod decreases over time. This, alongside the production of neutron absorbing elements (e.g. Pu and Gd) and minor actinides which act as poisons, means that fuel rods must be discharged while still containing much useful fissile material (e.g. ^{235}U). The processing of these discharged fuel rods is the main focus for the "back-end" of the fuel cycle and this project (see **Figure 2.3**).

When removed from the reactor, the fuel rods continue to produce large amounts of heat due to radiogenic heating effects. Thus, they are stored in large cooling ponds (for 6-12 months) to allow the highly active (but short lived) fission products to decay (e.g. ^{144}Ce) and the external temperature to reduce sufficiently to allow more extensive remote handling. The spent fuel has two possible destinations: one is long term storage and disposal; the other is reprocessing to separate out the useful Pu and U from the wastes. About half of the worlds discharged reactor fuel is stored with a view to eventual disposal without further treatment.

There are several different fuel rod designs depending on reactor type. The PWR (**Figure 2.2**) uses UO_2 enclosed within Zircaloy fuel cans. In first generation Magnox reactors, a U metal rod was used encased in Mg alloy (Magnox) fuel cans (Donald *et al.* 1997).

Zircaloy

The efficiency of nuclear power stations is increased if the reactor temperature can be raised. This is difficult to achieve using U metal due to various temperature limitations: swelling due to the formation of fission product gases which form bubbles; a crystallographic phase change ($\alpha - \beta$) at ca. 650 °C and oxidation above 450 °C. Because of their higher temperature stability (with no phase change up to the melting point of ca. 2800 °C) UO_2 fuels are used to allow increased reactor temperature.

The higher temperatures achievable with oxide fuel preclude the use of Magnox alloy as a fuel cladding so a Zr alloy is used (Zircaloy). Zircaloy has good corrosion resistance and mechanical properties, which are stable under irradiation. It also has extremely low absorption of "thermal" neutrons. It can be manufactured into tubes, bars, and plates which form the framework of nuclear fuel assemblies (Wilson1996, Heynes & Rawson 1961).

Reprocessing via the plutonium-uranium extraction process

The Plutonium-URanium EXtraction (PUREX) process normally involves the mechanical removal of the cladding material from fuel rods followed by dissolution of the core in concentrated nitric acid. This stage is then followed by chemical solvent extraction of the U and

Pu; these can be processed for re-use. The remaining aqueous solution (High Level Liquid Waste - HLLW) is stored in stainless steel tanks prior to calcination, vitrification, storage and eventual disposal (see **Figure 2.3**).

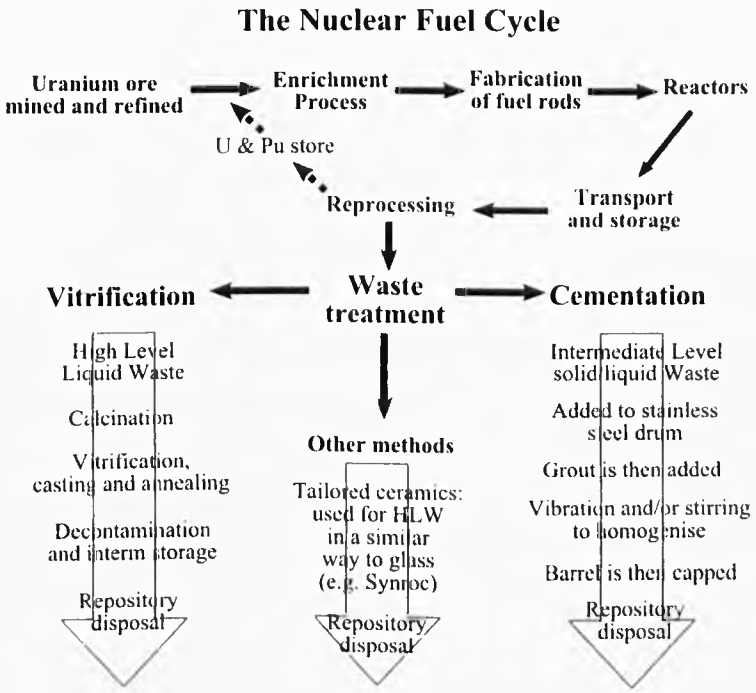

Figure 2.3: One form of the nuclear fuel cycle (after Wilson 1996).

Alternative reprocessing techniques

Two alternatives to the standard PUREX process have been proposed. These methods, electro-dissolution and Full Chemical Dissolution (FCD), involve partial dissolution of the fuel rod and fuel into solution (Rance 1998). This avoids mechanical processing of the fuel rods and so generation of related extraneous waste. Reprocessing of Zircaloy fuel rods by FCD would yield a waste composition high in Zr (see **Table 2.2**); this project is concerned, in part, with the vitrification of this waste stream.

2.1.3 Nuclear waste

Nuclear wastes are generated from a number of sources including the reprocessing of spent fuel, certain defence reprocessing operations, hospital, university, and commercial research activities. There are four main UK classifications of nuclear waste (Wilson 1996, DEFRA 2001):

- **High Level Waste (HLW):** wastes in which the temperature may rise significantly as a

result of radioactivity, so that this factor has to be taken into account when designing storage or disposal facilities. For example, spent fuel rods;

- **Intermediate Level Waste (ILW):** wastes with radioactivity levels exceeding the upper boundaries for low level wastes, but which do not require heating effects to be taken into account in the design of storage or disposal facilities. For example, fuel cladding;
- **Low Level Waste (LLW):** wastes containing radioactive materials other than those acceptable for disposal with ordinary refuse, but not exceeding 4 GBq/t alpha or 12 GBq/t beta / gamma. For example, shielding material;
- **Very Low Level Waste (VLLW):** wastes which can be safely disposed of with ordinary refuse (dustbin disposal), each 0.1 m^3 of material containing less than 400 kBq beta/gamma activity or single items containing less than 400 kBq beta/gamma activity per 0.1 m^3. For example, contaminated disposable safety gloves.

These waste streams may contain a wide range of elements from different sources, one example for HLW is shown in **Table 2.1**.

Source	Elements
Fission Products	Ge, As, Se, Rb, Y, Sr, Zr, Mo, Ru, Te, Nb, Ag, Cd, In, Sn, Cs, Ba, La, Ce, Pr, Sb, Dy, Nd, Sm, Eu, Gd, Tb
Actinides	Th, Pa, U, Np, Pu, Am, Cm
Corrosion Proucts	Fe, Cr, Ni, Nb, Mn
Cladding Materials	Mg, Al, Ni, Cr, Fe, Si, Zr, Nb
Fuel Additives	Be,Al, Fe, Cr, Ni, Mg, Ca, Si, Mn, Zr, Nb, Sb, Zn, Mo, Cd, P, Gd
Process Additives	Li, Na, Fe, SO_4, PO_4
Neutron Poison	Gd

Table 2.1: Source of some of the elements comprising blend waste (Magrabi 1988).

There are two main HLW streams dealt with at the Sellafield site. These are derived from reprocessing of Magnox and UO_2 fuels. Previously, Magnox HLW was vitrified at the Sellafield Waste Vitrification Plant (WVP). At present, Magnox and UO_2 HLW are blended in a 25:75 ratio (known as 'blend waste') prior to vitrification. Simplifed compositions can be found in **Table 2.2** with full compositions in the **Appendix B**.

Highly Active Storage Tank waste

The British nuclear program, at Calder Hall, grew from the Manhattan Project through to the first commercial nuclear reactor in 1956. During the early period of the nuclear industry many

different HLW waste streams were stored in Highly Active Storage Tanks (HASTs) on the Sellafield site. The composition of the waste contained in these tanks is similar to that of Magnox waste, however, the amounts of U, Al, Fe, and Cr are much increased. This project deals with wastes held in two HAST tanks, simplified compositions are shown in **Table 2.2** with the full compositions shown in **Appendix B**.

Oxide (mol%)	Magnox	Blend	High Zr	Tank A	Tank B
Al_2O_3	16.62	0.84		43.22	30.20
Cr_2O_3	1.44	1.53	3.45	0.70	1.91
Fe_2O_3	4.31	3.44	4.96	10.13	10.81
Gd_2O_3	0.49	4.33	0.57		
MgO	45.53	18.56		16.37	37.95
MoO_3	4.38	10.81	4.59	1.45	1.04
NiO			13.53	1.25	1.93
UO_3	Trace	Trace	Trace	14.24	6.83
ZrO_2	4.95	12.3	72.81	1.68	1.32
Other					

Table 2.2: Simplified compositions of main waste streams considered in this project. Showing the major components of FCD (High Zr) waste with comparison to two standard UK HLW compositions, Magnox and Blend (see below) (Magrabi 1988, Matlack *et al.*1999). See **Appendix B** for the full compositions.

2.1.4 Nuclear waste solutions

The aim of all nuclear waste management is the disposal of radioactive and/or toxic by-products of the nuclear industry in a manner which removes or minimises the possibility of environmental contamination.

Waste material is treated according to its form and the level of threat it poses. Thus, whereas VLLW can generally be incinerated and the ash put directly into landfill; HLW, dealt with here, must be immobilised within a host material. Ideally this should be a solid, stable and durable material, of minimum volume, that can be more easily stored or disposed of than the liquid waste. Immobilisation can be either by dissolution of waste elements on an atomic scale within a host lattice (e.g. glass or ceramic) or by encapsulation of the waste within an inert matrix (e.g. cement) (Donald *et al.* 1997).

After immobilisation, long term storage of the wasteform for up to 1 million years must be considered. Various methods have been suggested the most widely accepted being imprisonment within stable geological features. These can be either above the water table (e.g. Yucca mountain

in USA) or below in dry or low water flow conditions (e.g. salt mines in Germany or clay in Switzerland, respectively).

Assuming the resulting "vault" remains undisturbed (e.g. from tectonic activity, human interaction, or natural erosion) the only mechanism for the escape of radioactive and toxic elements would be aqueous dissolution of waste from ground water penetration. Using effective multi-barrier designs water penetration can be significantly delayed, ideally until radioactivity is at a safe level. However, should water penetration occur before this time any wasteform used must be durable enough to retain radioactive elements until they are sufficiently decayed (Donald *et al.* 1997, Pegg 2001). Another option is that of very deep geological disposal (Gibb 2000) within boreholes at such a depth (ca. 5 km) as to avoid mobile ground water altogether.

2.1.5 Vitrification

From the Latin *vitrum*, meaning glass, the art of vitrification or glass making has been known for thousands of years. However, the art / science of nuclear waste vitrification was only established 50 years ago in the UK, France, Germany, Italy, Canada, USA, former USSR, India and Japan. The principles are very simple: design a suitable glass host and dissolve the maximum level of HLW possible while retaining a stable, homogeneous melt that can be cast into large, durable glass blocks (Donald 1997, Pegg 2001).

In principle, glass is a good medium for nuclear waste immobilisation, having a flexible structure with a varying degree of connectivity allowing for the accommodation of large variations in composition. In other words, unlike crystalline ceramics, glass can act like a solvent with little need for a stoichiometic composition (Varshneya 1994).

The modern vitrification process predominantly uses alkali borosilicate glasses (glasses such as phosphates are also used or have been considered but are outside the scope if this work); which are discussed in more detail in **Section 2.2.1**.

Processing

The specific processing route used in the UK is shown in **Figure 2.4**. There are three main phases (Lutze & Ewing 1988, Donald 1997):

1. **Evaporation** of the radioactive waste concentrate to dryness at 100 °C;
2. **Calcination,** partial denitration to oxides, at temperatures up to 600 °C. Addition of sucrose (to avoid oxidation and volatilisation of ruthenium as RuO_4) and lithium nitrate

(this is added to act as a flux[1] within the glass melter and to prevent the formation of refractory phases (e.g. $MgAl_2O_4$)). Not all the nitrates are removed during calcination leaving the waste calcine sticky so reducing dust formation;

3. **Vitrification,** formation of a glass melt between the waste oxides and the glass formers. An inductively heated Inconel 601 melter is used. A sodium-lithium borosilicate frit is added with the calcine until ca. 25 wt% waste loading is achieved. This batch is held close to 1060 °C for 5-8 hours, and sparged with air. It is then poured into stainless steel canisters (400 kg; filled in two pours), cooled and stored. The melting temperature must be kept as low as possible to minimize volatilisation of fission products (e.g. ^{137}Cs) and to reduce corrosion of the melter.

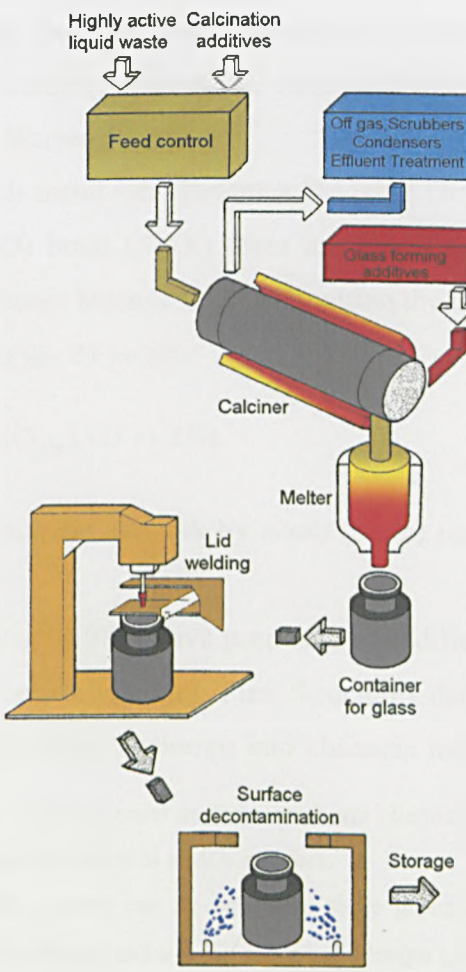

Figure 2.4: Flow chart for glass wasteform manufacture. (After Marples 1998).

[1] Flux: an additive that improves flow properties of melt, generally by reducing viscosity.

2.2 Glass structure

There are two general conceptual approaches to glass formation: one is *structural* and based upon geometric and chemical considerations; the other is *kinetic* and based on the avoidance of crystallisation (see **Section 2.6.2**). The first realistic structural model for glass was proposed by Zachariasen (1932).

In the Continuous Random[1] Network model (CRN), Zachariasen postulated that both crystals and glass have an extended three-dimensional network. Glasses have a non-periodic random network structure; i.e. for silicate glasses the neighbouring silicate tetrahedra are variably orientated, whereas in crystalline form this orientation is invariant. For silicate glasses the Zachariasen model consists of silicate tetrahedra in 5-8 membered rings with little or no long range order (periodicity). This structure is also postulated for alkali silicates but in this case alkali metal ions (e.g. Na^+, Li^+) randomly occupy the holes within these rings, this is known as the Zachariasen-Warren Model (Warren 1941).

The addition of each alkali metal ion changes a Bridging Oxygen (BO) bond (Si-O-Si) into a Non-Bridging Oxygen (NBO) bond ($Si\text{-}O^-$) these are thus known as network modifiers[2]. The alkali ions (e.g. Na^+) act to charge balance the NBOs within the network (see **Figure 2.7**):

$$Si-O-Si+Na_2O \rightarrow 2(Si-O^-)+2Na^+$$

or

$$Si(O_{1/2})_4+Na_2O \rightarrow Si(O_{1/2})_3(O^-)+2Na^+$$

Equation 2.2

This modification of the silicate network by alkali (earth) ions has significant effect on glass properties such as viscosity.

More recently Greaves *et al.* (1981) have proposed a modification to the Zachariasen-Warren Model. Based on XAFS (X-ray Absorption Fine Structure) data from Si and Na K-edges they proposed a system of bonded alkali clustering into channels interlacing the silicate network (see

---

[1] The use of the term random is controversial as there are basic chemical rules that control the range of angles subtained between corner linked MO_4 units in a MO_2 network.

[2] Constituent elements in oxide glasses can be split into three groups using the concept of field strength ($F=Z/a^2$) where Z is the ionic valence and a is the oxide bond length (Å) (Dietzel 1942):

1. Network formers, $F \approx 1.5-2.0$ (e.g. Si^{4+}, B^{3+}), glass formers by themselves or with other oxides ;
2. Network modifiers, $F \approx 0.1-0.4$ (e.g. Na^+, Ca^+), cations forming highly ionic bonds with oxygen. They modify the glass network by breaking bonds; and
3. Intermediates, $F \approx 0.5-1$ (e.g. Zr^{4+}, Ti^{4+})., behave somewhere in between a glass former and a modifier, and can more easily form a glass when combined with a second component.

Figure 2.5). This theory, the Modified Random Network (MRN) theory, has been supported by various authors including recently Voigt *et al.* (2005) in lithium silicate glasses. Using Rotational Echo Double Resonance (REDOR), NMR and MD simulations Voigt *et al.* showed a nano-phase channel like segregation of Li ions surrounded by Si tetrahedra with NBOs.

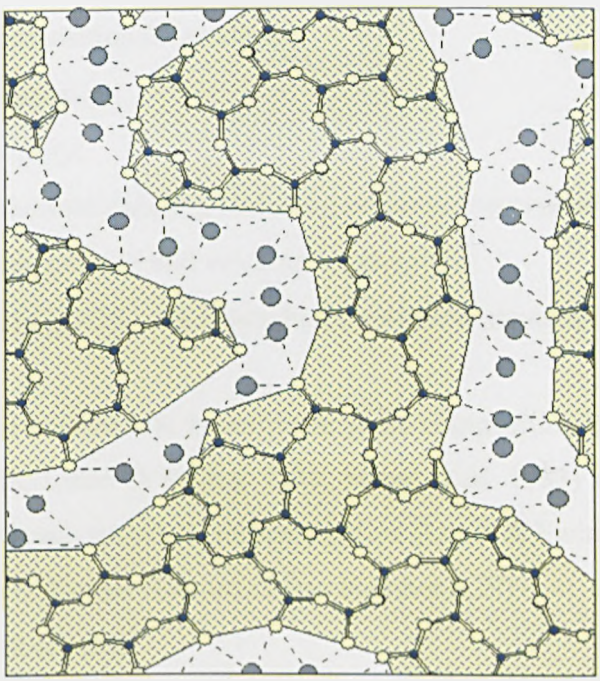

Figure 2.5: Two-dimensional schematic representation of the modified random network (MRN). Structure shows percolation channels formed by monovalent alkaline cations (in grey hash) loosely bonded with oxygen atoms (white) of surrounding silicate groups (in black). (Hand & Seddon 1997) after (Greaves *et al.* 1991).

2.2.1 Borosilicate glass

The structure of borosilicate glass is more complex than that of pure silicate glasses. This is due, in part, to the variation in boron co-ordination with composition (see below) and to the possibility of phase separation of the glass into B rich and Si rich zones. This can occur either when an emulsion of these phases forms, over time, in the melt (spinodal decomposition), and these phases remain separate on cooling; or, if an appropriate heat treatment is applied to an initially *homogeneous* glass. The high B region has a much reduced durability; an effect which is exploited in the production of Vycor glass (Varshneya 1994), but is undesirable in nuclear waste glasses.

Why use borosilicate glass?

The use of certain borosilicate glass compositions has long been preferred for immobilization of HLW. This is because these compositions meet many of the requirements for an effective nuclear wasteform (Donald 1997, Lutze & Ewing 1988, Pegg 2001):

- Good chemical durability (despite the issue of phase separation);
- Tolerance of compositional variations;
- Low thermal expansion;
- Mechanical integrity;
- Radiation and thermal stability, including resistance to crystallisation;
- Low melting temperature and working temperature;
- High waste loading, >25 wt% depending on waste composition.

The details of how the current UK borosilicate glass composition was developed are treated elsewhere (Hayward 1988, Lutze & Ewing 1988, Soper *et al.* 1983) and will not be discussed here. However, the role of each species is outlined below (Lutze & Ewing 1988, Volf 1984):

- Si^{4+}, cationic network former (Co-ordination Number (CN) = 4), strong bond with oxygen;
- O^{2-}, anionic network former;
- B^{3+}, network former (CN = 3, 4), acts as a flux in silicate glasses. Co-ordination is dependent on both composition and thermal history (see below);
- Na^{+}, network modifier (CN = 6, 8), acts as a flux and tends to decrease chemical durability;
- Li^{+}, network modifier (CN = 4), highly mobile in an electric field, thus aiding electric melting and smaller radius and high field strength giving stronger bond to oxygen (silicate network) so improved durability compared to Na. Li is thought to encourage phase separation.

Co-ordination environment of boron in glasses

The co-ordination of B can be as both 4 co-ordinate tetrahedral (^{IV}B) and 3 co-ordinate trigonal (^{III}B) units. The ratio of these two groups is mainly dependent on temperature, thermal history and glass composition. In a melt, increasing temperature (> 600 °C) will tend to stabilize lower co-ordination ^{III}B as compared to ^{IV}B. This has the effect of lowering melt viscosity. No definite change in environment with temperature is seen in the degree of polymerisation of the silicate glass network in borosilicate glasses (Sen *et al.* 1998).

At room temperature, the ratio of ^{III}B to ^{IV}B is dependent on the rate at which the melt is cooled (the degree to which the high temperature structure has been "frozen in") and the composition of the glass.

In a single alkali borosilicate glass, the introduction of alkali ions into the borate network first transforms the ^{III}B units, into $^{IV}B^{-}$ units without creating any NBOs, thus increasing network connectivity. The increased network connectivity leads to increased glass transition temperature (T_g – see **Section 2.6.2**) and thermal expansion. However, at a certain concentration of alkali oxide this trend is reversed and a decrease in these properties is observed, due to formation of NBOs (Zhong1989). The original Dell-Bray model is based on superstructural units in borate and borosilicate glasses, these have been left out of this description to simplify presentation. This is explained in more detail in **Figure 2.6** and below, where 'M' indicates an alkali ion (e.g. Na, Li, *etc*) (Dell *et al.* 1983):

$$R=\frac{[M_2O]}{[B_2O_3]} \text{ and } K=\frac{[SiO_2]}{[B_2O_3]} \qquad \textbf{Equation 2.3}$$

- **Region 1:** Fraction $^{IV}B \propto R$ – linear increase in ^{IV}B (converting from ^{III}B) -Within this region no interaction between the borate and silicate networks is expected to occur. This is a possible explanation as to why glasses in this composition region have a tendency to phase separate (see **Figure 2.7a**).

$$B(O_{1/2})_3+M_2O \rightarrow B(O_{1/2})_4+2M^{+} \qquad \textbf{Equation 2.4}$$

- **Region 2:** In this region, added alkali combines with the ^{III}B and ^{IV}B units however, this occurs at a reduced rate as there is also some depolymerisation of the silicate network (see **Figure 2.7b**).

$$Si(O_{1/2})_4+M_2O \rightarrow Si(O_{1/2})_3(O^{-})+2M^{+} \qquad \textbf{Equation 2.5}$$

- **Region 3:** No changes in ^{IV}B fraction. Depolymerisation of silicate network.
- **Region 4:** Depolymerisation of both borate and silicate networks, ^{IV}B changes to ^{III}B. In this region it is assumed that the alkali oxide divides itself proportionately according to the numbers of B and Si atoms in each unit.

This model will be used for comparison with computer simulation and laboratory data. Both Si and B co-ordination will be presented with reference to this model. Other models are available but the Dell Bray model (Dell *et al.* 1983) can be applied to any K value and any R value. It has also shown to be reasonably accurate for both the Si and B co-ordination (Bhasin *et al.* 1998).

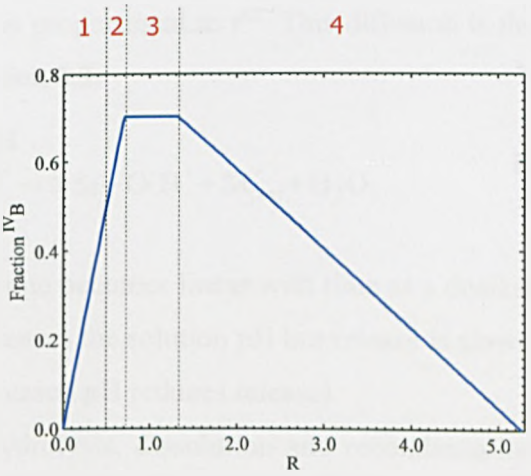

Figure 2.6: Change in fraction of four co-odinated B with addition of alkali ions to a borosilicate glass based on model proposed by Dell and Bray (Dell *et al.* 1983). Data based on $K = 3.27$.

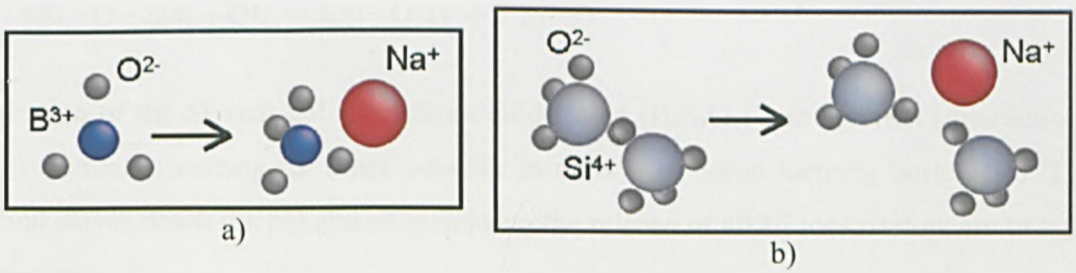

Figure 2.7: Schematic showing a) process of NBO formation and b) change from 3 to 4 co-ordinated boron when alkali cations are added to the glass. Ionic radii are not to scale.

2.2.2 Alkali borosilicate glasses: chemical durability and structure[1]

Glass durability is a function of many variables including: waste loading and composition; leachate composition, pH, and flow rate; redox potential; temperature; diffusion coefficients; formation of surface layers; crystallisation of the glass; phase separation; and the effects of radiolysis (Lutze & Ewing 1988). Below is presented a simplified mechanism for aqueous corrosion of an alkali borosilicate glass, the whole process is summarised in **Figure 2.8** and **Figure 2.9** (Bunker *et al.* 1990, Donald *et al.* 1997, Ellison *et al.* 1994b, Godon *et al.* 2003, Greenwood & Earnshaw 1993, Lutze & Ewing 1988, Ojovan *et al.* 2006)

In an aqueous static leaching scenario it is generally considered that the initial reactions involve ion-exchange of soluble alkali ions for H_3O^+ (also OH^-), this is a diffusion controlled process the rate of which is proportional to $t^{1/2}$. This diffusion is thought to occur along the alkali channels discussed in **Section 2.2**.

$$2H_2O \rightarrow H_3O^+ + OH^-$$
$$\equiv Si-O^-M^+ + H_3O^+ \rightarrow \equiv Si-O^-H^+ + M^+_{(aq)} + H_2O$$

Equation 2.6

Next, the alkali release rate becomes linear with time as a dealkanised hydrated surface layer is formed. Alkali release increases the solution pH but release is slowed by the build up of alkali and hydroxide in solution (increased pH reduces release).

Concurrently, partial hydrolysis, dissolution and recondensation of the glass network occurs with the formation of a (silica) gel layer. This process is accelerated by the high pH associated with highly alkaline solution, the pH increase associated with alkali release slows the alkali release rate but accelerates the hydrolysis reaction.

$$\equiv Si-O-Si\equiv + H_2O \rightarrow 2(\equiv Si-O^-H^+)$$
$$\equiv Si-O-Si\equiv + OH^- \rightarrow \equiv Si-O^-H^+ + \equiv Si-O$$

Equation 2.7

Hydration of the Si–rich gel can release silicic acid (H_4SiO_4) into solution (dissolution), with similar reactions occurring for other network formers (e.g. boron forming boric acid). This acid formation drives down the pH and so increasing the release of alkali ions. Below are two possible mechanisms:

---

[1] Some definitions: **chemical durability** – relative resistance of a material against attack from aqueous solutions measured in laboratory and field studies; **glass dissolution** - general term referring to the release of glass components into solution; **glass alteration** – refers to any physical or chemical change of the glass; **glass corrosion** – general term for all alteration mechanisms of glass caused by reaction with chemicals (i.e. water).

$$\equiv Si-O-Si(OH)_3+H_2O \rightleftharpoons \equiv Si-O^-H^+ + Si(OH)_4$$
$$\equiv Si-O-B(OH)_2+H_2O \rightleftharpoons \equiv Si-O^-H^+ + B(OH)_3$$

Equation 2.8

The above reactions depolymerise the glass network and produce silanol groups (Si-OH). The concentration of $H_4(SiO_4)$ in solution is reported to be a major factor in controlling glass dissolution rate, with increased $H_4(SiO_4)$ concentration giving decreased network dissolution rate. The hydrolysis of the glass network governs the overall rate of dissolution following an initial, short-lived period of ion exchange and surface gel layer formation.

$$2(\equiv Si-O^-H^+) \rightleftharpoons \equiv Si-O-Si\equiv + H_2O$$
$$(\equiv Si-O^-H^+)+H_4SiO_4 \rightleftharpoons \equiv Si-O-Si(OH)_3+H_2O$$

Equation 2.9

Precipitation from solution of amorphous and crystalline phases can also occur at the glass-solution interface. This can have major effects on glass dissolution as the process of precipitation removes elements from the solutions so providing a thermodynamic driving force for further dissolution (e.g. **Figure 2.10**)

Borosilicate glasses are resistant to mildly acidic solutions (with the exception of hydrofluoric or phosphoric acids), but are attacked more readily by alkaline solutions (Volf 1984).

Composition has a major effect on durability. Leach rates of borosilicate glasses are lowest when alkali oxide to boron content is equimolar (corresponding to mostly ^{IV}B boron) (Marples 1988), indicating the stability of ^{IV}B species. Leach rates are further lowered if the alkali oxide content is comprised of equimolar amounts of two different alkali oxides ('mixed alkali effect'). Higher Si content tends to produce high durability (due to fewer NBOs); also, the presence of Al, Ca and Zn in a borosilicate glass have all been shown to improve aqueous durability (Lutze & Ewing 1988, Marples 1988).

Another major effect on the reaction kinetics of glasses is temperature, with increased temperature of the contacting solution there is an increase in reaction kinetics thus giving increased leach rate. This effect is exploited during accelerated leach tests (see **Section 3.6.3**). One of the major effects of this is a much reduced transition time between ion exchange to hydrolysis dominated corrosion, also promoting the hydrolysis reactions.

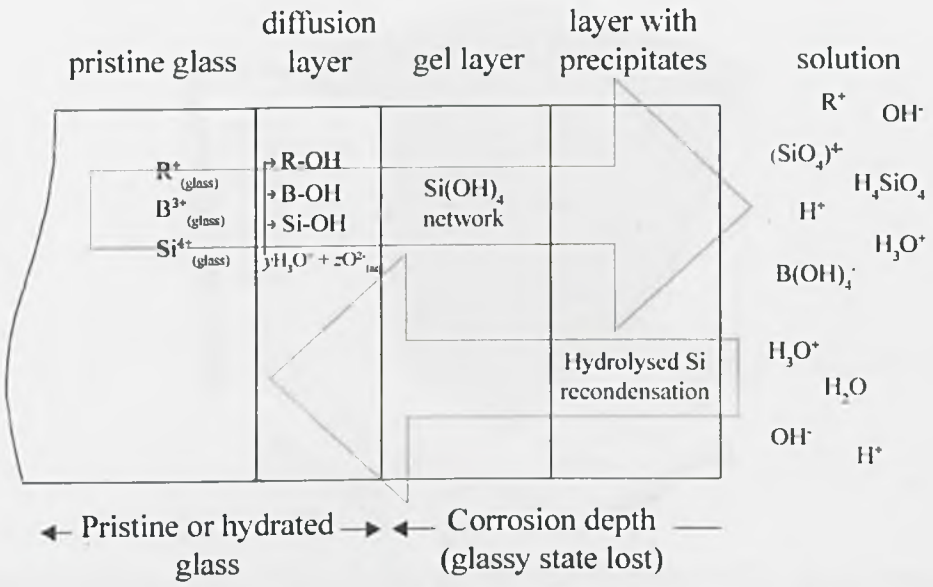

Figure 2.8: Schematic of corrosion processes in an alkali borosilicate glass.

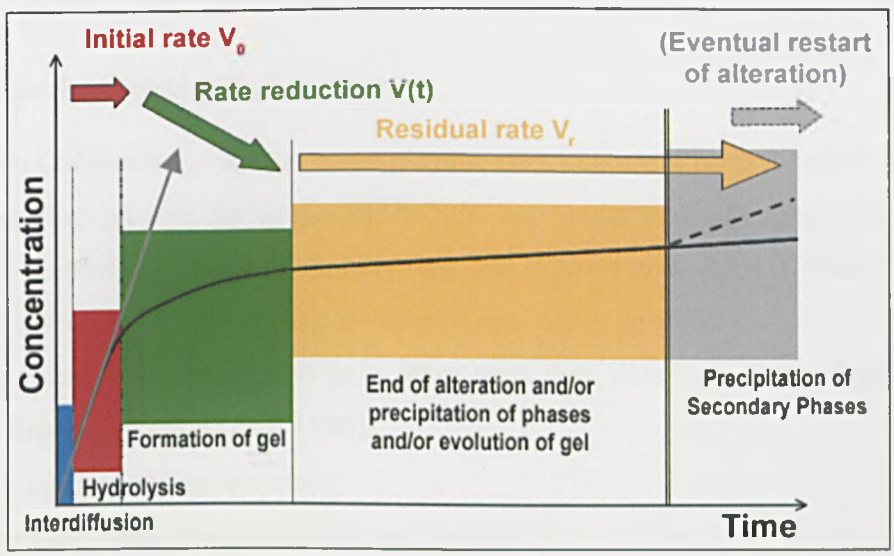

Figure 2.9: Schematic of corrosion processes for an alkali borosilicate glass in a static or slow moving aqueous system. Translated from original French from Godon *et al.* (2003).

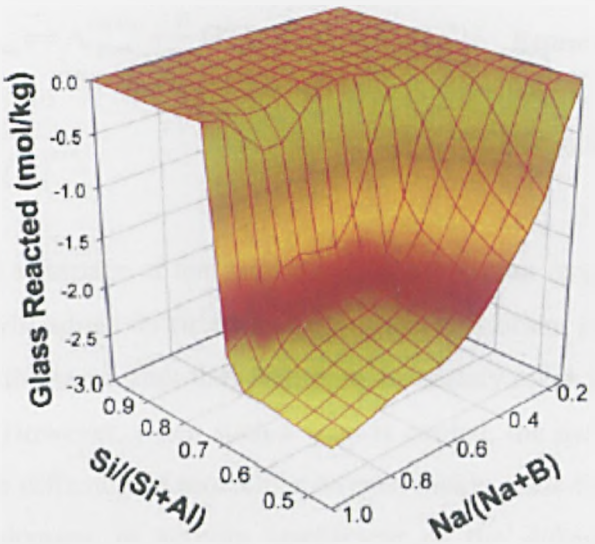

Figure 2.10: Durability of borosilicate glasses showing drop off in zeolite (analcine) formation region. The analcine forms on the glass during leaching and leads to a decrease in glass durability (Strachan 2001)

2.3 Redox and oxygen ion activity

The REDuction OXidation (redox) process plays a very important role in both the conventional glass manufacturing process (in preparing bubble free melts and adjusting colour) and HLW vitrification (in controlling element solubility (e.g. Pu) (Cachia *et al.* 2006)). Redox is particularly important in HLW glass due to the large number of polyvalent species.

Where polyvalent ions are present in a glass melt they distribute themselves into different valence states depending upon (Paul 1990):

1. Melting time and temperature;
2. Annealing, time and temperature at $T_g \pm 50$ °C;
3. Glass and batch composition;
4. Furnace atmosphere (partial pressure of O_2, f_{O_2});
5. The type and concentrations of polyvalent ion in the melt.

The general redox formula for glasses with a single polyvalent ion, A, with the equilibrium constant (K), where it is assumed polyvalent elements are sufficiently dilute for their ion activities to be replaced by concentrations, is given by **Equation 2.10** and **Equation 2.11** where $a_{O^{2-}}$ is the oxygen activity.

$$A^{m+}_{(glass)} + \frac{n}{4} O_{2(atm)} \rightleftharpoons A^{(m+n)}_{(glass)} + \frac{n}{2} O^{2-}_{(atm)}$$ **Equation 2.10**

$$K = \frac{[A^{(m+n)}]}{[A^{m+}]} \cdot \frac{a_{O^{2-}}^{n/2}}{(f_{O_2})^{n/4}}$$ **Equation 2.11**

A melt equilibrated in a furnace at temperature, *T*, at a constant oxygen partial pressure in the presence of a redox ion will adjust its structure to give an equilibrium standard free energy. If two redox ions are present in the same melt they will both separately reach an equilibrium free energy with limited interaction. However, when such a melt is cooled, the melt becomes "cut-off" from atmospheric oxygen since diffusion of molecular oxygen inside glass-forming melt is a very slow process. Now, due to changes in activity coefficient of the different redox elements with temperature, the free energy of different redox systems will follow different, diverging paths. This gives rise to mutual redox down to a viscosity (fictive temperature (see **Section 2.6.2**)) at which structural rearrangement becomes impossible (Paul 1990).

$$z\,A^{(m-y)+}_{(glass)} + y\,B^{n+}_{(glass)} \rightleftharpoons z\,A^{(m)}_{(glass)} + y\,B^{(n-2)}_{(glass)}$$ **Equation 2.12**

The driving force for these redox reactions can be measured using the electromotive force (emf) series (or electrochemical series). This series is common for aqueous systems (Atkins 1999) but more difficult to measure (due not least to the high temperatures involved) in a glassy systems. One example of the emf series in glasses is that of Schreiber *et al.* (Schreiber & Balazs 1984a). A selection of the results (those relevant to this project) are reproduced in **Figure 2.11**. Under standard conditions (RTP) –log f_{O_2} is equal to ca. 0.7 (on the y-scale) where log f_{O_2} can be thought of as the partial pressure of oxygen in the atmosphere during glass melting.

An alternative approach to the redox concept is that the process is governed by activity of oxygen ions[1], $[O^{2-}]$, within the glass (see **Equation 2.13**). In fact it could be said that all the redox dependences listed above affect the oxygen ion activity and this is then changing the redox of the glass. Increasing $[O^{2-}]$ leads to more oxidized polyvalent ions and more NBOs are produced within the glass. Obviously increasing oxygen concentration within the melt will increase $[O^{2-}]$, however, the compositional effects of cation additions on $[O^{2-}]$ are based on the relationship:

$$\Delta[O^{2-}] \propto \frac{1}{\Delta X}$$ **Equation 2.13**

[1] Oxygen ionic activity can be equated with the acid-base concepts in glasses where increased activity is equivalent to increased basicity (Douglas *et al.* 1965).

where χ is the electronegativity of the element addition. Thus, with alkali additions, $[O^{2-}]$ increases with $K^+ > Na^+ > Li^+$, with Li being the least electropositive and so restricting free electron donation (Duffy 1996).

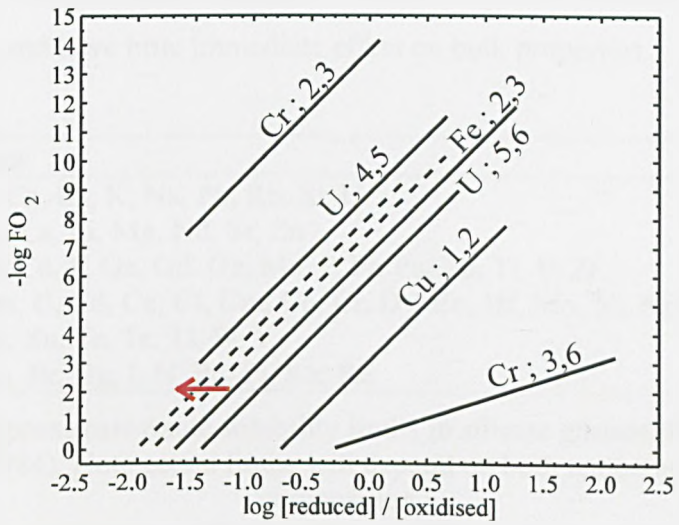

Figure 2.11: Change in redox of various multivalent ions with oxygen fugacity. Dashed lines indicate increasing Fe_2O_3 content (1 wt%, 5 wt%, and 10 wt% increasing with arrow). After Schreiber *et al.* (Schreiber & Balazs1984a).

2.4 Elements in glass

For simple systems the effect of compositional variation on physical properties[1] such as refractive index and density can be considered as the additive resultant of the constituent oxides (Volf 1988):

$$L = \Sigma l_i x_i \qquad \textbf{Equation 2.14}$$

where L represents the value of some property, x_i is the proportion of the ith oxide in the given glass and l_i is the effect of the ith oxide.

Unfortunately, this additive approach and other similar constitutive equations (Volf1988) have limited usefulness due to differences in structure between oxides and glasses and non-linear interactions between different components. This becomes more acute with more complex glass formulations (as used in the nuclear industry) where interactions between constituents, e.g. boron co-ordination and mixed alkali effect, become important; and where properties such as viscosity

[1] Of the type independent of chemical bonds i.e. dependent on electron configuration and polarizability of atoms.

and durability are considered[2].

In the following sections the experimentally observed effects of elements relevant to this project are discussed. Some approximate solubilities of various elements in borosilicate glass are shown in **Table 2.3**. Elements with solubility <1 wt% e.g. noble metals are mostly dispersed throughout the matrix and have little immediate effect on bulk properties.

Solubiliy	Element
>25 wt%	Al, B, Ca, Cs, K, Na, Pb, Rb, Si, U
15-25 wt%	Ba, Fe, La, Li, Mg, Nd, Sr, Zn
5-15 wt%	Be, Bi, Cu, F, Ga, Gd, Ge, Mn, P, Pr, Pu, Th, Ti, V, Zr
1-5 wt%	Am, As, C, Cd, Ce, Cl, Cm, Co, Cr, Dy, Eu, Hf, Mo, Ni, Np, Pm, Re, S, Sb, Se, Sm, Sn, Tc, Te, Tl, W, Y
<1 wt%	Ag, Au, Br, Hg, I, N, Pd, Pt, Rh, Ru

Table 2.3: Approximate oxide solubility limits in silicate glasses (Pegg & Joseph 2001, Volf 1984). Note actual limits will depend on both temperature and glass composition.

2.4.1 Zirconium (Zr)

Zirconium (^{40}Zr, [Kr].$4d^2.5s^2$) predominantly exists as Zr^{4+} and has 4 isotopes (including a radioactive isotope $^{40}_{96}Zr$, with natural abundance 2.76 %, $t_{1/2} = 3.6x10^{17}$ yrs). It has a high oxygen affinity occurring predominantly as zirconia (ZrO_2) which has a very high melting point (2710 ± 25 °C) and has a technologically important crystallographic phase change (from monoclinic to tetragonal at ca. 1170 °C) (Greenwood & Earnshaw 1993). ZrO_2 is chemically unreactive and has low solubility in glass. However, ZrO_2 and zircon can be broken down by reaction with sodium hydroxide (NaOH, ca. 600 °C), sodium carbonate ($NaCO_3$, ca. 1000 °C) or calcium oxide (CaO, > 1000 °C) (Stevens 1983), e.g:

$$ZrO_2 + Na_2CO_3 \rightarrow Na_2ZrO_3 + CO_2 \qquad \textbf{Equation 2.15}$$

ZrO_2 can impart the following properties to silicate glasses (Volf 1984):

- **Increased chemical durability.** This effect is significant in silicate glasses, increasing chemical resistance to water and acids, and particularly to alkaline solutions. Discussed in more detail below;
- **Increased density;**

[2] Properties such as electrical conductivity and thermal expansion are reliant on the type and energy of chemical bonds so are non additive. Durability is, in part, an interfacial effect and again not simply additive.

- **Increased viscosity and liquidus temperature;**
- **Decreased thermal expansion;**
- **Increased compressive and tensile strength** and decreased modulus of elasticity;
- **No colouration;**
- **Can promote phase separation,** as seen in Vycor glasses;
- **Can act as a nucleating agent.**

Zr and solubility

The high density of ZrO_2 and low solubility often lead to the settling of ZrO_2 during melting. The compositional dependence on ZrO_2 solubility has been reported by various authors (Andrews & Gates 1940, Dimbleby *et al.* 1927, Ellison *et al.* 1994a, King & Andrews 1941, Kinzie & Commons 1934, Volf 1984) and appear to have an additive effect:

1. The amount of ZrO_2 dissolved is approximately proportional to the alkali content with the effect increasing in the order Li < Na < K;
2. Al_2O_3, ZnO and MgO decrease the amount of ZrO_2 that may be dissolved (see below);
3. CaO, SrO, and BaO increase the solubility about 1 part for every 5 parts added;
4. Ratio of B_2O_3 to SiO_2 shows relatively small effect on the solubility of ZrO_2.

The need for charge balancing alkali (earth) ions with addition of Al_2O_3 to a glass decreases the number of available alkalis in the glass. It has been shown that change in solubility of ZrO_2 varies in a fixed stoichiometry with the number of alkali ions in excess of that needed to charge compensate aluminium[1] (Ellison & Hess 1986, Volf 1984). This indicates the need for alkali ions to be available for Zr to be incorporated in the glass. In a study of zircon solubility in felsic[2] melts (water saturated analogues of granitic liquids) Watson (1979) concluded that : "Zircon solubility in felsic melts appears to be controlled by the formation of alkali zirconosilicate complexes of simple (2 : 1) M_2O:ZrO_2 stoichiometry." However, these experiments were carried out under 2 kbar pressure at 700-800°C. This result was supported in a Raman study of potassium silicate glasses by Ellison and Hess (1994a). However, they suggested a ratio of 1:1. Work by Harrison and Watson (1983) showed that at higher temperatures a lower (Na,K):Zr ratio was required to stabilise the same amount of Zr^{4+} in the liquid. Batch pre-sintering (preventing settling) and

[1] Interestingly the addition of B_2O_3 appears to have little effect on this relationship (Davis2003).

[2] Felsic : a portmanteau of the words "feldspar" and "silica". It refers to silicate minerals, magmas, and rocks which are enriched in the lighter elements such as silicon, oxygen, aluminium, sodium, and potassium.

increased temperature also increase the solubility of ZrO_2 (Volf 1984). Using temperatures up to 1450 °C Wang *et al.* (2002) found that 23.5 wt% (12.2 mol%) ZrO_2 was soluble a glass of composition $56.9SiO_2$-$30.9Na_2O$-$12.2ZrO_2$. Similar solubilities were found in soda-lithia-silicate and soda-lithia-calcia-silicate glasses. This shows that high levels of alkali are required to dissolve high ZrO_2 concentrations.

Aqueous chemistry

The Zr^{4+} ion is extensively hydrolyzed. Only at very low concentration (ca. 10^{-4} *M*) and high acidities does a $Zr^{4+}_{(aq)}$ ion appear to exist. The existence of a ZrO^{2+} ion has not been confirmed. Instead, there seems to be a more or less direct conversion of $Zr^{4+}_{(aq)}$ to $[Zr_4(OH)_8(H_2O)_{16}]^{8+}$ and $[Zr_8(OH)_{20}(H_2O)_{24}]^{12+}$ species, the ratio being dependent on pH (Cotton *et al.* 1999).

Effect of ZrO_2 on durability

The first systematic work on glass durability with ZrO_2 was carried out by Dimbleby (1925). This work involved powdering various glasses with composition $(SiO_2)_6(Na_2O)_{2-x}(RO \text{ or } R_2O_3 \text{ or } RO_2)_x$ then applying a severe leaching technique where samples were washed and then boiled variously in water, NaOH, Na_2CO_3, and $HCl_{(aq)}$. ZrO_2 improved durability in all conditions more effectively than all the other elements (see **Figure 2.12**).

Horak and Sharp (1935) showed that by equimolar replacement of Al_2O_3 by ZrO_2 an improvement in durability of a sodium borosilicate glass could be achieved.

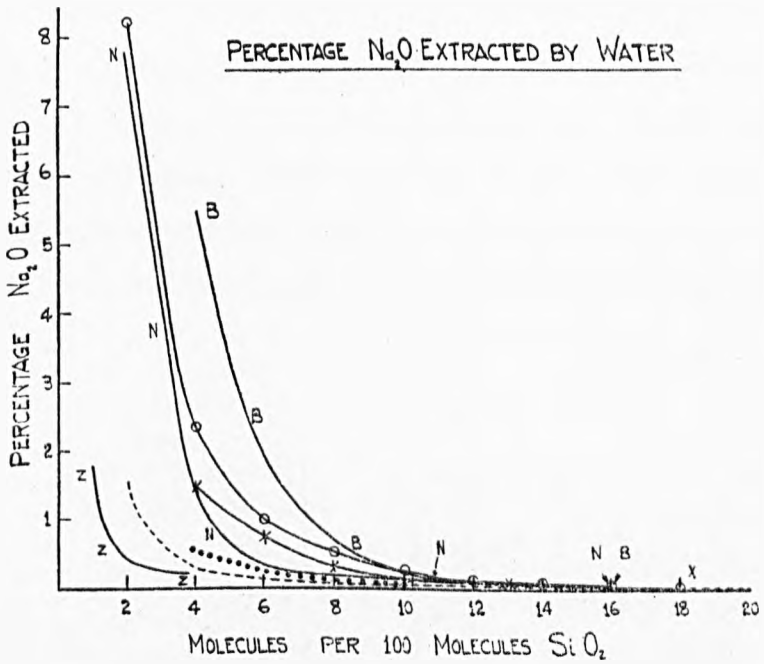

Figure 2.12: Effect on Na_2O extraction of various compositional additives within a $(SiO_2)_6(Na_2O)_{2-x}(RO \text{ or } R_2O_3 \text{ or } RO_2)_x$ glass where R = ZnO (N), ZrO_2 (Z), CaO (O), MgO (X), BaO (B), TiO_2 (---) and Al_2O_3 (····) (Dimbleby *et al.* 1925).

The simplified form of the reactions that are thought to occur during leaching of Zr from a borosilicate glass are shown in **Figure 2.13**.

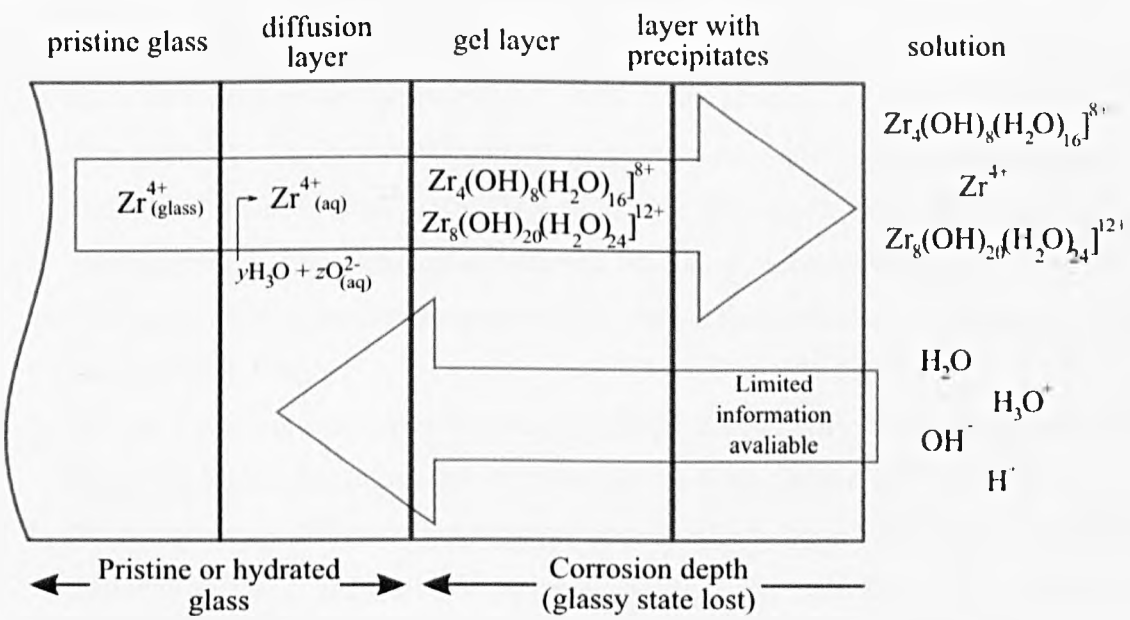

Figure 2.13: Proposed scheme for leaching of Zr^{4+} from a (boro)silicate glass.

Studies that tested borosilicate glass, so being more relevant to this project, were reported by Sicard *et al.* (2004) and Lobanova *et al.* (2002) both using a simplified borosilicate glass ($70SiO_2$-$15Na_2O$-$15B_2O_3$). Lobanova *et al.* used powdered and washed samples under room temperature static leach conditions, tested over two months. Their results show that with increasing ZrO_2 content an overall increase in durability for all elements is seen (see **Figure 2.14**). However, at low ZrO_2 concentrations (<2 mol%) there is a higher leach rate than at 0 mol%.

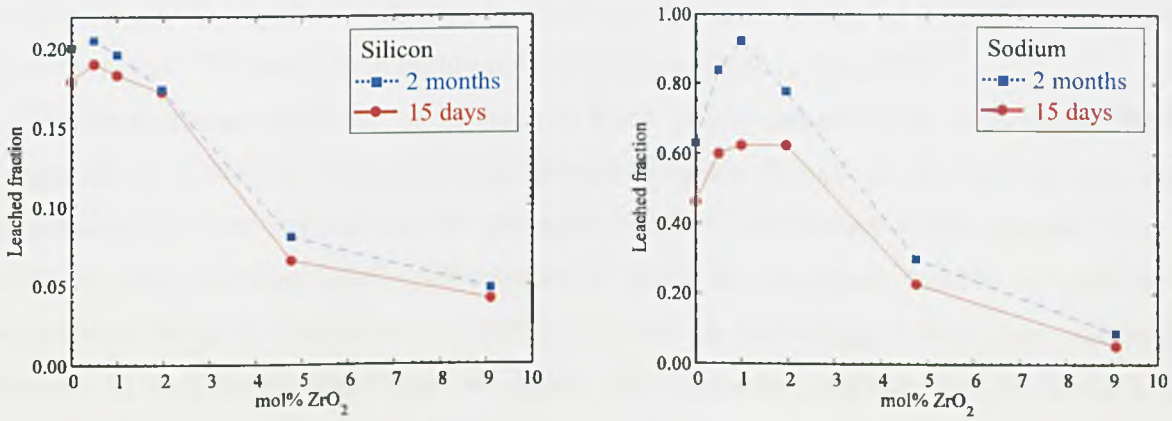

a) b)

Figure 2.14: Leaching of Na and Si from glasses of composition shown with varying amounts of ZrO_2 Base glass composition (mol%): $70SiO_2$-$15Na_2O$-$15B_2O_3$ After (Lobanova2002).

Combining leach tests and Small Angle X-ray Scattering (SAXS) experiments Sicard *et al.* (2004) propose an overall model for the effect of ZrO_2 on durability.

1. The addition of ZrO_2 reduces the alteration layer pore size (increasing surface area) of the glass. This is due to the low solubility Zr which both inhibits a complete rearrangement of the skeleton and offers a very good recondensation site for silica;
2. The large specific area of the altered layer delays the formation of the protective dense silica alteration layer;
3. At low ZrO_2 concentrations the glass is highly altered with the altered-layer skeleton being easily dissolved, thus the alteration proceeds by dissolution of the glass;
4. With increasing ZrO_2 the hydrolysis resistant Zr-O-Si bond becomes the predominant factor making it difficult to dissolve the skeleton entirely, the alteration depth decreasing accordingly.

Glass structure around Zr

Structural investigations of Zr co-ordination environments (e.g. silicate glasses) have been carried out by both the geological sciences, as an igneous trace element, and in the nuclear sciences, due to its presence in various waste streams and its effects on durability.

XAS[1] data show that within silicate glass octahedral like co-ordination with oxygen (ZrO_6 species or ^{VI}Zr) appears dominant (similar to the mineral zektzerite ($NaLiZrSi_6O_{15}$)). ZrO_7 and ZrO_8 (^{VII}Zr, ^{VIII}Zr) species have also been reported. McKeown *et al.* (1999) Suggested that the proportion of ^{VII}Zr increased with increasing Zr concentrations. Farges *et al.* (1991) suggested that the presence of ^{VIII}Zr but only in highly polymerised glasses (e.g. few NBO).

The next-nearest neighbour of Zr has not been clearly defined from experiment. Work by Farges *et al.* (1991) on aluminosilicate glasses suggests Si and Al (or Na) as next nearest neighbours; however, limited data are presented to allow verification of this analysis. They also proposed that increased glass polymerisation gives an increased number of next nearest neighbours. Work by Galoisy *et al* (1999), focussed on borosilicate waste glass compositions proposes Si next nearest neighbours but, again, little supporting evidence was put forward. There has been little evidence of Zr-O-Zr bonds within glasses, only Farges (1996) suggested their presence from EXAFS spectra with a separation of ca. 3.67 Å which is characteristic of edge shared ZrO_8 polyhedra as in zircon. The presence of ^{VIII}Zr had already been shown in the glass.

Bond Valence (BV) theory calculations from Farges *et al.* (Pauling 1929, Farges *et al.* 1991) indicate that ^{VI}Zr should bond preferentially to NBO (due to Si-O and Al-O bond length considerations) and would require charge compensation (see **Figure 2.15**). ^{VIII}Zr should preferentially associate with BOs with Al-O-Si being preferable to Si-O-Si hence giving increased levels in highly polymerised glasses. This implies ^{VIII}Zr is accommodated in the voids between network forming tetrahedra (Farges *et al.* 1991). See **Section 8.2** for more bond valence calculations. However, this calculation is not in agreement with the model presented by Ellison and Hess (1994a) where alkali ions are involved in this stabilisation of ^{VIII}Zr within a glass. Since ^{VIII}Zr has only been observed in highly polymerised glasses where the availability of alkalis for charge balancing is limited (Farges *et al.* 1991, Watson 1979). The model presented by Farges appears more feasible.

[1] For full explanation of XAS theory see **Section 3.5.2**

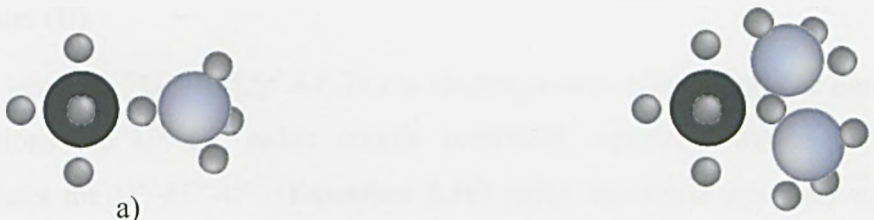

Figure 2.15: a) Zr^{VI} cluster bonding to a NBO and b) Zr^{VI} cluster bonding to a BO. Ionic radii not to scale.

Due to the low backscattering amplitude of B-atoms (see **Section 3.5.2**) XAS fails to give detailed information as to the possibility of Zr-O-B bonds. This is an aspect not discussed in previous work. In fact little work appears to have been done in relation to Zr and B in glass; some evidence comes from leached phase-separated glasses (e.g. Vycor) (Yazawa1994). Chemical analysis of the leached high borate region and the remaining high silica regions shows that ZrO_2 is found in both the high borate region and the high silica region. This implies ZrO_2 does form Zr-O-B bonds and this possibility can be supported with BV calculations (see **Section 8.2**). To the author's knowledge no detailed work has been reported on the change in B environment with Zr content.

Effect of Zr on bulk structure

There have been a limited number of studies into this aspect of Zr additions to glasses. A series of papers based on the $CaO-ZrO_2-SiO_2$ system (Montorsi *et al.* 2002, Barbieri *et al.* 2004) using MAS-NMR and MD indicated that increasing Zr content had little effect on the Q-number (a measure of polymerisation of the glass network - see **Section 3.4.2**) of Si within the glasses. However, the concept of Q-species used in this paper does not draw a distinction between Si-O-Si and Si-O-Zr co-ordination. Work by McKeown *et al.* (2000) using Raman spectroscopy with complex waste composition borosilicate glasses indicates that increasing ZrO_2 content decreases Si-O-Si linkages and increases the number of Q^2 species compared to Q^4 and Q^3. Again the possibility of Si-O-Zr bonds was not discussed.

Zr and crystallisation

The use of Zr in glass ceramics is well documented (McMillan 1979). Within nuclear waste glasses various crystalline phases have been shown to form (e.g. zekzerite and zircon) (Rose *et al.* 2004).

2.4.2 Uranium (U)

As with all *f*-elements, ^{92}U ([Rn].$5f^3.6d^1.7s^2$) is electropositive (Greenwood & Earshaw 1993). In aqueous solutions the U^{6+}-U^{4+} redox couple commonly operates. Within (boro)silicate and phosphate glasses the U^{6+}-U^{5+}-U^{4+} (**Equation 2.16**) redox equilibria generally operate. U^{3+} has also been observed but only in the presence of a strong reducing agent e.g. metallic aluminium (Schreiber *et al.* 1982a).

$$4U^{6+}_{(melt)} + 2O^{2-}_{(melt)} \rightleftharpoons 4U^{5+}_{(melt)} + O_{2(gas)}$$
$$4U^{5+}_{(melt)} + 2O^{2-}_{(melt)} \rightleftharpoons 4U^{4+}_{(melt)} + O_{2(gas)}$$

Equation 2.16

The relative proportion of these valence states depends on conditions listed in **Section 2.3**. Generally, under air atmosphere, U^{6+} is in the majority being about 90-100 % of U in (boro)silicates.

U is an important trace element in igneous systems providing information about the age, origin and crystallisation history of magmas. It is amongst the last elements to crystallise from cooling magmas and one of the first to enter the liquid on melting (Farges *et al.* 1992).

Various U oxides are available for glass melting. This project uses UO_3 which can be obtained by heating $UO_2(NO_3).6H_2O$ in air at 400 °C. This forms an orange-yellow powder, UO_3, which decomposes to U_3O_8 on heating (200-650 °C) with T_m = 1150 °C (Greenwood & Earnshaw 1993). The effect of U on the properties of glasses are similar to that of Th and include (Volf 1984, Jantzen 2005):

- **Increasing density and refractive index;**
- **Decreasing thermal expansion**; depending on redox condition, the effect increases from UO_2^{2+} to U^{4+};
- **Viscosity**; little or no effect <5.8 wt% U_3O_8 (equivalent to ca. 5.9 wt% UO_3);
- **Colouration**, dependent on redox (e.g. in Vaseline glasses) see **Table 2.4**.

U bearing silicate and phosphate glasses have been investigated as reactor fuel elements but rejected due to problems producing a glass with thermal stability at the high temperatures required (Heynes & Rawson 1961, Wirkus & Wilder 1962).

Radioactivity and toxicity

U emits α-particles and decay of its fission products produces β- and γ-radiation. The half-life of

the U^{238} nucleus is 4.50 x 10^9 yr, so its specific activity is relatively low (ca. 12.4 kBq/g) (Cotton *et al.* 1999).

There are two major effects of α emission on materials (Ewing *et al.* 1995):

1. As an α-particle passes through a material, outer shell electrons can be striped from the atoms it interacts with. As the particle slows, elastic collisions can also occur between the α-particle and constituent atom;
2. Recoil of the U atom after α-emission can cause damage to glass structure through ballistic cascades. However, this damage is often "annealed out" due to the high temperature (400 °C) produced in radiologically heated HLW glasses during the early cooling period.

Environment of U in borosilicate glasses

This is dependent on the redox state of the U ion (see **Table 2.4**). The most common form, U^{6+}, exists as a UO_2^{2+} group (uranyl). The uranyl group is believed to form by combinations of appropriate metal 6*d* and 5*f* orbitals overlapping with the three 2*p* orbitals of each oxygen to produce one σ and two π bonds. This geometry is similar to that in MoO_2^{2+} and comparisons have been drawn between 4*d* orbitals in Mo and the 5*f* orbitals in U. The difference being the repulsive effect of the 6*p* electrons present in the U which, it was proposed, favour a linear form of UO_2^{2+} (Greenwood & Earnshaw 1993, Tatsumi & Hoffman 1980).

The uranyl species is a large, but low charge, cationic cluster and it has been suggested that is has some properties similar to a modifier within the glass (Greaves *et al.* 1989). In crystal structures, the uranyl ion is co-ordinated by four, five or six anions in square, pentagonal or hexagonal bipyramidal arrangements respectively. In borosilicate glasses the uranyl group (axial U-O distance *ca.* 1.8 Å) has been observed co-ordinated to 4-5 equatorial oxygen ions at longer distances than for the axial oxygen ions (ca. 2.2 Å) (Farges *et al.* 1992). In crystal structures the equatorial oxygen ions may share edges and corners, commonly resulting in quasi-infinite sheets, with the axial oxygen ions orientated approximately perpendicular to the sheet, the sheets are most often connected through weaker bond to interlayer cations (Burns *et al.* 1997).

In a study of corrosion layers using glancing-angle EXAFS Greaves *et al.* (1989) suggest that the uranyl groups sit in the alkali channels in the MRN model of glass. This is based on the short U-U separation suggested from EXAFS data (indicating clustering, or rafting) and by comparison to crystalline materials where the uranyl species is observed in uranates (e.g. $Na_2U_2O_7$ where it has a

layered structure, see **Figure 2.16**) but not in U silicates (e.g. $Na_2UO_2SiO_4$). A similar concept was suggested by Knapp *et al.* (1984) where again EXAFS results suggested uranyl clustering within a sodium silicate glass.

Species	Colour *	Co-ordination environment	Ionic radius (Å)	U-O distance ** (Å)	Notes
U^{3+}	Red	6 (or 8)	1.165		Difficult to form Low solubility in borosilicate glass
U^{4+}	Blue-green	6 (or 8)	1.14	2.26-2.29 (2.4)	
U^{5+}	No colour	6 (some distorted 4)	0.90	2.19-2.24 (unknown)	
U^{6+}	Green-yellow†	UO_2^{2+} (with 4-5 oxygen ions)	0.87		

Table 2.4: Details of coordination environment and optical properties for glasses containing various U ions. * Colours apply to both aqueous solution and silicate glass (although may vary with glass composition and processing parameters) (Schreiber1982a), † green-yellow fluorescence due to short U-O bonds (Volf 1984), ** (Farges *et al.* 1992).

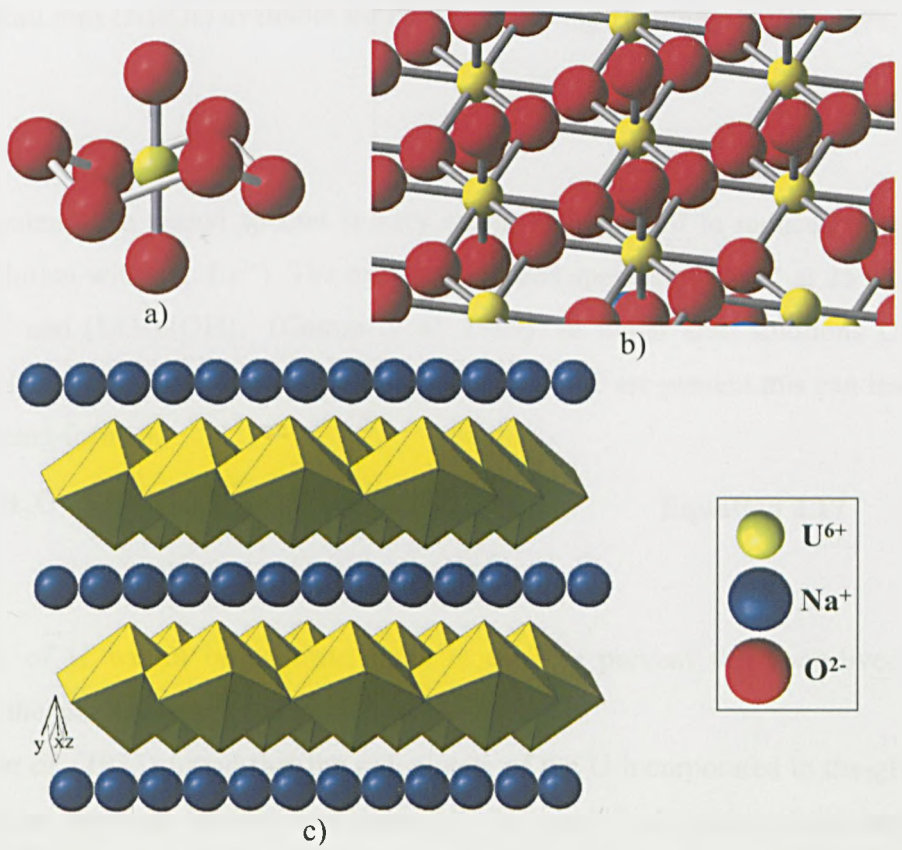

Figure 2.16: Showing structural aspects of the uranyl group: a) shows the uranyl group with equatorial oxygen; b) shows the rafting mechanism as observed in $Na_2U_2O_7$ and c) shows the layer structure of $Na_2U_2O_7$.

Effect of UO_3 additions on bulk glass structure

Very little work has been done in this area. A neutron and x-ray scattering study on iron phosphate glasses by Badyall *et al.* (1999) showed there was very little change in the bulk structure of the glass with U additions. They concluded the U^{6+} occupies interstitial sites in an otherwise relatively undisturbed glass structure.

Solubility

The solubility of U is a function of many system properties. The major dependence is on the redox state. In borosilicate glasses under reducing conditions ca. 10 wt% U will dissolve in a borosilicate glass, while >40 wt% will dissolve under an atmosphere of air (Schreiber *et al.* 1982b).

The solubility of U in (boro)silicate melts is thought to be enhanced by several structural factors including; high oxygen anion activities (i.e. increased NBOs and NFOs). It is known to have low solubility in high silica (highly polymerised) glasses and this is thought to be because of the lack of alkali ions (NBOs) available for charge balancing (Domine & Velde 1985, Farges *et al.* 1992).

Aqueous chemistry

In aqueous systems the uranyl species is very stable and difficult to reduce (although it can be reduced in solution with e.g. Cr^{2+}). The main hydrolyzed species of UO_2^{2+} at 25 °C are UO_2OH^+, $(UO_2)_2(OH)_2^{2+}$ and $(UO_2)_3(OH)_5^+$ (Cotton *et al.* 1999). In molar acid solutions U^{4+} ion is only slightly hydrolyzed (see **Equation 2.17**). If F^-, PO_4^{3-} and IO_3^- are present this can lead to insoluble precipitates being formed.

$$U^{4+} + H_2O \rightleftharpoons U(OH)^{3+} + H^+ \qquad \textbf{Equation 2.17}$$

Durability

The retention of U within borosilicate glass is vital to prevent this long-lived radionuclide escaping into the environment.

Schreiber *et al.* (1985) found that the redox state of the U incorporated in the glass appears to have no effect on leaching. Glasses containing U^{4+}, U^{5+}, or U^{6+} all exhibited the same patterns for the leaching of U under the experimental conditions. Thus, the oxidation of the reduced U present in the glass to U^{6+} at the glass / leachate interface must be rapid and cannot be the rate determining

step in the leaching process. Schreiber *et al.* (1985) proposes a reaction mechanism as shown in **Figure 2.17.**

In opposition to this, Dunn (1987) proposes that diffusivities decrease with increasing ionic charge taken $(UO_2)^{2+} > U^{4+} > U^{5+}$. Certainly, the proposed presence of UO_2^{2+} within the alkali channels would suggest a more rapid diffusion, and so leaching, of uranyl over that incorporated in the network (U^{4+} and U^{5+}). The diffusivities measured by Dunn were similar to those seen for Cs in previous work.

Calestani *et al.* (1986) in glass similar to that used in this project (a sodium lithium borosilicate) found only a small change in durability with addition of U_3O_8. However, the experimental procedure was non-standard with 0.6 g of glass in 100 ml of distilled water. This is expected to lead to very high leach rates with the leachate not achieving silicon saturation. Lack of silicon saturation will reduce the likelihood of leach layer formation (as observed) and so the U would be continuously leach and not be incorporated into a protective surface layer.

It has been shown that U can be incorporated (and enriched (Maeda *et al.* 2001)) in the gel layer of leached glasses in the U^{6+} form, with uranyl bonding and equatorial oxygen ions (Jollivet *et al.* 2002). Its presence was explained by Maeda *et al.* (2001) as being due to the hydrated nature of the uranyl species. The glass investigated was a complex waste glass. The hydrate ions migrate in the porous alteration layer towards the layer / solution interface, the solubility limit of the uranyl hydroxide ceases the migration, and precipitation occurs as $UO_2(OH)_{2(s)}$. There was no direct evidence given for the presence of $UO_2(OH)_{2(s)}$ the conclusion being reached from equilibrium thermodynamic calculations. It was thus suggested that the concentration of U in solution is controlled by the solubility of $UO_2(OH)_{2(s)}$.

In a study of Chernobyl "lava" (a silicate vitreous material containing 2-3.2 wt% U) weathering was found to produce certain crystalline surface phases including (Burakov *et al.* 1996):

1. $UO_3.2H_2O$ – epiianthite;
2. $UO_4.4H_2O$ – studtite.

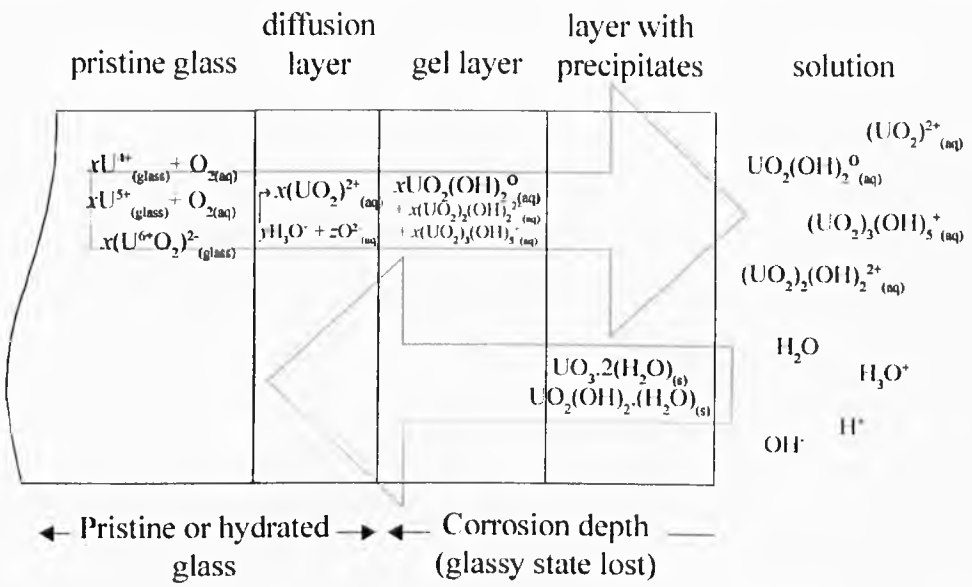

Figure 2.17: A simplified schematic for mechanism of corrosion and reprecipitaion of U during leaching of borosilicate glass as proposed by Schreiber *et al.* After (Schreiber *et al.* 1985).

2.4.3 Chromium (Cr)

Chromium (^{24}Cr) is a transition metal ([Ar].$3d^5.4s^1$) with a partially filled d-shell. The tri- and hexa- valent forms are the most prevalent (Cr^{3+} and Cr^{6+}) with Cr^{2+} also present under highly reducing conditions (Greenwood & Earnshaw 1993, Paul 1974, Weyl 1951).

$$4Cr^{6+}_{(melt)} + 6O^{2-}_{(melt)} \rightleftharpoons 4Cr^{3+}_{(melt)} + 3O_{2(gas)} \qquad \textbf{Equation 2.18}$$

Cr_2O_3 has limited effect on most glass properties due to its low solubility (Volf 1984). Limited details gone into here as Cr_2O_3 additions make up only a minor part of this work. However, in general Cr_2O_3 additions tend to:

- **Increases density;**
- **Increases thermal expansion,** roughly in the same way as Na_2O when present in the same molar ratio;
- **Colouration,** dependent on redox (See **Table 2.5** and **Figure 2.18**).

Solubility

Cr_2O_3 shows poor solubility in glasses in general owing to its refractory nature (T_m = 1900 °C) and its poor miscibility with SiO_2. In borosilicate glasses the solubility is generally <2 wt%. If this

limit is exceeded crystallisation can occur. If sufficient levels of spinel forming components are present (e.g. Fe, Ni, etc) the Cr^{3+} will partition to spinel crystals. In the absence of these components Cr tends to precipitate as eskolaite (Cr_2O_3). Cr^{6+} will tend to segregate as a liquid chromate phase. Eskolaite formation has been shown not to adversely effect glass durability. However, chromate segregation is undesirable (Hrma *et al.* 2006). Increasing temperature and oxygen ion activity (e.g. increase alkali content) improve the solubility of Cr_2O_3 (Kim *et al.* 2001, Volf 1984).

Species	Colour in silicate glass	Co-ordination environment	Ionic radii (Å)	Notes
Cr^{2+}	Blue	6	0.87	Unstable except in reducing conditions
Cr^{3+}	Blue-green	6	0.755	Is very stable in glass as Cr^{3+}-O-Cr^{6+}
Cr^{6+}	Yellow-green	Possibly as CrO_4^{2-} or $Cr_2O_7^{2-}$	0.55 or 0.71	

Table 2.5: Details of co-ordination environment and optical properties for glasses containing various Cr ions. Co-ordination environment applies to (boro)silicate glass (Greenwood & Earnshaw 1993, Volf 1984). Colours may vary with glass composition and processing parameters.

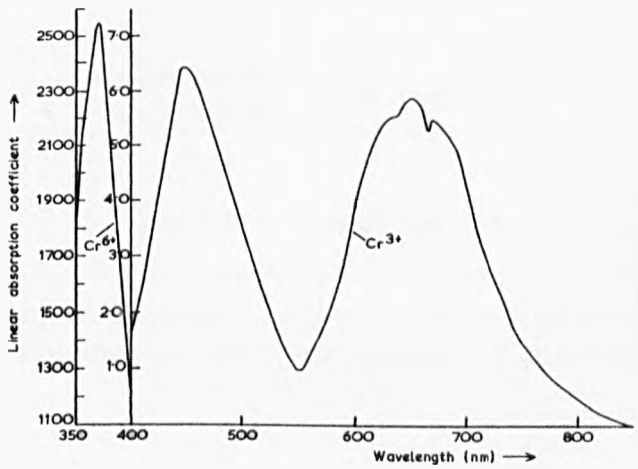

Figure 2.18: The optical absorption spectrum for Cr within a silicate glass showing the two most common valence states (Bamford 1977).

2.4.4 Iron (Fe)

Iron (^{56}Fe) is a transition metal ([Ar].$3d^6.4s^2$) with generally only two oxidation states in (boro)silicate glasses. Many works have investigated the co-ordination and distribution of Fe^{2+} and Fe^{3+} ions in glass (see **Table 2.6**) (Bingham *et al.* 2002, Dingwell & Moore 1953).

$$4Fe^{3+}_{(melt)} + 2O^{2-}_{(melt)} \rightleftharpoons 4Fe^{2+}_{(melt)} + O_{2(gas)}$$ **Equation 2.19**

The effect of iron additions on glass properties is complex due to the multiple oxidation states and co-ordination environments. Fe^{3+} is generally seen in a tetrahedral co-ordination but octahedral co-ordination is possible, Fe^{2+} occurs generally as octahedral co-ordination but tetrahedral co-ordination has been observed. There has also been some evidence for 5 co-ordinated Fe^{3+} (Burns 1993, Farges *et al.* 2004). Some general trends in glass properties with iron oxide additions are stated below (Volf 1984). Only limited details are given into the effect of iron oxides additions as they make up only a minor part of this work.

- **Chemical durability,** Fe^{2+} tends to decrease chemical durability of (boro)silicate glasses whereas Fe^{3+} tends to increase chemical durability;
- **Increased density,** increases density of glass;
- **Increased refractive index,** in a similar manner to density;
- **Mechanical properties,** both hardness and Youngs modulus are increased;
- **Colouration,** changes optical spectrum depending on redox (see **Table 2.6** and **Figure 2.19**).

Species	Colour	Co-ordination environment	Ionic radii (Å)	Notes
Fe^{2+}	Blue, green	6	0.75	
Fe^{3+}	Yellow, brown	6 and 4	0.69 and 0.63	$[FeO_4]$ requires alkali (earth) for charge balance

Table 2.6: Co-ordination environment applies to (boro)silicate glass. Colours may vary with glass composition and processing parameters (Greenwood & Earnshaw 1993, Volf 1984).

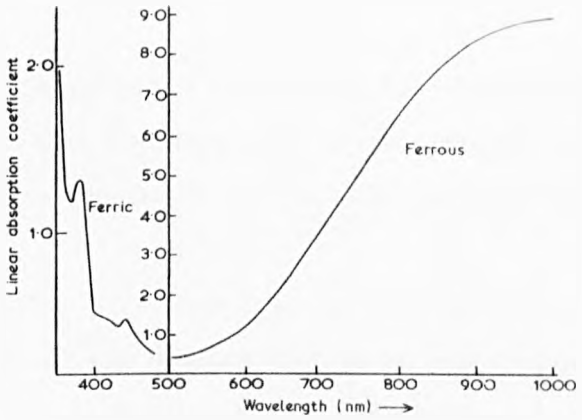

Figure 2.19: The optical absorption spectrum for Fe within glass showing the two most common valence states (Bamford 1977).

2.5 Glass melting

The methods of glass melting used in the nuclear industry are treated elsewhere (Lutze & Ewing 1988, Pegg & Joseph 2001) and their science is well established. For this reason they are not discussed here.

2.5.1 Viscosity

The viscosity of a glass is the measure of its ability to flow. It is a transport property which is dependent on the bonding forces and on the deformability of ions or their groups. In a homogeneous glass it can only truly be controlled *via* composition and thermal history.

From a structural view point the viscosity can be viewed as being a function of ionic radii, σ_i and charge, z_i, of atom, *i* (Volf 1988):

$$\rho \propto \frac{z_i}{\sigma_i}$$ **Equation 2.20**

Increasing deformability of inter-atomic bonds results in a considerable decrease in viscosity. The charge on an ion also effects the viscosity with increased charge giving increased viscosity.

2.5.2 Volatilisation

Volatilisation is a serious problem for nuclear glass production due to the volatility of Cs and Ru. This limits melting temperatures to <1150-1200 °C (Soper *et al.* 1983). Practically, temperatures greater than 1100 °C are rarely used due to economic and technological considerations.

2.6 Modelling

The accurate modelling of glass properties and structure has a long history in glass science, from empirical property equations (see **Equation 2.14**) to full atomistic simulations. Modelling has many advantages over laboratory investigations, but must always be checked against reality. The major advantages are:

1. Provides information on hypothetical (or non-laboratory achievable) amorphous materials giving insight into fundamental theoretical aspects of glasses;
2. Permits various intrinsic structural and dynamic features of a material to be established without the need for complex or dangerous laboratory work (e.g. work with highly radioactive materials);
3. Allows rapid exploration of parameter space while also allowing significance of individual parameters to be studied while eliminating from consideration the effect of other parameters.

This project deals with atomistic simulations of glasses; Molecular Dynamics (MD) and the Reverse Monte Carlo (MC) method are suitable for this purpose. MD will be used here as it more closely mimics the formation of a laboratory glass, whereas the RMC method requires atom positions be adjusted from laboratory results and so is subject to availability and accuracy of laboratory data. Constitutive equations and other qualitative relationships will not be discussed here as they are not used further within this project.

2.6.1 Historical perspective

Modern day computer simulations of glasses are possible due to the development of the digital computer (Metropolis *et al.* 1953) and the earlier pioneers of techniques, algorithms and hardware. One such technique is Molecular Dynamics[1]; MD involves numerically solving Newton's equations of motion for a many-bodied system of atoms interacting through known potentials, with the configuration evolving with time.

The basic method of solving Newton's equations of motion for a many-bodied problem was first laid down in the late 1950's by Alder and Wainwright (1957, 1959) who carried out MD simulations on liquids and glasses using simple hard sphere potentials. Other MD simulations around this time were mainly focused on simple Lennard-Jones type liquids (e.g. argon (Rahman

[1] For a full explanation of MD modelling see **Section 3.7**.

1964)).

Forland (1968) applied the Monte Carlo method[1] to the study of a molten ionic salt in two dimensions. These initial investigations (and many subsequent ones, notably (Woodcock *et al.* 1971a, 1971b, 1976)) into molten salts and Lennard-Jones type fluids laid the groundwork for more complex modern silicate glass simulation.

There has been very little development in the basic techniques used in MD simulations since the 1970's; recent innovations have centred around improvements in computing power and so the ability to model larger and more complex systems (Vashita *et al.* 1999, Delaye & Ghaleb 1996b). Alongside this commercial (e.g. Materials Studio (Accelrys 2005)) and academic (e.g. DL_POLY (Smith & Forester 1996)) codes have been developed allowing wider access to these powerful techniques.

2.6.2 Kinetic theory of glass formation

Simulation of glass formation using MD follows a similar route to the laboratory process; an initial structure (usually crystalline) is 'melted' or equilibrated at a high temperature and then 'quenched' or temperature scaled at such a rate as to by-pass crystallisation. The quenching process is more than just the formation of a super-cooled liquid. **Figure 2.20** shows a clear discontinuity in the cooling curve for derivative thermodynamic properties[2] at the glass formation temperature or, more correctly, the glass transition temperature[3] (T_g).

Below T_g a "metastable" solid exists; metastable because given sufficient time free energy considerations mean the glass must evolve toward a stable solid (crystalline) state. A stable glass is only formed if the configurational barriers to this process are sufficiently large so that atoms cannot diffuse into new positions.

Thermal history has a significant effect on glass structure. Increased cooling rate through T_g "freezes-in" a structure representative of a higher "fictive" temperature (T_f) (**Figure 2.20**). Higher T_f also relates to a less compact solid with higher residual entropy. Heat treatment can also alter the glass; if the glass is annealed at around T_g:

---

[1] Essentially a statistical mechanics, free energy minimisation approach; involving generation of atomic configurations which are adjusted in such a way that minimises the configurational energy.

[2] E.g. enthalpy, specific heat, thermal expansion and specific volume.

[3] A second-order transition in which a supercooled melt yields, on cooling, a glassy structure. Below the glass-transition temperature the physical properties vary in a manner similar to those of the crystalline phase (IUPAC 2007).

- **The glass structure will approach a more equilibrium state (reduce T_f).** This is a time-dependent change and does not occur above T_g. The ultimate point in this "stabilisation" would be the structure of a glass that was cooled infinitely slowly;
- **Devitrification may occur**. Increased energy availability allowing configurational barriers to be overcome and so diffusion and crystallisation. This process is a common problem in "real-world" nuclear waste glasses (Rose *et al.* 2004); however, is not often seen in MD simulations due to time limitations.

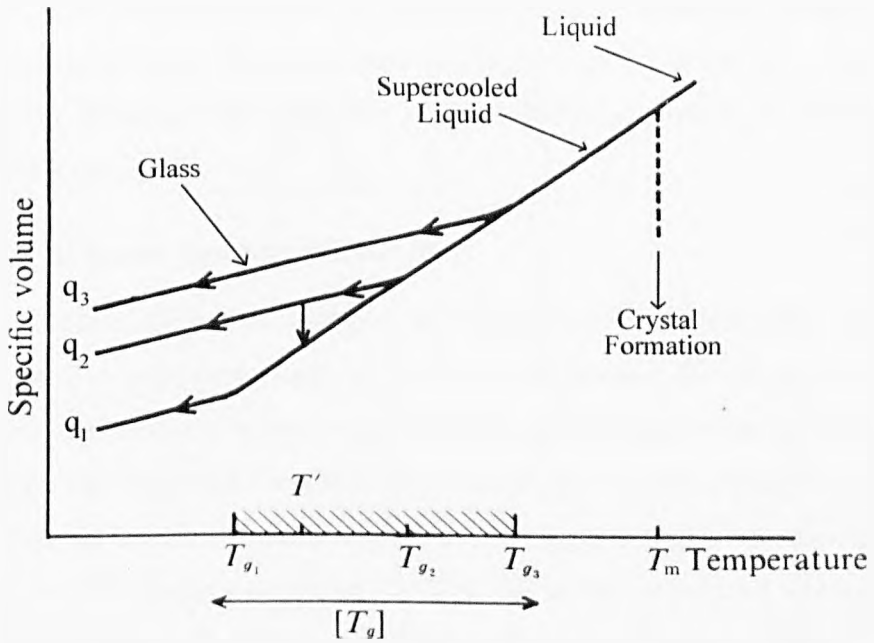

Figure 2.20: The relationship between glassy, liquid and solid states. Also shows influence of cooling rate on the position of the transition point T_g with cooling rate of $q_1 > q_2 > q_3$. The hatched portion represents the transition interval $[T_g]$. After Zarzycki (1991).

2.6.3 Modelling of silicate glasses

In their pioneering study Woodcock *et al.* (1976) used empirical two-body potentials calibrated against the laboratory determined Radial Distribution Function (RDF) for SiO_2 glass of Mozzi and Warren (1969). They achieved good agreement with the first peak due to Si-O pair interactions, although the O-O pair function separation was slightly reduced, and the Si-Si separation was slightly larger than that experimentally observed. Subsequent simulations have shown that using only two-body potentials the Si co-ordination distribution cannot be accurately reproduced (Stillinger & Weber 1985).

Later simulations by Soules (1979) using Born-Mayer-Huggins (BMH) potentials began to simulate more industrially applicable compositions and showed that addition of a sodium ion converted an equal number of NBOs (see **Equation 2.2**). Later work showed the possibility of simulating the boron co-ordination variation with composition (**see below**) (Soules & Varshneya 1981).

The use of three-body potentials lead to great improvements in the accuracy of MD simulations (Feuston & Garofalini 1988, Stillinger & Weber 1985), showing only 1-2 % five co-ordinate Si. A small number of these SiO_5 species can be seen (ca. 0.1%) in laboratory glasses formed under atmospheric pressure, however, this percentage is increased with high pressure and rapid quench rates (Greaves 1985, Stebbins 1991); thus this 1-2 % may be due to the high quench rates or show a need for improved potentials.

2.6.4 Modelling of borate and borosilicate glass

The modelling of borate and borosilicate glasses has proved a major challenge for the potentials and techniques used in MD simulation. To reproduce accurately the structure of these glasses involves the reproduction of the boron oxide anomaly and the glass structure related to this (see **Section 2.2**). Below are discussed two papers from the literature with relevance to this work.

One of the first molecular dynamic studies was by Soules and Varshneya (1981) studying various sodium borosilicate glasses. Using just 200 atoms and a constant energy ensemble, the boron coordination achieved shows remarkable agreement with laboratory data (see **Figure 2.21**). In 1987 Inoue *et al.* (1987) reproduced both the laboratory boron coordination and reasonable ring structures in a borate and sodium borate glass.

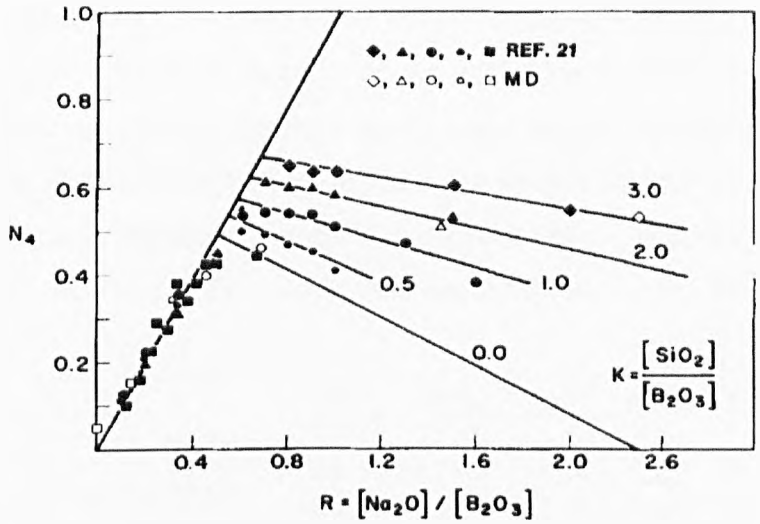

Figure 2.21: Result from paper by Soules and Varshneya (1981) showing agreement between N4 (^{IV}B fraction) and change in *R* compared to laboratory results..

In fact the majority of studies have been concerned with the simpler borate glasses and few studies have looked at borosilicate compositions. The complex nature of alkali borosilicate glasses makes them a challenge for MD simulation, however, their commercial and scientific relevance make such studies of great interest.

The use of three-body-potential for the O-B-O bond angle varies in the literature. Soules and Varshneya used only pair potentials allowing the system to form more freely, whereas Inoue used a 3-body potential giving strong control of the O-B-O angles.

2.6.5 Modelling of Zr in (boro)silicate glass

To the author's knowledge the first MD studies of Zr bearing silicate glasses were undertaken by Delaye and Ghaleb (1996a, 1996b). The arrangement of the major components (see **Table 2.7**) of French nuclear waste glass R7T7 was studied. BMH potentials were used with the Stillinger and Weber (SW) (1985) three-body potentials. These studies are highly detailed; however, the simulation time was short (32.4 ps). The structural parameters such as bond angles and lengths appear reasonably close to the EXAFS results presented by Delaye and Ghaleb. These studies also compared laboratory and MD values of density, Na diffusion coefficient and viscosity. Na diffusion coefficients and density gave good agreement with laboratory values shown; the viscosities gave much higher values than laboratory values shown. There was no discussion as to the effect of ZrO_2 additions on the bulk glass structure.

A more recent study by Montorsi *et al.* (2002) looked at a calcium silicate glass containing

high levels of Zr (**Table 2.7**). This showed the effect of changes in initial structure and quench rates on the glass. Little effect was observed on the final glass of initial structure; although this study suggests a random starting structure gave results closest to laboratory Si and Zr co-ordination. Addition of Zr ions appears to increase the amount of SiO_5 species observed. Zr is suggested to be a network former as comparison between glasses with and without Zr shows a reduction in Si-NBO content; also Zr co-ordination mainly involves Zr-O-Si bonds.

Study	SiO_2	B_2O_3	Na_2O	ZrO_2	Al_2O_3	CaO
Delaye & Ghaleb (1996a)	67.25	17.68	13.32	1.74		
Delaye & Ghaleb (1996b)	63.79	17.02	13.39	1.85	3.96	
	60.14	15.84	12.75	1.80	3.86	5.60
Montorsi *et al.* (2002)	48			10		42

Table 2.7: Comparison of previously simulated Zr-bearing glass compositions. All values are in mol%.

2.6.6 Limitations of MD simulation of glasses

There is some controversy within the literature as to the validity of using MD for glass simulations. Although the basic concept of glass production using MD is similar to that used within a laboratory the details vary dramatically. **Table 2.8** shows the difference in quench rate, temperatures, and total simulation time between laboratory glasses and MD glasses. The high temperature and very fast quench rates raise an argument that simulations produce a structure representative of a much higher temperature than a laboratory glass. This is often considered to limit MD simulations applicability. This is a problem of the computing power and time available to researchers which limits length of simulations possible.

Another disadvantage of the very high cooling rate is that it is impossible for devitrification to occur within the glass. Also, due to the nature of the simulations it is not possible to get "undissolved batch" within the simulations. These facts prevent MD simulated glasses from being considered as facsimiles of laboratory glasses, but do not prevent them providing detailed information about glass structure; however, care must be taken in analysis of results.

Property	Laboratory	Calculation (MD)
Equilibrium (Melting) temperature (°C)	1000-1500	4000-8000
Approximate cooling rate (°C/min)	1-500	6×10^{14}
Glass transition temperature (°C)	500-600	>>600
Total glass melting time	1-24 hours	1000 ps

Table 2.8: Comparing formation of a laboratory and a calculated MD glass (McMillan & Wolf 1995).

2.7 Chapter summary

This chapter has set out the scientific basis and background for this project. Items from this chapter will be referenced throughout the proceeding chapters.

3 Experimental Methods

3.1 Sample preparation

The basic glass compositions chosen in this project (see **Table 3.1** and **Table 3.4**) are based on the BNFL glass frit composition (FLi-0) which is added to waste calcine during vitrification. A variation on this composition with half the level of Li_2O (HLi-0) was also used in the ZrO_2 bearing glasses as a comparison. These glass compositions were used as they are industrially relevant to the UK nuclear waste glasses and have a simple composition which facilitates experimental analysis. Both as-batched and measured compositions are presented below, all plots use measured compositions.

3.1.1 Zirconia bearing glasses

Glasses were melted in a 147.5 cm^3 (internal volume) electric furnace with Kanthal SiC elements. The temperature of the glass furnace was regulated by a Eurotherm controller with melting temperatures depending on composition.

Melts were undertaken in Pt crucibles with a 5 hr melt time, including 1 hr initial melting time and 4 hrs stirring (with a Pt stirrer) rotating at 60 rpm; glasses were then poured into preheated steel block moulds. Batch was "filled-on" in small quantities to avoid carry over[1]; usually around 3 additions over 30 mins were made (not included in the overall melt time).

Target compositions are given in **Table 3.1**, with examples of finished glasses in **Figure 3.1**. Raw materials from the same source were used for all glass melts. All raw materials used were high purity, the following are the major constituents: SiO_2 from SiO_2 (Sigma, ca. 99 %, purity, particle size 0.5 – 10 μm); B_2O_3 from $Na_2B_4O_7.10H_2O$ (Fisons, 99.5 % purity); Na_2O from Na_2CO_3 (Sigma, >99 % purity); Li_2O from Li_2CO_3 (Sigma, > 99 % purity); and ZrO_2 from ZrO_2 (Aldrich, 99 % purity, 5 μm particle size).

Table 3.2 shows the analysed compositions of glasses used in this work. The difference in

[1] Carry-over, loss through volatilisation and loss of batch powder due to air currents and rapid water evaporation / gas evolution ejecting batch from the crucible.

analysed and as-batched compositions are mainly within the boron content of the glasses. This is believed to be due to volatilisation during melting. This difference was taken into account with all calculations within this work.

Melting conditions

The temperature of melting was varied across the glass compositions due to the large changes in viscosity with increasing ZrO_2 (see **Table 3.3**). For samples FLi-5 and HLi-5 melted at 1250 °C melts were still highly viscous with bubbles present, whereas FLi-0 and HLi-0 melting easily at 1050 °C and were smooth flowing. All samples were annealed at 500 °C.

Sample No.	Sample	SiO_2	B_2O_3	Na_2O	Li_2O	ZrO_2	Waste Loading
1	HLi-0	63.91	19.55	11.03	5.51	0.00	
2	FLi-0	60.57	18.53	10.45	10.45	0.00	
3	HLi-1	63.76	19.50	11.00	5.49	0.25	
4	FLi-1	60.42	18.49	10.42	10.42	0.24	
5	HLi-2	63.53	19.48	11.01	5.48	0.49	
6	FLi-2	60.28	18.44	10.40	10.40	0.48	
7	HLi-3	62.96	19.26	10.86	5.42	1.50	
8	FLi-3	59.69	18.26	10.30	10.30	1.46	
9	HLi-4	62.23	19.08	10.79	5.38	2.52	
10	FLi-4	59.08	18.08	10.20	10.19	2.45	
11	HLi-5	61.30	18.75	10.58	5.28	4.10	
12	FLi-5	58.15	17.79	10.03	10.03	3.99	
13	French	67.26	17.41	13.55	0.00	1.78	
14	Blend[a]	53.6	16.8	9.4	9.3	1.4	9.3
15	Mangox[a]	50.9	16.0	8.9	8.9	0.8	14.5
16	High Zr[b]	58.4	18.4	10.3	5.0	5.8	2.2

Table 3.1: Target (as batched) compositions of glasses used in this project (mol%). FLi = Full Lithia and HLi = Half Lithia. For full waste compositions see **Appendix B**. [a] 25 wt%, [b] 15 wt% waste loading.

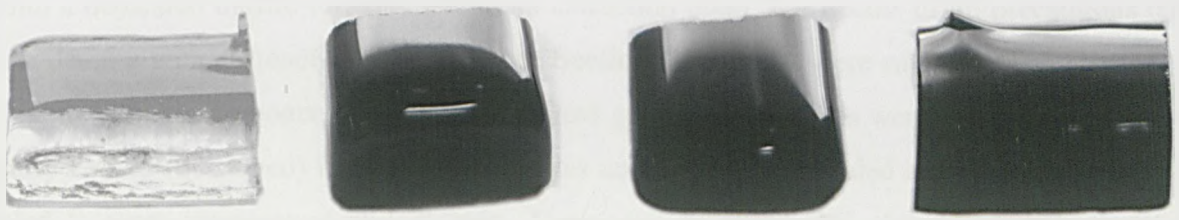

a) b) c) d)

Figure 3.1: Typical sample pictures: a) HLi-2; b) Blend; c) Magnox; and d) High Zr.

Sample No.	Sample	SiO_2	B_2O_3	Na_2O	Li_2O	ZrO_2
1	HLi-0	65.93	17.51	11.74	4.81	0.00
2	FLi-0	60.71	15.34	10.77	13.18	0.00
3	HLi-1	64.79	18.42	11.57	4.96	0.25
4	FLi-1	60.38	16.68	10.91	11.78	0.25
5	HLi-2	63.89	18.96	11.81	4.94	0.39
6	FLi-2	60.77	16.11	10.71	11.96	0.45
7	HLi-3	64.79	17.21	11.61	4.90	1.49
8	FLi-3	59.95	16.03	10.52	12.12	1.37
9	HLi-4	64.07	17.86	10.63	3.40	3.05
10	FLi-4	59.98	14.81	10.74	11.51	2.96
11	HLi-5	63.03	18.08	11.08	4.97	3.84
12	FLi-5	58.16	15.65	10.26	12.24	3.69

Table 3.2: As measured compositions of glasses used in this project (mol%) (measured using XRF and ICP[1]). FLi = Full Lithia and HLi = Half Lithia. For full waste compositions see **Appendix B**. [a] 25 wt%, [b] 15 wt% waste loading.

Sample	Melting temp. (°C)	Sample	Melting temp. (°C)
HLi-0	1050	FLi-0	1050
HLi-1	1050	FLi-1	1050
HLi-2	1080	FLi-2	1060
HLi-3	1100	FLi-3	1080
HLi-4	1180	FLi-4	1150
HLi-5	1250	FLi-5	1250
French	1100	Mangox[a]	1050
Blend[a]	1050	High Zr[b]	1250

Table 3.3: Melting temperatures used in melting glasses listed. Glass compositions can be found in **Table 3.1** and **Table 3.2**.

3.1.2 U bearing glasses

Due to the radiological hazards involved in handling U oxide powders, all melts were performed within a dedicated muffle furnace, within an extraction hood. For details of all precautions taken when dealing with radioactive materials (see **Section 3.2**). Melts were carried out at 1100 °C for 24 hrs to ensure a homogeneous and equilibrated glass. Two samples were then poured, one was rapidly cooled (quenched) between metal plates and the other annealed at 550 °C for 5 hrs and cooled to room temperature at 1 °C/min. There was no observable change in viscosity of the glasses during pouring with increasing UO_3.

The major batch component was glass frit supplied by James Kent Ltd, in a particulate form

[1] Glass sample compositions were measured at the University of Leicester, Department of Geology. See **Section 3.4.3** for details.

(1-5mm). This frit is the same as that used at Sellafield in the full scale vitrification process. Due to the static nature of the melts the frit was ground down to 75-500 μm (using a Tema mill) and then ball milled with required batch (e.g. UO_3, Li_2CO_3, and Fe_2O_3) in a HDPE container with magnesium stabilised zirconia media for 10 hrs. This gave a homogeneous starting material allowing good quality glasses to form without the need for stirring. Reagents were batched in a glove box and all equipment used was dedicated equipment to reduce contamination by radioactive material.

Table 3.4 shows the as-batched compositions used in this work, **Table 3.5** shows the analysed compositions for selected glasses. This shows that there is a difference in the analysed compositions especially in the boron concentration possibly due to volatilisation during melting. This difference is taken into account with all composition based calculations.

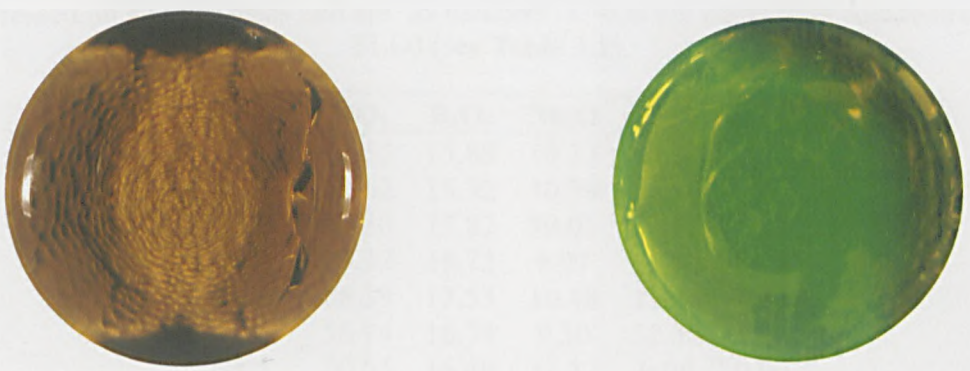

Figure 3.2: Typical sample pictures: a) U-4 glass; b) U-4 glass under UV light.

Sample	SiO_2	B_2O_3	Na_2O	Li_2O	UO_3	Fe_2O_3	Cr_2O_3
U-0	60.57	18.53	10.45	10.45			
U-1	60.54	18.52	10.44	10.44	0.05		
U-2	60.27	18.44	10.40	10.40	0.50		
U-3	59.96	18.34	10.35	10.35	1.00		
U-4	59.37	18.16	10.24	10.24	1.98		
U-5	57.66	17.64	9.95	9.95	4.80		
Fe-1	59.37	18.16	10.24	10.24		1.98	
FeU-1	58.22	17.81	10.04	10.04	1.94	1.94	
Cr-1	60.45	18.49	10.43	10.43			0.20
CrU-1	59.25	18.13	10.22	10.22	1.98		0.20
FeCrU-1	58.18	17.80	10.04	10.04	1.94	1.94	0.07
FeCrU-2	58.11	17.78	10.02	10.02	1.94	1.94	0.19
FeCr-1	59.25	18.13	10.22	10.22		1.98	0.20
Na-1	60.57	18.53	20.90				
NaU-1	59.37	18.16	20.49		1.98		

Table 3.4: Compositions of glasses shown in this report. All compositions are expressed on a molar basis and are 'as batched'. U-0 is the eqiuvalent composition to FLi-0 (see **Table 3.1**).

Sample	SiO_2	B_2O_3	Na_2O	Li_2O	UO_3
U-0	61.65	15.88	10.37	12.10	0.00
U-1	62.62	15.32	10.39	11.56	0.11
U-2	60.80	15.87	10.01	12.80	0.52
U-3	60.32	16.72	9.97	12.01	0.99
U-4	58.39	17.53	10.48	11.76	1.84
U-5	56.94	16.74	9.20	12.30	4.83
Na-1	60.65	16.69	22.57	0.09	0.00
NaU-1	61.09	15.22	22.99	0.01	1.80

Table 3.5: Compositions of glasses shown in this report. All compositions are expressed on a molar basis and are measured from ICP and XRF[1].

3.1.3 U bearing ceramic phases

Due to the radiological hazards involved in handling U oxide powders all preparations were performed within a dedicated muffle furnace, within an extraction hood. Various alkali uranates were prepared in the laboratory to act as standards for comparison to glass structure.

The method used was a standard mixed oxide route using the heating schedule set out by Volkowich (Volkovich *et al.* 1998). Initially, UO_3 oxide was converted to U_3O_8, to guarantee stoichiometry, by heating overnight at 700 °C. Conversion was checked by XRD of a representative sample. The U_3O_8 was mixed with a stoichiometric quantity of either Na_2CO_3 or

[1] Glass sample compositions were measured at the University of Leicester, Department of Geology. See **Section 3.4.3** for details.

Li_2CO_3 and ground using a mortar and pestle to a fine homogeneous powder. This mixed oxide precursor was then heated at 1 °C/min to 800 °C, and the temperature held for 7 hrs, with a 2 °C/min furnace cool. The resulting material was then reground and the same temperature cycle employed, except that the heating rate of 2 °C/min; this process was applied until the material appeared phase pure with powder x-ray diffraction (ca. 4 regrinds). The phases produced by this method were $Li_2U_2O_7$, and $Na_2U_2O_7$.

3.2 Radiological hazard precautions and safety

In order to deal with uranium bearing materials in a safe and effective manner certain radiological protection precautions had to be taken. As part of the Immobilisation Science Laboratory in the Department of Engineering Materials (University of Sheffield) a specific laboratory (M10) has been established / commissioned to produce glasses and ceramics containing uranium. For handling active powders a glovebox (see **Figure 3.3**) was used in order to isolate workers from loose powders.

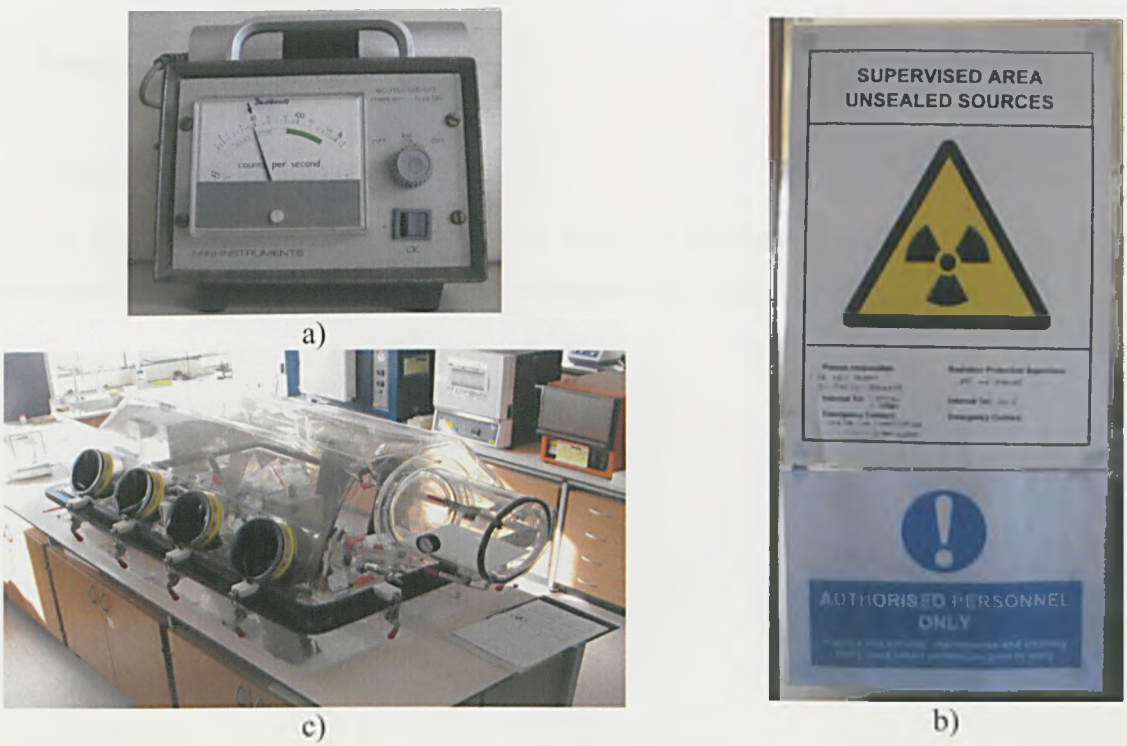

Figure 3.3: Safety equipment, a) Geiger counter; b) sign placed on laboratory door; and c) Glove box used for radioactive materials.

For each procedure carried out within the laboratory a full risk assessment and COSHH analysis was carried out and all possible risks minimised. Where furnaces were used in the

preparation of glasses and ceramics, all work was performed within an extraction hood. Surfaces were monitored for contamination both before and after carrying out experimental work and any contamination found was removed by thorough cleaning.

When samples were taken to other parts of the Department or to other Departments or facilities (e.g. the University of Durham or Daresbury Laboratory), materials were prepared as far as possible within the laboratory and then placed in sealed plastic boxes. Each individual sample was double bagged to reduce the possibility of contamination leaving the lab. For polishing and cutting of samples dedicated equipment within M10 was used.

When handling radioactive materials in the laboratory face masks and impervious gloves were used. To monitor the air within the laboratory, an extraction system which pulled air at ca. 80 $Lmin^{-1}$, though a filter paper, was employed. This extraction system was activated 1 hr before, and left running one hr after any work involving uranium was carried out. After this time the filter paper was tested for alpha emission to check uranium oxide powder particulates had not entered the air.

3.3 Imaging Techniques

3.3.1 Scanning electron microscopy

Scanning Electron Microscopy (SEM) uses a beam of electrons directed at the sample to gain information about the topography and microstructure of the specimen (see **Figure 3.4**).

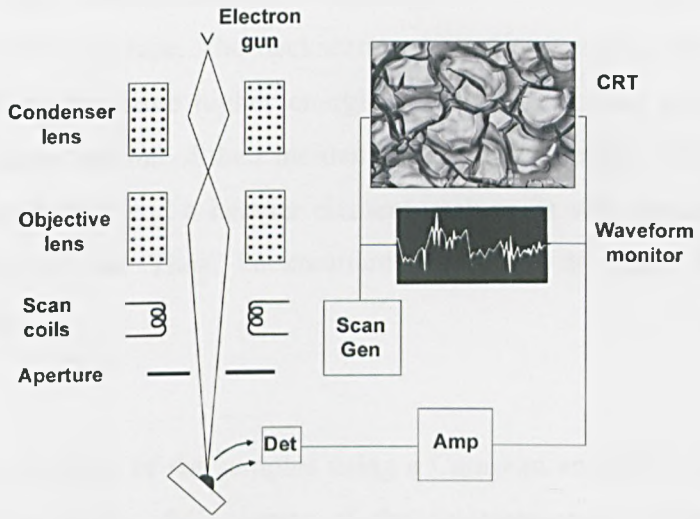

Figure 3.4: Schematic showing lay out of SEM. Image appears on Cathode Ray Tube (CRT). After Goodhew *et al.* 2001.

The electron source was a thermionic tungsten filament type. The electrons produced by the source are accelerated to an energy between 1 and 30 keV – usually around 20 keV for bulk samples. The beam is demagnified by 2 or 3 condenser lenses before it hits the specimen. The diameter of the beam can be as small as 10 nm, dependent upon the capability of the microscope. The region of the specimen penetrated by the electrons is known as the interaction volume (see **Figure 3.5**).

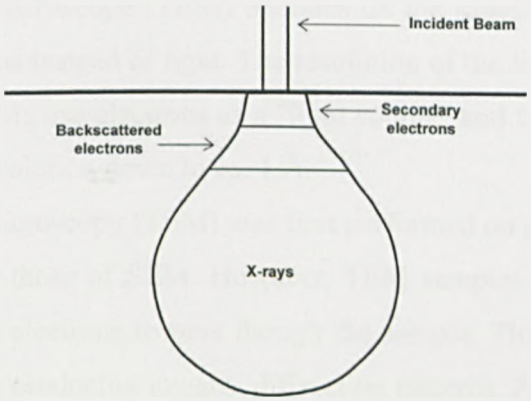

Figure 3.5: SEM interaction volume. After Goodhew *et al.* (2001).

The imaging techniques used in this project were Backscattered Electron Imaging (BEI) and Secondary Electron Imaging (SEI).

The secondary electrons used in SEI imaging are electrons which have undergone inelastic scattering at (or within a short distance of) the surface of the sample and so have lost a detectable

amount of energy. These electrons have low energy (<50 eV) but are abundant and allow topological imaging of the surface. The backscattered electrons used in BEI are less numerous than secondary electrons but have higher energies. They are incident electrons that leave the surface still having a large fraction of their incident energy. The number of backscattered electrons varies with atomic number, Z, e.g. a heavier element such as Zr will appear much brighter than lighter elements such as Na. Thus, backscattered electrons are used for images showing compositional contrast.

SEM Experimental

SEM was carried out on many of the samples using a Camscan and JEOL 6400 SEM. Both SEI and BEI were used to give a full picture of the microstructure. Energy Dispersive x-ray Spectroscopy (EDS) was also used to give qualitative compositional analysis of the material (see **Section 3.5.3**). Samples were examined using an accelerating voltage of 10-20 kV, depending on the sample.

Samples were mounted in epoxy resin then ground and polished to 0.25 μm. They were then carbon coated and silver 'dag' (colloidal silver paste) was applied to the side of the sample to aid conduction.

3.3.2 Transmission electron microscopy

The transmission electron microscope (TEM) operates on the same basic principles as the light microscope but uses electrons instead of light. The resolution of the light microscope is limited by the wavelength of light. TEMs use electrons as a "light source" and their much lower wavelength makes it possible to get a resolution down to ca. 1 Å.

Transmission Electron Microscopy (TEM) was first performed on glass in 1952 (Slayter 1952), it uses principles similar to those of SEM. However, TEM samples are very much thinner than SEM samples, allowing the electrons to pass though the sample. There are many 'modes' that a TEM can be operated under producing images, diffraction patterns, Z-contrast images and energy dispersive spectroscopy (EDS) scanning. Images can easily be magnified up to 1 x 10^6 times.

Theory

TEM is an imaging technique whereby a beam of electrons is transmitted through a specimen forming an image. This image is magnified and directed to appear either on a fluorescent screen or a layer of photographic film, or to be detected by a sensor such as a CCD camera.

A schematic of the TEM can be seen in **Figure 3.6**. The electron gun produces a stream of monochromatic electrons. This stream is focused to a small, thin, coherent beam by a series of condenser lenses. The beam can then be restricted by the condenser aperture. The beam strikes the specimen and some of the electrons are transmitted. This transmitted portion is focused by the objective lens into an image. The image is passed down the column through the intermediate and projector lenses, being enlarged all the way. The image strikes an imaging screen (e.g. phosphourous or CCD).

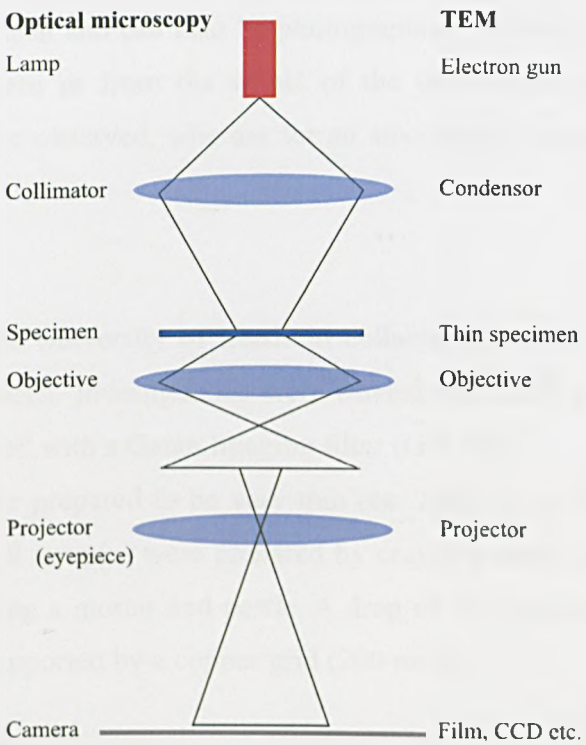

Figure 3.6: Schematic of Transmission Electron Microscope (TEM), showing the lense system within evacuated TEM column and comparing to an optical microscope used in transmission.

The intensity of the transmitted beam is affected by the crystallinity (*via* diffraction), the volume and the density (Z-number) of the material through which it passes. A high-contrast image can therefore be formed by blocking electrons deflected away from the optical axis of the microscope by placing an aperture to allow only unscattered electrons through, this is known as bright field TEM. The image produced is a "shadow" picture where more transparent regions appear brighter.

The quality of photographs may be improved by dark field imaging. In this, only the electrons diffracted away from the region of interest are allowed to recombine to form the image. Using the

TEM in dark field mode a Z-contrast image can be produced. This can be thought of as a map revealing the scattering power of the material at an atomic resolution. Electrons that have been scattered over relatively large distances are collected. The inelastic scattering power of an atom is proportional to the square of its atomic number Z, which means that atoms with a higher atomic number appear brighter. This gives some compositional indication of the structure that is being examined (Pennycook 1992).

By changing the relative position of the viewing screen, a diffraction pattern, rather than the image, of the specimen is seen and can also be photographed. Diffraction patterns can either be performed on a selected area or from the whole of the illuminated region. For a crystalline material a series of spots are observed, whereas for an amorphous silicate glass a series of rings are formed.

TEM experimental

TEM was carried out at the University of Leeds in collaboration with Dr. Andy Brown at the Institute of Materials Research. Investigations were carried out using a FEI CM200 FEG-TEM operating at 197 kV and fitted with a Gatan Imaging filter (GIF 200).

In TEM samples must be prepared to be very thin (ca. 2000 Å) to allow the transmission of electrons. For this project all samples were prepared by crushing small fragments of glasses with analytical grade ethanol using a mortar and pestle. A drop of the suspension was pipetted onto a lacy or holey carbon film supported by a copper grid (200 mesh).

3.3.3 Optical microscopy

Figure 3.6 shows a schematic of an optical microscope being used in transmission mode. In this work a Polyvar optical microscope was used in reflection mode. This is similar to transmission mode except the light is incident on the sample from above (or in **Figure 3.6** from the bottom). The microscope had a digital imagining camera attached with software that allowed a graticule to be added to the images. Samples were prepared in a similar manner to that for SEM; however, no carbon coating was applied as it is unnecessary.

3.3.4 Photography

Images of samples were taken using a digital camera (Cannon PowerShot A610). Samples containing uranium were also photographed under UV light to demonstrate the fluorescence seen in such glasses under UV light.

3.4 Spectroscopic techniques

Spectroscopy: the scientific study of spectra. Where spectra is the plural for spectrum which has a range of meanings, the most relevant being: the range of colours obtained by refraction (e.g. in a rainbow) or frequencies of electromagnetic waves. Its etymology is from the Latin *spectrum*: a ghostly apparition. In this project spectroscopic techniques at a variety of radiation frequencies were used (see **Figure 3.7**)

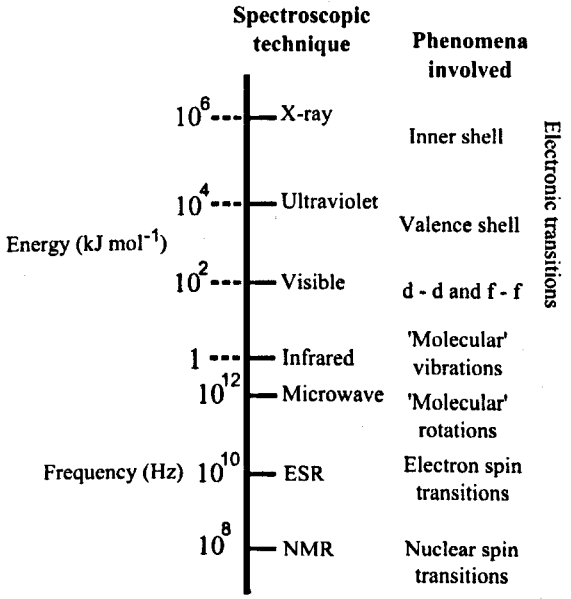

Figure 3.7: Principle regions of the electromagnetic spectrum and the associated spectroscopic techniques. After (West 1999).

3.4.1 Optical absorption spectroscopy

In the presence of incomplete 3*d*, 4*f*, and 5*f* electron shells visible light may be absorbed by an element at well-defined wavelengths. The energy at which incident light is absorbed (through electron excitation) is dependent on both the valence of the element in the glass and the co-ordination environment.

Using optical absorption spectroscopy the position and intensity of these absorptions can be found. Plots of absorbance against wavelength (or a function of wavelength) of that radiation are produced and can be analysed in a number of ways but often with reference to standard tables.

Theory

Transitions of electrons between outermost energy levels are associated with energy changes in the range ca. 10^4 to 10^5 cm^{-1} or 1.2 to 12 eV. These energies span the NIR (Near infra-red) through

the visible to the UV (Ultra-Violet) and are often associated with colour. However, above a certain energy, known as the ultraviolet edge, intense absorption occurs[1] preventing information being gained above this energy. In (boro)silicate glasses this occurs in the UV region and is caused by transition of types 2 and 3 shown of the 4 general mechanisms given here:

1. Promotion of an electron from a localised orbital on one atom to a higher energy localized orbital on the same atom;
2. Promotion of an electron from a localized orbital on one atom to a higher energy localized orbital on an adjacent atom, charge transfer spectra;
3. Promotion of an electron from a localized orbital on one atom to a delocalized energy band, the conduction band, which is characteristic of the entire solid;
4. Promotion of an electron from one energy band, the valence band, to another band of higher energy, the conduction band.

The broad absorption peaks or bands, which are the source of the majority of useful information, arise primarily from Type 1 transitions.

Samples are placed within a collimated and monochromated beam of light (the light source varies depending on wavelength region) and the wavelength scanned through the specified range (see **Figure 3.8**). This transmitted light is then compared to a reference (air) and the difference in absorption recorded as a function of wavelength thus cancelling source fluctuations.

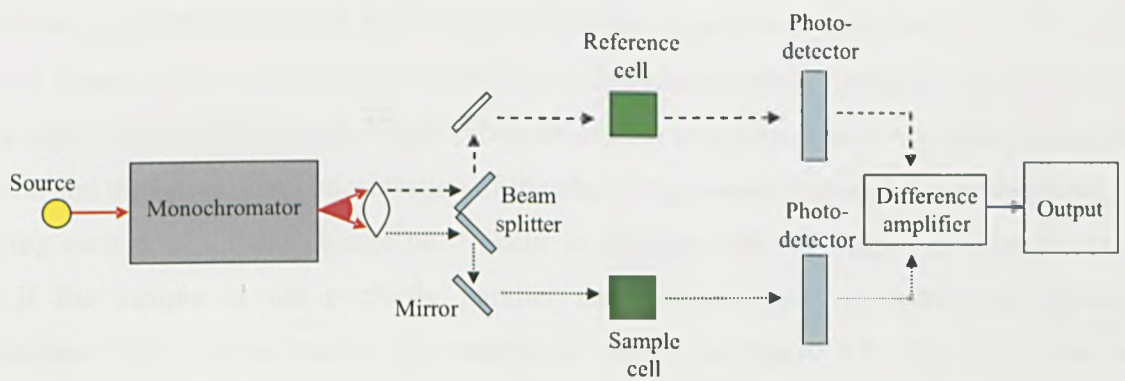

Figure 3.8 Set up of an optical absorption spectrometer.

[1] This is believed to be due to transition of a valence electron of a network anion to an excited state. Formation of a NBO will lower the energy required for the electronic excitation, and so shift the UV edge to lower frequencies (Shelby 2005).

Data analysis

In order to compare spectra from different samples, a normalisation process must be undertaken. All samples must be of defined thickness and be as optically similar as possible with planer, polished and parallel surfaces. Normalisation must take into account the reflection at the two glass-air interfaces and the optical absorption in the body of the glass sample. The reflection losses can be taken into account with **Equation 3.1** and **Equation 3.2** where the reflection coefficient (r) is related to the refractive index (n) of the glass. In these experiments a constant value for n of 1.51 is assumed for all glasses (Bamford 1977).

$$r=\left[\frac{n-1}{n+1}\right]^2 \qquad \textbf{Equation 3.1}$$

The reflection loss (R) at both surfaces is calculated thus:

$$R=(r-1)^2 \qquad \textbf{Equation 3.2}$$

The reflection losses must be subtracted from any spectral transmission data. This is achieved using the Lambert-Beer Law:

$$I=I_0\exp(-\alpha cl) \qquad \textbf{Equation 3.3}$$

where I and I_0 are the transmitted and incident intensities respectively (assumed to be unity minus reflection losses), α is the absorption coefficient, c the concentration of absorbing species (units often g mole / litre), and l the path length. Analysis used in this project has only taken into account reflection and thickness. The concentration of the absorbing species has not been normalised.

During each scan a lamp change must occur to complete the full region of interest. At this point, if the sample is not perfectly parallel and polished, the spectrum may feature a characteristic "step" in the results. An example is shown in **Figure 3.9**. This effect has been minimised, as far as possible, by careful sample preparation as set out below.

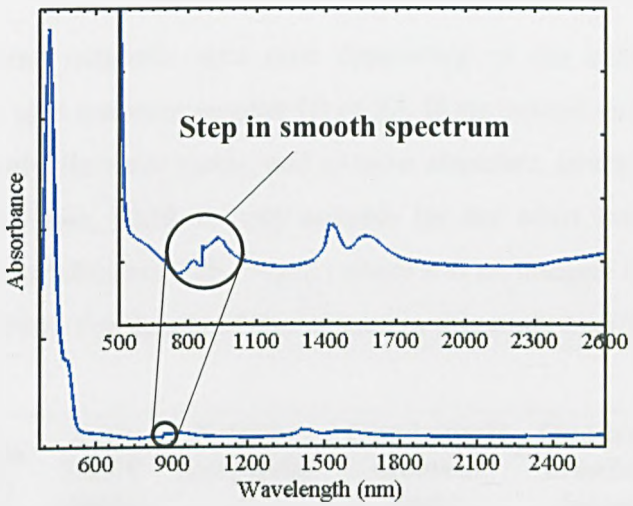

Figure 3.9: Lamp-change step in smooth optical spectrum for a U bearing alkali borosilicate glass.

Experimental

Optical spectra were measured and recorded using a Perkin-Elmer Lambda 900 Spectrometer connected to a PC. Data points were acquired at 1 nm intervals over a range of wavelengths: 185 and 3300 nm.

Each sample was initially cut using a diamond saw, ground and polished to 6 μm using oil based lubrication and then further polished with a cerium rouge impregnated wheel (2-3 μm). The samples were 1-2 mm thick and parallel sided. The planer nature of the sample was checked with 5 measurements using a set of vernier callipers insuring each measurement was within 0.01 mm.

3.4.2 Nuclear magnetic resonance spectroscopy

Nuclear Magnetic Resonance (NMR) spectroscopy uses an applied magnetic field to split the degenerate energy levels of elements with a non-zero nuclear spin. Through a high frequency transmitter, transitions between these energy levels can be stimulated giving rise to a resonance signal. From this process isotope specific local environment information can be extracted. Originally used for molecular liquids, solid state NMR typically gives broad featureless peaks from which little direct structural information can be obtained. In more recent Magic Angle Spinning NMR (MAS-NMR) techniques, used in this project, much more solid state structural information can be gathered.

Theory

All isotopes have an overall magnetic spin state depending on the number of neutrons, and protons (each possessing a spin quantum number (I) of ½). If the overall value of $I > 0$ the isotope is NMR active. Unfortunately, the most stable, and so most abundant, isotopes of interest (e.g. ^{12}C, ^{16}O, ^{28}Si, etc) have $I = 0$. Thus, NMR is only suitable for the often lower abundant isotopes (sometimes using isotopic enrichment) with $I = n/2$ (where n is an integer) these include ^{11}B, ^{23}Na, ^{27}Al, ^{29}Si (Stebbins *et al.* 1995). For details of nuclei used in this study (see **Table 3.6**).

Nuclei	Natural Abundance (%)	Spin (I)	ν_0 at 7.05 T (MHz)	Relative receptivity *	Quadrupole moment (mb)	Quadrupole broadening factor **	Sternheimer antishielding factor
^{29}Si	4.70	1/2	59.601	1	n/a	n/a	n/a
^{23}Na	100	3/2	79.44	2.51×10^{2}	104	2.64	-5.5
^{11}B	80.1	3/2	96.32	3.59×10^{2}	40.6	2.83×10^{-1}	0.19
^{7}Li	92.5	3/2	16.67	7.35×10^{2}	-40.1	2.28×10^{-1}	0.2

Table 3.6: Properties of NMR active nuclei use in this study (Mackenzie & Smith 2002).
* Relative receptivity normalised to ^{29}Si,
** quadrupole broadening normalised to ^{27}Al.

Practically, an externally imposed magnetic field is used to force the magnetic moments of the active isotopes to align and to spilt between two energy levels, depending on whether the nuclear spins are aligned parallel (low energy) or anti-parallel (high energy) with the applied magnetic field (see **Figure 3.10**). The application of a static magnetic field H_o removes the degeneracy of the spin energy levels. If $I = 1/2$, the nucleus has two energy levels and behaves as a magnetic dipole. If $I > 1$, the nucleus has more than two energy levels and behaves as a magnetic quadrupole. The difference in energy levels is relatively small, thus the population of the lowest level is only marginally more than those of the higher levels, and thus the sensitivity of the NMR experiment is low but can be increased by using a stronger magnetic field, which increases population difference and the absorption intensity (Atkins *et al.* 2006).

The energy of the transition (ΔE) between the levels is directly proportional to the applied field (B) at the nucleus, this value is small ca. 0.01 $Jmol^{-1}$ for an applied magnetic field of 10^4 G (1 T) (West 1999) this energy is associated with the radio frequency region of the electromagnetic spectrum:

$$\Delta E = \frac{|\gamma|}{2\pi} Bh$$ **Equation 3.4**

where γ is the gyromagnetic ratio which is characteristic of each nuclide and h is Planck's constant. Due to shielding of the nucleus from the applied magnetic field by the chemical environment (surrounding electrons) the local magnetic field experienced by the nucleus is slightly different from the external magnetic field B_Φ. This, along with e.g. quadrupolar effects and dipole-dipole interactions, causes 'chemical shifts' (δ) in the observed spectrum.

$$\delta = \frac{\nu - \nu_0}{\nu_0} \times 10^6$$ **Equation 3.5**

where ν and ν_0 are the resonant frequencies of the sample nuclei and standard nuclei respectively. A value $\delta < 0$ ppm indicates the nucleus is shielded relative to the standard and $\delta > 0$ ppm indicates the nucleus is deshielded compared to the reference. The influence of structural factors on chemical shift usually follows the hierarchy: change in co-ordination number > nearest neighbour substitution > next nearest neighbour substitution (Eckert 1992, Mackenzie & Smith 2002).

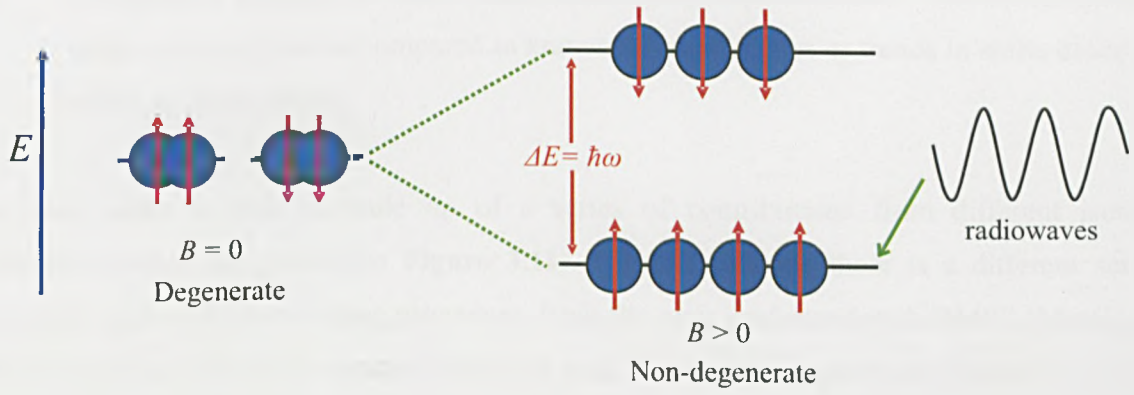

Figure 3.10: Schematic of nucleus spin splitting due to the application of a magnetic field (i.e. $B > 0$). Radio waves applied are of energy in the order of ΔE to cause transition between levels.

To extract this information from a sample, a constant magnetic field is applied (4 to 18 Tesla) while pulses of high frequency radiation (usually radio frequencies) are scanned. The nuclear transitions are excited by this radiation and the re-emission of this energy is then observed in real-time and Fourier transformed to give the frequency-domain spectrum.

Nuclides with $I = 1/2$, such as ^{29}Si, yield narrow peaks with positions at the expected isotropic chemical shift value. Quadrupolar nuclides (such as ^{11}B and ^{7}Li) often yield peaks that are

broadened and split. The position of these peaks are often field dependent moving closer to the isotropic chemical shift value with increased field (Mackensie & Smith 2002).

MAS-NMR reproduces the quasi-random orientation of liquid samples, and so collapsing the broad lines to reveal fine structure. This is done by high speed mechanical rotation of the sample about a single axis. The sample is spun at the "magic angle" of 54.7° to the direction of the magnetic field. This angle is chosen because, put simply, the equations for the orientation dependence of line broadening effects contain the chemical shift anisotropy factor ($3\cos^2\theta - 1$), where θ is the angle between the external magnetic field and the sample orientation. This factor vanishes at $\theta = 54.7°$ thus removing orientation dependence of line broadening.

Data analysis

The data extracted from are of two types, either:

1. Peak area: the area under a resonance signal is proportional to the number of resonating atoms that give rise to a signal. It can be measured by integration;
2. Chemical shifts (δ): these are expressed with respect to an internal standard (e.g. $(CH_3)_4Si$) to account for field differences between spectrometers. The chemical shift peaks observed can be compared to known standard values or trends in shifts observed with e.g. composition.

The area under a peak is made up of a series of contributions from different isotope environments within the glass (see **Figure 3.11**). For each isotope there is a different set of environments and so different fitting procedure. Peak fits were performed with DMFit (Massiot *et al.* 2002). It can not always be assumed that each peak fitted under a spectrum represents a single isotope environment; for this reason care must be taken when interpreting data. An assumption must be made that there is no preferential site selection for different isotopes so that results for a particular elemental isotope are representative of all the isotopes of that element. All data in this study are normalised to a peak height of 100 to allow easier comparison.

^{29}Si MAS-NMR spectrum (Lippmaa *et al.* 1980) of silicate glasses gives peaks whose position is dependent on the chemical environment of the ^{29}Si nucleus. In particular, due to the lack of quadrupolar broadening, it can distinguish the average number of BO, n, around each Si atom, expressed as a Q-value[1], Q^n. For each Q-value a range of chemical shifts are observed, this shift is dependent on the number of BO and the nature of the bridging species (e.g. Si-O-Si or Si-O-B). A

[1] Where Q signifies "quarternary" (four bonds).

selection of these can be found in **Table 3.7**, the values presented here are very precise, in general for aluminosilicates the shifts for each Q^n species cover a range for example Q^4(4Si) is about -102 to -116 ppm. This makes analysis difficult in systems with Si, B, Zr and U all of which could form Si-O-X bonds, making the individual contributions very difficult to assign. In this project four Gaussian peaks were fitted to the spectra. Two of these were used to fit the spinning sidebands and two to fit the main peak. The spinning side bands[1] were assumed to be due to Q^3 and other axial symmetric contributions (e.g. Q^4(B), Q^4(Zr), and Q^4(U)). Two more Gaussian peaks were fitted under the main peak: one peak (Peak 1) was fixed at the centre of the two side bands (amplitude and width were allowed to refine). A second peak (Peak 2 - nominally Q^4) was allowed to freely refine (see **Figure 3.11d**).

System		Peak shift (ppm)	Si environment
Glass	$Na_2Si_2O_6$	-78	Q^2(2Si)
Glass	$Na_2Si_2O_6$	-88	Q^3(3Si)
Zircon	$ZrSiO_4$	-81.6	Q^4 (4Zr)
Thompsonite	$NaCa_2[Al_5Si_5O_{20}]$-$6H_2O$	-83.5	Q^4(4Al)
Natrolite	$Na_2Al_2Si_3O_{10}$-$2H_2O$	-87.7	Q^4(3Al)
Natrolite	$Na_2Al_2Si_3O_{10}$-$2H_2O$	-95.4	Q^4(2Al)
Glass	$Na_2Si_2O_6$	-100	Q^4(4Si)

Table 3.7: Example MAS-NMR ^{29}Si peak shifts for a range of minerals (Sherriff & Grundy 1988, Mackenzie & Smith 2002).

For ^{23}Na MAS-NMR spectra (see **Figure 3.11a**) there were assumed to be three "environments" fitted with Gaussian curves; amplitude, position and width were allowed to refine for all peaks (including spinning sidebands).

For ^{7}Li MAS-NMR spectra (see **Figure 3.11b**) there were assumed to be two "environments" fitted with Lorentzian curves (amplitude, position and width being allowed to refine). A third environment (Peak 3) appeared only with addition of UO_3 and was treated as the first two.

Both high and low field ^{11}B data were fitted in the same manner (peak positions being independent of field). The ^{IV}B peak was fitted using two pseudo-Voigt factors (η=0.5 [2]) with the

[1] Spinning side bands occur in the presence of axially symmetric (Q^1 and Q^3) and asymmetric (Q^2) but not spherically symmetric (Q^0,Q^4) Q species.

amplitude, position and width being allowed to refine. The two ^{III}B peaks were fitted using Q_{mas} 1/2 curves with amplitude, position, EM (apodisation of the theoretical lineshape), and η_Q (quadrupolar frequency) being allowed to refine. The asymmetry parameter of the curves (eta_Q) is fixed at 0.28. η_Q measures the deviation from local cylindrical symmetry (Du & Stebbins 2003a). Starting values were taken from the work of Parkinson *et al.* (2005) and Rodderick *et al.* (2007) who obtained their parameters on very similar glasses to those used in this work.

^{IV}B values were corrected with the resolved ^{III}B fraction being increased by 4%. This increase was necessary due to the loss, under MAS, of central (1/2, 1/2) transition intensity from the ^{III}B centre band into the spinning sidebands. This does not happen for the ^{IV}B sites with their much smaller quadrupole interaction so that all of the central (1/2, 1/2) transition intensity appears in the centre band (Mackenzie & Smith 2002). The four peaks were assigned as shown in **Table 3.8**. The shift between ^{IV}B Peak 1 and ^{IV}B Peak 2 is due to increased shielding effect of Si in the second co-ordination sphere.

Peak	Assignment
^{IV}B Peak 1	^{IV}B(1B,3Si)
^{IV}B Peak 2	^{IV}B(0B,4Si)
^{III}B Peak 1	Symmetric ($^{III}B(O_{1/2})_3$)
^{III}B Peak 2	Asymmetric ($^{III}B(O_{1/2})_2(O^-)$)

Table 3.8: Peak assignments for ^{11}B MAS-NMR spectra (Parkinson *et al.* 2005, Rodderick *et al.* 2007, Mackenzie & Smith 2002).

Errors are calculated as the standard deviation of 5 separate peak fittings from different starting points (typically within ± 2 %). All fitted spectra for all samples are shown in **Appendices D & E.**

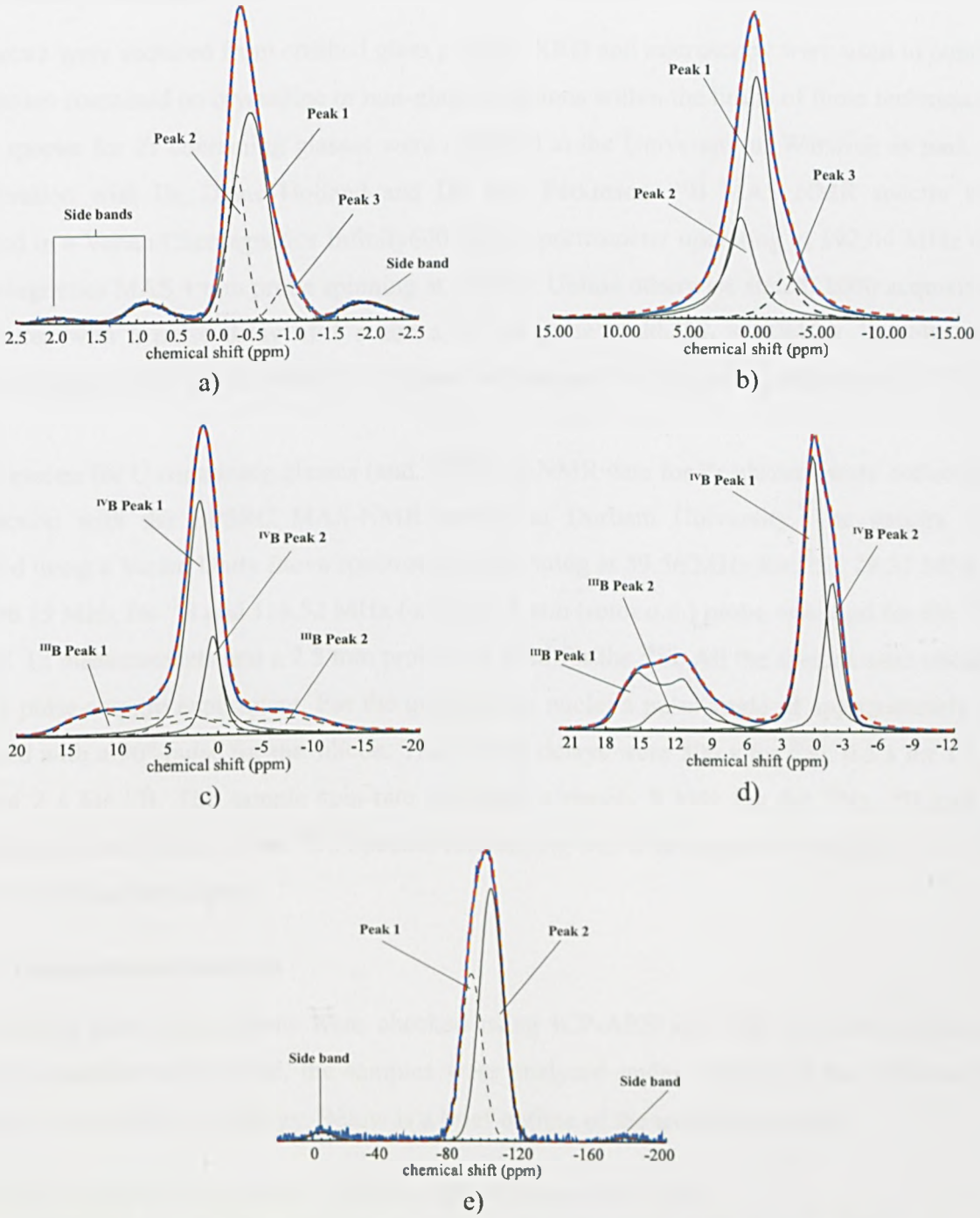

Figure 3.11: Fitting curves for various isotope MAS-NMR spectra: a) ^{23}Na spectra fitting; b) ^{7}Li spectra fitting; c) ^{11}B spectra fitting (96.19 MHz); d) ^{11}B spectra fitting (192.04 MHz); and e) ^{29}Si spectra fitting. See **Section 3.4.2** for details.

MAS-NMR experimental

All spectra were acquired from crushed glass powder. XRD and microscopy were used to confirm that glasses contained no crystalline or non-glass inclusions within the limits of these techniques.

^{11}B spectra for Zr containing glasses were collected at the University of Warwick as part of a collaboration with Dr. Diane Holland and Dr. Ben Parkinson. ^{11}B MAS NMR spectra were obtained in a Varian/Chemagnetics Infinity600 NMR spectrometer operating at 192.04 MHz with a Chemagnetics MAS 4 mm probe spinning at 15 kHz. Unless otherwise stated, 1000 acquisitions were taken with a pulse delay of 1 s and a 0.7 μs pulse width ($B_1 \approx 60$kHz). Samples were referenced against BPO_4 solid taken as -3.3 ppm with respect to the primary reference $Et_2O{:}BF_3$ at 0 ppm.

All spectra for U containing glasses (and ^{29}Si MAS-NMR data for Zr glasses) were collected in conjunction with the EPSRC MAS-NMR service at Durham University. The spectra were obtained using a Varian Unity Inova spectrometer operating at 59.56 MHz for ^{29}Si, 79.31 MHz for ^{23}Na, 96.19 MHz for ^{11}B and 116.52 MHz for ^{7}Li. A 5 mm (rotor o.d.) probe was used for the ^{23}Na, ^{11}B and ^{7}Li measurements and a 7.5 mm probe was used for the ^{29}Si. All the spectra were obtained using a pulse-acquire experiment. For the quadrupolar nuclei a pulse angle of approximately 22° was used with a 90° pulse for the silicon. The recycle delays were 300 s for ^{29}Si, 0.5 s for 1 s for ^{7}Li, and 2 s for ^{11}B. The sample spin-rate was approximately 8 kHz for the ^{23}Na, ^{11}B and ^{7}Li measurements and 5 kHz for the ^{29}Si. Spectral referencing was with respect to 1M NaCl, 1M LiCl, BF_3/OEt or tetramethylsilane.

3.4.3 Compositional analysis

The nominal glass compositions were checked using ICP-AES and XRF. As these techniques were not available in Sheffield, the samples were analysed under contract at the University of Leicester, Department of Geology. Below is a brief outline of the techniques used.

Inductively Coupled Plasma Atomic Emission Spectroscopy (ICP-AES)

Inductively Coupled Plasma Atomic Emission Spectroscopy (ICP-AES) is a widely used technique for analysing trace elements in solutions. In this technique, the atom is not excited, but merely dissociated from its chemical bonds by placing it into unexcited, un-ionized ground state. This atom is then capable of absorbing radiation at a discrete wavelength over a narrow bandwidth. A number of ways are available for dissociating elements of interest from their bonds,

and the energy required can be generated in a number of ways. Currently only plasma devices, burners and furnaces are used commonly. The flame technique was used for samples in this project.

ICP-AES was used for analysis of all elements in leachate samples. Due to the problems of analysing Li and B by XRF, ICP-AES was used to analyse these elements for the glass samples. The glass must initially be dissolved in an appropriate solution, the most common methods are; dissolution by fusion decomposition and dissolution by acid attack decomposition. Decomposition by fusion commonly uses a lithium metaborate flux, followed by leaching using a mineral acid. The advantage of this method of dissolution is the formation of a low melting eutectic mixture hence volatile elements can be analysed using this method. However, the desire for B and Li content of glasses meant that the acid acid attack method was used. Acid attack does not use a flux, so reducing the amount of dissolved solid content. HF is commonly used at temperatures up to 100 °C (Walsh 2005).

X-ray fluorescence

Wavelength-dispersive X-Ray Fluorescence spectrometry (XRF) is a non-destructive analytical technique used to identify and determine the concentrations of the elements present in solids, powders and liquids. XRF is capable of measuring all elements from ^{4}Be to ^{92}U. When a specimen is irradiated using a beam of sufficiently short wavelength x-ray radiation, a characteristic x-ray spectrum can be observed from the excited sample. Utilising high intensity x-ray tubes, detector and x-ray optics, XRF is a quantitative analytical method. It may be noted that the detection limit is dependent on the peak to background ratio of the spectral lines but the method has a detection limit for most elements of approximately 5 ppm.

Although the technique itself is non-destructive to produce an appropriate sample for analysis the sample must be dissolved in a lithium tetraborate flux and formed into a fusion bead. It is this bead that is analysed. The use of the lithium tetraborate flux makes this technique unsuitable for analysis of Li and B within the glass samples and so ICP was used for this (see above). XRF was used to analyse for Na, Si, Zr, and U.

3.5 X-ray techniques

X-rays have two properties which make them attractive for materials analysis:

1. X-ray wavelengths are of the same order of magnitude as inter-atomic distances. This is used in x-ray diffraction analysis where analysis of interference patterns can give rise to detailed structural information from well-ordered materials (i.e. unit cell dimensions, atomic positions and symmetry).
2. The energy of the x-ray photon is of the order of binding energy of the most tightly bound electrons. This is exploited in X-ray Absorption Spectroscopy (XAS) which can give detailed information on non-periodic systems (i.e. co-ordination environments, atom types and contact distances).

3.5.1 X-ray diffraction

In this project X-Ray Diffraction (XRD) is used mainly to identify crystalline compounds. The technique is based on Bragg's law:

$$n\lambda = 2d\sin\theta \qquad \textbf{Equation 3.6}$$

where n is an integer, λ is wavelength, d is crystalline lattice spacing and θ is the angle of diffraction.

Powdered samples were placed at the centre of the diffractometer circle. A static x-ray source was incident on the sample with a detector placed to receive the diffracted X-rays. In the standard technique the sample rotates at θ °/min while the detector rotates about the circle with rotation speed 2θ °/min (so the angles of incidence and diffraction are maintained equal). The intensity and angle of the diffracted beam is measured (see **Figure 3.12**).

Experimental

In this work a Philips x-ray powder diffractometer (operating at 40 kV and 30 mA) was used with Cu $K_{\alpha 1}$ radiation (λ = 1.54051 Å). For glasses data were collected from 5 to 80 °2θ with a step size of 0.02° running at 0.1 °min^{-1} and giving an overall collecting time of ca. 12 hrs. For crystalline materials data were collected over the same range but with a step size of 0.02° running at 1.2 °min^{-1}, giving an overall collecting time of ca. 1.5 hrs. Samples were analysed as powders being first ground and sieved to <52 μm.

The patterns obtained were matched to reference patterns of compounds contained in the International Crystalline Diffraction Database (ICDD) using the STOE x-ray diffraction analysis software WinXPOW, all crystalline phases identified will be referred to by their ICDD number shown by square brackets e.g. ZrO_2 - [20-684].

The use of an aluminium sample holder means that peaks are often seen in the XRD traces at the indicative 2θ values. To make observation of XRD traces easier these peaks have been removed from all traces (see **Figure 3.13**). This was done using by removing the data points associated with the Al peaks with care being taken not to effect the rest of the data.

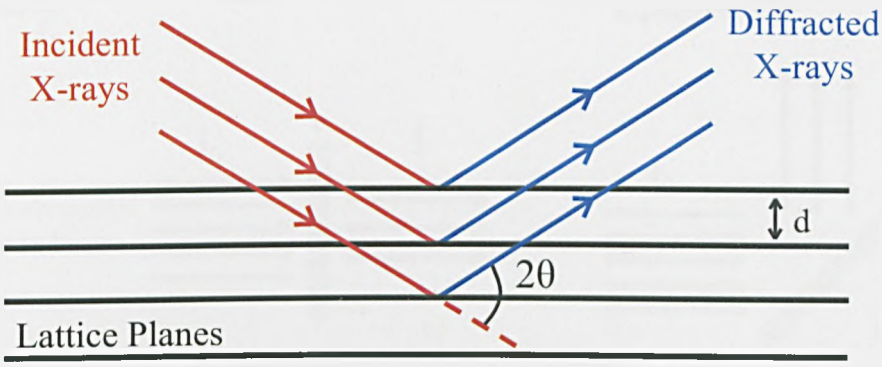

Figure 3.12: Diffraction of X-rays within a crystal.

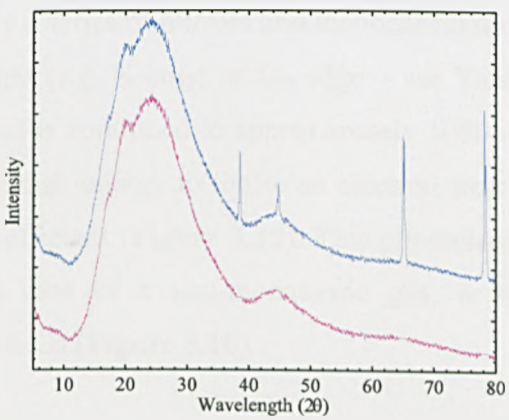

Figure 3.13: Removal of Al peaks which result from sample holder.

3.5.2 X-ray absorption spectroscopy (XAS)

X-ray Absorption Spectroscopy (XAS) is sensitive to the short range atomistic arrangement around a specified atom within a material. The basic method is very simple: a thin homogeneous sample is prepared and high energy (usually synchrotron) X-rays are incident upon it. The intensities of the incident and the transmitted (or fluorescent) x-ray beam are recorded while the incident beam energy is increased (see **Figure 3.14**).

The absorption is calculated differently for transmittance intensity (I_T) and fluorescence intensity (I_F). In transmission the intensity of the transmitted beam is recorded (see **Equation 3.7**).

In fluorescence, the intensity of x-rays released from a secondary x-ray emission process are recorded (see **Equation 3.8**).

$$\alpha(E)=\ln\left(\frac{I_0}{I_T}\right) \qquad \textbf{Equation 3.7}$$

$$\alpha(E)=\frac{I_F}{I_0} \qquad \textbf{Equation 3.8}$$

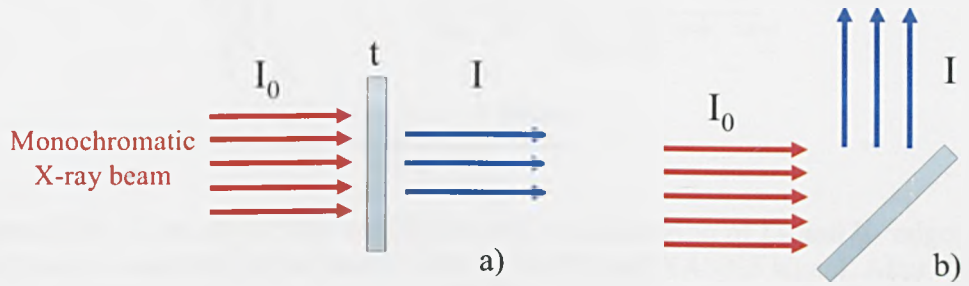

Figure 3.14: A schematic representation of x-ray absorption spectroscopic measurements in a) transmission mode and b) fluorescence mode.

The x-ray energy (tuned by a series of mirrors and monochromators) is chosen as an absorption edge of the element of interest (e.g. K-edge or L_{III}-edge – see **Table 3.9**). The scan begins just below the absorption edge and is continued to approximately 1000 eV beyond. At the absorption edge incident X-rays have enough energy to ionise an electron from a core orbital giving a large increase in the absorption coefficient (**Figure 3.15**). This photoelectron is emitted as a spherical wave which, except in the case of a non-monatomic gas, is then backscattered from the surrounding atomic electron shells (**Figure 3.16**).

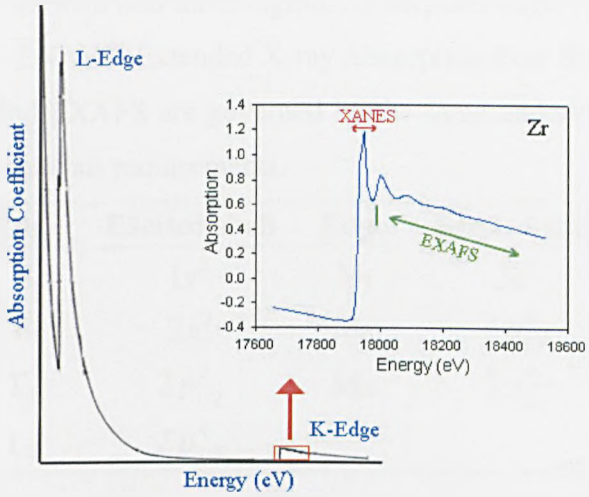

Figure 3.15: X-ray absorption coefficient of Zr in the region of L- and K- edges. The box area is expanded in the inset to show EXAFS and XANES signal. After PN-G (2007).

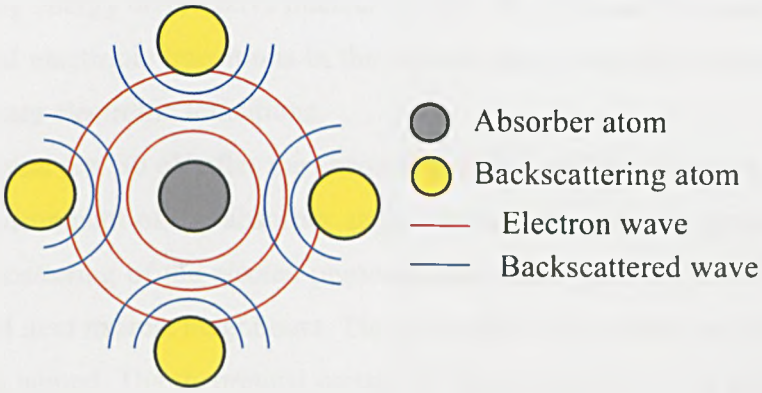

Figure 3.16: Wave nature of photoelectron as it leaves the inner shell of atom, also showing interaction with surrounding atoms.

The interference between outgoing and backscattered waves affects the probability of incident x-ray photon absorption. With the increasing (x-ray) photon energy the wavevector[1], **k**, of the photoelectron wave increases, leading to alternating constructive and destructive interference (oscillations) in the absorption spectrum (see **Figure 3.16**).

These oscillations can be used to determine detailed atomic structure (including the atomic number, distance and co-ordination number of the atoms surrounding the element whose absorption edge is being examined), and electronic and vibrational properties of the material.

[1] The photoelectron wavevector is given by: $k = 2\pi/\lambda$

The oscillations can be divided into three regions: absorption edge; XANES (X-ray Absorption Near-Edge Structure); and EXAFS (Extended X-ray Absorption Fine Structure) (see **Figure 3.15**). Although, both XANES and EXAFS are governed by the same underlying mechanisms, they are separated due to different analysis requirements.

Edge	Excited shell	Edge	Excited shell
K	$1s^2$	M_I	$3s^2$
L_I	$2s^2$	M_{II}	$3p^2_{1/2}$
L_{II}	$2p^2_{1/2}$	M_{III}	$3p^4_{3/2}$
L_{III}	$2p^4_{3/2}$		

Table 3.9: Absorption edges are named according to the electron that is excited.

XANES and the absorption edge

The absolute edge energy depends on the oxidation state of the absorber atom. This is due to the dependence of binding energy on effective nuclear charge. The shape of the absorption edge arises from multiple internal electronic transitions in the excited atom. Pre-edge features are commonly attributed to bound state electronic transitions.

In the XANES region (ca. 30 eV after the absorption edge) excited electronic energy levels are sensitive to local environment of the absorber atom. XANES features are generally attributed to single and multiple-scattering of the ejected photoelectron wave from the central absorbing atom among its nearest and next nearest neighbours. Thus, valuable information on chemical bonds and site symmetry can be gained. The theoretical picture of these transitions is in general too complex to allow a comprehensive quantitative analysis and so results are gained by comparison with standards of known composition and structure, often using Linear Combination Analysis (LCA).

EXAFS

The probability of x-ray absorption (and so the EXAFS oscillations) is determined by the interference between the outgoing and backscattered wave. Thus, the expression for the backscattered wave is proportional to the absorption coefficient ($\chi_i(k)$) and is a function of:

- **The amplitude of the backscattered wave ($T_j(2k)$),** which itself is a function of the electronic structure of the neighbouring atoms;
- **The phase shift,** introduced by a wave of wave number, k, travelling the distance $2r_j$ from the absorber and back, $2kr_j$; and

- **The phase shift**, due to the varying potential between absorber and shell, $\xi_i(k)$.

This gives:

$$\chi_j(k)=\frac{T_j(2k)}{r_j^2}\sin[2kr_j+\xi_j(k)] \qquad \textbf{Equation 3.9}$$

for multiple scatterers sum over all j scatterers:

$$\chi(k)=\sum_j A_j(\mathbf{k})\sin[2kr_j+\xi_j(k)] \qquad \textbf{Equation 3.10}$$

the amplitude factor $A_i(k)$ represents the jth shell scattering amplitude and can be written:

$$A_j(\mathbf{k})=\frac{S_0^2 N_j}{kR_j^2}F_j(\mathbf{k})e^{-2\sigma_j^2 k^2} \qquad \textbf{Equation 3.11}$$

where N_j represents the number of atoms in the jth shell, F_j relates to the photoelectron backscattering magnitude, and σ^2 is the mean-square disorder in the distribution of interatomic distances, where disorder includes both static and dynamic (thermal) disorder (the root-mean-square deviation of the interatomic distance over R_j) (Sayers *et al.* 1971, Koningsberger & Prins 1988).

Limitations of XAS

The length scale of XAFS as a structural probe is governed by the fact that a high-energy, excited photoelectron state is not infinitely long lived, but must decay as a function of time and distance and hence cannot probe long-range effects. This decay is due primarily to inelastic losses as it traverses the material either by interacting with and exciting other electrons in the solid, or by creating collective excitations (i.e. plasmon production). Thus the original outgoing wave of the excited photoelectron dies away as it moves further away from the absorbing atom. Ultimately, it becomes too weak to lead to any significant reflections from distant atoms. The returning reflected waves also suffer this same type of extinction. The net effect is that XAFS can only measure the local atomic structure over a range limited by the effective mean free path of the excited photoelectron. This range is ideally tens of angstroms. However, in practice it is found to be less than 5 Å.

Another problem of XAS sensitivity concerns elements with low electron density. This is a

particular problem for lithium sodium borosilicate glasses due to the presence of B and Li. These elements have low electron density, and so low back scattering amplitude (see **Figure 3.17** and **Figure 3.18**).

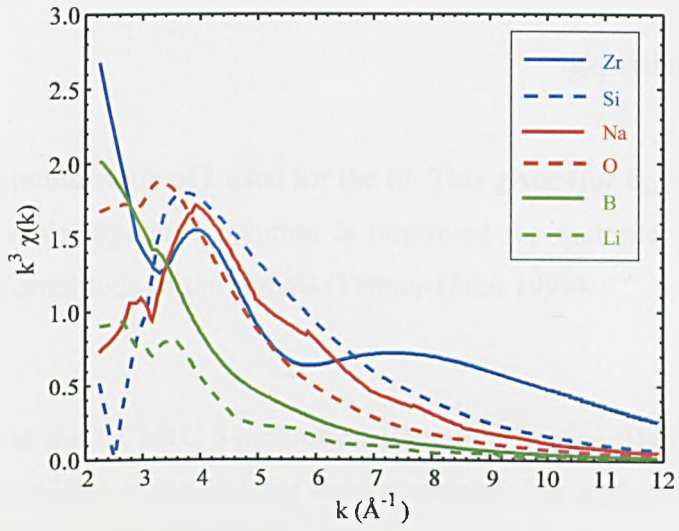

Figure 3.17: Dependence of back scattering amplitude on x-ray energy (for Zr K–edge) calculated using EXCURV98 (Binsted 1998).

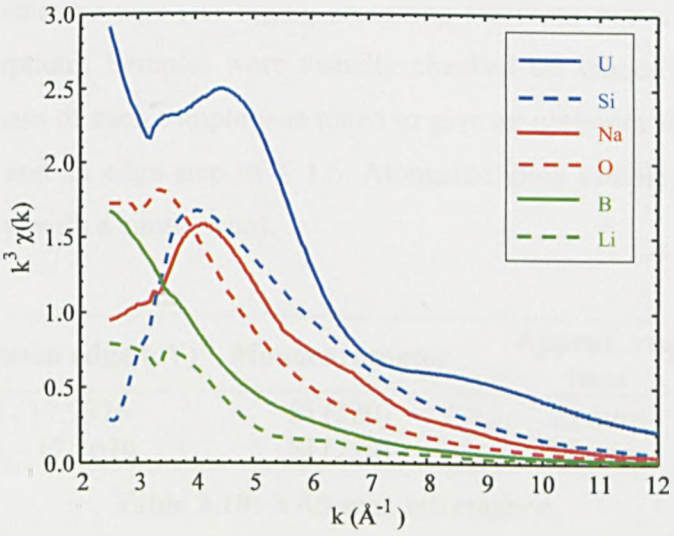

Figure 3.18: Dependence of back scattering amplitude on x-ray energy (for U L_{III}-edge) calculated using EXCURV98 (Binsted 1998).

Finally, the finite *k* range of the EXAFS spectrum limits the bond-length resolution of any model. Two scattering shells can only be resolved if they differ sufficiently in frequency to cause a detectable change in the EXAFS amplitude, due to interference between the two EXAFS

components. For small differences in distance, the interference simply introduces an exponential damping factor; indistinguishable from an increased disorder term. For ideal data, two shells of the same scatterer should become resolvable when the difference in their distances, δR, is large enough to cause a 'beat' in the EXAFS amplitude. This occurs for:

$$\delta R \geq \frac{\pi}{2 k_{max}} \qquad \textbf{Equation 3.12}$$

where k_{max} is the maximum value of k used for the fit. This gives (for k_{max}=12 Å^{-1}) $\delta R \approx 0.13$ Å but this is a optimistic value. Spatial resolution is improved for multiple types of scatters due to changes in phase and amplitude of the signals (Penner-Hahn 1999).

XAS experimental

Data were collected at the CCLRC Synchrotron Radiation Source, Daresbury (UK), each glass sample was scanned at least twice and the data combined. For each sample the edge step was maximized. Compositions were checked for elements with similar edge energies to Zr (e.g. Y, Nb).

In this project, all samples were in the form of powders (sieved to <52 μm) which were attached to layers of adhesive tape (for highly absorbing standards boron nitride was intimately mixed to reduce absorption). Samples were visually checked for inhomogeneities prior to data acquisition. The thickness of each sample was tuned to give an optimum absorbance (ln (I_o/I_t)) of ca. 2.6 after the edge and an edge step of ≤ 1.6. Alongside glass samples, crystalline standards were examined (usually with a single scan).

Element	Absorption edge (eV)	Monochromator	Approx. run time	Scan range (Å^{-1})
Zr	K - 17.9976	Si (220)	25 mins	0-12
U	L_{III} - 17.1670	Si (220)	25 mins	0-13

Table 3.10: XAS scan information.

The L_{III}-edge was chosen for U as it gives equivalent structural results to M_3, M_4, and M_5. without the inherent problems of dealing with very low energy X-rays. Also M_4 and M_5 thresholds are dominated by a "white line" due to transitions from the 3*d* core level to unoccupied *f*-states. The strong absorption is due to the atomic resonance in the 3*d*-5*f* atomic cross section (Kalkowski *et al.* 1986).

Data analysis

Data analysis was carried out using the suite of programs provided remotely from Daresbury Laboratory. The process is shown graphically in **Figure 3.20**. The raw data were initially normalised in such a way to allow comparison of data from different beam lines on different visits. The relationship between mass absorption co-efficient $\alpha(E)$ and $\chi(k)$ is:

$$\alpha(E)=\alpha_0(E)(1+\chi(k)) \qquad \textbf{Equation 3.13}$$

which means that:

$$\chi(k)=\frac{\alpha(E)-\alpha_0(E)}{\Delta\alpha_0} \qquad \textbf{Equation 3.14}$$

where $\alpha_0(E)$ is the smoothly varying atomic-like background absorption (including contributions, if any, from other edges), and $\Delta\alpha_0$ is a normalising factor that arises from the net increase in the total atomic background absorption at the edge in question.

To prepare the data for EXAFS analysis a series of spline functions was fitted to the data (using the EXSPLINE (2000) program). Prior to this, the EXCALIB program (EXC) was used to extract values for energy and absorption from the data and to extract an approximate edge energy (mid-point of edge) for input into EXSPLINE.

Structural analysis of this background subtracted data was undertaken using the program EXCURV98 (Binsted 1998). The original EXCURVE program was written in 1982 for analysis of EXAFS spectra, making use of the new fast spherical wave method (Gurman *et al.* 1984). The revised version can consider both single and multiple scattering (see **Figure 3.19**).

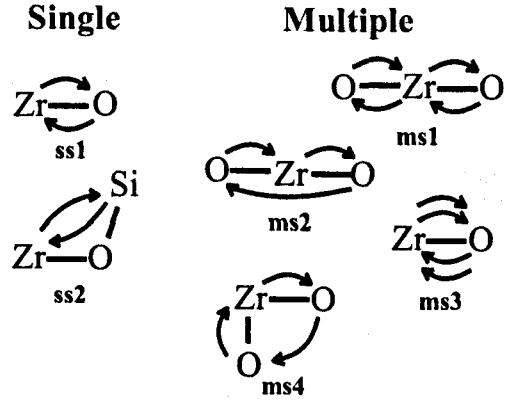

Figure 3.19: Examples of multiple and single scattering for a (O-)Zr-O(-Si) system.

Structural parameters were obtained by fitting of a cluster model function to the measured EXAFS spectra in *k*-space. This model is then refined to give: interatomic distances; the number of neighbours per shell; and the corresponding $2\sigma^2$ factor. The estimated accuracy of the refined parameters is given in **Table 3.11**.

The quality of fit of model to laboratory data is tested using the R-factor (expressed as a percentage).

$$R_{EXAFS}=\sum_{i}^{n}\frac{1}{\sigma_i|\chi_i^{lab}(k)-\chi_i^{th}(k)|} \qquad \textbf{Equation 3.15}$$

A value of around 20 % would normally be considered a reasonable fit and a value of 10 % considered unlikely without filtering of the data. An absolute index of goodness of fit, which takes account of the degree of over determinacy in the system is given by the reduced χ^2_{EXAFS} function (Lytle *et al.* 1989):

$$\chi^2_{EXAFS}=\frac{1}{(N_{ind}-p)(N_{ind}/N)\sum_{N}^{i} w_i(\chi_i^{lab}(k)-\chi_i^{th}(k))^2} \qquad \textbf{Equation 3.16}$$

where N_{ind} is the number of independent data points, N the number of data points and p the number of parameters. N_{ind} is calculated within limits shown by:

$$N_{ind}=\frac{2(r_{max}-r_{min})(k_{max}-k_{min})}{\pi} \qquad \textbf{Equation 3.17}$$

The absolute value of χ^2_{EXAFS} is not meaningful only the relative value on addition of a new shell, compared to the previous shell value, decrease in χ^2_{EXAFS} suggesting the validity of an added shell.

Parameter	1st Shell	Outer shell
N	± 10 %	± 25 %
R (Å)	± 0.01	± 0.04
$2\sigma^2$ (Å^2)	± 10 %	± 25 %

Table 3.11: Worst case scenario precision of XAS data output (Lytle *et al.* 1989).

XANES and edge data were examined using a linear combination approach. The data are normalised to the edge step and then all data are rebinned at the same energy interval as a selected standard. A least squares routine is then run to minimize the difference between a chosen sample and standards. Thus it minimizes (for 3 standards A, B, and C):

$$\sum_{i} X_i-aA_i-bB_i-cC_i \qquad \textbf{Equation 3.18}$$

With the constraints:

$a, b, c < 1 \quad a+b+c=1$ **Equation 3.19**

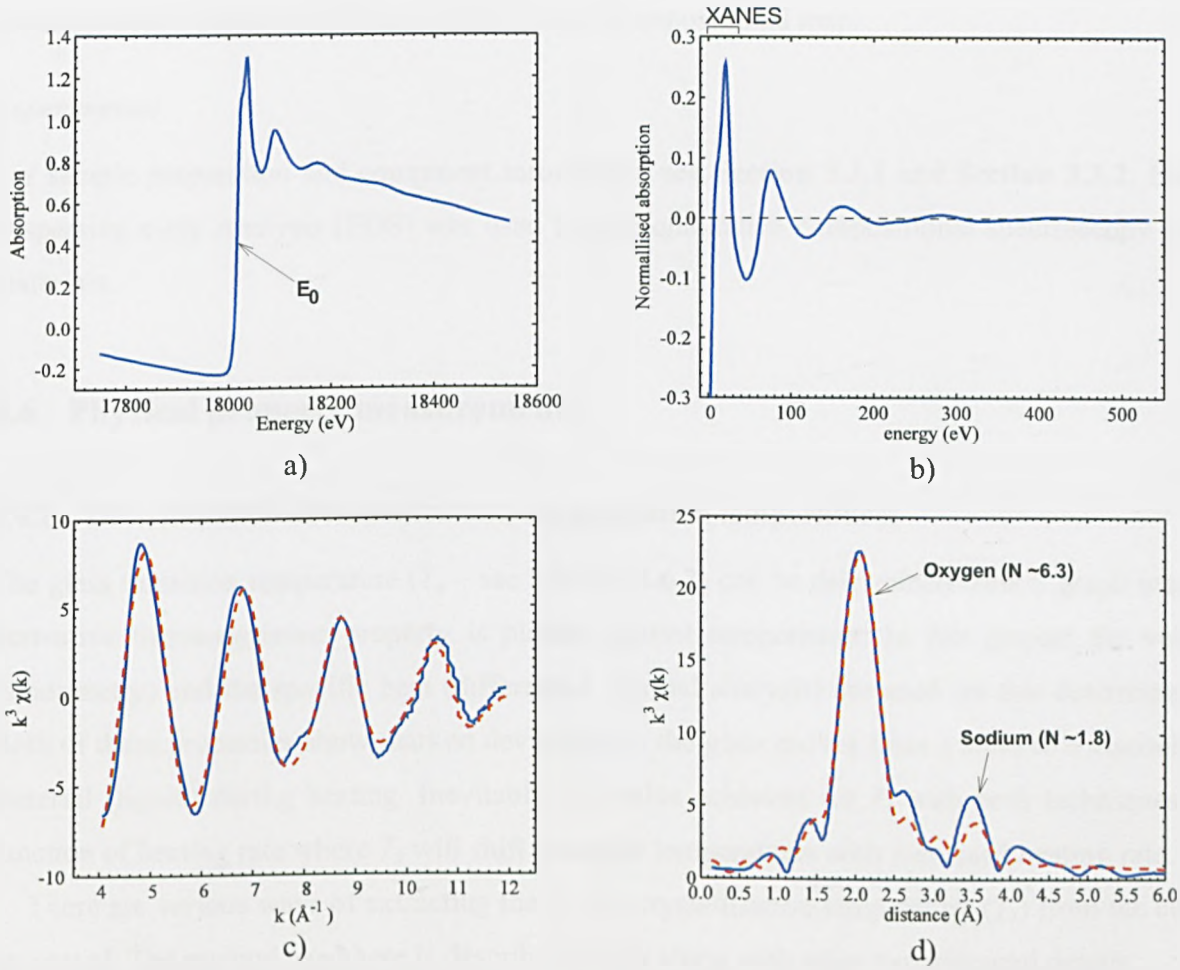

Figure 3.20: Process of data processing and data analysis. a) raw XAS data, b) background subtracted XAS data, c) fitted EXAFS data, and d) FT EXAFS data with fit. Data is shown in blue solid line and fit in red dashed line.

3.5.3 Energy Dispersive x-ray Spectroscopy (EDS)

This form of spectroscopy takes advantage of X-rays produced from a sample when using SEM and TEM (**Section 3.3**). Energy Dispersive x-ray Spectroscopy (EDS) is a technique that makes use of the X-rays produced when incident electrons excite atoms to a higher energy state at the surface, which then relax to a lower energy state, releasing X-rays. The energy of the x-ray photon is equal to the difference in energy between the states involved in transition and so, by measuring this energy, it is possible to determine the elements present in the specimen. Due to the large interaction volume X-rays from a larger volume than desired are often collected (**Figure 3.5**).

EDS can either be taken at a single point where all elements are scanned for or it can be carried

out on a selected range of elements in either line scan or mapping mode. Line scanning involves an EDS scan along some predefined trajectory giving a 1D compositional map , mapping involves rastering over a predefined area to build up a 2D compositional map.

Experimental

For sample preparation and equipment information see **Section 3.3.1** and **Section 3.3.2**. Energy Dispersive x-ray Analysis (EDS) was used to give qualitative compositional spectroscopy of the materials.

3.6 Physical property measurements

3.6.1 Determination of transition and crystallisation temperatures

The glass transition temperature (T_g – see **Section 2.6.2**) can be determined from a graph where a derivative thermodynamic property is plotted against temperature. In this project the volume (dilatometry) and the specific heat (differential thermal analysis) are used for this determination. Both of these properties show marked deviations as the glass moves from a solid to a viscoelastic material (liquid) during heating. Inevitably, the value achieved for T_g with both techniques is a function of heating rate where T_g will shift to higher temperatures with increased heating rate.

There are various ways of extracting the T_g and crystallisation temperature (T_x) from the curves generated. The method used here is described below along with other experimental details.

Differential thermal analysis

Differential Thermal Analysis (DTA) was performed using a Perkin Elmer DTA 7, which was calibrated using Al (M_r 26.98, T_m = 660 °C), and Au (M_r 196.97 and T_m = 1063.0 °C) standards in air, and the Perkin Elmer thermal analysis suite Pyris V.6. The analysis was conducted on a powdered sample, ground to <75 μm using a silicon carbide Tema mill.

Around 50 mg of the sample was weighed and to ± 0.0005 g using an electronic microbalance. The standard consisted of an equivalent amount of finely divided alumina (Al_2O_3) powder which was also weighed to an accuracy of ±0.0005 g and placed in a Pt crucible. The sample was placed in an identical crucible. Both sample and standard were heated to ca. 1000 °C at 10 °C min^{-1}. Temperature and ΔT measurements were taken every 0.1 s. Two specimens of each sample were analysed. Cooling curves provided little information of interest and so were not recorded. Pt

crucibles were used to avoid contamination from Al_2O_3. Values for T_g (first endothermic peak) and T_x (the large exothermic peak) were each taken at 2 points on the curve (see **Figure 3.21**).

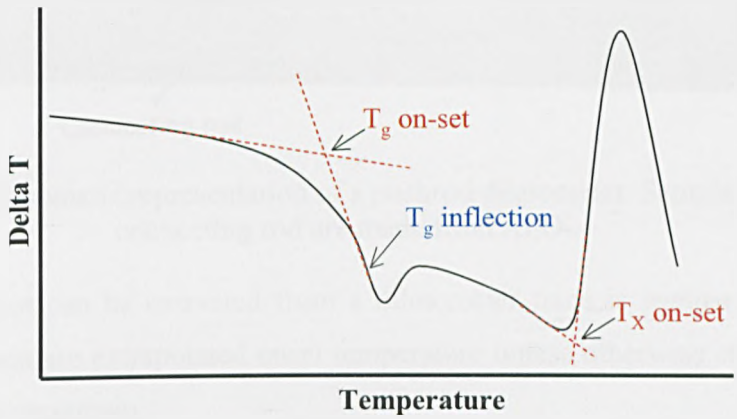

Figure 3.21: Idealised schematic showing the method for measurement of T_g and T_X from DTA data. T_g inflection taken from minima in first derivative curve.

Dilatometry

This technique measures thermally induced dimensional changes in a sample derived from phase changes, mass transfer, crystallisation and other thermally activated processes. It is used here to determine T_g, dilatometric softening point (T_d) and thermal expansion (α) of glass samples. The technique has been used with U bearing glasses in preference to thermal gravimetric analysis or DTA due to reduced potential for radioactive contamination of equipment.

The experimental set up used in this study is shown in **Figure 3.22**. The specimen was held between a connecting rod and the flat wall of the measuring system. The sample was heated at 5 °C/min. As the sample was heated, changes in the length of the sample were transmitted though the connecting rod and measured by the strain gauge. At T_d the specimen undergoes apparent contraction due to specimen softening (viscosity 10^9 - 10^{10} Pa.s). Heating and measurements were stopped when a shrinkage of 0.15 % was observed (see **Figure 3.23**). Samples were wrapped in Pt foil for all experiments to avoid glass adherence to the instrument. Two specimens of each sample were tested.

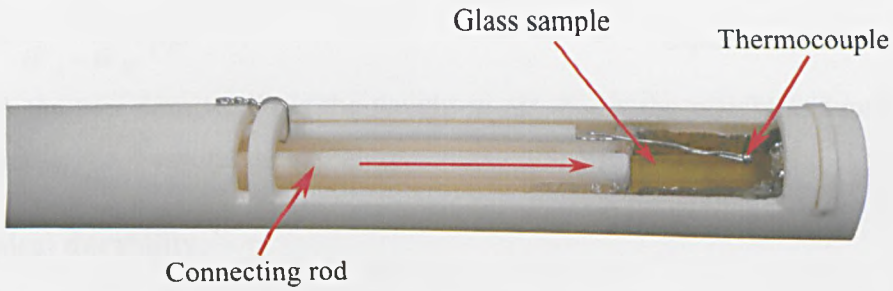

Figure 3.22: Schematic representation of a pushrod dilatometer. Sample holder and connecting rod are made from Al_2O_3.

The information that can be extracted from a dilatometer trace is summarised **Figure 3.23**. Values for T_g in the text are extrapolated onset temperature unless otherwise stated. The value of T_d is taken at the peak maximum.

To allow comparison between DTA and dilatometry results a DTA trace was obtained for the base glass (U-0, see **Table 3.4**). This sample was heated at 5 °C/min to allow comparison between DTA and dilatometry.

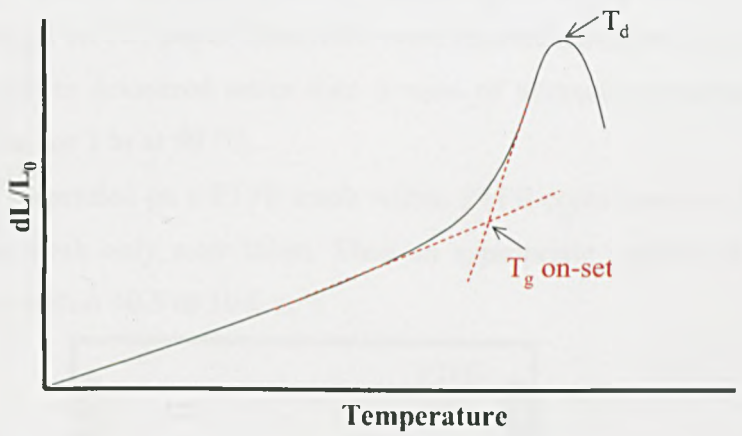

Figure 3.23: Schematic representation of dilatometer data showing how T_g and T_d values were extracted.

3.6.2 Density measurements

Density measurements were carried out using the standard Archimedes method. A sample of glass was weighed dry (minimum weight 20 g) to 4 d.p. and was then weighed suspended in boiled, distilled water of known temperature (ca. 20 °C). Using a standard water density-temperature chart, the sample density was calculated. Zero porosity was assumed for all samples.

$$\rho_{TRUE} = \frac{W_A}{W_A - W_W} \rho_W \qquad \textbf{Equation 3.20}$$

where ρ_{TRUE} is the true density, W_A is the weight in air, W_W is the weight in liquid and ρ_W is the density of liquid at the measured temperature.

3.6.3 Chemical durability

There are various standard tests available for measuring the chemical durability of a glass. Those considered for this project are shown in **Table 3.12**. It was decided to use the MCC-1 test protocol for this project using the ASTM standard method (ASTM 2004). This method was chosen due to the improved resolution of surface composition and reaction layer features (under SEM) available compared to powder samples.

Representative monolithic test specimens were used. Five specimens of each glass were prepared (for 3, 7, 14, 21, and 28 day tests). Samples were prepared so that the surface area was as close to 400 mm^2 as sample size allowed; with approximate dimensions 10 x 10 x 5 mm (no dimension was allowed to be less than 4 mm), measured with a micrometer. All surfaces were prepared down to 280 grit on SiC paper. Monoliths were cleaned using the following procedure: 5 mins of ultrasonic wash in deionized water then 5 mins of ultrasonic cleaning in acetone. The samples were then dried for 1 hr at 90 °C.

The samples were suspended on a PTFE mesh within PTFE containers (see **Figure 3.24**). The weight of sample and mesh only were taken. Then an appropriate volume of water was added (surface / volume ratio within ±0.5 of 10.0 m^{-1}).

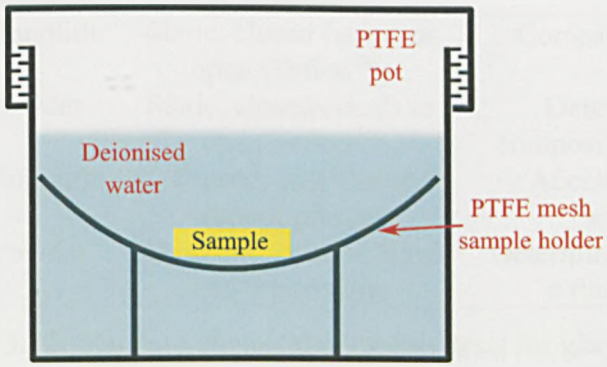

Figure 3.24: PTFE MCC-1 experimental set-up.

The lids of the 5 sample containers and the 28 day blank (no sample only water in container) were then tightened and within 30 mins the vessels were placed within a preheated furnace at 90 °C. The time and day the vessels were placed into the furnace was recorded. The leach-vessel lids

were retightened at 1 hr and then daily until no further slack was present.

After the appropriate time the samples were removed and allowed to cool for one hr. The vessels (with sample) were then weighed to ensure weight was not less than 90 % of starting value. The monolith and mesh were then removed and put under vacuum for 48 hrs to dry. Two specimens (10 ml) of each leachate were taken and removed to separate containers. One of these was first filtered though a glass fibre filter to remove any solid colloids (>0.2 μm) in the leachate. To all samples 1 ml of 11 % HNO_3 was added. The pH of the remaining leachate was recorded using a calibrated electronic pH meter.

The same procedure was undertaken with 2 blanks. One blank was analysed at the beginning of the run (no heat treatment). The second was treated as a 28 day sample (28 days at 90 °C). All filtered solutions were sent for ICP analysis for Si, B, Na, Li, U and / or Zr[1], non-filtered solutions were kept in reserve.

After drying the monoliths, a selection were mounted for microscopy. Non-active glasses were mounted on metal studs using silver dag and then carbon coated. The surface layer was then analysed under SEM. After this, the monolith was removed from the stud and mounted in epoxy resin. This was then ground down to expose a through thickness cross section of the alteration layer and bulk glass. This was again analysed using SEM. A similar procedure was undertaken for the active glasses except optical microscopy was undertaken not SEM due to the active nature of the samples.

Test name	T (°C)	Sample	Conditions	Used for
MCC-1	≤ 90	Monolith	Static, closed (steel) or open (Teflon™)	Comparison of wasteforms
PCT	90	Powder	Static, closed (steel) or open Teflon™	Determining effects of composition and homogeneity
VHT	200	Monolith	Closed, only water vapour present	Accelerated formation of altered products
SPFT	≤ 90	Powder	Dynamic, open to flow and atmosphere	Determination of dissolution as a function of flow rate

Table 3.12: Standard chemical durability tests for glasses.

Data analysis involved the use of the following Equations (ASTM 2004):

[1] Leachate compositions were measured at the University of Leicester, Department of Geology. See **Section 3.4.3** for details.

Mass leached

Mass leached m_i, initial volume of leachate in test vessel, V_i, with concentration of element i in leachate, C_i, and blank C_b.

$$m_i=(C_i-C_b)\cdot V_i \qquad \textbf{Equation 3.21}$$

Normalised elemental mass loss

Normalised elemental mass loss, $(NL)_i$, f_i mass fraction of element i in the unleached specimen, A_s surface area (mm^2)

$$(NL)_i=\frac{m_i}{(f_i\cdot A_S)} \qquad \textbf{Equation 3.22}$$

3.7 Molecular dynamic calculations

3.7.1 Overview of technique

In the simplest version of Molecular Dynamics (MD), an atomic system is represented by a small (by macroscopic standards) set of N particles occupying a box of fixed volume. The particles are each given an initial velocity and position. The system is then allowed to evolve with time, the position of each particle being obtained by numerically solving a set of $3N$ second-order Newtonian equations of motion using a finite difference scheme.

To ensure a stable integration algorithm and to obtain good energy conservation, the timestep employed in MD is typically of the order of 1 femtosecond (10^{-15} s). This limits the amount of real time that may be simulated in MD to typically a few 10s of nanoseconds (longer times may be achievable at the expense of greater computational effort or through use of a smaller system size). Thermodynamic properties such as the hydrostatic pressure can be obtained as a time average of an appropriate function of the instantaneous positions and velocities of the particles.

The forces that appear in the equations of motion may be derived from a given potential energy function *via*:

$$m_i\ddot{\boldsymbol{r}}_i=-\nabla_i U\equiv \boldsymbol{f}_i \qquad \textbf{Equation 3.23}$$

where m_i is the particle mass, $\ddot{\boldsymbol{r}}_i$ its acceleration, $\boldsymbol{f}_i$ is the total force acting a particular particle, ∇

is Cartesian spatial gradient operator and U is the potential energy of the system of particles. The interaction between the particles can be described by potential energy functions, $U(r_1, r_2, r_3, ...r_N)$. This can be expressed as the sum of one-, two-, three-body potentials *etc.*:

$$U(\boldsymbol{r}_1, \boldsymbol{r}_2, \boldsymbol{r}_3, ..., \boldsymbol{r}_n) = \sum u_1(\boldsymbol{r}_i) + u_2(\boldsymbol{r}_i, \boldsymbol{r}_j) + u_3(\boldsymbol{r}_i, \boldsymbol{r}_j, \boldsymbol{r}_k) + ... + u_N(\boldsymbol{r}_1, \boldsymbol{r}_2, \boldsymbol{r}_3, ..., \boldsymbol{r}_n) \quad \textbf{Eq. 3.24}$$

where the one body potential u_1, represents an external potential. For the simulations described in this work, there is no external potential, and therefore the 1-body term is zero. A great deal of simulation work involves the use of simple pair potentials due to the expense of calculating the higher order contributions. Contributions from higher order terms diminish rapidly although the 3-body contribution can make a significant contribution in some work.

For the simulation of solids, a good empirical model for the intermolecular potential that is widely used is based on the sum of a Born-Mayer repulsive contribution and a leading $|r_{ij}|^{-6}$ attractive contribution as shown in **Equation 3.25:**

$$U(\boldsymbol{r}_{ij}) = A \exp\left(\frac{-|\boldsymbol{r}_{ij}|}{\rho_{ij}}\right) + c|\boldsymbol{r}_{ij}|^{-6} \qquad \textbf{Equation 3.25}$$

the first term here is a repulsive term where $\boldsymbol{r}_{ij}$ is the separation between atoms i and j *and* ρ_{ij} and A are adjustable parameters. The second term is an attractive term where c is an adjustable parameter. The potentials used in this work do not involve dispersion and hence $c = 0$. For charged species, a Coulombic term is added to the above potential. In this work an Ewald summation is employed to calculate the Coulombic contribution to the energy, forces and virial (Allen & Tildesley 1987).

It is difficult in glass simulations, using only two body potentials, to accurately reproduce SiO_4 tetrahedra. To address this difficulty a 3-body-potential is typically employed, e.g. (Takada *et al.* 1995):

$$u_\theta = \frac{1}{2} C_\theta (\theta - \theta_0)^2 \qquad \textbf{Equation 3.26}$$

where a bond angle, θ, (e.g. Si-O-Si) is kept close to an equilibrium angle, θ_0 as possible.

The kinetic energy of the system, K, is given by:

$$K = \frac{1}{2} \sum_{i=1}^{N} m_i (\dot{\boldsymbol{r}}_i)^2 \qquad \textbf{Equation 3.27}$$

where $\dot{r}_i$ are the Cartesian velocities of the particles. The temperature is related to the mean K per particle *via* the equipartition principle:

$$k_B T = \langle 2K \rangle \qquad \textbf{Equation 3.28}$$

where k_B is the Boltzman constant.

To simulate bulk properties, surface effects imposed by limited system size must be removed by considering a pseudo-infinite system. Thus, periodic boundary conditions are used to form a quasi-infinite system. The simulation box is surrounded by identical images of itself (see **Figure 3.25**). Only the position of the particles in the central box are independent and must be calculated. An atom leaving the central box will be replaced by an atom entering from the antipole direction.

Evidently we cannot calculate the interaction of each atom with an infinite number of neighbours. Thus, no atom further than a defined cut-off distance is considered. This cut-off is initially a region equal in size to the simulation box (assuming the atom in question is at the centre of this region) this is known as the minimum image convention. Because the majority of potential contributions are short ranged, the potential is usually truncated by employing a spherical cut-off. The cut-off radius must be < L / 2, where L is the length of a cubic simulation box. This method may be generalised to handle non-cubic boxes.

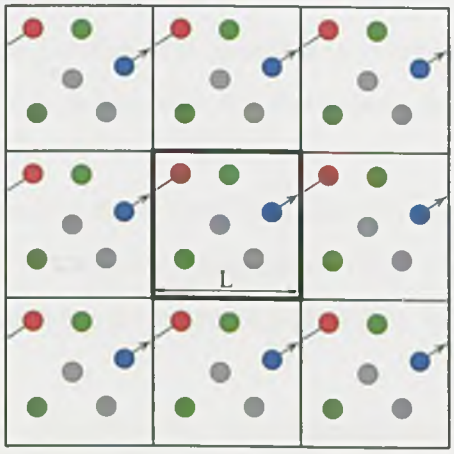

Figure 3.25: Schematic representation of periodic boundary conditions in 2-D.

It should be noted that Newton's equations for a many particle system cannot be solved exactly. Thus, a good numerical integration algorithm must be used. This project makes use of the time reversible Verlet algorithm (Frenkel & Smit 2002), which is correct up to order $(\delta t)^3$ (where δt is time-step) The value of δt must be at least about two orders of magnitude smaller than the time constant of elementary physical motions in the system e.g. The period of vibration of covalent Si-

O bonds to bond angles, which are significantly less than one pico second: therefore it becomes necessary to choose a $\delta t \approx 10^{-15}$ s to obtain stable integration. This significantly limits the physical time which can be covered (around 1-10 ns) which has two major effects on this work:

1. Thermal equilibration must be undertaken at very high temperatures (3000-7000 K) to achieve thermal equilibrium in the limited time available;
2. The speed of cooling of the thermally equilibrated atomic arrangement to a lower temperature (required for glass formation) must be fast (ca. 6 x 10^{14} °C min^{-1}).

3.7.2 Ensembles

Newton's equations of motion conserve energy. MD therefore mimics an isolated thermodynamic system (constant number of atoms; *N*, constant volume; *V*, and constant energy; *E*), commonly refereed to as the *NVE* ensemble.

In many practical applications of molecular simulations the *NVE* ensemble is inconvenient as it does not resemble laboratory conditions. It is more appropriate to work with ensembles in which either temperature is controlled (*NVT* ensemble) or both temperature and pressure are controlled (*NPT* ensemble). Both of these latter ensembles have been used in this project.

3.7.3 Thermostats and barostats

Thermostats and barostats are used within MD simulations to control the temperature and pressure within the simulation. Within this work only the Berendsen thermostat and barostat are used (Berendsen 1984).

A thermostat works by connecting the system to a heat bath to ensure that the average system temperature is maintained close to a required temperature (T_{ext}). This can be achieved in a number of different ways including modifying the equations of motion or the use of a velocity rescaling algorithm (see **Section 3.7.2**).

In the Berendsen thermostat algorithm the instantaneous temperature is pushed towards the desired temperature by scaling the velocities at each step by a factor, χ, while conserving total momentum.

$$\chi \leftarrow \left[1+\frac{\Delta t}{\tau_T}\left(\frac{T_{ext}}{T}-1\right)\right]^{1/2}$$

$$r(t+\Delta t) \leftarrow r(t)+\Delta t\, v(t+\frac{1}{2}\Delta t)$$

Equation 3.29

where χ is the friction coefficient, and τ_T is a specified time constant.

A barostat works by allowing the simulation cell size and shape to be dynamically altered in order to obtain a desired average pressure (P_{ext}).

$$\frac{dP}{dt}=\frac{(P_{ext}-P)}{\tau_P} \qquad \textbf{Equation 3.30}$$

The cell volume is scaled by a factor η and the co-ordinates, by $\eta^{1/3}$ where:

$$\eta=1-\frac{\beta\Delta t}{\tau_P}(P_{ext}-P) \qquad \textbf{Equation 3.31}$$

and β is the isothermal compressibility of the system. In practice β is a specified constant which DL_POLY_2 takes to be the isothermal compressibility of liquid water. Alongside the Berendsen barostat the Berendsen thermostat (see above) is applied to enable simultaneous control of temperature and pressure (Smith & Forrester 1996, Berendsen 1984).

3.7.4 Confirming glass formation and comparison to laboratory glasses

Formation of a glass using MD follows a very similar procedure to that used under laboratory conditions where an initial structure (usually crystalline) of N atoms is 'melted' or equilibrated at a high temperature and then 'quenched', or temperature scaled, at such a rate as to bypass crystallisation. This forms an atomic arrangement in which the position of every atom is known. However, determination of whether this arrangement can be termed a glass is difficult.

In a laboratory, the amorphous nature of a material is confirmed by demonstrating a lack of crystallinity. This is done using a variety of methods ranging from visual examination to x-ray or electron diffraction (Shelby 2005). However, a material being amorphous does not guarantee a glassy state; this must be proved by showing the presence of a glass transition temperature (T_g) (see **Section 2.6.2**). For a simulated atomic arrangement alternative methods must be used:

1. From **Section 2.6.2** a deviation from linearity in a plot of a derivative thermodynamics property of the simulation should demonstrate a T_g and so a glass like nature. The most obvious property to choose is that of volume (see **Figure 2.20**). Unfortunately, the rapid nature of the quench and the statistical noise makes reliable observation of such a deviation very difficult and so this technique was not be used in this study;
2. The Radial Distribution function (RDF) will show sharper structural peaks than that of a liquid (see **Figure 3.26**). However, this can be misleading as an unstable glassy state

may form which degrades with time;

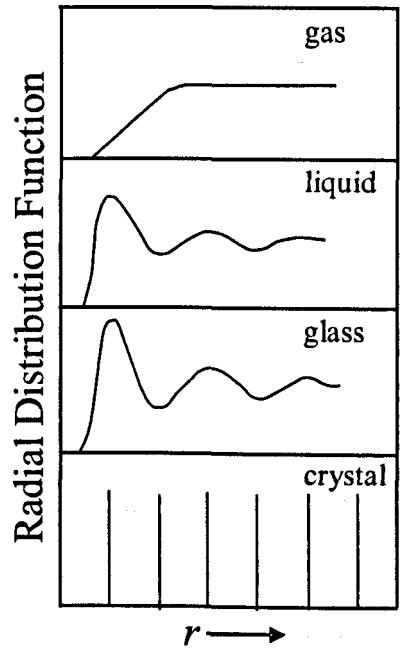

Figure 3.26: Comparison of the radial distribution function of a glass with that of the gaseous, liquid and crystalline states (Paul1990).

3. Time correlation functions, these are a measure of the correlation between properties measured at two different times. For example the correlation in position of a species at time $r_i(0)$ and $r_i(t)$, this can be measured by the Einstein relation:

$$MSD(t)=2Dt=\frac{1}{3}\langle|r_i(t)-r_i(0)|^2\rangle \qquad \textbf{Equation 3.32}$$

where <...> represents the time average of a property and D is the diffusion coefficient. This is the Mean Square Displacement (*MSD*) and must be checked over a run at constant temperature to confirm an stable solid has formed.

How closely the atomic arrangement of an MD glass resembles that of a laboratory glass can be investigated by comparison with laboratory obtained bond lengths, atomic co-ordinations, bond angle distributions, NMR data and by comparison to structure factors from a diffraction or spectroscopic technique. Use of Bond Valence (BV) theory (see **Appendix A**) can also be used, as shown by Rossano *et al.* (Rossano *et al.* 2002); however, care must be taken as BV theory has limited applicability for glasses.

3.7.5 Potentials used in molecular dynamics

The potentials chosen for this work were those of Delaye and Ghaleb (1996a) as potentials were available for interactions between the main elements of interest in this work. The potentials used were Born-Mayer-Huggins (BMH) pairwise potentials with parameters as shown in **Table 3.13** and pictorially in **a** with $r_{ij} = 0.29$ Å (except $r_{o\text{-}o} = 0.35$ Å) and $b = 0.221$ eV:

$$U(r_{ij}) = b\left(1 + \frac{z_i}{n_i} + \frac{z_j}{n_j}\right)\exp\left(\frac{\sigma_i + \sigma_j - r_{ij}}{\rho_{ij}}\right) + \frac{1}{4\pi\varepsilon_0}\cdot\frac{z_i z_j}{r_{ij}} \qquad \textbf{Equation 3.33}$$

Parameter	Si	O	B	Na	Li	Zr
Ionic charge (z_i)	+4	-2	+3	+1	+1	+4
No. valence electrons (n_i)	8	8	2	8	2	8
Ionic radii (σ_i)(Å)	1.1008	1.42	0.72	1.17	0.8	1.425

Table 3.13: Pairwise potential information for use with BMH potential (**Equation 3.4**). All from (Delaye & Ghaleb 1996a) except Li information which was added by the author.

Potentials for all the elements of interest except Li were available from the literature; the Li potential was added by the author (see below). Alongside these pairwise potentials three-body-potentials were also used to control the formation of the silicate network. The potential was a Stillinger and Weber (1985) potential with parameters as shown in **Table 3.14** and shown in **Figure 3.27b**:

$$U(r_{ij}, r_{ik}, \theta_{ijk}) = \lambda_i \exp\left(\frac{\gamma_{ij}}{|r_{ij}| - r_{ci}} + \frac{\gamma_{ik}}{|r_{ik}| - r_{ci}}\right) \mathrm{x}(\cos(\theta_{ijk}) - \cos(\theta_0))^2 \qquad \textbf{Equation 3.34}$$

where γ, λ, and r_{ci} are adjustable parameters. This potential was not available within DL_POLY and so had to be programmed in (see **Appendix C**). It should be noted that the relative restriction placed on the bond angles for the 3-body potential is defined by λ and is 24 times greater for O-Si-O than Si-O-Si angles.

Parameter	O-Si-O	Si-O-Si
λ (10^{-18} J)	24	1
γ (Å)	2.6	2
r_c (Å)	3	2.6
θ_0	109.47	160.0

Table 3.14: Three body potential information for use with Stillinger-Weber (1985) potential. Values taken directly from (Delaye & Ghaleb 1996a).

The 3-body potential for the O-B-O angle that was used in the original paper (Delaye & Ghaleb 1996a) has not been used in this work as it inhibits variation in B-O co-ordination which is a property of interest in this study.

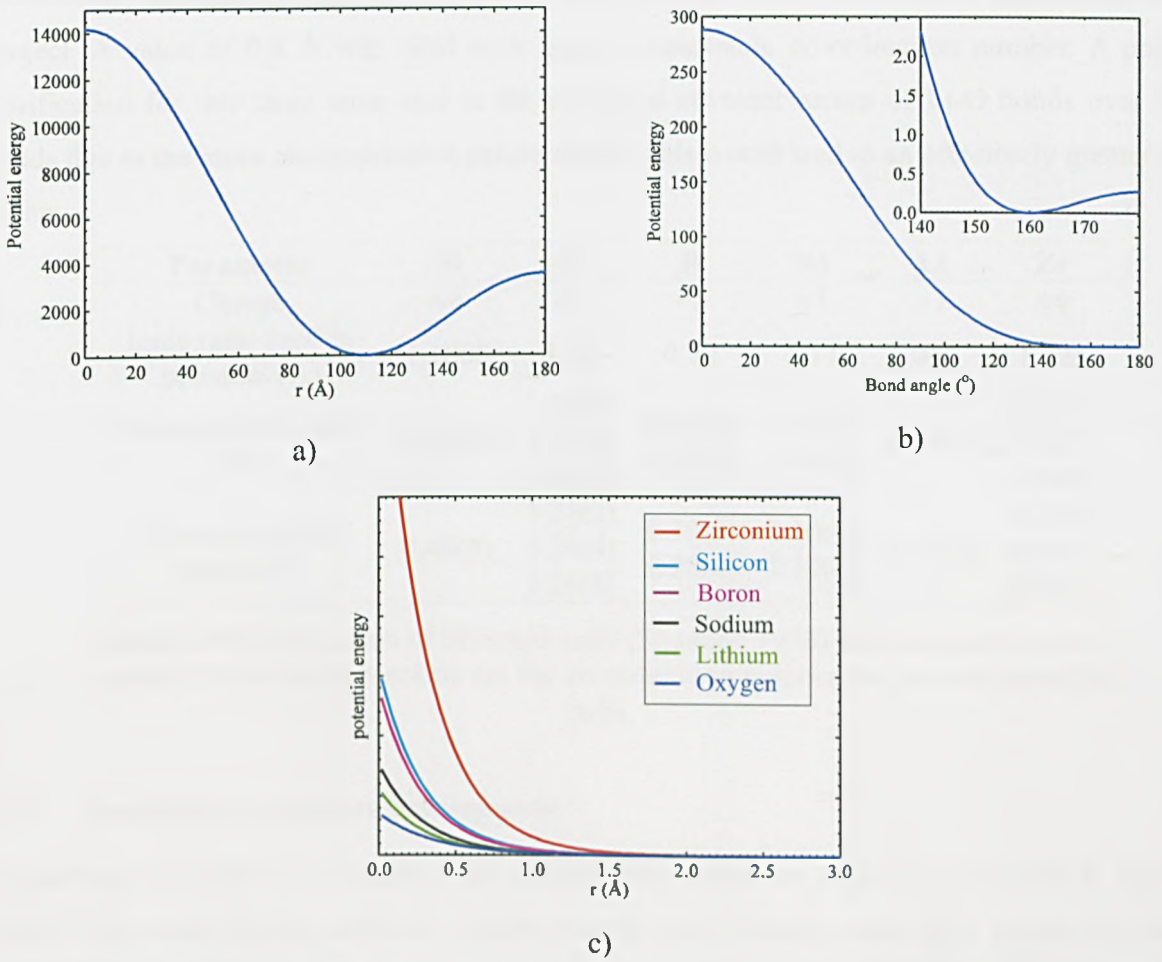

Figure 3.27: Graphical representation of potential energy generated by and a) O-Si-O 3-body-potential with change in angle, b) Si-O-Si 3-body-potential with change in angle, and c) 2-body-potential (BMH) with change in atom separation for oxides (e.g. Si-O separation)

Li potential development

A basic assumption made when developing the Li potential was that the basic potential was of the same form as for the other cationic elements within the glass, with ionic charge and number of valence electrons adjusted as appropriate (see **Table 3.15**). The unknown quantity was that of ionic radius for the Li^+ ion.

Initial simulations used the Shannon crystal radius (see **Table 3.15**) for Li^+ (generally 4 co-ordinate), this value was used as the Na^+ crystal radius (+0.01 Å) had been used for the Na^+

potential (assuming 6 coordinate Na^+). A radius 0.72 Å gave a Li-O co-ordination of 2.6 much less than standard literature value of 4 (Volf 1984). Thus, several simulations were tried with increasing Li radii. Previous simulations using Li in the literature gave the Li radius as up to 0.92 Å however, the radii of other elements and the potentials used differ greatly from those in this project. A value of 0.8 Å was used as it gave a reasonable co-ordination number. A possible justification for this large ionic size is the increased covalent nature of Li-O bonds over Na-O bonds due to the more electropositive nature of Na. This would lead to an effectively greater ionic radius.

Parameter	Si	O	B	Na	Li	Zr
Charge	+4	-2	+3	+1	+1	+4
Ionic radii used in potential (Å)	1.1008	1.42	0.72	1.17	0.8	1.425
Shannon ionic radii (Å)	0.26(4)	1.35(2) 1.38(4) 1.40(6)	0.01(3) 0.11(4)	1.02(6) 1.18(8)	0.59(4)	0.72(6) 0.78(7) 0.84(8)
Shannon crystal radii (Å)	0.40(4)	1.21(2) 1.24(4) 1.26(6)	0.15(3) 0.25(4)	1.16(6) 1.32(8)	0.73(4)	0.86(6) 0.92(7) 0.98(8)

Table 3.15: Comparison of Shannon radii (Shannon 1976) and ionic radii used in potential. Number in brackets are the co-ordination number for the corresponding radii.

3.7.6 Simulations procedure development

Simulations were carried out using a pre-written code called DL_POLY_2.14 (Smith & Forrester 1996). The initial starting structure chosen was an face centred cubic (fcc) lattice with atoms placed at random on the sites (see **Figure 3.28**). This starting structure is both convenient and has been shown (Montorsi *et al.* 2002) to have no effect on the final glass structure if appropriate thermal treatment is applied (see below). The process of producing a glass using MD simulation is not standardised. Each author uses an approach depending on the system, potentials and computing power available (see **Table 3.18**). From this table it can be seen that temperatures, quench rates and ensembles vary dramatically between studies. For this reason it was decided to investigate the important steps from each study and devise a simulation scheme from those. The main steps are:

1. **Removal of initial structure:** the need to remove the initial fcc structure from the system requires a high temperature phase to remove this initial structure;
2. **A thermal equilibration step:** using a lower temperature (4000-5000 K) to allow a

structure representative of a lower temperature to form;

3. **Rapid quench:** quench to room temperature, the aim being to cool the glass at such a rate to avoid devitrification. In MD simulations the reality of this is that the slowest MD cooling rates are far in excess of those used in a laboratory. Thus, the slowest rate possible with MD is used to (**Table 2.7**) "freeze-in" a low temperature structure (give low T_f);
4. **Thermal equilibration step:** To allow low temperature structure to stabilise and collect data for analysis.

With these steps in mind the quench schemes shown in **Table 3.16** and **Table 3.17** were developed. The length of the equilibration steps was chosen so that the system had reached a steady state (no change in temperature, pressure, energy, volume, etc). The quench rates were chosen to be as slow as possible with the computing power available. It was decided to run both *NVT* and *NPT* (this is discussed further in **Chapter 5**).

Stage	Temp range	No. time steps	Cumulative time (ps)	τ
1	8000	100000	-	10
2	7990-4010	1000 per 10 °C	499	10
3	4000	150000	649	10
4	3990-310	1000 per 10 °C	1018	10
5	300	150000	1168	10
6	300	50000	1218	10

Table 3.16: *NVT* quench scheme. Time step is 1 fs. Quench rate is 10 K ps^{-1} (1 x 10^{13} K s^{-1}).

Stage	Ensemble	Temp range	No. time steps	Cumulative time (ps)	τ
1	NVT	8000	100000	-	10
2	NVT	7990-4010	1000 per 10 °C	499	10
3	NVT	4000	100000	649	10
4	NPT	4000	300000	949	10
5	NPT	3990-310	1000 per 10 °C	1318	10
6	NPT	300	150000	1468	10
7	NPT	300	50000	1518	10

Table 3.17: Combined *NVT* and *NPT* quench scheme. Time step is 1 fs. Quench rate is 10 K ps^{-1} (1 x 10^{13} K s^{-1}).

Author(s)	Delaye, Ghaleb	Gou *et al.*	Soules	Cormack and Cao
Year	(1996a)	(2001)	(1979)	(1996)
No. of atoms	1536	1080	ca. 200	ca. 900
Ensemble	NVT	NPT	*NVE*	?
Initial structure	Cristobalite	$Na_2Si_2O_5$	Sodium silicate glass	β-cristobalite
Atoms	O,Si,B,Na,Zr	O,Si,B,Na	O,Si,B,Na	O, Si,Al,Na,Li,Ca
Potential	BMH	BMH	BMH	Buck
Three body	Si,B	Si,(B)	none	Si
Thermostat	Not known	Not known	Not known	Not known
Initial temp. (K)	5500	4000	6000	6000 or 8000
Hold time (ps)	6	300	2.5	10
Quench rate (Kps^{-1})	500	N/A	760*	285*
Final temp. (K)	300	1000	293	300
Hold time (ps)	10	300	2.5	10

Table 3.18: Selection of simulation procedures from the literature. * Stepped quench. BMH stands for Born-Mayer-Huggins and buck stands for Buckingham potential.

3.7.7 Alkali borosilicate experimental procedure

In order to confirm the validity of these potentials literature laboratory data (Rodderick *et al.* 2001) and simulation results were compared. The compositions used can be seen in **Table 3.19** and **Table 3.20** where the number of Si and B atoms (defined by *K*) have been kept constant with variation in Na, Li and O (as Li_2O and Na_2O) these changes being defined by the value of *R*. These data were chosen due to the similarity in composition to the BNFL base glass (Fli-0 which has values of $K = 3.27$, and $R = 1.13$ – see **Table 3.1**).

Element	NL0	NL1	NL2	NL3	NL4	NL5
K	3	3	3	3	3	3
R	0	0.15	0.25	0.379	0.5	0.545
O	1737	1766	1785	1810	1833	1842
Si	579	579	579	579	579	579
B	386	386	386	386	386	386
Na	0	29	48	73	96	105
Li	0	29	48	73	96	105
Total	2702	2789	2846	2921	2990	3017
Box length (Å)	34.031	33.859	33.793	33.639	33.669	33.708

Table 3.19: Compositions of model data adapted from literature (Rodderick *et al.* 2001).

Element	NL6	NL7	NL8	NL9	NL10	NL11
K	3	3	3	3	3	3
R	0.75	1	1.263	1.6	1.7	2.25
O	1882	1930	1981	2046	2065	2171
Si	579	579	579	579	579	579
B	386	386	386	386	386	386
Na	145	193	244	309	328	434
Li	145	193	244	309	328	434
Total	3137	3281	3434	3629	3686	4004
Box Length (Å)	33.754	33.916	34.233	34.750	34.911	35.784

Table 3.20: Further compositions of model data adapted from literature (Rodderick *et al.* 2001).

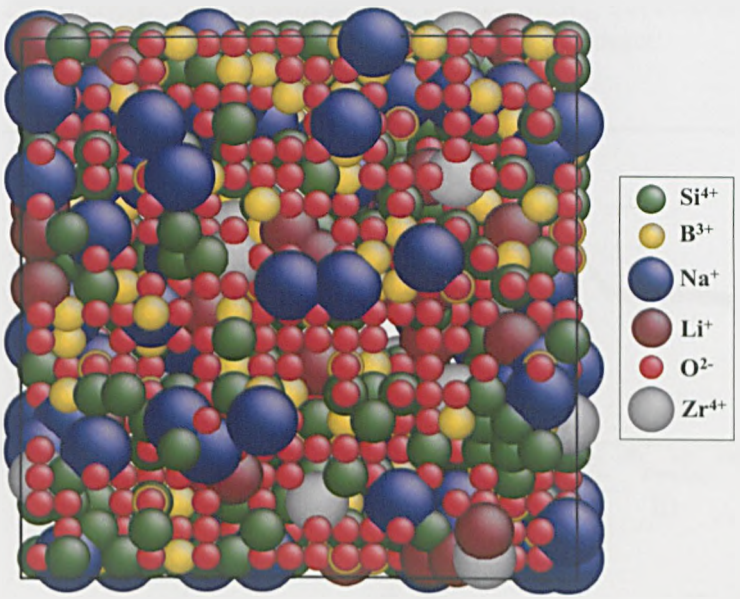

Figure 3.28: Initial fcc lattice structure with atoms put at random onto the lattice sites. Oxygen ions are not to scale to allow easier visualisation.

The routine used for each simulation can be seen in **Table 3.16** and **Table 3.17**. Each simulation starts off as an *NVT* simulation with the box size calculated from the laboratory density (Rodderick *et al.* 2001). Each stage was run for long enough such that the system came to a state of approximate equilibrium before the next stage was started (see **Figure 3.29** and **Figure 3.30**). The initial heating to 8000 K was used to remove any record of the initial starting structure, subsequently the system was cooled in such a way as to form a room temperature glass.

A Berendsen thermostat (and barostat) (Berendsen 1984) were used for both *NVT* and *NPT* simulations. A quench rate from 4000 K to 300 K of 5 $x10^{14}$ Ks^{-1} was used due to time constraints with the computing power available (see **Figure 3.29** and **Figure 3.30**). An example glass

structure is given in **Figure 3.31**.

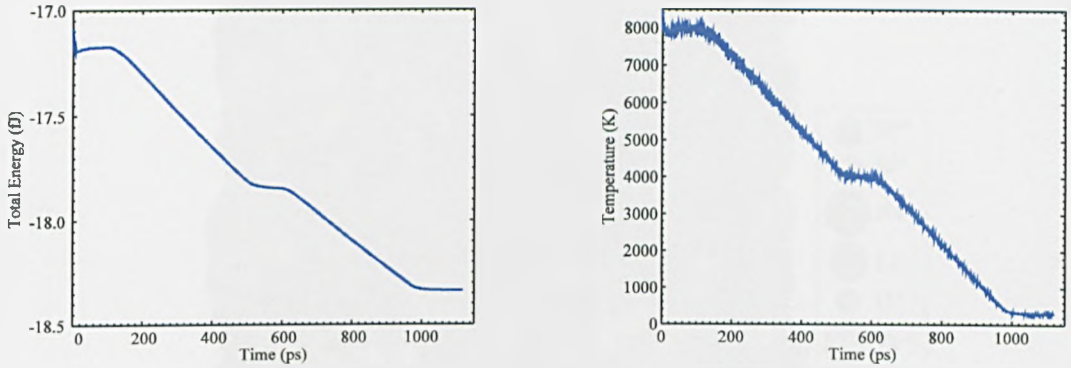

Figure 3.29: a) energy and b) temperature change during quenching of a melt from 8000°K to 300°K under *NVT* conditions.

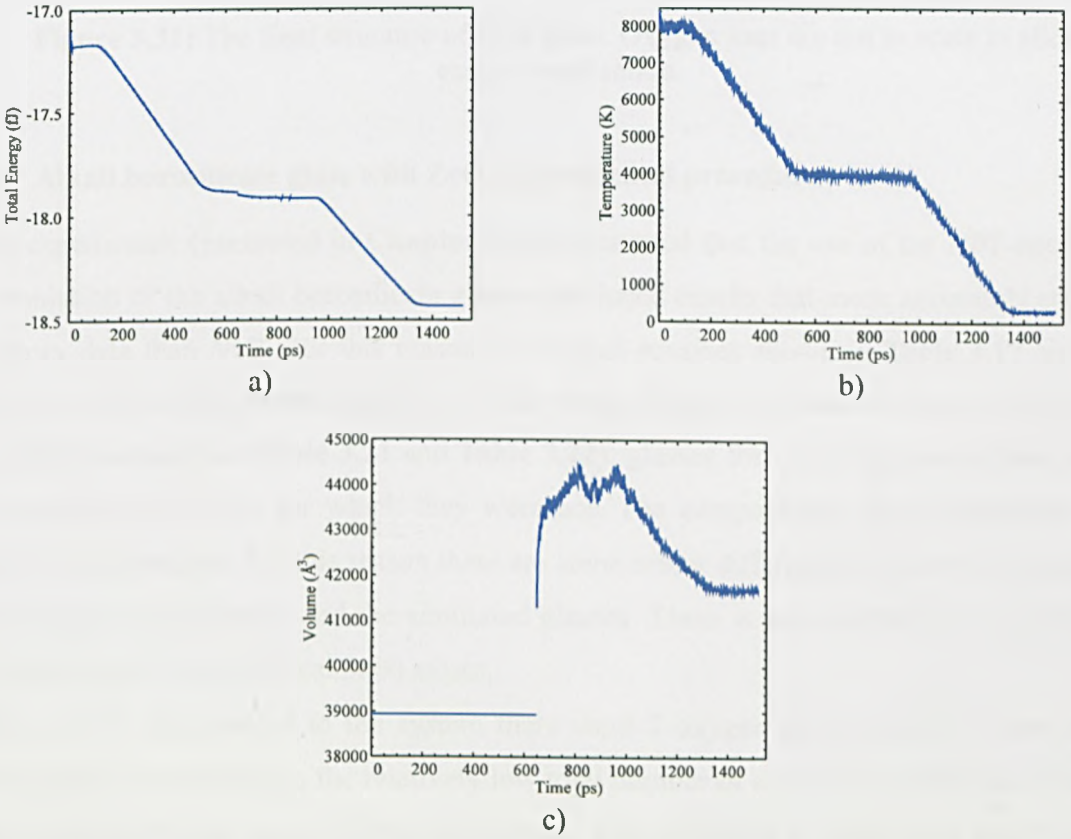

Figure 3.30: a) energy. b) temperature and c) volume change during quenching of a melt from 8000°K to 300°K under *NPT* conditions.

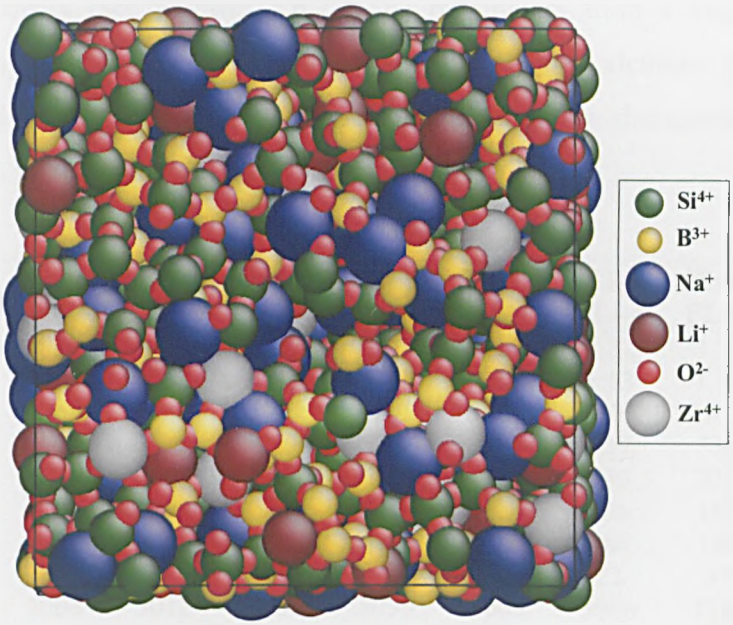

Figure 3.31: The final structure of NL4 glass. Oxygen ions are not to scale to allow easier visualisation.

3.7.8 Alkali borosilicate glass with ZrO_2 experimental procedure

Initial experiments (presented in **Chapter 5**) demonstrated that the use of the *NPT* ensemble for the simulation of the alkali borosilicate glasses produced results that more accurately reproduced laboratory data than *NVT*. For this reason the quench routines shown in **Table 3.17** and **Figure 3.30** were used for ZrO_2 bearing glasses. A wide range of glass compositions were simulated using this quench routine (see **Table 3.21** and **Table 3.22**), glasses for which laboratory data analogies were available and some for which they were not. The compositions chosen represent the "as batched" compositions. For this reason there are some minor differences between the composition of the experimental glasses and the simulated glasses. There is also a difficulty in getting exact mole percentages from only ca. 3000 atoms.

For each Zr atom added to the system there were 2 oxygen atoms added to keep the ZrO_2 stoichiometry. Unfortunately, the relatively low total number of atoms means that each simulation has a low number of Zr atoms. These low numbers were necessary to balance the need to keep the simulations relevant to laboratory glasses and the large amount of computing time required for these simulations.

Simulations were carried out as for previous simulations with the atoms initially placed, at random, on an FCC lattice. The initial volume of the system was defined from laboratory

measurements of density (see **Section 3.6.2**). The parameters from a line of best fit though laboratory densities were taken and this equation used to calculate all densities (being extrapolated beyond laboratory measured glasses). The Berendsen thermostat and barostat were used with conditions as stated in **Section 3.7.7** and **3.7.8**.

Model Lab*	FLi-A FLi-0	FLi-B FLi-1	FLi-C FLi-2	FLi-D	FLi-E FLi-3	FLi-F	FLi-G FLi-4	FLi-H FLi-5	FLi-I	FLi-J
K	3.27	3.27	3.27	3.27	3.27	3.27	3.27	3.27	3.27	3.27
R	1.13	1.13	1.13	1.13	1.13	1.13	1.13	1.13	1.13	1.13
O	1759	1763	1767	1779	1785	1801	1803	1833	1867	1909
Si	539	539	539	539	539	539	539	539	539	539
B	330	330	330	330	330	330	330	330	330	330
Na	186	186	186	186	186	186	186	186	186	186
Li	186	186	186	186	186	186	186	186	186	186
Zr	0	2	4	10	13	21	22	37	54	75
Total	3000	3006	3012	3030	3039	3063	3066	3111	3162	3225
Initial box length (Å)	32.787	32.816	32.845	32.941	32.984	33.113	33.118	33.345	33.591	33.894

Table 3.21: Composition of ZrO_2 bearing FLi glasses simulated using MD. * Shows equivalent composition in laboratory glasses.

Model Lab*	HLi-A HLi-0	HLi-B HLi-1	HLi-C HLi-2	HLi-D	HLi-E HLi-3	HLi-F	HLi-G HLi-4	HLi-H HLi-5	HLi-I	HLi-J
K	3.27	3.27	3.27	3.27	3.27	3.27	3.27	3.27	3.27	3.27
R	0.84	0.84	0.84	0.84	0.84	0.84	0.84	0.84	0.84	0.84
O	1796	1800	1806	1816	1822	1838	1842	1872	1906	1950
Si	565	565	565	565	565	565	565	565	565	565
B	346	346	346	346	346	346	346	346	346	346
Na	195	195	195	195	195	195	195	195	195	195
Li	97	97	97	97	97	97	97	97	97	97
Zr	0	2	5	10	13	21	23	38	55	77
Total	2999	3005	3014	3029	3038	3062	3068	3113	3164	3230
Initial box length (Å)	33.096	33.127	33.183	33.256	33.302	33.435	33.466	33.702	33.958	34.294

Table 3.22: Composition of ZrO_2 bearing HLi glasses simulated using MD. * Shows equivalent composition in laboratory glasses.

3.7.9 Analysis

Various analysis techniques were used for the analysis of the glass structure. The most useful in the initial stages to compare MAS-NMR data and simulation data was co-ordination[1] information:

[1] The definition of co-ordination number is a difficult one. For the present work co-ordination number of an ion will be defined as the number of ions which it is linked by electrostatic flux (Brown 2002). However the difficulty of defining this from MD results means the "cut-off" technique (above) must be employed – i.e. the first shell of

particularly the number of oxygens around each boron atom and the distributions of Q species within the silicate network. This was done using code written by the author (calibrated on well defined structures). The code searches within a certain cut-off distance of each atom and counts the number of atoms within that distance. The cut-offs used were chosen from radial distribution plots with the first minima after any initial peak being taken as the cut-off. These values were used throughout the analyses and can be seen in **Table 3.23** with example plots shown in **Appendix H**. The use of a cut-off technique is not ideal for the co-ordination of alkali ions due to the high disorder around these atoms.

Bond angles were also calculated using the cut-offs shown in **Figure 3.23**, they were calculated using the cosine rule. Plot data were normalised such that the area under the curve was unity.

All analysis was carried out by taking a time average of properties over 50000 time steps at 300 K (see **Section 3.7.7** and **3.7.8**). For MD modelling data errors are very difficult to assign. Due to the statistical nature of the simulations, multiple simulations would ideally be run for each composition, and an average (and so standard deviation) calculated. Unfortunately, the computing time required for such experiments is impractical. Thus, to give some idea of the error on the measurements taken from MD simulations in this work, errors were calculated as the standard deviation of the time averaged property measured.

One error that must be considered is that with only ca 3000 atoms accurately reproducing laboratory compositions is inevitable difficult. When preparing starting configurations for MD glasses care was taken to get accurate compositions; the result was a worst case error of ± 0.01 mol%.

Atoms	Cut-off (Å)	Atoms	Cut-off (Å)	Atoms	Cut-off (Å)	Atoms	Cut-off (Å)	Atoms	Cut-off (Å)
O-O	2.8	O-Si	2.1	O-B	2.15	O-Li	2.66	O-Zr	2.88
Si-O	2.1	Si-Si	3.37	Si-B	3.28	Si-Li	4.98	Si-Zr	3.95
B-O	2.15	B-Si	3.28	B-B	3.1	B-Li	3.65	B-Zr	3.84
Na-O	3.53	Na-Si	4.8	Na-B	4.39	Na-Li	4.22	Na-Zr	4.63
Li-O	2.66	Li-Si	3.98	Li-B	3.65	Li-Li	3.88	Li-Zr	4.2
Zr-O	2.88	Zr-Si	3.95	Zr-B	3.84	Zr-Li	4.2	Zr-Zr	5.76*

Table 3.23: Cut-offs used for analysis of glass structure. * Value chosen as twice Zr-O length as not enough information for good g(r) characterisation.

atoms around a central atom.

3.8 Analysis of data – coding and visualisation

Analysis of data from both laboratory and computer based experiments was carried out using various programs. Some of these were 'off the shelf', others written by the author. Many are referred to in the text, however, a full list of the programs used is given in **Appendix G**. It is relevant here to make a note about the coding style and reliability. Each code was checked against other code or tested on standard materials. For example, the author written code for calculating $g(r)$ was checked against the program equivalent, but less flexible, code within DL_POLY_2.14.

3.9 Errors

Experimental error was estimated taking into account random error (from machine/system operating parameters and calibrations) and systematic error.

The standard deviation is the most commonly used measure of error and was calculated from the square root of the variance in the usual way:

$$\sigma = \sqrt{\frac{1}{N}\sum_{i=1}^{N}(x_i - \bar{x})^2} \qquad \textbf{Equation 3.35}$$

where N is the total number of samples, $\bar{x}$ is the mean of all samples $x_1,...x_N$. In most applicable techniques used within this work, an estimation of experimental error will be cited within the results or in the following discussion of the results. Error bars in Figures and errors tabulated within tables will be given to either σ or 2σ (see **Table 3.24**) depending on relevance (indicated within figures and tables as '(σ)' and '(2σ)' respectively).

Range	CI (%)
σ	68.26895
2σ	95.44997

Table 3.24: Confidence intervals (CI) for multiple standard deviations (σ) assuming a Gaussian distribution of errors.

Quality of fit for lines of best fit and data fitted with curves (e.g. NMR data) will be judged using the R^2 value[1]:

$$R^2 = 1 - \frac{SS_E}{SS_T} \qquad \textbf{Equation 3.36}$$

[1] These values should not be confused with R_{exafs}^2 as this value is calculate in a difference manner.

$$SS_T=\sum_i (y_i-\bar{y})^2 \quad SS_E=\sum_i (y_i-x_i)^2$$ **Equation 3.37**

where y_i represents observed experimental (where $\bar{y}$ is the mean of all samples $y_1,...y_N$) data and x_i represents fit to data.

4 The Effect of Zr on the Structure and Properties of Alkali Borosilicate Nuclear Waste Glass

4.1 Introduction

This Chapter presents the results of an investigation into the structure and properties of a series of ZrO_2 bearing alkali borosilicate glasses (see **Table 3.1**). ZrO_2 is an important element in geological and nuclear waste glasses. The motivation for this chapter is to gain an understanding of the process of ZrO_2 solubility and effect on glass structure in order to better vitrify waste streams high in ZrO_2 (see **Appendix B** and **Section 2.1.3**). Many aspects of the relationship between ZrO_2 and (boro)silicate glasses have been described in **Section 2.4.1**.

Results of various techniques show the complex nature of the interaction between the Zr^{4+} ion and the alkali borosilicate glass structure and properties. The local environment of the ZrO_2 and its effect on bulk structure will be examined. This analysis will be related to various physical properties of the glasses, including density and durability.

4.2 Density and thermal analysis data

Figure 4.1 shows the change in density with increasing ZrO_2 additions for both FLi and HLi glasses. The method used for density measurements is described in **Section 3.6.2**. The increase in density with increasing ZrO_2 is linear for both FLi and HLi glasses with a very similar rate of increase in density with ZrO_2 addition for both glasses. An increase with increasing ZrO_2 is expected due to the greater atomic weight of ZrO_2 in comparison to the other elements in the glasses.

The densities measured for the FLi glasses are consistently ca. 0.02 gcm^{-3} higher than those for the HLi glasses, for an equimolar increase in ZrO_2. This increased density with Li addition is due to the small size of the Li^+ ion which fits into interstices within the glass network so decreasing

the free volume (Shelby 2005).

Figure 4.2 shows stack plots of the DTA traces for the results of thermal analysis carried out on the HLi and FLi glasses with addition of ZrO_2. The methods used for thermal analysis and the analysis techniques used are presented in **Section 3.6.1**. From the traces presented in **Figure 4.2** values for T_g and T_X have been extracted and are shown in **Figure 4.3.**

From **Figure 4.3** it can be seen that the FLi glasses generally have a lower T_g and lower T_x than the HLi glasses. The higher lithia content in FLi glasses can be considered to have two effects; increased depolymerisation of the Si network and change in ^{IV}B fraction (see **Section 2.2**). Feller *et al.* observed that increasing ^{IV}B fraction increases T_g (Feller *et al.*1997). The difference in T_g and T_x between HLi and FLi indicates that the depolymerisation of the Si glass network has a greater effect on T_g than increase in ^{IV}B fraction, this may be due to the higher percentage SiO_2 within the glasses than B_2O_3 (see **Section 3.1**).

There is considerable scatter in the values obtained for T_g and T_X. However, it is possible to see that there is a general increase (ca. 6 °C) in both T_g and T_X with addition of ZrO_2. This increase is expected from the literature (see **Section 2.4.1**) and from the significant increase in observed viscosity with increased ZrO_2 during melting. An increased viscosity is normally associated with an increase in T_g and T_X. There are several possible reasons for the scatter in T_g results:

1. Differences between as-batched composition and actual composition;
2. Effect of changes in structure (e.g. changes in ^{IV}B fraction) seen later in this Chapter which may effect T_g;
3. Errors in data analysis, however, the DTA spectra are not overly noisy and the analysis was highly reproducible (see **Figure 4.2**).

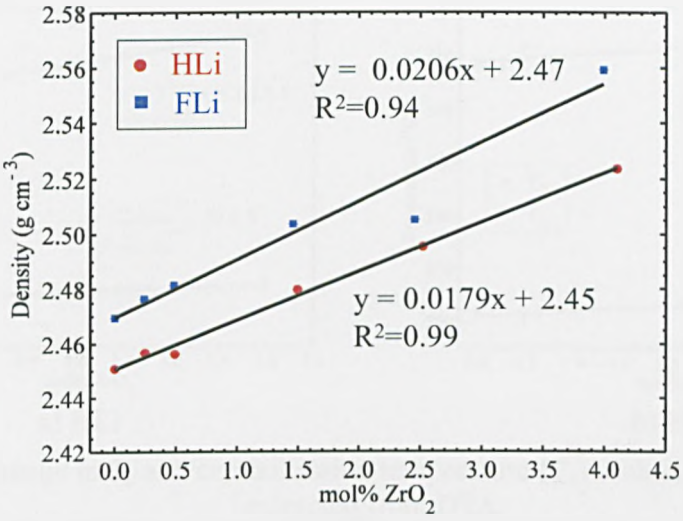

Figure 4.1: Change in density with increasing ZrO_2 content for both HLi and FLi glasses.

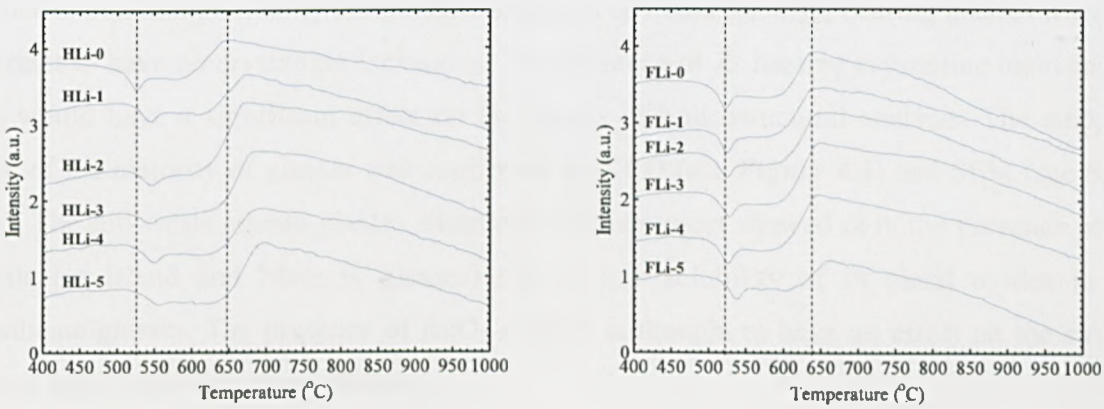

a) HLi b) FLi

Figure 4.2: Stack plot showing change in DTA trace with composition.

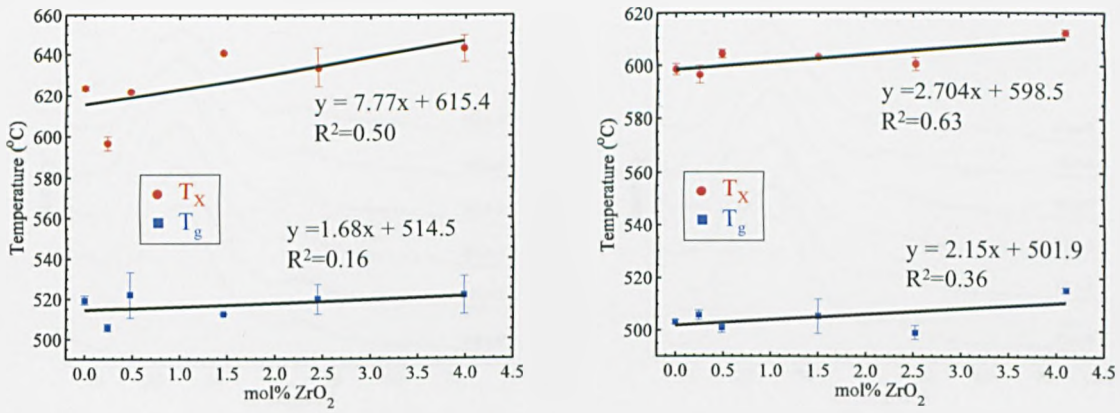

Figure 4.3: Change in T_g and crystallisation temperature (T_x) with increasing ZrO_2. Data extracted from DTA.

4.3 Sample morphology

In order to obtain high quality and reliable spectroscopy data for ZrO_2 bearing glasses it was very important to have no crystalline inclusions. The presence of Zr bearing crystalline inclusions in a glass would have a significant effect on the results of bulk structural analysis. The amorphous nature of the majority of glasses was confirmed by XRD (see **Figure 4.4**) and SEM (see **Section 4.7.4**). The full waste stream glasses examined in this project showed only the presence of RuO_2 crystals (in Blend and Magnox glasses) due to low solubility of Pt metal oxides in alkali borosilicate glasses. The presence of RuO_2 crystals is thought to have no effect on the structural analysis tools applied to these glasses.

High Zr bearing waste (see **Table 3.1**) appeared amorphous by XRD, however, under SEM a small number of Zr crystalline inclusions could be seen. These had the appearance of undissolved batch (see **Figure 4.5**). This was the highest ZrO_2 bearing composition of all glasses produced in this work. Attempts to introduce ZrO_2 contents into the glasses was unsuccessful, however, attempts were not exhaustive and more work is required to establish solubility limits.

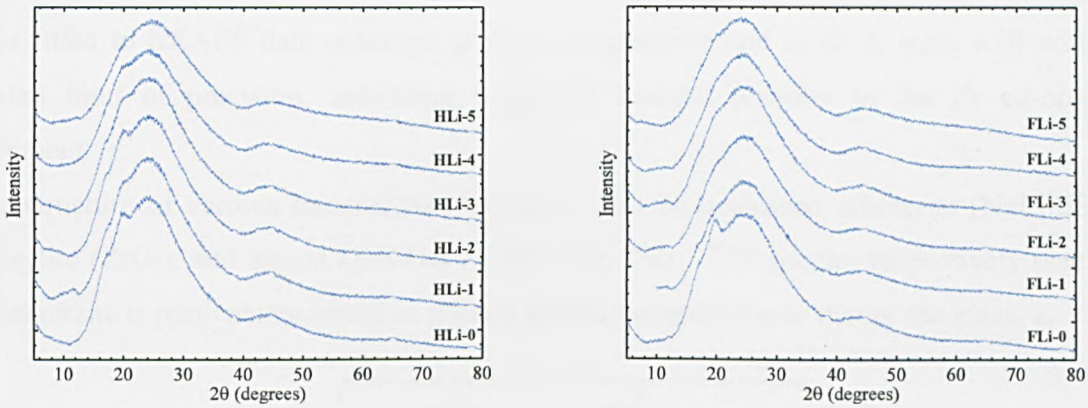

Figure 4.4: XRD traces of ZrO_2 bearing glasses used in this study. Traces shown sample are amorphous.

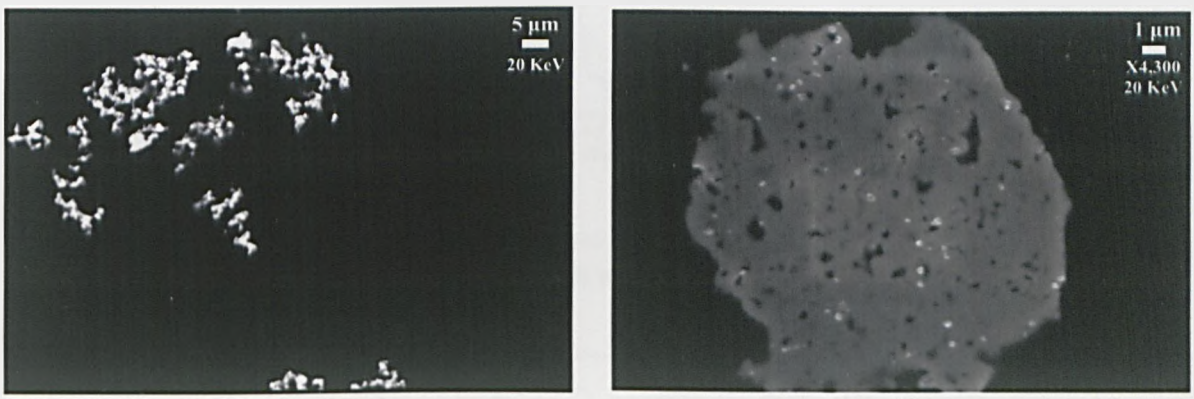

Figure 4.5: SEM images of a) Ru containing crystals in Magnox glass and b) Zr containing crystals in High Zr glass.

4.4 XAS of Zr K-edge

4.4.1 EXAFS

Analysis of EXAFS data was undertaken using a series of shells where each shell represents a discrete distance range from the absorbing atom (see **Figure 4.6**). As an example of the fitting process, the results for each shell are presented in turn for a model glass with the composition FLi-4 (see **Table 3.1**). Comparisons are made to other data sets where appropriate. The EXAFS data for all the samples produced in this study are shown in **Figure 4.7**. These data appear very

similar, suggesting a comparable Zr environment in these glasses, irrespective of composition. Models fitted to EXAFS data collected at room temperature and at 80 K were well within the estimated limit of precision, indicating negligible thermal disorder in the Zr co-ordination environment.

The structure of various mineral standards will also be discussed zektzerite ($NaLiZrSi_6O_{15}$), baddeleylite (ZrO_2), and zircon ($ZrSiO_4$) exhibit ^{VI}Zr, ^{VII}Zr, ^{VIII}Zr species respectively (see **Table 4.1**). Zekterzite is particularly useful as it has a similar composition to that of the glass.

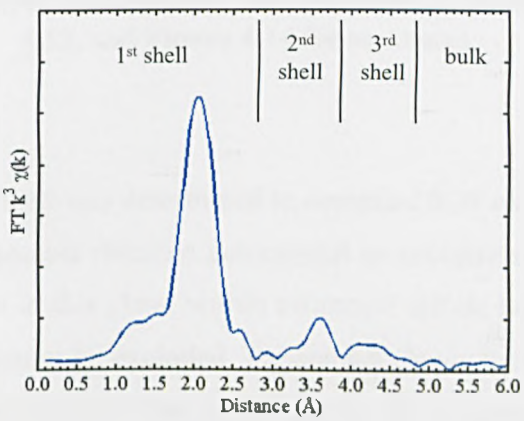

Figure 4.6: Fourier Transform of example glass EXAFS data showing shell structure used in analysis.

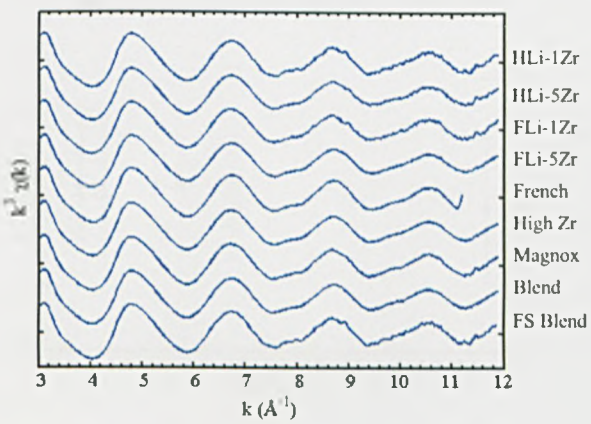

Figure 4.7: EXAFS data for all samples. Showing similarity between samples of different composition.

Formula	N_O	R_{Zr-O} (Å)	N	R_{Zr-X} (Å)	N	R_{Zr-X} (Å)	N	R_{Zr-X} (Å)	N	R_{Zr-X} (Å)
ZrO_2	7	2.05-2.27	Zr(7)	3.34-3.46	O(6)	3.58-3.92	Zr(2)	3.93		
$ZrSiO_4$	8	2.13-2.26	Si(2)	2.99	Zr(4)	3.62	Si(4)	3.62		
$LiNaZrSi_6O_{15}$	6	2.06-2.09	Li(2)	2.97	Na(1)	3.39	Si(6)	3.44-3.49	O(6)	3.79-3.90

Table 4.1: Selected reference bond lengths (<4 Å) for standards used in XAS experiments. Bracketed numbers are number of atoms of specified elements within distance range (Hazen1979, Ghose1978, Winterer2002,). See **Figure 4.12**, **Figure 4.13**, and **Figure 4.14** for structures.

4.4.2 First shell

For the model glass, the first shell was determined to comprise 6.33 oxygen atoms at a distance of 2.09 Å, similar to the Zr-O contact distance determined in zektzerite (**Table 4.1**). This suggests that ^{VI}Zr species are dominant in this glass, within estimated errors; however, a small minority of ^{VII}Zr, and / or ^{VIII}Zr species cannot be excluded. **Figure 4.8** shows the results of first shell for all samples, within the estimated level of precision there is no evidence of increased oxygen co-ordination with increased polymerisation or Zr content. A stable fit could not be obtained with the addition of a second shell of oxygen atoms at 2.22 Å, as reported by Farges *et al.* (1991).

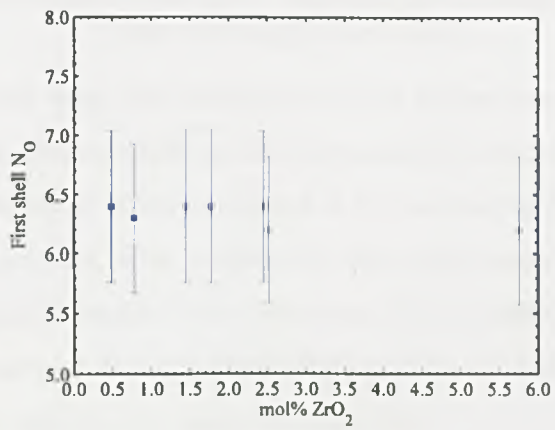

Figure 4.8: The change in N_O with mol% ZrO_2, standard errors shown in **Table 3.11**.

4.4.3 Second shell

In the model composition only Na, Si, O, and Zr have a sufficiently large backscattering cross-section to be resolved as potential second shell next nearest neighbours (see **Section 3.5.2).**

Cluster models containing oxygen and each of these atoms separately were tested (a second shell containing oxygen produced an unstable fit and so is not shown). Based on comparison of goodness of fit indicators, the best model comprised a second shell of 1.77 Na atoms at a distance of 3.45 Å from the central Zr atom (**Table 4.2**)

Alternative models provided chemically sensible second shells comprising 1.15 Si or 0.52 Zr atoms at a distance of 3.73 Å or 3.71 Å, respectively, from the central Zr atom, however, these models resulted in higher goodness of fit parameters (**Table 4.2**). In general, a second shell comprising, on average, 1.88 (±0.11) Na atoms at a distance of 3.45 Å (± 0.01) from the central Zr atom was found to provide the best fit to the EXAFS of all compositions in this study. This Zr-Na distance is similar to that of 3.39 Å determined in the mineral zektzerite (**Table 4.1**). The presence of Na around the Zr^{4+} ion is supported by current understanding of the requirement of charge balancing cations for Zr^{4+} stabilisation (**Section 2.4.1**).

Property	**Model 1-1**		**Model 1-2**		**Model 1-3**	
Element	**O**	**Na**	**O**	**Si**	**O**	**Zr**
N_O	6.31	1.77	6.31	1.15	6.27	0.52
$R_{Zr\text{-}X}$ (Å)	2.09	3.45	2.09	3.73	2.09	3.71
$2\sigma^2$ (Å^2)	0.012	0.004	0.012	0.004	0.012	0.005
E_F (eV)	-3.6439		-3.2433		-3.51	
R-factor	16.61		18.69		17.98	
χ^2	1.30		1.65		1.66	

Table 4.2: Analysis of the second shell. Showing significantly better fit statistically than with single shell model.

Multiple element models were also considered in the second co-ordination shell as shown in **Table 4.3**, and **Figure 4.9**. Second shell models containing O, Na and Si or O, Na and Zr show a reduced R-factor but increased χ^2 when compared to the second shell model involving Na only. It is therefore difficult to ascertain, with confidence, the composition of the second co-ordination shell around Zr in the glasses studied here. However, the presence of intermediate range order around Zr can be confirmed and it would seem likely that the second co-ordination shell involves Na, but the presence of Si, and also Zr, cannot be excluded.

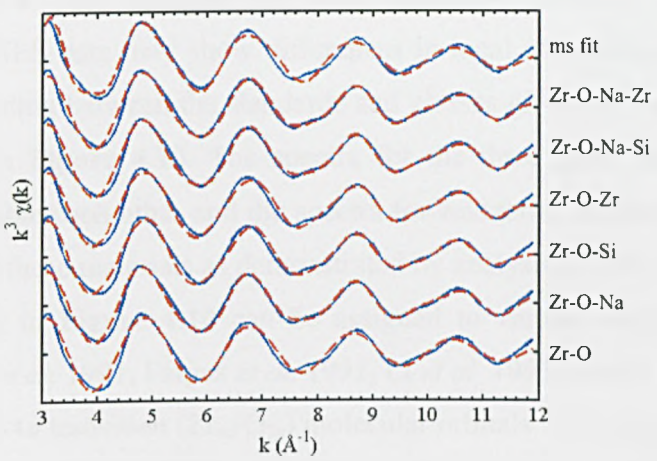

Figure 4.9: EXAFS data and simulated curves for the 1, 2, and 3 shell models. Where ms is multiple scattering.

Property	Model 2-1			Model 2-2		
Element	O	Na	Si	O	Na	Zr
N_X	6.30	1.67	0.44	6.30	1.72	0.39
$R_{Zr\text{-}X}$ (Å)	2.09	3.45	3.72	2.09	3.46	3.70
$2\sigma^2$ (Å^2)	0.012	0.006	0.005	0.012	0.006	0.012
E_F(eV)	-3.5796			-3.6954		
R-factor	15.87			15.95		
χ^2	1.39			1.40		

Table 4.3: Analysis of the second shell multiple scattering elements present.

The presence of Si-O-Zr (and possible B-O-Zr) bonds within the glasses studied here suggests a strengthening (or polymerisation) of the glass network. This is reflected in an increase in T_g and T_x with increasing ZrO_2 additions for both HLi and FLi glasses.

4.4.4 Third shell

It is unusual to achieve structural information in amorphous materials from EXAFS beyond the second co-ordination shell. In this case analysis showed an apparent third shell at ca. 4.2 Å to have multiple scattering contributions from the Zr-O bond (ca. 2.09 Å), see **Figure 4.9**. Analysis also suggests the presence of oxygen in this shell; however, the small contribution of this shell to the overall EXAFS spectra meant this result could not be confirmed.

4.5 XANES

The complex nature of the XANES process makes deconvolution of the experimental data, in a

similar manner to EXAFS, very difficult for such chemically complex systems. However, comparison between XANES data may show differences in local co-ordination very effectively. Differences in Zr-O speciation between the standards and glasses gives rise to the variation in the XANES spectra shown in **Figure 4.10**. The spectra for the three glass samples presented in **Figure 4.10** closely resemble each other and the spectra for zektzerite, indicating a similar Zr co-ordination environment in these materials as demonstrated by analysis of EXAFS data.

The features identified in **Figure 4.10** can be assigned to various electron transitions and scattering effects (Brown *et al.* 1991, Farges *et al.* 1991, Li *et al.* 1993, Farges 1996):

A. Attributed to 1*s*-4*d* transition (Zr_{4d}/O_{2p}) molecular orbitals. Indicating a ^{VI}Zr site without a centre of symmetry;

   a. The height and position of pre-edge feature is a function of the degree of *p-d* mixing and oxidation state (constant here at +4).

B. Due primarily to single scattering from second neighbour element (e.g. Si);

C. Due primarily to multiple scattering involving first neighbour O around Zr;

D. First EXAFS oscillation – position dependent on Zr-O bond length.

The relative intensity of features B and C depends on the structure of the materials, this effect is, in part, related to *Z* of next nearest neighbour.

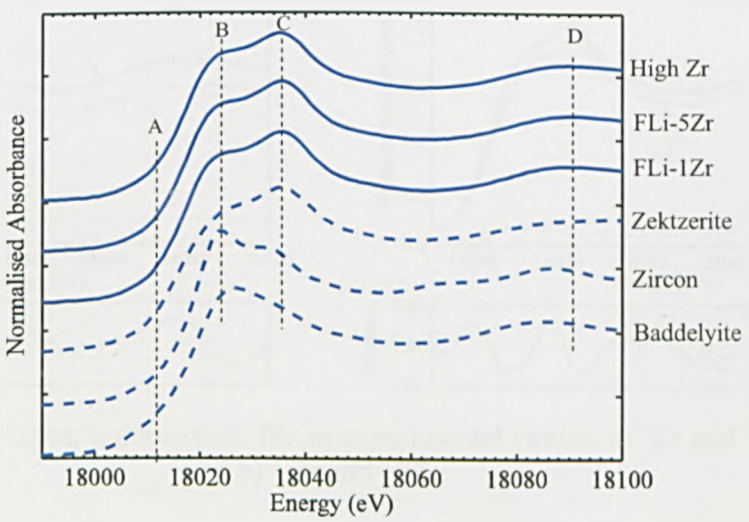

Figure 4.10: XANES data for the two standards and three glass samples. A range of ZrO_2 content glasses has been selected and the difference between the data sets is below significance.

The XANES spectrum for the glasses can be considered as the sum of the XANES spectra for

the individual contributions. Thus, fitting a linear combination of the XANES spectra of zekterzite, baddelyite, and zircon to the XANES spectrum of the glass affords on estimate of the proportion of ^{VI}Zr, ^{VII}Zr, and ^{VIII}Zr species present. (see **Section 3.5.2**). The resulting fits can be seen in **Figure 4.11**. Only the fits for ^{VI}Zr-^{VII}Zr and ^{VI}Zr-^{VIII}Zr are shown as the fit with all three standards present was the same as that for ^{VI}Zr-^{VII}Zr. **Table 4.4** shows the proportion of each spectra in the fits. It shows that fitting with only ^{VI}Zr and ^{VII}Zr produces a slightly better fit than fitting with ^{VIII}Zr. Also, when fitting with all three spectra the presence of ^{VIII}Zr did not produce a better fit. From the different combinations available the best fit came from a mixture of ^{VI}Zr and ^{VII}Zr.

	^{VI}Zr and ^{VII}Zr	**^{VI}Zr and ^{VIII}Zr**	**all**
Fraction ^{VI}Zr	0.85	0.92	0.85
Fraction ^{VII}Zr	0.14	0	0.14
Fraction ^{VIII}Zr	0	0.077	0
R^2	0.99940	0.99926	0.99940
χ^2	0.038	0.053	0.038
Average	6.08	6.14	6.08

Table 4.4: Results of linear combination fitting procedure sample XANES spectra for sample HLi-5.

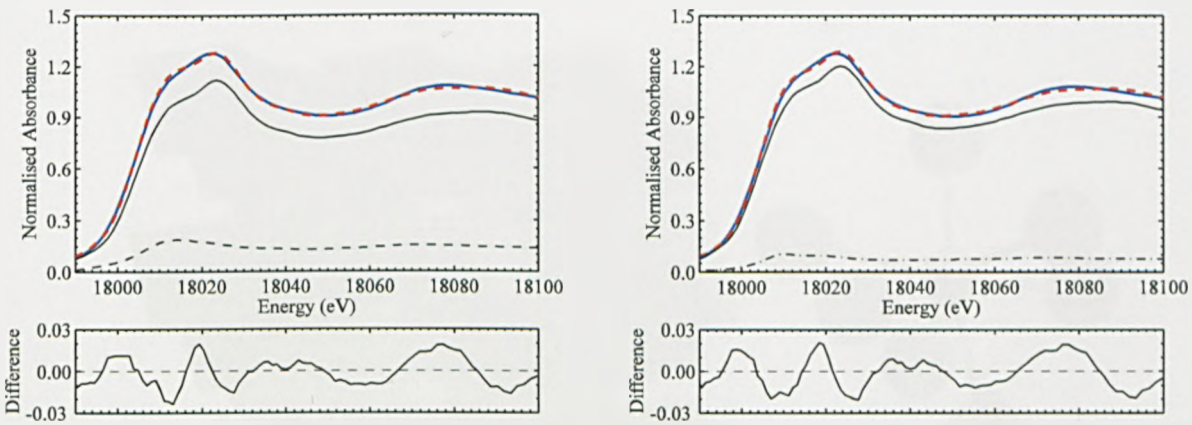

Figure 4.11: Linear combination fits to experimental values. a)^{VI}Zr and ^{VII}Zr and b) ^{VI}Zr and ^{VIII}Zr.

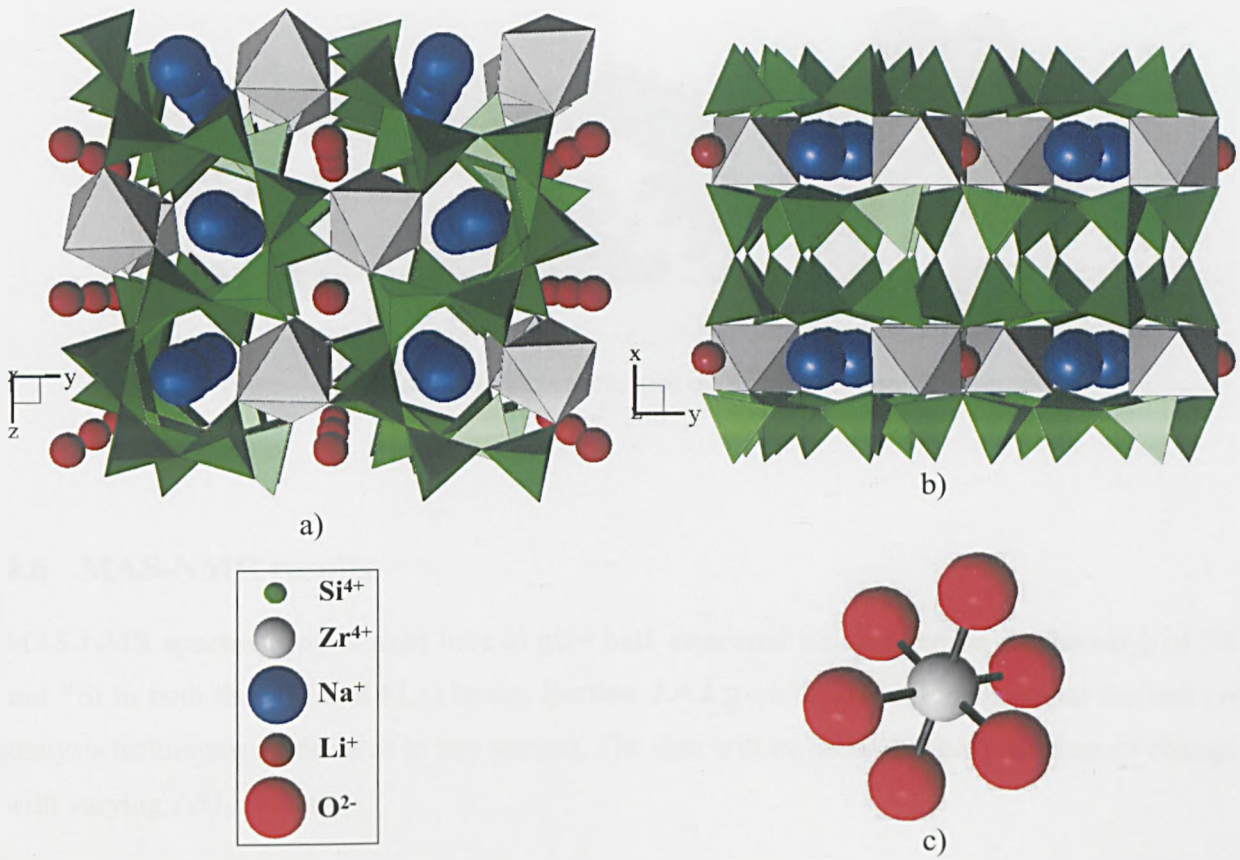

Figure 4.12: Images of the structure of ^{VI}Zr in zektzerite (Ghose & Wan 1978).

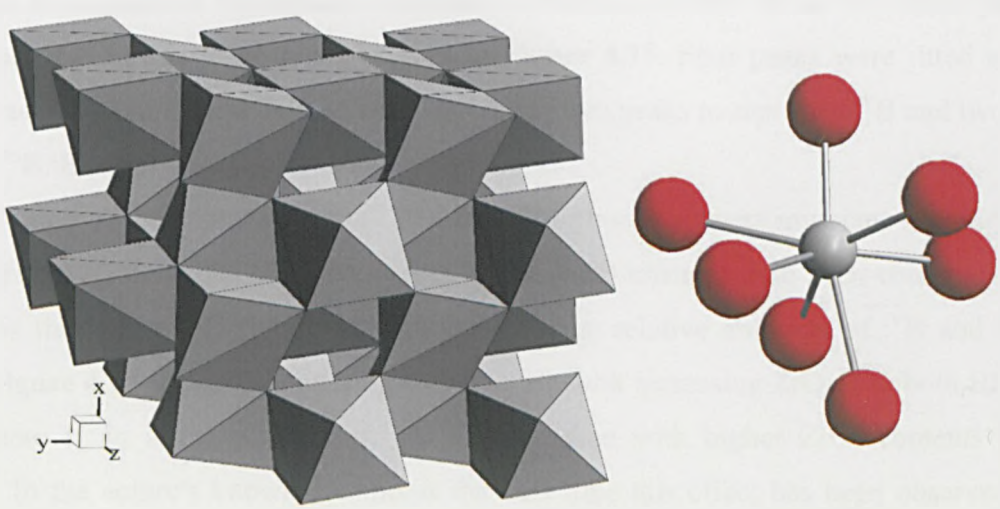

Figure 4.13: Images of ^{VII}Zr in baddelyite (Hazen & Finger 1979).

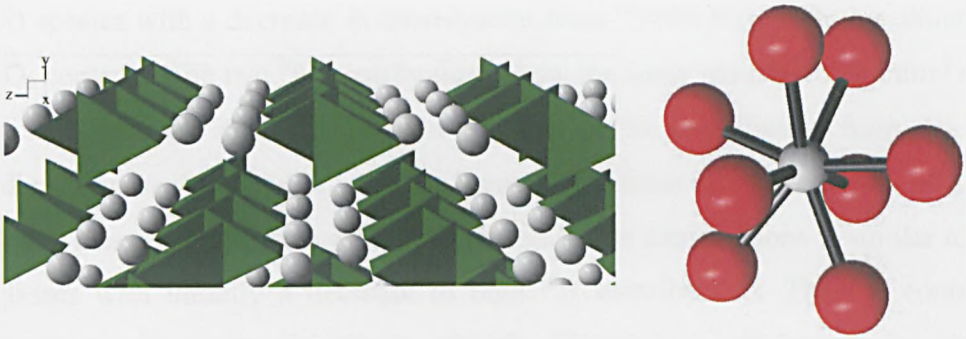

Figure 4.14: Images of the structure of ^{VIII}Zr in zircon (Winterer *et al.* 2002).

4.6 MAS-NMR results

MAS-NMR spectroscopy is used here to give bulk structural information on the bonding of ^{11}B, and ^{29}Si in both the HLi and FLi glasses. **Section 3.4.2** gave details of experimental method and analysis techniques made us of in this section. The data will be presented here in terms of changes with varying ZrO_2 content.

4.6.1 ^{11}B NMR results

The primary information available from analysis of ^{11}B MAS-NMR spectra is that of B co-ordination. It is assumed that the co-ordination of boron is either ^{IV}B or ^{III}B. Stack plots of the spectra collected in this project can be seen in **Figure 4.15**. Four peaks were fitted under each spectrum as shown in **Figure 3.11** and **Section 3.4.2**; two peaks to represent ^{IV}B and two peaks to represent ^{III}B. Example fits can be seen in **Figure 4.16.**

The position of these peaks for both FLi and HLi glasses appears invariant with ZrO_2 content (see **Figure 4.17**). However, the relative area of the peaks changes with ZrO_2 content (see **Figure 4.19**). It is the area under the peaks that provides the relative amounts of ^{IV}B and ^{III}B in the glasses. **Figure 4.18** shows the change in ^{IV}B fraction with increasing ZrO_2. For both HLi and FLi glasses there is an initial increase in ^{IV}B fraction then with higher ZrO_2 contents there is a decrease. To the author's knowledge this is the first time this effect has been observed in alkali borosilicate glasses.

Figure 4.19 shows the relative contributions from the individual peaks fitted under the ^{11}B MAS-NMR spectra. Each of these peaks can be assigned a physical significance (see **Table 4.5**). **Figure 4.19a** shows that for the FLi glasses there is an initial increase in the contribution from the

$^{IV}B(1B,3Si)$ species with a decrease in contribution from $^{IV}B(0B,0Si)$ with this situation reversed at high ZrO_2 contents. The two ^{III}B contributions show the same trend with an initial decrease and then an increase at high ZrO_2 content. The increase in the contribution from the $^{IV}B(OB,4Si)$ species indicates an increase in mixing of the borate and silicate networks.

For the HLi glasses (see **Figure 4.19a**) the change in the contributions is similar to that seen in the FLi glasses with initially a decrease in both ^{III}B contributions. The ^{IV}B contributions are different to those seen in the FLi glasses with the $^{IV}B(1B,4Si)$ contribution decreasing and the $^{IV}B(0B,4Si)$ initially increasing then decreasing at higher ZrO_2. The reason for the difference between FLi and HLi glasses is unknown. This is discussed further in **Section 4.8** and **Chapter 8**.

Peak	Assignment
^{IV}B Peak 1	$^{IV}B(1B,3Si)$
^{IV}B Peak 2	$^{IV}B(0B,4Si)$
^{III}B Peak 1	Symmetric ($^{III}B(O_{1/2})_3$)
^{III}B Peak 2	Asymmetric ($^{III}B(O_{1/2})_2(O^-)$)

Table 4.5: Peak assignments for ^{11}B MAS-NMR spectra (Parkinson *et al.* 2005, Rodderick *et al.* 2007, Mackenzie & Smith 2002).

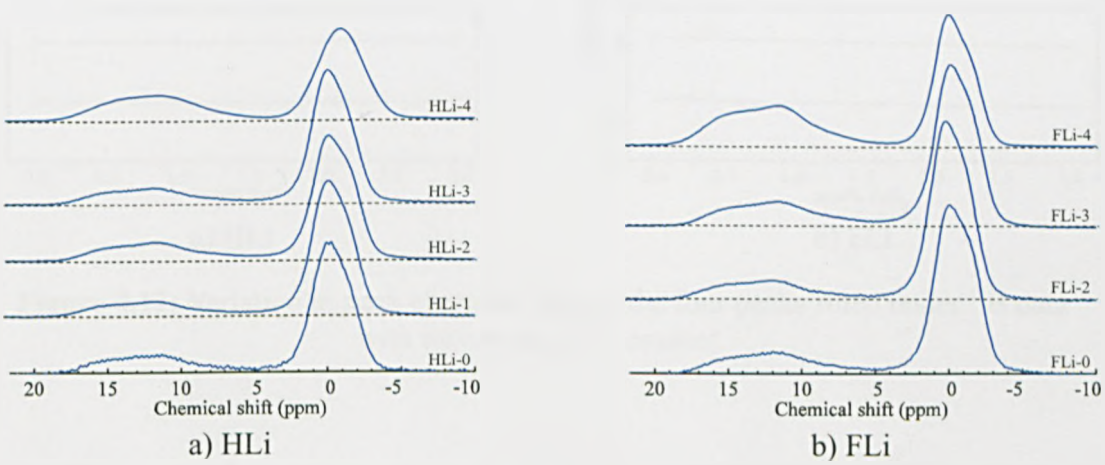

Figure 4.15: Stack plot of ^{11}B MAS-NMR results. Shows change in peak position and shape with increasing ZrO_2 content.

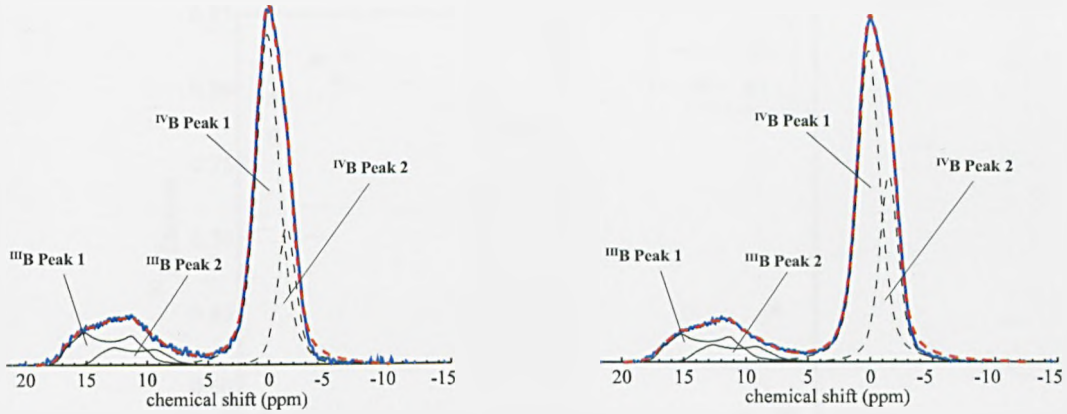

Figure 4.16: ^{11}B MAS-NMR example fits.

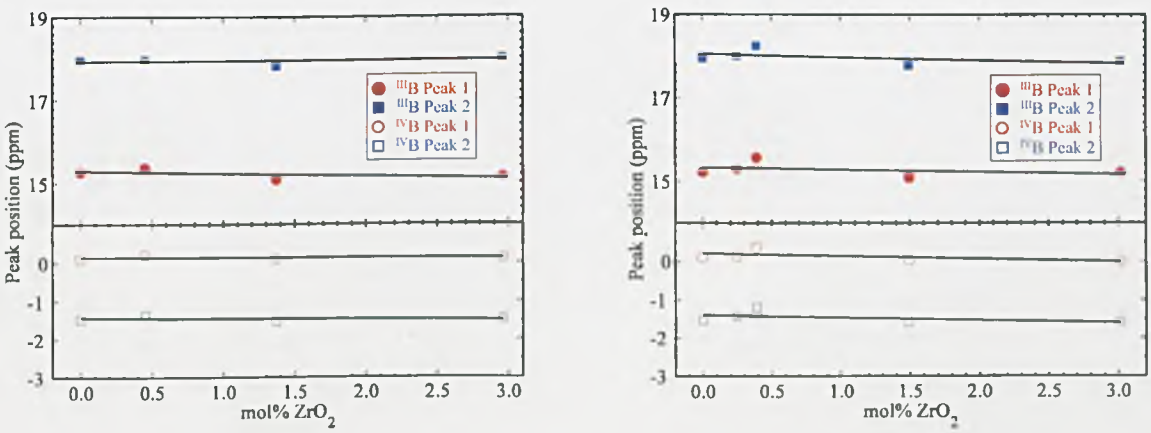

Figure 4.17: Variation in peak chemical shift of the four peaks fitted under ^{11}B data with increasing ZrO_2 content.

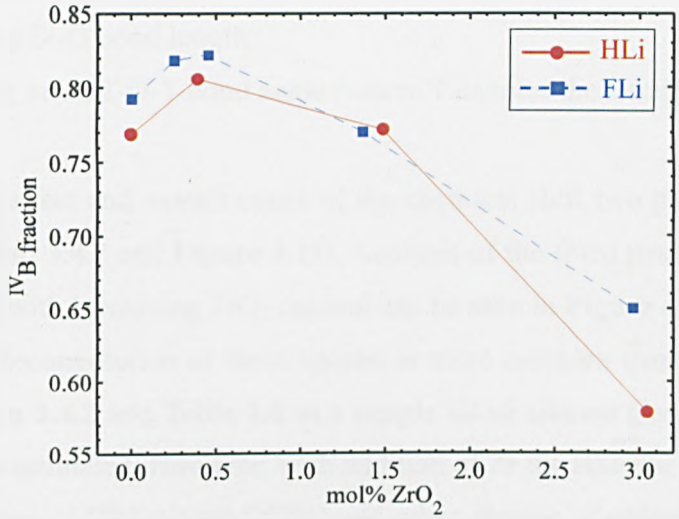

Figure 4.18: Change in ^{IV}B fraction with increasing ZrO_2.

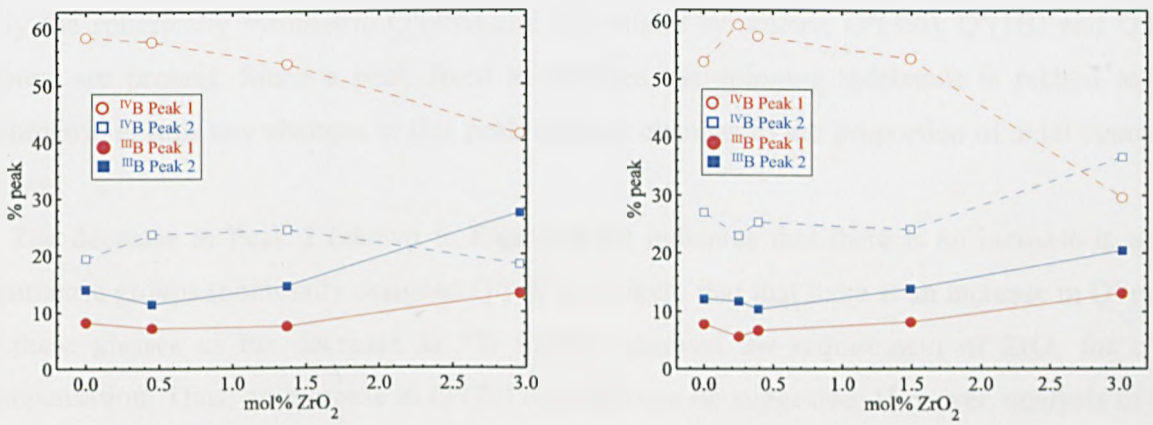

Figure 4.19: Variation in peak intensity of the four peaks fitted under ^{11}B data with increasing ZrO_2 content.

4.6.2 ^{29}Si MAS-NMR results

From the line shapes of the ^{29}Si MAS-NMR spectra the degree and nature of the bonding between silicate tetrahedra can be elucidated (**Section 3.4.2**). The difficulties involved in extracting information from ^{29}Si MAS-NMR are described in **Section 3.4.2**. A comparison of spectra with increasing ZrO_2 content can be seen in **Figure 4.20**. This shows that the chemical shifts of the spectra become more negative with increasing ZrO_2 content. In general it is found that chemical shifts becomes more negative with (Mackenzie & Smith 2002) (see **Table 3.7**):

1. increasing electronegativity of the surrounding groups;
2. decreasing Si-O bond length;
3. increasing mean T-O-T bond angle (where T denotes the tetrahedral atom).

To quantify this effect and extract cause of the chemical shift two peaks are fitted under each spectrum (see **Section 3.4.2** and **Figure 3.11**). Analysis of the fitted peaks chemical shift for both HLi and Fli glasses with increasing ZrO_2 content can be seen in **Figure 4.21**.

Analysis of the deconvolution of these spectra is more complex than that for ^{11}B MAS-NMR. As shown in **Section 3.4.2** and **Table 4.6** in a simple alkali silicate glass the relative proportions of Q^4 and Q^3 can be estimated. However, with addition of Zr the situation becomes more complex. The possible presence of $Q^n(Zr)$ (and $Q^n(B)$) and other species of unknown peak position makes analysis very difficult. The analysis technique used in **Section 4.6.2** showed that if an assumption is made as to what units are present information can be extracted. Initially, it must be assumed that only the spherically symmetric $Q^4(4Si)$ and the axially symmetric $Q^3(3Si)$, $Q^4(1B)$ and $Q^4(1Zr)$ groups are present. Since a peak fixed in between the spinning sidebands is related to axial symmetric groups any changes in this peak indicate changes in the proportion of axial symmetric groups.

The decrease in Peak 2 (shown in **Figure 4.22**) indicates that there is an increase in axially symmetric groups (nominally assigned Q^4). It is unlikely that that there is an increase in Q^3 groups in these glasses as the decrease in ^{IV}B fraction showed the requirement of ZrO_2 for charge compensation. Thus, an increase in $Q^4(Zr)$ or $Q^4(B)$ can be suggested. However, analysis of XAS data (and MD simulations – see **Chapter 6**) shows the presence of Si-O-Zr bonds and so $Q^4(Zr)$ is seen as the most likely group.

Figure 4.21 shows the change in peak positions with increasing ZrO_2. For the HLi glasses there is only a very small change in peak position with increasing ZrO_2.

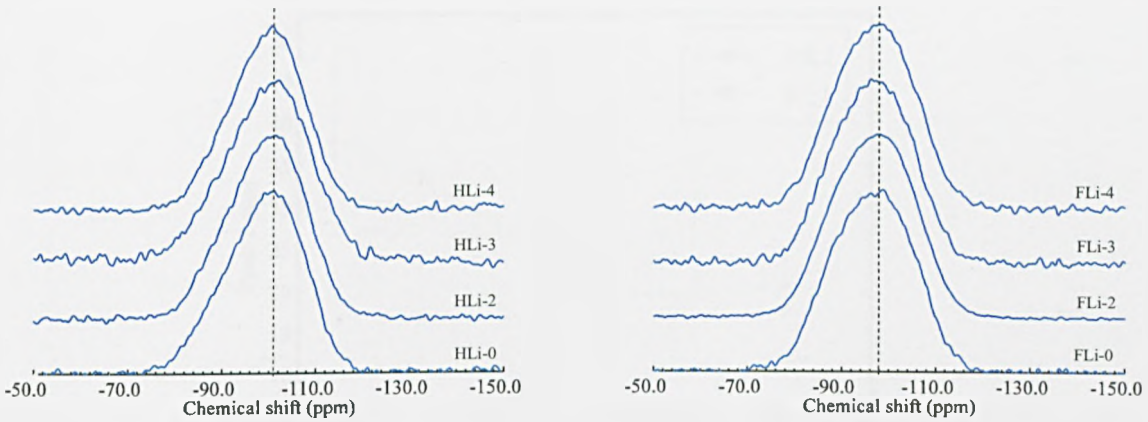

a) HLi b)FLi

Figure 4.20: Stack plot of ^{29}Si MAS-NMR results. Shows change in peak position and shape with increasing ZrO_2 content.

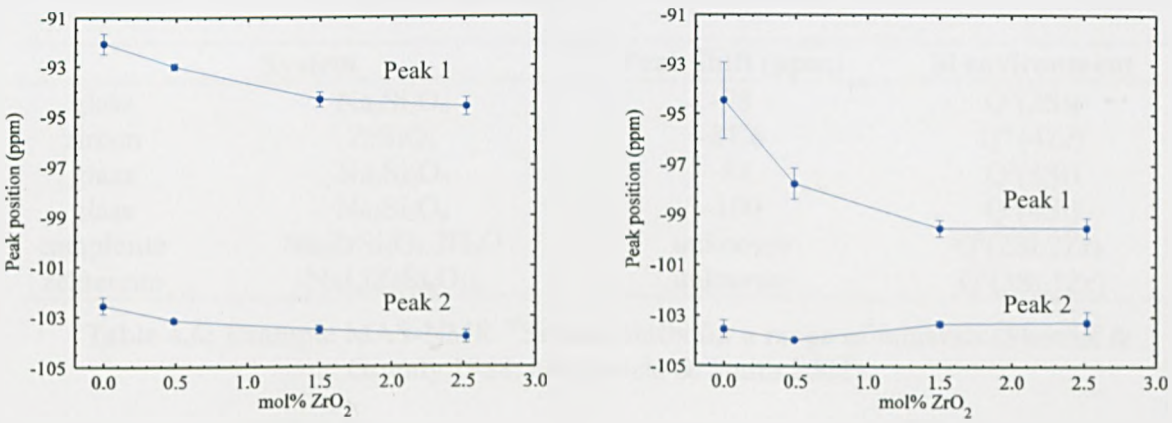

a) HLi b) FLi

Figure 4.21: Change in chemical shifts for Peak 1 and Peak 2 under the ^{29}Si spectra.

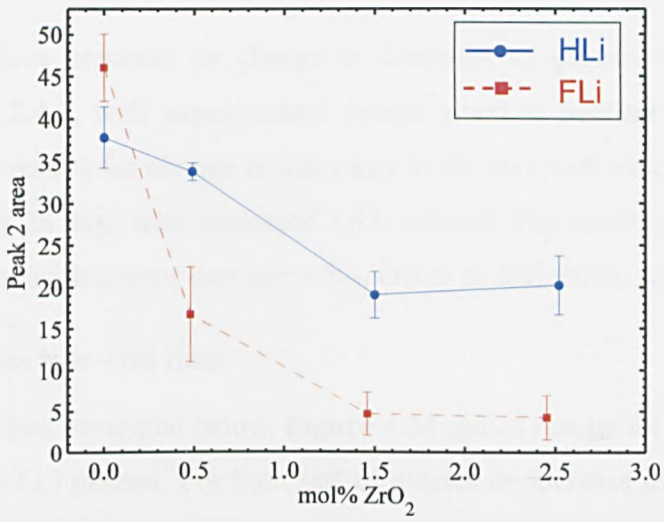

Figure 4.22: Change in Peak 2 area (%) with increasing ZrO_2 contents. Peak 2 to can be considered equivalent to Q^4 species.

	System	Peak shift (ppm)	Si environment
glass	$Na_2Si_2O_6$	-78	Q^3(2Si)
zircon	$ZrSiO_4$	-81.6	Q^4 (4Zr)
glass	$Na_2Si_2O_6$	-88	Q^3(3Si)
glass	$Na_2Si_2O_6$	-100	Q^4(4Si)
catapleiite	$Na_2ZrSi_3O_9.2H_2O$	unknown	Q^4(2Si,2Zr)
zekterzite	$NaLiZrSi_6O_{15}$	unknown	Q^4(3Si,1Zr)

Table 4.6: Example MAS-NMR ^{29}Si peak shifts for a range of minerals (Sherriff & Grundy 1988, Mackenzie & Smith 2002).

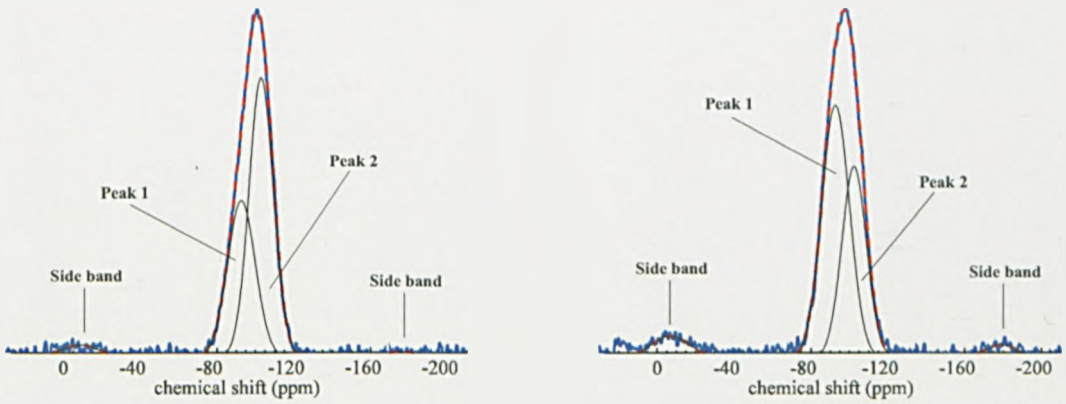

Figure 4.23: Example fits for ^{29}Si MAS-NMR data.

4.7 Durability results

A discussion of previous literature on change in durability of glasses with addition of ZrO_2 is presented in **Section 2.4.1**, with experimental details given in **Section 3.6.3**. **Figure 4.24** and **Figure 4.25** show the results for change in mass loss at 28 days with time and **Figure 4.26** shows change in mass loss at 28 days with increased ZrO_2 content. The results are discussed below and in **Chapter 8**. All composition error bars are ± 5%, errors as defined by supplier of analysis.

4.7.1 Change in mass loss with time

There are two sets of data presented below, **Figure 4.24** shows results for HLi glasses and **Figure 4.25** shows results for FLi glasses. For both sets of glasses an increase in mass loss over 28 days is seen. From **Section 2.2.2** it would be expected that at longer time a steady state would be reached in mass loss. However, it is clear from both **Figure 4.24** and **Figure 4.25** that this has not occurred; however, there is a decreased rate of change of mass loss with time. This indicates that the majority of the glasses are in the gel formation region.

For glasses containing ZrO_2 the mass loss for Zr is more complex, showing an initial increase and then a decrease. This anomaly could be attributed to condensation of Zr phases onto the leach layer. These phases appear under SEM as an increase Zr concentration in the leach layer over that of the bulk glass (see **Section 4.7.4**). However, the nature of these phases is unknown.

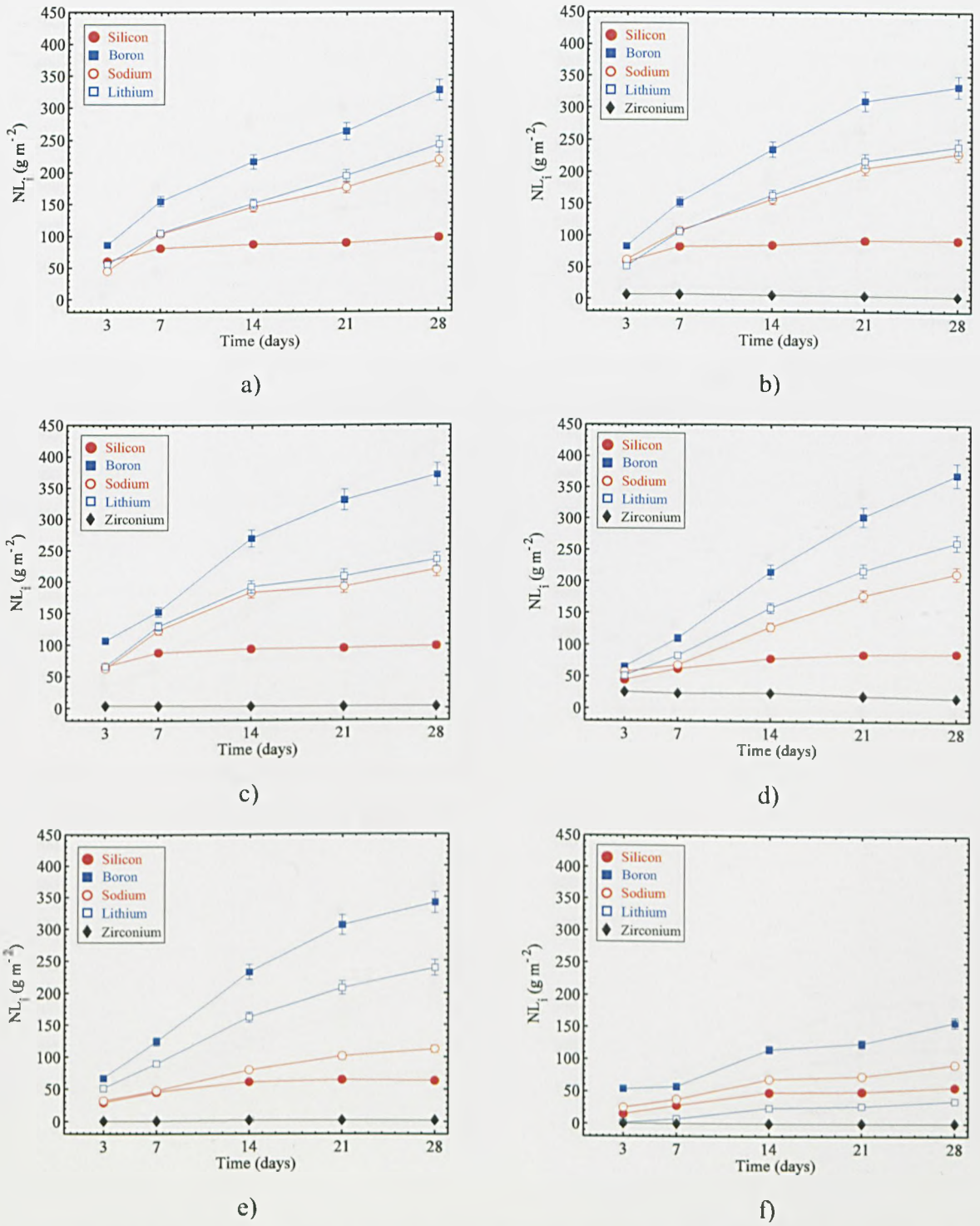

Figure 4.24: Durability of HLi glasses with time. a) HLi-0, b) HLi-1, c) HLi-2, d) HLi-3, e) HLi-4, and f) HLi-5.

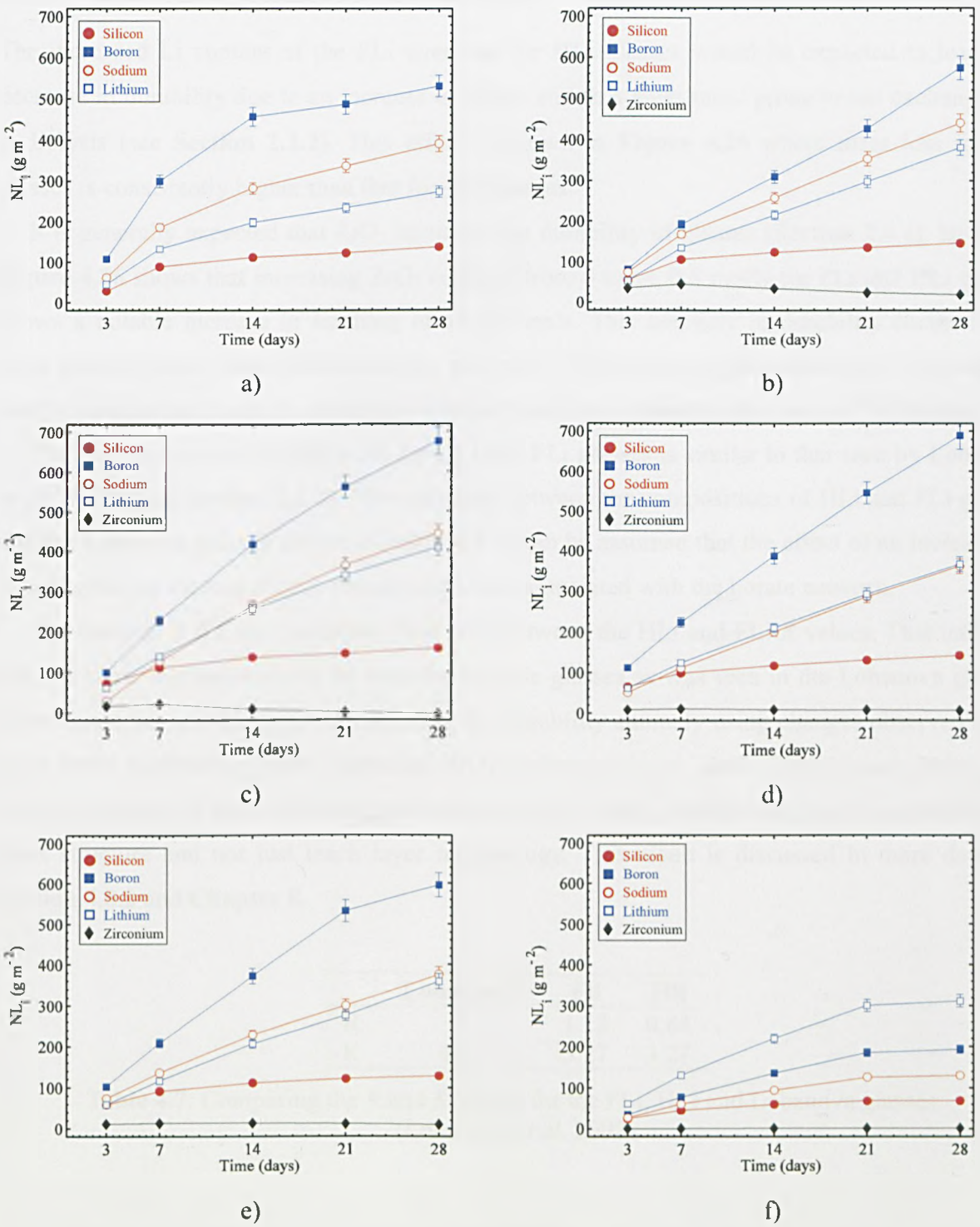

Figure 4.25: Durability of FLi glasses with time. a) FLi-0, b) FLi-1, c) FLi-2, d) FLi-3, e) FLi-4, and f) Fli-5.

4.7.2 Effect of ZrO_2 content on glass durability

The increased Li content of the FLi over that for HLi glasses would be expected to lead to a decrease in durability due to an increase in NBOs and so a glass more prone to ion exchange and hydrolysis (see **Section 2.2.2**). This effect is shown in **Figure 4.26** where mass loss for FLi glasses is consistently higher than that for HLi glasses.

It is generally expected that ZrO_2 increases the durability of glasses (**Section 2.4.1**), however, **Figure 4.26** shows that increasing ZrO_2 contents from 0 to ca. 0.5 mol% for FLi and HLi glasses shows a notable increase in leaching of all elements. This anomaly in durability occurs in the same compositional range as the anomaly see in the ^{IV}B fraction (see **Section 4.6.1**). This implies that the non-linearity seen in durability with composition is related to that seen in ^{IV}B fraction.

The non-linearity in durability for the HLi and FLi glasses is similar to that seen by Lobanova *et al.* (2002) (see **Section 2.2.2**). The similarity between the compositions of HLi and FLi glasses and the Lobanova glass is shown in **Table 4.7**. It can be assumed that the effect of an increased *K* is negligible, as the majority of the alkali ions are associated with the borate network.

The value of *R* for the Lobanova glass is in between the HLi and FLi *R* values. This indicates that the same mechanism may be working in these glasses as was seen in the Lobanova glasses. Lobavona *et al.* and Sicard *et al.* explained the durability anomaly using changes observed in the leach layer morphology with increasing ZrO_2 (Lobanova *et al.* 2002, Sicard *et al.* 2004). The results presented in this chapter suggest that the effect of ZrO_2 on durability may be a function of glass structure and not just leach layer morphology. This result is discussed in more detail in **Section 4.8.2** and **Chapter 8.**

	Lobanova[1]	Fli	Hli
R	1	1.13	0.84
K	4.67	3.27	3.27

Table 4.7: Comparing the *R* and *K* values for the FLi, HLi and Lobanova glasses. [1](Lobanova *et al.* 2002).

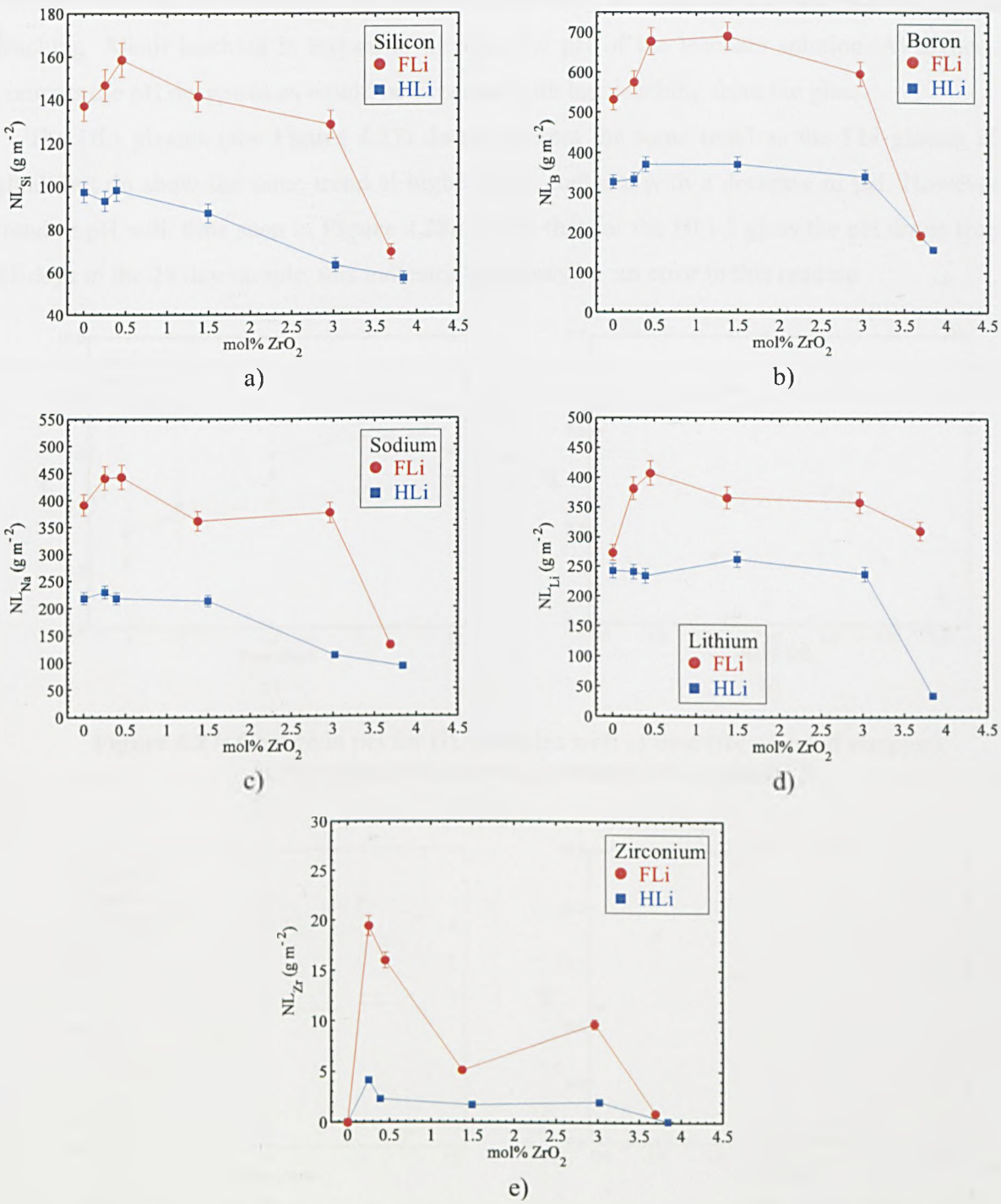

Figure 4.26: Mass loss after 28 days for HLi and FLi glasses with increasing ZrO_2 content.

4.7.3 Leaching of ZrO_2 bearing glass - pH

The change in pH with increasing ZrO_2 can be seen in **Figure 4.27** and **Figure 4.28**. The change in pH with increasing ZrO_2 for the FLi glasses follows the same trend as that seen with the

durability results with an initial increase, corresponding to the initial increase in boron and alkali leaching. Alkali leaching is known to increase the pH of the leachate solution. At higher ZrO_2 contents the pH decreases as would be expected with less leaching from the glass.

The HLi glasses (see **Figure 4.27**) do not present the same trend as the FLi glasses at low alkali but do show the same trend at higher ZrO_2 contents with a decrease in pH. However, the trend in pH with time seen in **Figure 4.28a** shows that for the HLi-2 glass the pH drops from the 21 days to the 28 day sample, this indicates there may be an error in this reading.

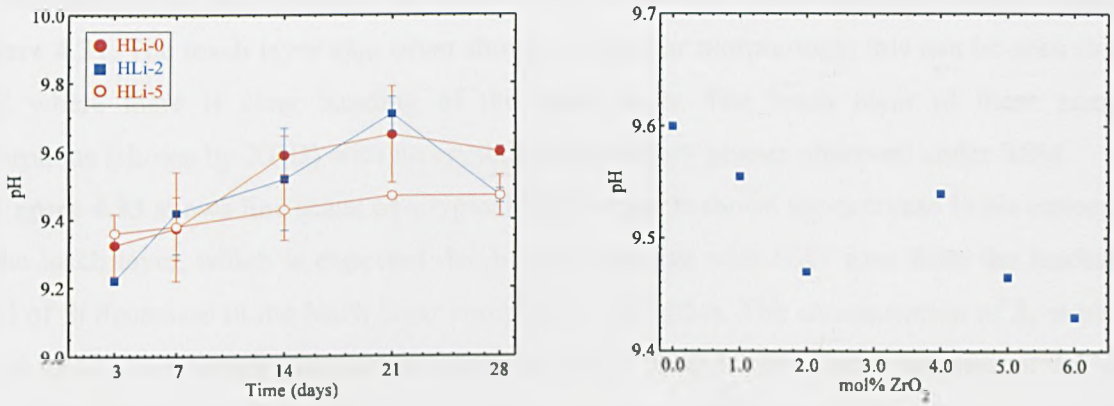

Figure 4.27: Change in pH for HLi samples with a) time (for selected samples), and b) pH at 28days with increasing ZrO_2 content.

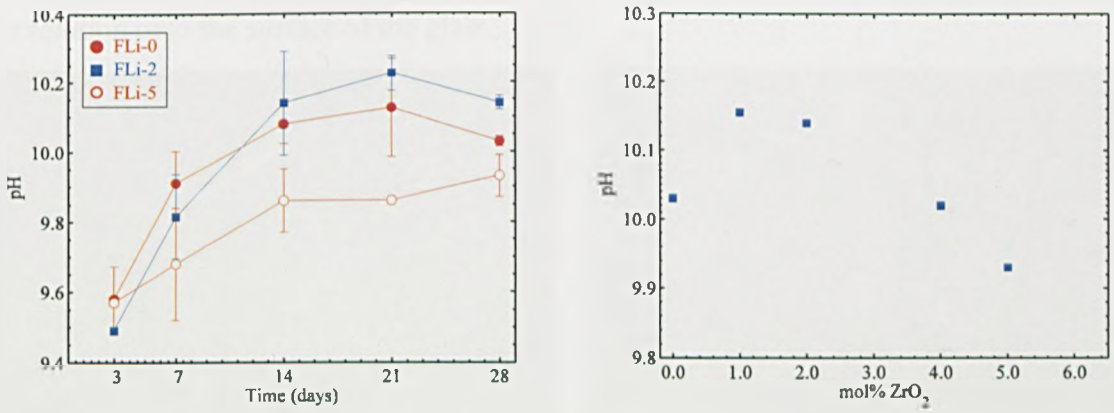

Figure 4.28: Showing change in pH for FLi samples with a) time (for selected samples), and b) pH at 28days with increasing ZrO_2 content.

4.7.4 Morphology of the leach layer

Images of leach layer cross sections and leached sample surface morphology were captured using

SEM. SEM was generally carried out in BEI mode to give compositional resolution. **Figure 4.29** shows the surface of two leached samples. **Figure 4.29a** shows a typical surface morphology after a short leaching time. **Figure 4.29b** shows a typical surface morphology after longer leaching times. The level of alternation is significantly different between the two samples with only limited leach layer formation after 3 days. The cracked surface of **Figure 4.29b** can be seen in cross section in **Figure 4.30b** which shows cracking of a friable surface layer. The cracking is assumed to have occurred during sample dehydration.

The leach layer itself tends to lift away from the surface of the glass very easily as shown in **Figure 4.31**. The leach layer also often showed a laminar morphology, this can be seen in **Figure 4.32** where there is clear banding of the leach layer. The leach layer of these samples is amorphous (shown by XRD) with no crystalline secondary phases observed under SEM.

Figure 4.33 shows line scans of a typical leach layer. It shows the decrease in Na concentration in the leach layer, which is expected due to ion exchange with H_3O^+ ions from the leachate. The level of Si decreases in the leach layer compared to the glass. The concentration of Zr is increased in the leach layer as compared to the unaltered glass, there is also a large increase at the leachate -leach layer interface. This can also be seen in **Figure 4.30a** where the surface appears brighter which indicates a higher average atomic weight for this area (i.e. higher Zr). This increase in concentration is also seen in the Si, and to a lesser extent the Na. The reason for this increase in predominantly Zr, but also Si and Na at the surface is not known, it maybe due to reprecipitation from solution onto the surface of the glass.

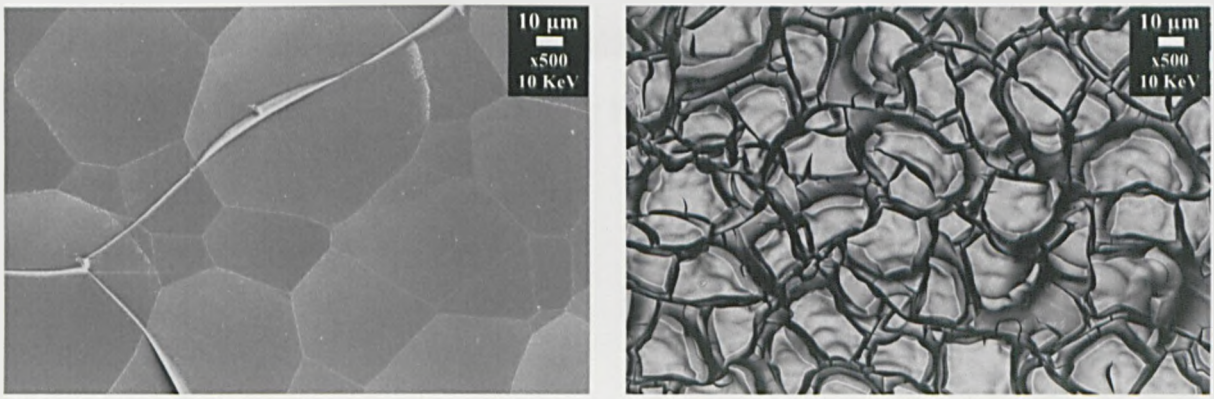

a) b)

Figure 4.29: BEI SEM images a) HLi-2 3 days, b) HLi-4 21 days.

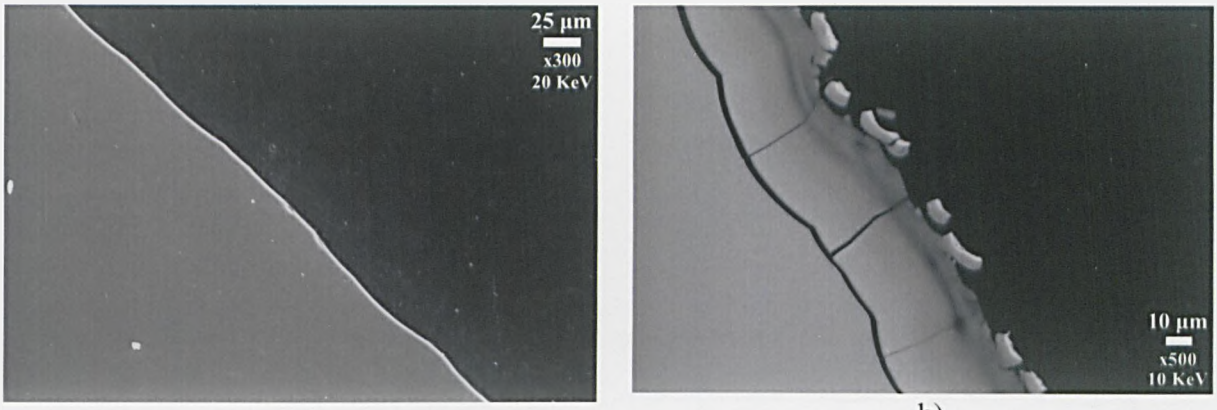

a) b)

Figure 4.30:a) SEI SEM image HLi-4 3 days, b) BEI SEM image HLi-4 21 days.

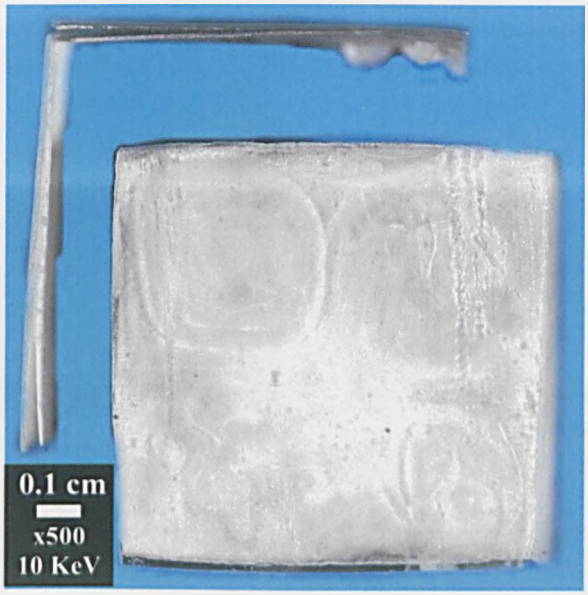

Figure 4.31: HLi-0 28 days

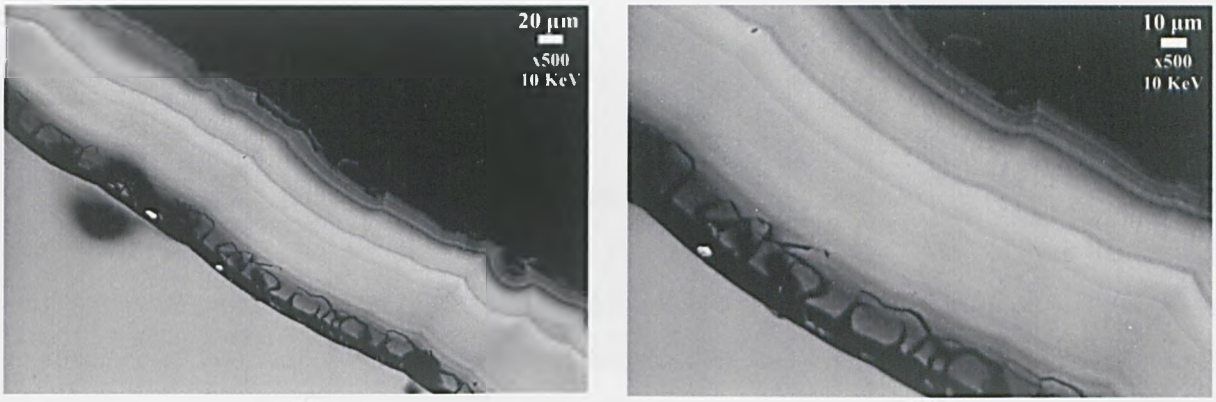

Figure 4.32: BEI SEM pictures of leach layers. a) and b) both Fli-2 14 days

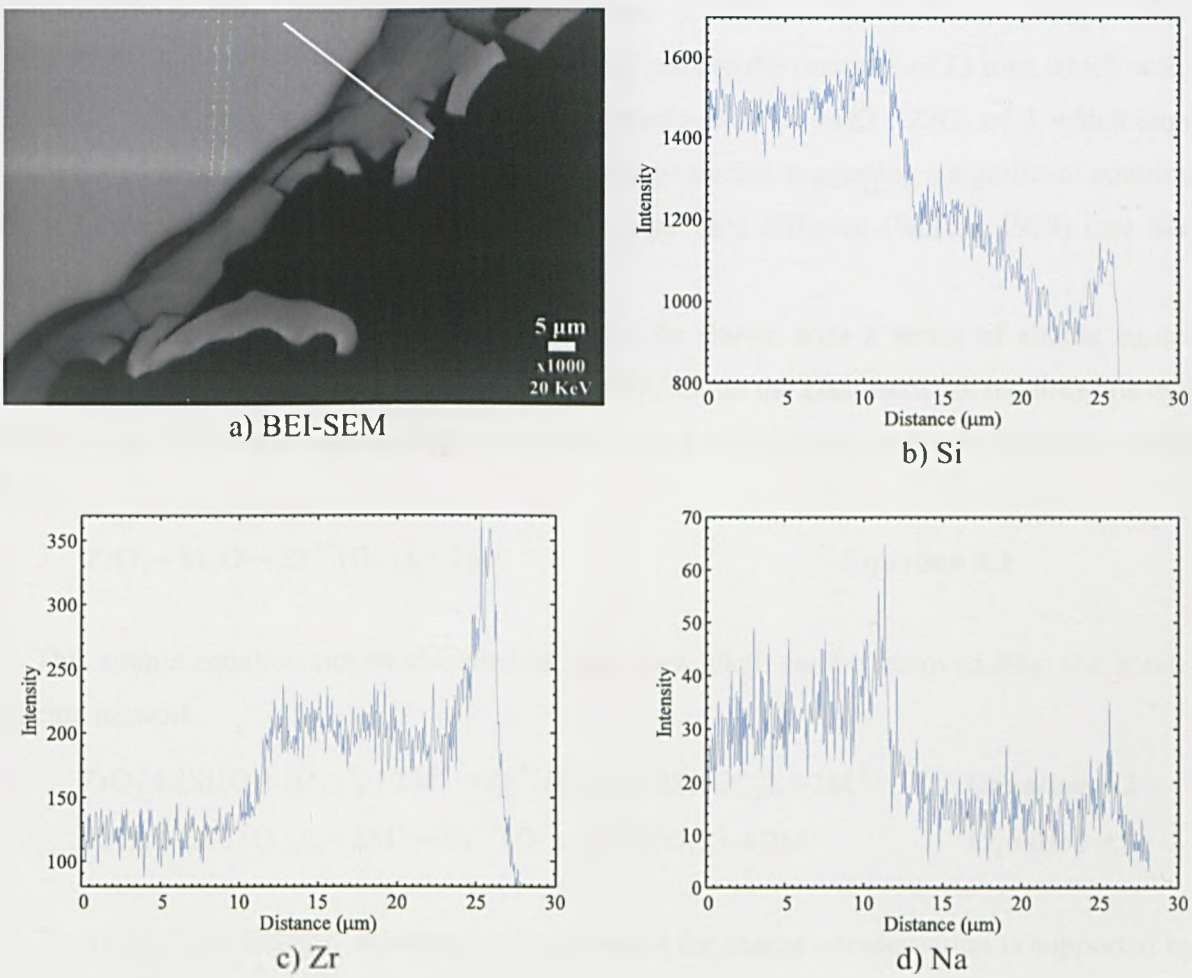

Figure 4.33: Line scan traces across typical leach layers (sample HLi-4 7 days) shown in a) with white line showing trajectory of scan. The equipment could not resolve Li, B and O due to the low energies of these elements.

4.8 Chapter Summary

4.8.1 Structure

Zr K-edge XAS data indicates that Zr is primarily present in both HLi and FLi glasses as ^{VI}Zr species with a Zr-O bond distance of ca. 2.09 Å. A small fraction of ^{VII}Zr (or, less likely ^{VIII}Zr) species may be present. In general, a second shell comprising, on average, 1.88 (± 0.11) Na atoms at a distance of 3.45 Å (± 0.01 Å) from the central Zr atom was found to provide the best fit to the EXAFS data of all glass compositions in this study. However, the possible contribution of Si and / or Zr to this second shell cannot be excluded.

The presence of ca. 2 Na ions around the Zr is supported by the work of Ellison and Hess (Ellison1994a) who demonstrated the presence of alkali zirconosilicate groups with a M_2O : ZrO_2 ratio of 1:1. However, EXAFS cannot resolve the presence of Li ions which would be expected to be present. Work by Watson suggested a ratio of M_2O : ZrO_2 of 2 which suggests more than 2 alkali ions are required for charge compensation suggesting a significant contribution from Li ions, however, the melting conditions were very different (Watson 1979) (see **Section 2.4.1**).

The need for charge compensation can easily be shown with a series of simple equations. **Equation 4.1** shows that to charge balance the ZrO_2 within the glass network requires one mole of alkali oxide. This partly supports the results above and will be discussed in more detail in **Section 8.3.1**.

$$ZrO_2+M_2O \rightarrow Zr^{4+}(O_{1/2})_6+2M^+ \qquad \textbf{Equation 4.1}$$

This simple equation can be extended to show how alkali can be removed from the borate and silicate network.

$$ZrO_2+2Si(O^-)_1(O_{1/2})_3+2M^+ \rightarrow Zr^{4+}(O_{1/2})_6+2Si(O_{1/2})_4+2M^+ \qquad \textbf{Equation 4.2}$$

$$ZrO_2+2B^{3+}(O_{1/2})_4+2M^+ \rightarrow Zr^{4+}(O_{1/2})_6+2B(O_{1/2})_3+2M^+ \qquad \textbf{Equation 4.3}$$

The result from EXAFS showing the requirement for charge compensation is supported by the MAS-NMR data presented in this Chapter. The decrease in ^{IV}B with additional alkali and the change in the ^{29}Si MAS-NMR spectra with increased alkali are indicative of alkali ions being removed from the borate and silicate networks to provide charge compensation for the ZrO_2. The number of moles of alkali oxide removed from the borate network can be quantified using

literature data. Rodderick *et al.* (2002) measured the ^{IV}B fraction for a series of alkali borosilicate glasses with varying *R*. If the MAS-NMR ^{IV}B fractions for the glasses in this work are overlaid on to these literature data the number of moles of alkali oxide required for charge compensation can be calculated. In order to do this, a modified *R* value must be calculated (see **Equation 4.4**). Where the value *x* is effectively the number of moles alkali oxide the addition of ZrO_2 removes. This process is discussed in more detail in **Chapters 5** and **6**.

Figure 4.34 shows the result of this process with values of $x = 1$. There is a reasonable fit with the literature data with $x = 1$, the values are off-set due to compositional differences. This supports the assertions made above that two alkalis ions are required for charge compensation (one mole of alkali oxide).

$$R_{ZrO_2} = \frac{([Na_2O]+[Li_2O]-x[ZrO_2])}{[B_2O_3]} \qquad \textbf{Equation 4.4}$$

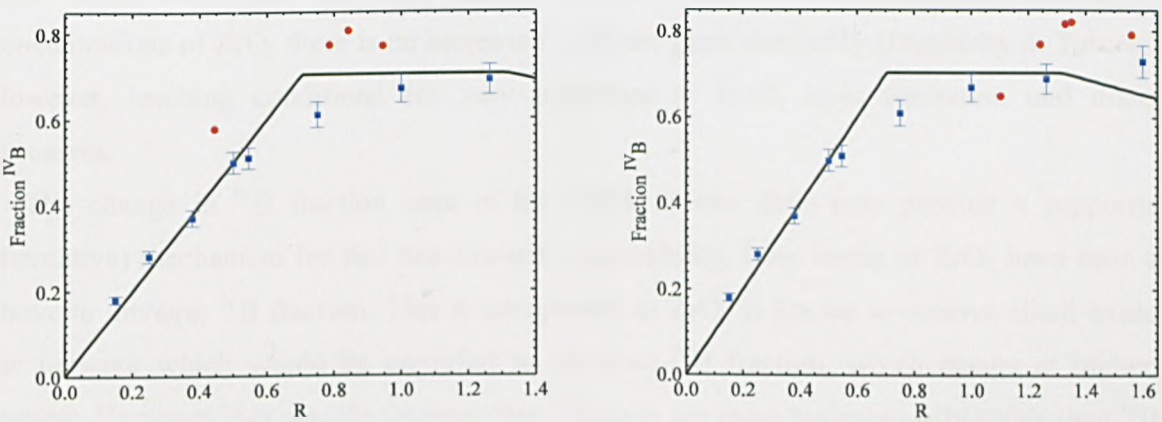

Figure 4.34: Fraction ^{IV}B of literature data (Rodderick2001) with laboratory data rescaled onto the *R*-axis with $x = 2$ (see **Equation 4.4**).

Figure 4.34 shows the complex nature of the interaction between ^{IV}B fraction and ZrO_2 additions for the FLi glasses. This is discussed in more detail in **Section 4.8.2** and **Chapter 8**.

The change in ^{IV}B fraction for the HLi and FLi glasses indicates that the competition for charge compensation is in the order: (Al >) Zr > B. This result is supported by the work of Du *et al.* (2001) who showed a similar decrease in ^{IV}B with increasing ZrO_2 . The work by Du *et al.* also presents data showing there was little change in Si co-ordination with increased ZrO_2, this may be due to having a relativity low alkali content and so being in Region 1 of the Dell Bray model. This would mean that very little, or no, alkalis are associated with the silicate network. Also, no non-

linearity in the ^{IV}B fraction was seen.

4.8.2 Durability and structure

From literature data on alkali silicate glasses it is expected that increasing ZrO_2 increases the durability of glasses (see **Section 2.4.1**). This is believed to occur due to the requirement for charge compensation alkali cations which are removed from the network and so increase network polymerisation (and so hydrolysis stability). The presence of hydrolysis resistant Zr-O-Si bonds will reduce the possibility of dissolution of the network.

However, for borosilicate glasses presented in this work, and in the work of Lobanova *et al.* and Sicard *et al.* (Lobanova *et al.* 2002, Sicard *et al.* 2004), the situation for borosilicate glasses is more complex with a decreased durability in alkali borosilicate glasses at low ZrO_2 content. Then, at higher ZrO_2 contents the durability does increase. In the work of Lobanova *et al.* this effect was attributed to changes in leach layer morphology. It is surprising that this effect, if purely a leach layer based effect, has not been seen in studies of alkali silicate glasses as even at low concentrations of ZrO_2 there is an increase in silicate glass durability (Dimbleby & Turner 1925). However, leaching conditions are very important to leach layer formation and dissolution processes.

The change in ^{IV}B fraction seen in this work at low ZrO_2 may provide a supporting (or alternative) mechanism for this non-linearity is durability. Low levels of ZrO_2 have been shown above to increase ^{IV}B fraction. This is unexpected as ZrO_2 is known to remove alkali oxide from the network which would be expected to decrease ^{IV}B fraction, which occurs at higher ZrO_2 content. However, it is usually accepted that ^{IV}B units are more hydrolytically stable than ^{III}B units due to their higher level of polymerisation. This appears to no longer be the case when ZrO_2 is present in the glass.

One possible mechanism for this non-linearity is set out below:

1. The presence of ^{IV}B-O-Zr bonds is unlikely (see **Section 8.2**) due to over-bonding of the B atom;
2. Thus, increasing $^{IV}B(1B,3Si)$ species at low ZrO_2 levels in the FLi glass suggests a level of phase separation of ^{IV}B (possible creation of ^{IV}B-O-^{IV}B linkages) from the main network;
3. This ^{IV}B phase would be much less hydrolytically stable than the ^{III}B and silicate phase due to the hydrolytically stable Zr-O-^{III}B and Zr-O-Si. This will lead to leaching of a ^{IV}B,

alkali rich phase;

4. Increased alkali leaching would lead to an increased pH and so increased Si leaching;
5. At high ZrO_2 content although the phase separation would be present the increased durability of the silicate and ^{III}B part of the network will increase the overall durability.

It has been seen in the literature that ZrO_2 can enhance phase separation (see **Section 2.2** and **Section 2.4.1**) within borosilicate glasses (Volf 1984). ^{IV}B-^{IV}B bonding has previously been shown to destabilise the glass network (Parkinson *et al.* 2007). This is discussed more in **Chapters 6** and **8.**

5 Molecular Dynamic Simulations of Alkali Borosilicate Glass

5.1 Introduction

The aim of this Chapter is to explore the potential of Molecular Dynamic (MD) techniques for simulating the structure, at the atomic level, of British nuclear waste glass. A review of the literature on MD of glasses can be found in **Section 2.6** with a description of how this study was undertaken in **Section 3.7**.

In order to show that the atomic arrangement created using MD is equivalent to that found in laboratory glasses literature data from Rodderick *et al.* (2001) has been used for comparison. Rodderick *et al.* present ^{11}B MAS-NMR and density data for a series of mixed alkali borosilicate glasses of very similar composition to the British nuclear waste base glass (see **Section 3.7.7**). The use of literature compositions allows the values for ^{IV}B fraction calculated from MD to be compared directly to literature data, so demonstrating the ability of MD to model accurately the structure of British nuclear waste glasses.

The classical description for the change in both ^{IV}B fraction and Q^n average with R from Dell and Bray (Dell *et al.* 1983) has also been used for comparison. A full description is given in **Section 2.2.1**. Within this Chapter it is shown that laboratory data does not always follow the Dell-Bray model; however, this is because the Dell-Bray model is based on simplified assumptions. Thus, agreement with laboratory data is more critical than agreement with the Dell-Bray model.

A controversial aspect of MD simulations of glasses is the high quench rate compared to that for laboratory glasses (see **Table 2.8**). This has led to questions as to whether an atomic arrangement quenched from a "melt" using MD is truly a glass or actually a supercooled liquid (see **Section 3.7.4**). For this reason this chapter starts by asking; is the atomic arrangement created using the MD method used in this work a true glass?

5.2 Is it a glass?

The definition of a glass is very difficult (see **Section 2.2**), from a thermodynamic standpoint it is a material that undergoes a second order phase transition in some temperature range (T_g) (see **Section 2.6.2**). In laboratory glasses, methods such as DTA and dilatometry (see **Section 3.6.1**), which monitor a derivative thermodynamic property with temperature (e.g. volume), can be used to measure T_g. However, as explained in **Section 3.7.4,** it is very difficult to model such properties with MD. For this reason the atomic arrangements formed in this study must be examined to show initially that the structure is amorphous and then that it is in a glassy state (see **Section 3.7.4**).

If a partial distribution function, or $g_{ij}(r)$ (where i and j can be Si, B, O etc.), is determined for a glass it should have an appearance between that of a liquid (little long range order) and a solid (short and long range order) (see **Figure 3.26**). Thus, a $g(r)$ for a glass should show short range order but limited, or no, long range order. Example $g(r)$s for a glass in this work are shown in **Figure 5.1**. For each oxide pair $g(r)$, there are strong and sharp peaks at short distances (short range order corresponding to well defined bond lengths). At longer range there is a much more liquid like structure with weak and diffuse peaks. It is interesting to note that the $g(r)$s for the network forming atom pairs (Si-O and B-O) have much sharper initial peaks that those for the network modifying Na-O and Li-O. This is expected due to the increased disorder in the environment of these ions (due to a higher degree of ionic bonding).

Another important aspect of a simulated glass is the stability of the structure over time. It is important that the system has formed a solid phase and not a supercooled 'metastable' liquid which will flow with time. **Figure 5.2** shows a mean square displacement (*MSD*) for a typical simulation, this is a cumulative description of how far atoms have moved from their initial positions with time (see **Section 3.7.4**). The slope of a *MSD* plot is proportional to the (self) diffusivity coefficient. A zero gradient *msd* indicates a solid material (little or no cumulative movement of atoms with time); a positive gradient on an *msd* indicates a liquid (atoms have moved from their staing positions); with the steeper gradient indicating a higher fluidity (movement).

The zero gradients for all the oxide pairs shown in **Figure 5.2** demonstrate that atomic arrangement achieved though MD is stable with time. There is a small variation in the *msd* slopes for the elements after longer times, this is due to the blocking averaging method used to calculate the *msd* and is not significant.

The combination of $g(r)$ peak shape and *msd* demonstrated here indicate that the atomic

arrangements achieved with MD can be considered glassy.

In the following sections the structural agreement between the simulated glasses and laboratory glasses will be examined.

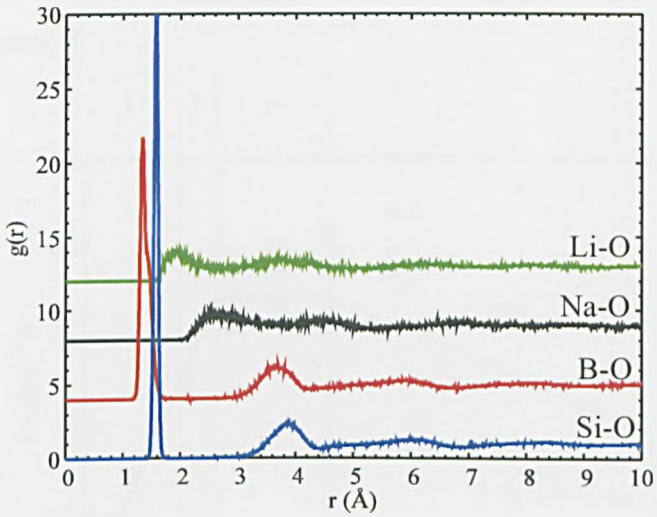

Figure 5.1: *g(r)* for elements with element-oxygen pairs within simulated glass.

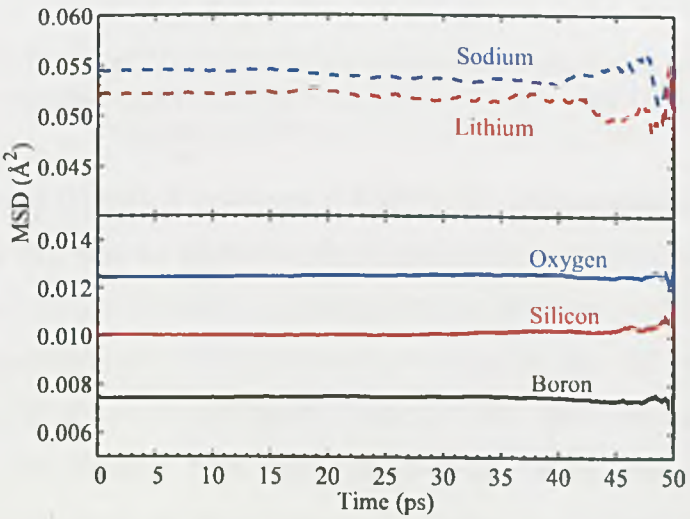

Figure 5.2: *MSD* for elements within a simulated glass.

5.3 Constant volume results

Initial work was carried out under *NVT* conditions (constant number of atoms, constant volume and constant temperature). The volume was defined from laboratory density data (Rodderick *et al.*

2001) and the simulations run as shown in **Section 3.7.7**.

The variation in the fraction ^{IV}B with R, calculated from the MD glass structure (see **Section 3.7.9**), is shown in **Figure 5.3.** There is good agreement up to R = 1.0 between laboratory and MD results. After R = 1.0 there is a divergence with increasing R value which becomes more significant with increasing R.

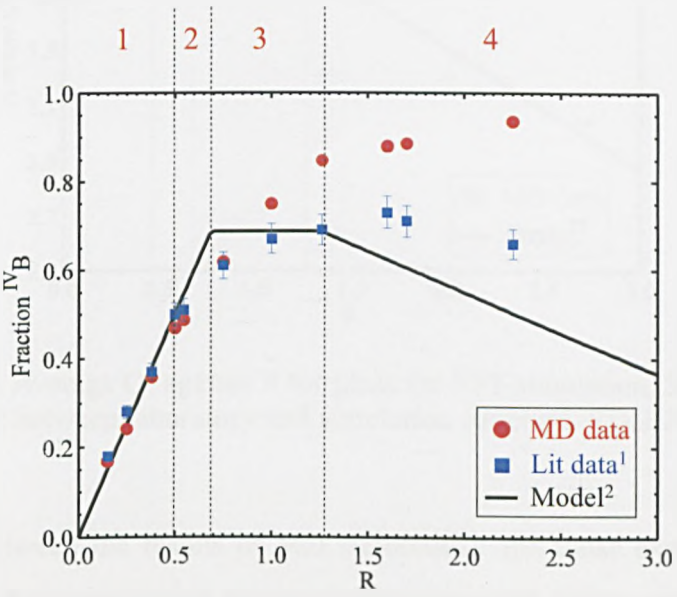

Figure 5.3: Fraction ^{IV}B against R ($[Na_2O]/[B_2O_3]$) for glass for *NVT* simulation showing good agreement between laboratory and simulation structure. [1](Rodderick2001)(±5 %), [2](Dell1983) (2σ).

The change in average Q^n with R is shown in **Figure 5.4**. Unfortunately, there are no laboratory data to compare the MD data to. However, the model of Dell and Bray (Dell *et al.* 1983) can be used for comparison. At low R, there is good agreement between model and MD data, with the Dell-Bray model predicting an initially invariant average Q^n, the MD data shows only a small decrease in average Q^n at low R (in Regions 1 and 2). This small decrease at low R is expected from the literature (see **Section 2.2.1** and (Bhasin *et al.* 1998)). The agreement between MD average Q^n and the Dell-Bray model decreases in regions 3 and 4 but follows the same trend of decreasing average Q^n with increasing R.

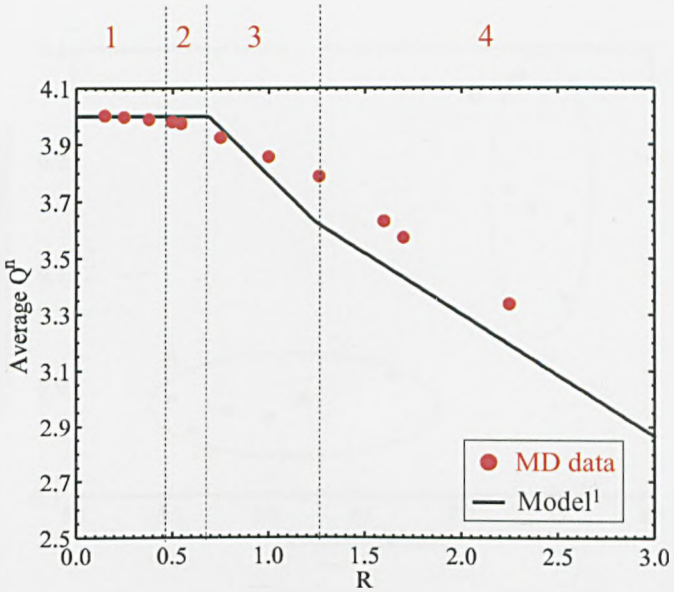

Figure 5.4: Average Q^n against *R* for glass for *NVT* simulation. Shows good agreement between laboratory and simulation structure. [1](Dell1983) (2σ).

The deviation seen between the results of MD simulations and those expected from laboratory data shown in **Figure 5.3** indicate that glasses created using the *NVT* ensemble only recreate the structure of laboratory glasses over a relatively small compositional range. An alternative ensemble that can be used for this system is the *NPT* ensemble (constant number of atoms, pressure, and temperature). This ensemble allows the simulation to reach a more "natural" volume (i.e. one defined by the potentials and atom sizes / charges). The empirical nature of the potentials used in this study means that the use of an ambient pressure would be inappropriate. This is shown in **Figure 5.5** where the pressures evolved under the NVT ensemble vary from ca. 55 and 75 kbar[1]. **Figure 5.5** shows the average pressure over 50,000 time steps at 300 K plotted against the deviation between laboratory and MD ^{IV}B fraction. The results can be divided into two clusters A and B. The assumption is made that the pressure that produced good agreement between MD and laboratory ^{IV}B fraction under the *NVT* ensemble (Cluster A) will produce an accurate ^{IV}B fraction under *NPT* conditions. Thus, the median value for the pressures found in Cluster A was taken (62 kbar).

[1] A pressure of 60 kbar is approximately equivalent to the pressure at a depth of 180 km within the Earth.

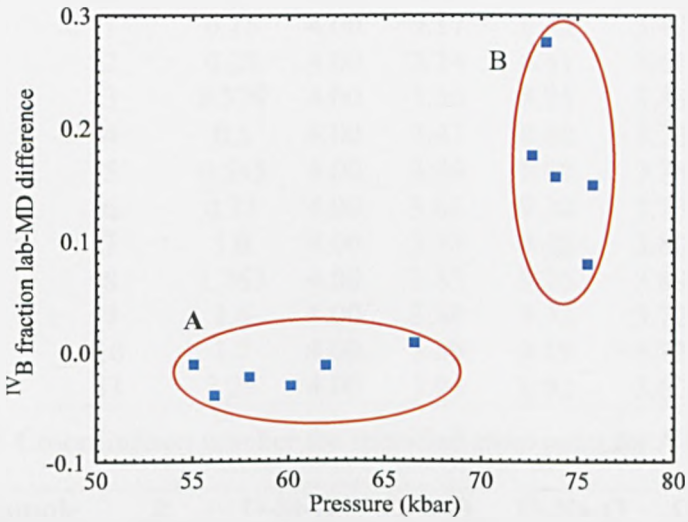

Figure 5.5: Average pressure over 50000 t. steps at 300 K. Showing two regions of pressure which differ in quality of fit to ^{IV}B data.

5.4 Some important results of NVT simulations

Table 5.1, **Table 5.2**, and **Table 5.3** show the cation-anion relationships for various parameters.

Sample	*R*	Si-O	B-O	Na-O	Li-O
1	0.15	1.58	1.37	2.85	2.10
2	0.25	1.58	1.38	2.84	2.13
3	0.379	1.58	1.39	2.86	2.13
4	0.5	1.58	1.41	2.81	2.12
5	0.545	1.58	1.41	2.83	2.12
6	0.75	1.58	1.42	2.84	2.10
7	1.0	1.57	1.44	2.82	2.09
8	1.263	1.57	1.45	2.80	2.07
9	1.6	1.57	1.45	2.78	2.04
10	1.7	1.57	1.45	2.78	2.04
11	2.25	1.57	1.46	2.75	2.01

Table 5.1: Bond distance (Å) for specified bond for *NVT* simulations.

Sample	*R*	Si-O	B-O	Na-O	Li-O
1	0.15	4.00	3.17	8.43	3.42
2	0.25	4.00	3.24	8.41	3.61
3	0.379	4.00	3.36	8.95	3.88
4	0.5	4.00	3.47	8.62	3.73
5	0.545	4.00	3.49	8.90	3.78
6	0.75	4.00	3.62	9.30	3.73
7	1.0	4.00	3.75	9.48	3.80
8	1.263	4.00	3.85	9.26	3.89
9	1.6	4.00	3.88	9.32	3.72
10	1.7	4.00	3.89	9.19	3.72
11	2.25	4.00	3.94	8.92	3.60

Table 5.2: Co-ordination number for specified atom pairs for *NVT* simulations.

Sample	*R*	O-Si-O	O-B-O	O-Na-O	O-Li-O
1	0.15	109.37	116.58	95.70	105.08
2	0.25	109.37	115.51	96.07	102.52
3	0.379	109.36	114.12	95.60	103.90
4	0.5	109.37	112.96	95.86	102.93
5	0.545	109.37	112.84	95.73	104.93
6	0.75	109.36	111.70	96.06	104.78
7	1.0	109.36	110.80	95.82	104.02
8	1.263	109.36	110.15	96.12	104.41
9	1.6	109.36	110.01	95.96	106.44
10	1.7	109.36	109.94	96.27	105.91
11	2.25	109.38	109.67	96.25	107.62

Table 5.3: Bond angles (°) for specified bond for *NVT* simulations.

5.5 Constant pressure results

Simulations using the *NPT* ensemble were carried out as shown in **Section 3.7.8**. The compositions simulated under the *NVT* ensemble are all simulated here under *NPT* allowing direct comparison between the results. **Figure 5.6** shows that there is good agreement between ^{IV}B fraction obtained under *NPT* and the laboratory data. The agreement is greatly improved over that shown under *NVT*. The agreement extends up to $R \approx 1.7$ with little divergence.

Figure 5.7 shows the change in Q^n average with *R*, the agreement between the Q^n average from MD and that from the Dell and Bray model (Dell *et al.* 1983) is similar to that seen under *NVT*. This may be due to the use of 3-body potentials on the silicate network. This effect is discussed in more detail below.

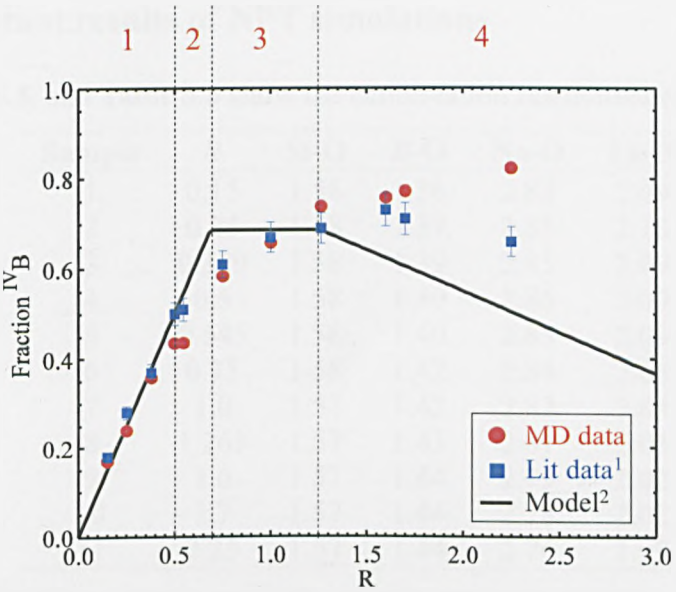

Figure 5.6: Fraction ^{IV}B against R (=[Na_2O]/[B_2O_3]) for glass for *NPT* simulation. Shows good agreement between laboratory and simulation structure. [1](Rodderick *et al.* 2007)(±5 %), [2](Dell *et al.* 1983) (2σ).

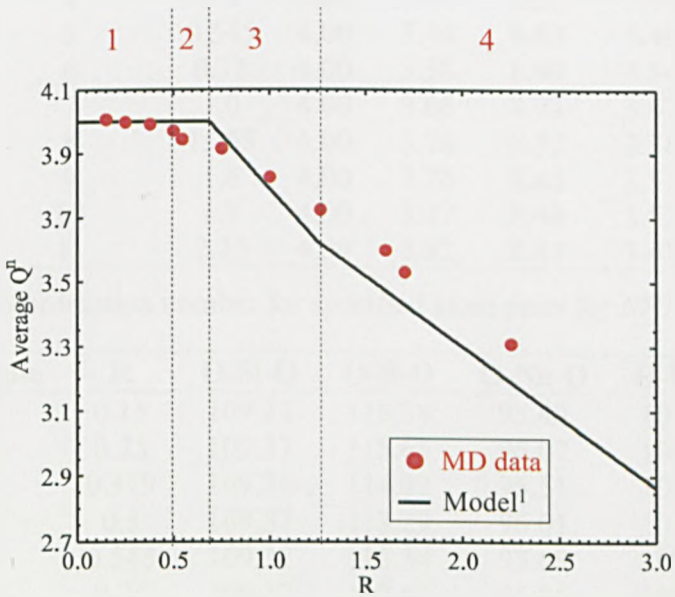

Figure 5.7: Average Q^n against R (=[Na_2O]/[B_2O_3]) for glass for *NPT* simulation. Shows good agreement between laboratory and simulation structure. [1](Dell *et al.* 1983) (2σ).

5.6 Some important results of NPT simulations

Table 5.4, Table 5.5, and **Table 5.6** show the cation-anion relationships for various parameters.

Sample	*R*	Si-O	B-O	Na-O	Li-O
1	0.15	1.58	1.36	2.83	2.09
2	0.25	1.58	1.37	2.85	2.10
3	0.379	1.58	1.39	2.85	2.09
4	0.5	1.58	1.40	2.86	2.09
5	0.545	1.58	1.40	2.83	2.09
6	0.75	1.58	1.42	2.84	2.08
7	1.0	1.57	1.42	2.82	2.04
8	1.263	1.57	1.43	2.81	2.03
9	1.6	1.57	1.44	2.79	2.02
10	1.7	1.57	1.44	2.78	2.02
11	2.25	1.57	1.44	2.76	1.99

Table 5.4: Bond distance (Å) for specified bond for *NPT* simulations.

Sample	*R*	Si-O	B-O	Na-O	Li-O
1	0.15	4.00	3.17	7.85	3.39
2	0.25	4.00	3.24	8.38	3.48
3	0.379	4.00	3.36	8.37	3.45
4	0.5	4.00	3.44	8.29	3.41
5	0.545	4.00	3.44	8.63	3.49
6	0.75	4.00	3.58	8.90	3.54
7	1.0	4.00	3.66	8.73	3.47
8	1.263	4.00	3.74	8.57	3.38
9	1.6	4.00	3.76	8.43	3.51
10	1.7	4.00	3.77	8.40	3.52
11	2.25	4.00	3.82	8.45	3.41

Table 5.5: Co-ordination number for specified atom pairs for *NPT* simulations.

Sample	R	O-Si-O	O-B-O	O-Na-O	O-Li-O
1	0.15	109.37	116.38	95.49	105.28
2	0.25	109.37	115.65	96.07	106.08
3	0.379	109.36	114.02	95.51	105.10
4	0.5	109.37	113.29	96.01	107.02
5	0.545	109.37	113.34	95.68	105.23
6	0.75	109.37	112.03	95.86	104.50
7	1.0	109.38	111.45	95.79	107.52
8	1.263	109.38	110.86	95.79	108.13
9	1.6	109.38	110.78	95.84	106.88
10	1.7	109.38	110.65	96.10	107.54
11	2.25	109.38	110.37	96.21	109.61

Table 5.6: Bond angles (°) for specified bond for *NPT* simulations.

5.7 Density and ^{IV}B fraction

The average volume for *NPT* simulations was calculated over 50,000 time steps (In the same manner as an average pressure for *NVT* simulations - see **Section 3.7.9**). Since the composition and molar mass of the sample are known (see **Section 3.7.7**), sample density can be calculated. **Figure 5.8** shows the density for the *NPT* simulations with changing composition together with laboratory densities for comparison.

The density for laboratory glasses increases with increasing R then levels off to give an approximately constant value when $1.2 < R < 2.3$. The laboratory densities follow other composition-density trends reported in the literature, if a higher R glass was produced and the density measured it would be expected that the density would begin to decrease (Feil *et al.*1990).

The MD simulations show a lower density for all compositions with increasing divergence from laboratory density with increasing R. The levelling off seen in the laboratory data is seen to a lesser extend in the MD density. However, at $R < 1.5$ the density begins again to increase. The density under *NVT* is a fixed value due to the constant volume nature of the ensemble.

The difference in density between the *NPT* and laboratory glasses may be related to the inter-atomic potentials used, the pressure, or the high cooling rate. The close similarity between densities at low R suggests it is unlikely to be a function of pressure, or cooling rate. Since inter-atomic potentials define the separation of atoms this will have a significant effect on density. However, **Table 5.4**, **Table 5.5**, and **Table 5.6** show that reasonable values for oxide bond lengths, angles and co-ordination are modelled for these glasses. This makes the sources of the difference in density difficult to ascertain.

There is an established relationship between density of borate (and borosilicate) glasses and the fraction of ^{IV}B. An increase in ^{IV}B fraction is known to give an increase in density due to the increase in co-ordination (Feil *et al.* 1997). As the fraction of ^{IV}B decreases, at around $R = 1.7$, there are several competing processes:

1. The density increase due to decreasing co-ordination of boron;
2. The density increase due to alkali addition;
3. Depolymerisation of the silicate and borate network reducing the in density.

The laboratory data demonstrate that for $1.2 < R < 2.3$ these effects cancel each other out giving a constant density. This effect is not observed for the MD *NPT* glasses. **Figure 5.9** shows that for laboratory glasses at $R < 1.5$ the density is constant but the ^{IV}B fraction decreases. The equivalent

plots are shown in **Figure 5.10** for the MD simulated glasses. These show that even where the density is fixed in the *NVT* simulations the ^{IV}B fraction increases. When the density is allowed to vary in the *NPT* simulations the density and ^{IV}B fraction follow the same trend to high *R*.

The low density shown for *NPT* simulations compared to laboratory density and the deviation in ^{IV}B at R < 1.5 shows that some aspect of the laboratory glass structure is not being reproduced within the simulations presented in this work.

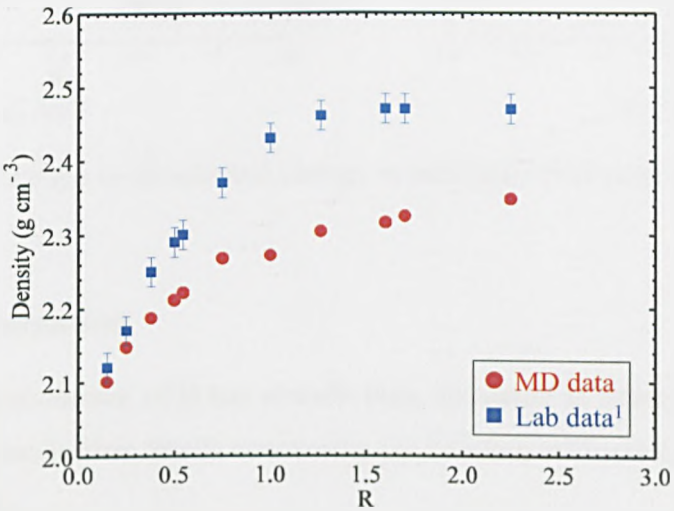

Figure 5.8: Density of *NPT* simulations comparing MD and laboratory densities. [1](Rodderick *et al.* 2007) (±0.02 gcm^{-3})(2σ).

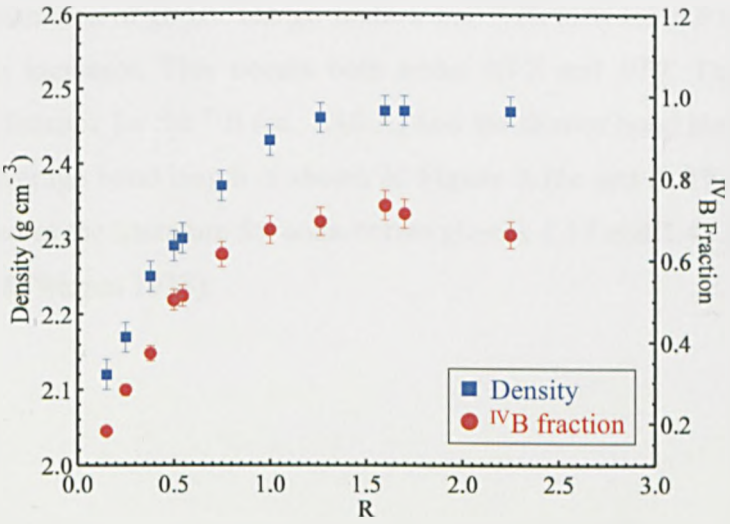

Figure 5.9: Change in density and change in measured ^{IV}B with increasing *R* from laboratory data [1](Rodderick *et al.* 2007)(±0.02 gcm^{-3}) (±5 %).

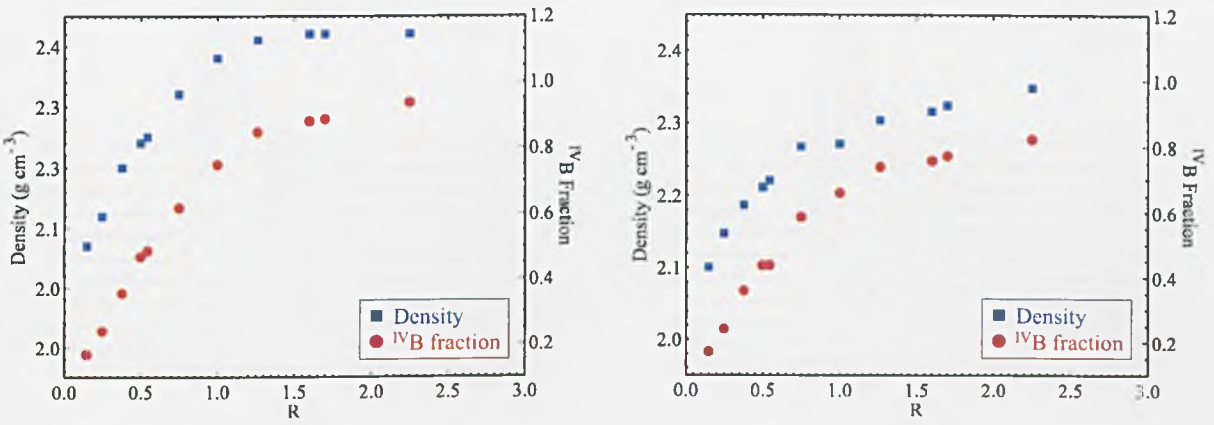

a) *NVT* b) *NPT*

Figure 5.10: Change in density and change in measured IVB with increasing *R* (2σ).

5.8 Boron co-ordination

The co-ordination environment of B has already been discussed in terms of the fraction of ^{IV}B in the glass. In this section further details concerning the bonding environment of B atoms within the glasses are presented.

5.8.1 Boron-oxygen bond distance

The stacked plots shown in **Figure 5.11a** and **b** show *g*(*r*)s for B-O between 1 and 2 Å (see **Section 3.7.9** for explanation of *g*(*r*)s). The *g*(*r*)s show that with increasing *R* the proportion of the longer bond distance increases. This occurs both under *NVT* and *NPT*. The longer B-O bond distance is the bond distance for the ^{IV}B (ca. 1.46 Å) and the shorter bond length for ^{III}B (ca. 1.34 Å). The change in average bond length is shown in **Figure 5.11c** and **d**. These bond lengths are close to those reported in the literature for soda-borate glasses 1.37 and 1.42 for ^{III}B-O and ^{IV}B-O respectively (Biscoe & Warren 1938).

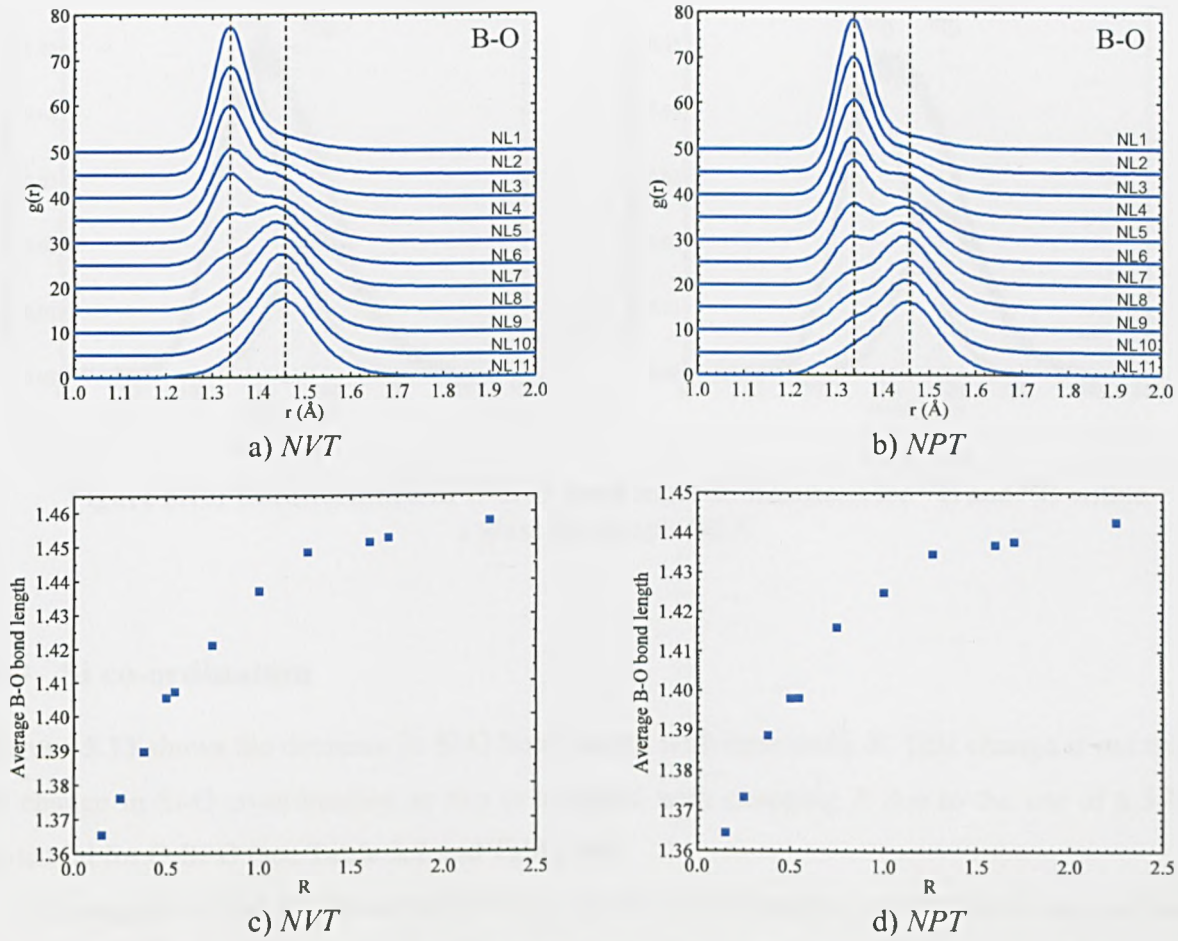

Figure 5.11: a) and b) stacked plot showing change in B-O bond length with change in *R*, with *R* increasing down the plot. c) and d) are change in average B-O bond length with *R*. Lines are as a guide to the eye only (2σ).

5.8.2 Boron-oxygen bond angles

The O-B-O bond angles for ^{IV}B and ^{III}B are well characterised in the literature (Varshneya2006) with the planar ^{III}B being taken to have a O-B-O angle of ca. 120 ° and ^{IV}B having the tetrahedral angle of ca. 109.47 °. **Figure 5.12** shows the overall bond angle distribution for O-B-O with the O-^{IV}B-O and O-^{III}B-O contributions (see **Section 3.7.9**). The average ^{III}B and ^{IV}B angles indicated in **Figure 5.12** show that the bond angles are very close to those observed in literature glasses (Varshneya 2006). Unlike the O-Si-O bond angle there is no restriction on the O-B-O bond angle in any simulation in this work (see **Section 3.7.5**). **Figure 5.12** also shows that there is no significant difference between the *NVT* and *NPT* bond angle distributions.

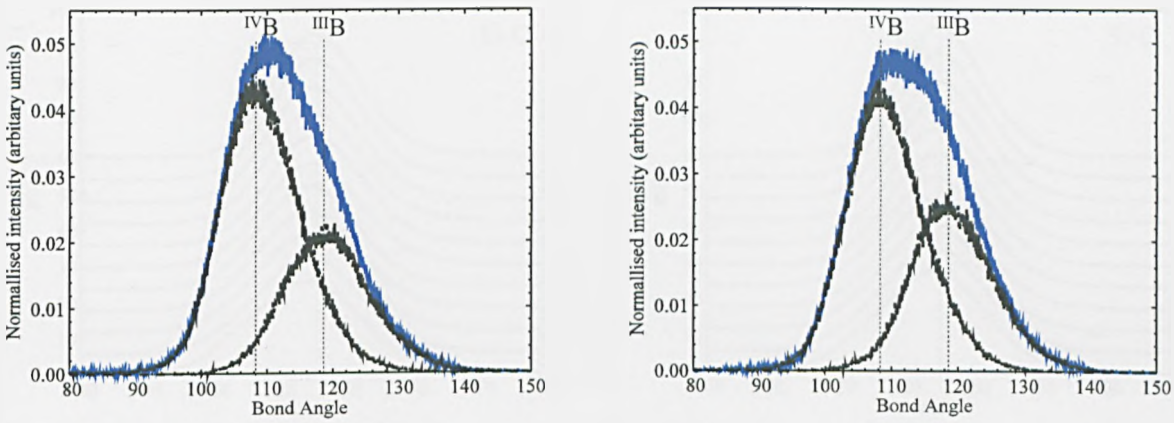

Figure 5.12: Deconvolution of O-B-O bond angle distributions for ^{IV}B and ^{III}B within a glass for sample NL5.

5.9 Si co-ordination

Figure 5.13 shows the decrease in Si-O bond length with increasing *R*. This change is not related to change in Si-O co-ordination as this is invariant with changing *R* due to the use of a 3-body potential for O-Si-O (see **Table 5.2** and **Table 5.5**).

It is suggested that the observed decrease in Si-O bond length may be due to an increase in NBOs (NBOs having a shorter Si-O bond than BOs) with increased alkali content and this supposition is supported by measurements of average Q^n (see **Section 3.4.2**). The Si-O bond length is slightly longer in the *NVT* simulations than in the *NPT* simulations, however, the trend with increasing *R* is is very similar. The reason for this difference is not known but may be related to the bond angle distributions shown in **Section 5.11**.

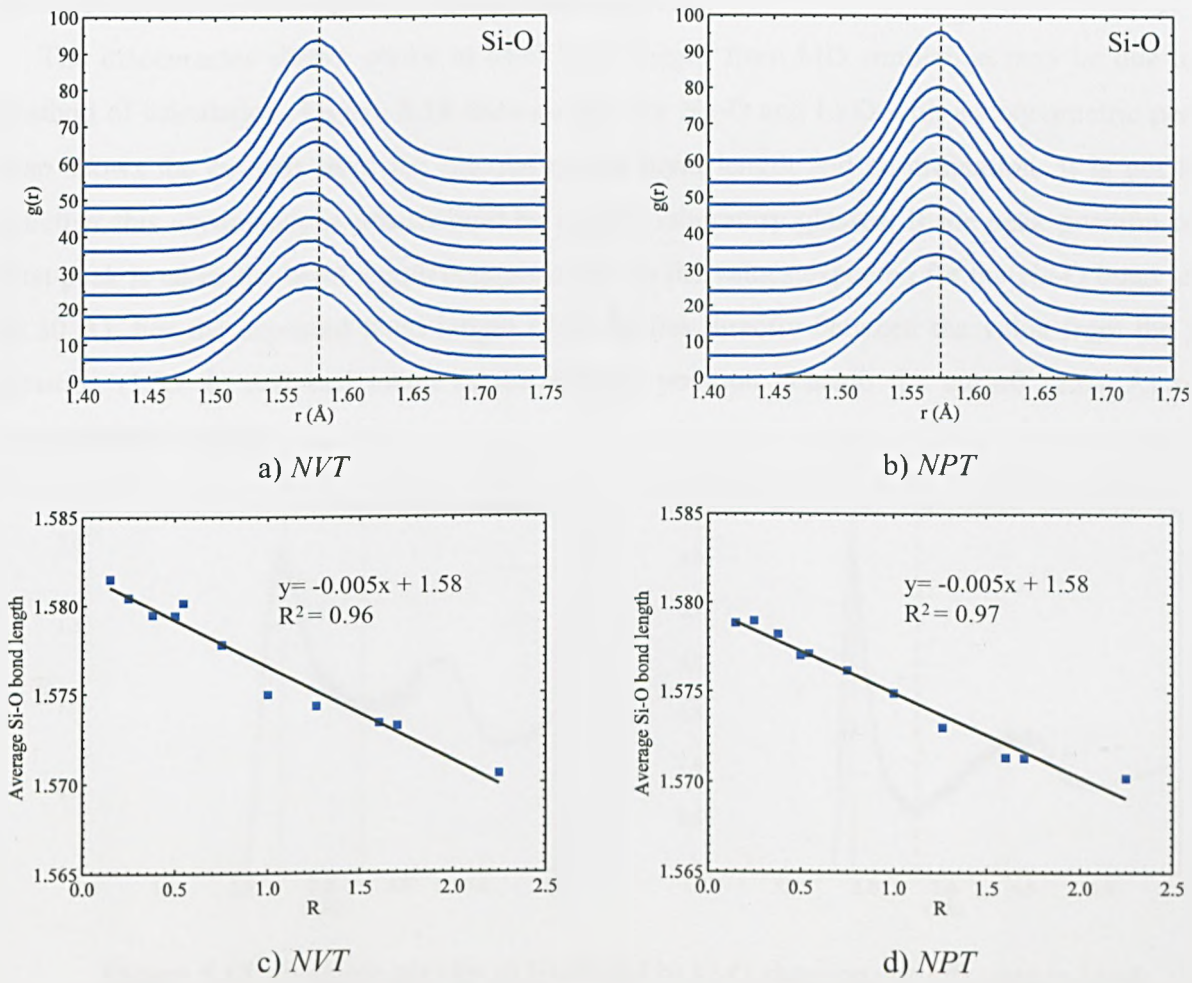

Figure 5.13: Change in Si bond length with increasing alkali content (2σ).

5.10 Alkali co-ordination

The average co-ordination, bond length and O-M-O bond angles for the alkali ions are shown in **Table 5.2** to **Table 5.5**. The average Na-O bond length is ca. 2.82 Å(σ = 0.03) and the average co-ordination number is ca. 8.72 (σ = 0.41). For Li-O the average bond length is ca. 2.07 Å(σ = 0.04) and the average co-ordination is ca. 3.59 (σ = 0.17).

For comparison values for bond length can be calculated from ionic radii[1]. The ^{VI}Na-O bond length is 2.38 Å, for ^{VIII}Na-O bond length is 2.54 Å and for ^{IX}Na-O bond length is 2.60 Å. This shows that the Na-O bond length from simulation is higher than that expected within a glass. For Li the ^{IV}Li-O bond length is 1.95 Å, no ionic radii is available for ^{III}Li. This shows that the Li-O

[1] To the authors knowledge no literature values exist for M-O bond lengths in these glasses. However, bond lengths can be calculated from addition of ionic radii of the alkali ion and $^{III}O^{2-}$. This is discussed further in **Appendix A**.

bond length measured from MD is longer than expected.

The inaccuracies shown above in M-O bond length from MD simulation may be due to the method of calculation. **Figure 5.14** shows a $g(r)$ for Na-O and Li-O with an asymmetric peak. It also shows the cut-offs used for calculating the bond length and co-ordination. It is not know whether this asymmetry is what would be seen in laboratory glasses. If the peak position of the first peak is taken the bond length become closer to the values expected for the Na-O bond length (2.50 Å). For the expected bond length (1.95 Å) lies directly between the value from the peak position (1.95 Å) and that taken as the average position beneath the cut-off (2.07 Å) so no improvement is seen.

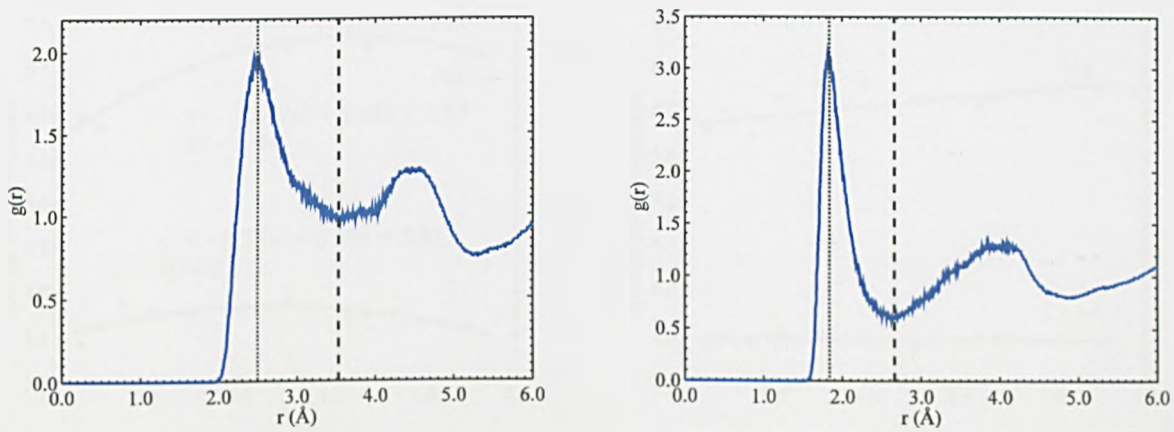

Figure 5.14: Example $g(r)$ for a) Na-O and b) Li-O showing cut-offs used in bond length and co-ordination calculations (dashed line) and position of first peak (dotted line). Sample NL-10.

The co-ordination of Na-O is larger than expected, Na is normally considered to be co-ordinated to between 6-8 oxygen ions. For Li the co-ordination number is low, normally Li is 4 co-ordinated within glasses (Volf 1984). The differences may be due to the method of measurement (see **Figure 5.14**), the atomic radii used for the potentials or the nature of the potentials themselves (see **Section 3.7.5**).

Figure 5.15 shows that there is change in both bond length and co-ordination with increasing R of the glasses. The shortening of the Na-O and Li-O bond length, with increasing R, may be governed by the number of alkali ions in a charge compensating role, where alkalis in charge compensating roles tend to have longer M-O bonds (Angeli *et al.* 2000).

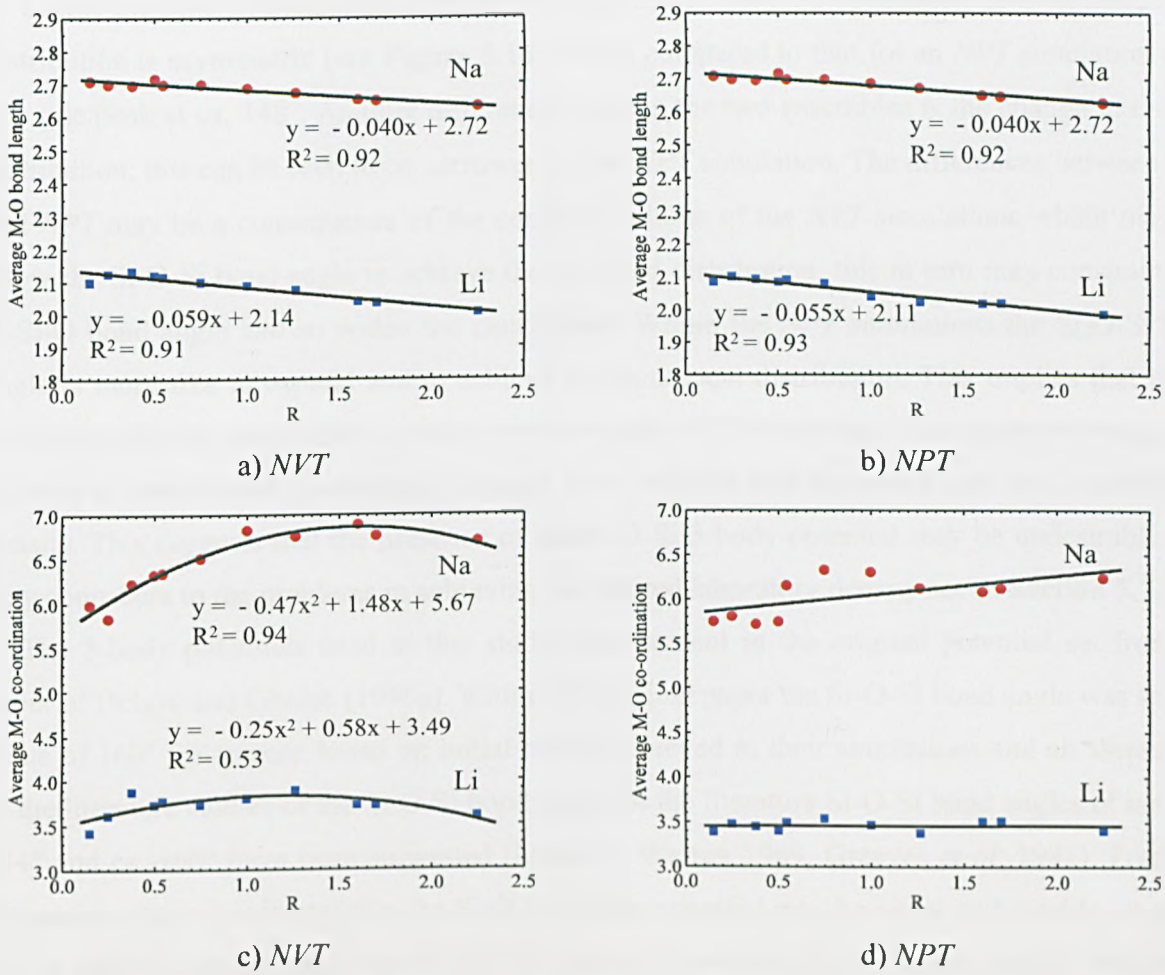

Figure 5.15: a) and b) Change in alkali oxygen bond length with increasing alkali content. c) and d) Change in co-ordination with increasing *R*. Lines shown in figures c) and d). Lines are as guides for the eye only (2σ).

5.11 Difficulties with three body potentials

The three body potentials used in this work are described in **Section 3.7.5**. They are applied to the O-Si-O bond angle and the Si-O-Si bond angle. The effect of the 3-body-potential is to reduce the distribution of bond angles and provide a driving force to make the average bond angle a specified value (this is described in more detail in **Section 2.6.3**). The strength of the applied driving force for the O-Si-O is 24 times greater than that for the Si-O-Si bond (see **Table 3.14**). This allows the Si-O-Si bond to have a wider distribution than the O-Si-O distribution (see **Figure 5.16**). There has been limited work within the literature to provide laboratory bond angle distributions for comparison to simulation distributions.

Unlike the Si-O-Si bond angles in the *NPT* simulations the *NVT* simulation Si-O-Si bond angle distribution is asymmetric (see **Figure 5.16**). When compared to that for an *NPT* simulation there is a side peak at ca. 148°. Another difference between the two ensembles is the change in O-Si-O distribution; this can be seen to be narrower for the *NPT* simulation. The differences between *NVT* and *NPT* may be a consequence of the confined volume of the *NVT* simulations which may not allow the Si-O-Si bond angle to achieve the expected distribution, this in turn may constrains the O-Si-O bond angle and so widen the distribution. Within the *NPT* simulations the Si-O-Si bond angle is more free to expand and to achieve a symmetrical distribution. This implies that the 3-body-potential has some effect on volume when under *NPT* conditions. The extension required to achieve a symmetrical distribution requires extra volume and so would lead to a decrease in density. This suggests that the presence of the Si-O-Si 3 body-potential may be undesirable as it may contribute to the problems in achieving the desired laboratory density see in **Section 5.7**.

The 3-body potentials used in this study were present in the original potential set from the paper of Delaye and Ghaleb (1996a). Within the original paper the Si-O-Si bond angle was set to a value of 160° for reasons based on initial results achieved in their simulations and an assessment of the literature studies of the Si-O-Si bond angle. In the literature Si-O-Si bond angles of both ca. 144° and ca. 160° have been suggested (Mozzi & Warren 1969, Greaves *et al.* 1981). From the discussion above it indicates that the Si-O-Si 3-body potential may be either undesirable, or of the wrong angle (a smaller angle would tend to expand the volume less). Further work is required to fully investigate this effect (see **Section 9.6**).

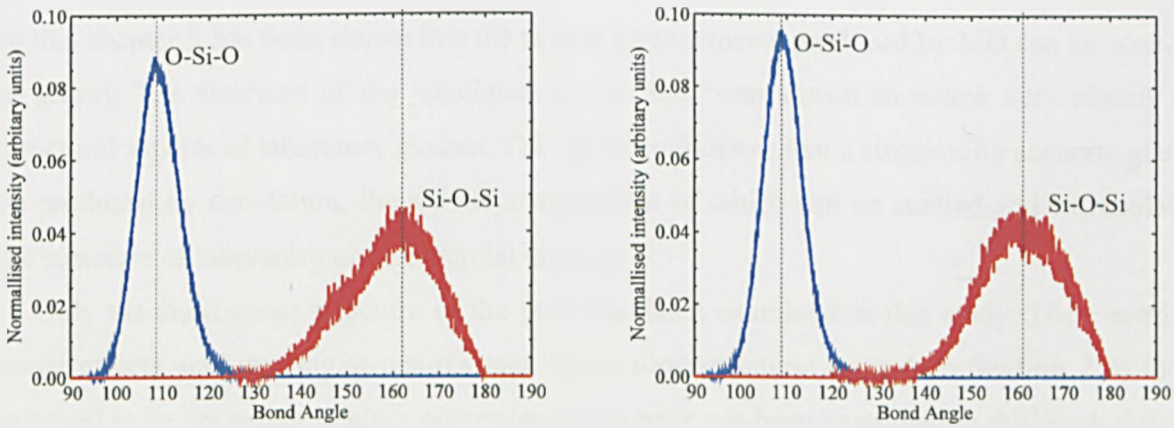

a) NVT *b) NPT*

Figure 5.16: Bond angle distributions for Si-O-Si and O-Si-O. Shows difference between different ensembles (see **Section 3.7.9** for details of the calculation).

5.12 Polymerisation of the silicate network

The level of polymerisation in the Si network is usually examined using Q^n values (see **Section 3.4.2**). The results shown in **Figure 5.4** and **Figure 5.7** are deconvoluted in **Figure 5.17** showing the proportions of Si-O-X where the X is either B or Si. It can be seen that with increasing *R* the number of Si-O-X atoms where X is B increases and the overall Q^n average decreases. This indicates greater mixing of the Si and B networks with increasing alkali content as would be expected from the literature (Du *et al.* 2003a, Du *et al.* 2003b).

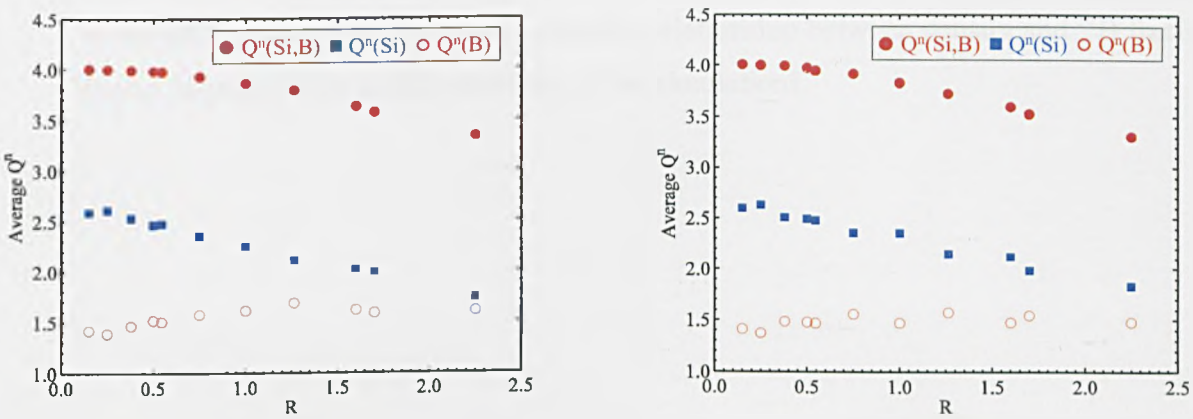

a) *NVT* b) *NPT*

Figure 5.17: Q^n averages with contributions from B and Si separated (2σ).

5.13 Chapter summary

In this chapter it has been shown that the atomic arrangements produced by MD can be considered as glassy. The structure of the simulated glasses has been shown to match very closely some structural aspects of laboratory glasses. This gives confidence that a structurally accurate glass can be produced by simulation, the atomic arrangement of which can be studied and extrapolated to the structure of laboratory or commercial glasses.

Only the short range structure of the glass has been examined in this study. There are longer range effects such as ring structures and boron superstructural units (see **Section 2.2**) that are believed to be important in glass properties which have not been examined in this work due to the complexity of these units.

For the purposes of future discussion it is important to bring out certain aspects of the structural changes with increasing alkali addition:

1. The decrease in Q^n average with increasing alkali is as a result of reduced Q^n(Si) not

$Q^n(B)$. **Figure 5.17** shows that the number of $Q^n(B)$ is approximately invariant with increasing alkali. This indicates that increased alkali increases borate and silicate network mixing;

2. The density of the glasses produced by MD is less than that produced from laboratory data, it has been suggested that this error may be related to the use of the Si-O-Si 3-body potential;
3. At high alkali levels ($R > 1.8$) the trend in ^{IV}B with increasing alkali content is not equivalent for the laboratory and MD data. There is no reduction in ^{IV}B fraction or density in the MD glasses. This indicates a possible relationship between density and ^{IV}B fraction. It also imposes limits on the reliability of the simulations.

6 Molecular Dynamic Simulations of ZrO_2 in an Alkali Borosilicate Glass

6.1 Introduction

In this chapter the results for molecular dynamic simulations of mixed alkali borosilicate glasses with added ZrO_2 will be shown. The compositions simulated and the methods used are defined in **Section 3.7.8**. The results will be presented in a similar manner to those presented in **Chapter 5**. The compositions of the glasses studied in this chapter are based on the laboratory glass compositions[1] examined in this work (see **Chapter 4**). This allows the results found in this chapter to be directly compared to the experimental results in **Chapter 4**.

Chapter 5 showed that MD is capable of producing an atomic arrangement representative of a glass. It showed that aspects of the structure of simulated glasses were very similar to those seen in laboratory glasses reported by Rodderick *et al.* (2002) and elsewhere in the literature. In this chapter a detailed analysis of ZrO_2 bearing glasses will be presented with reference to the literature and laboratory results shown in **Chapter 4**. Some shortcomings of the technique will be highlighted in **Chapter 8**, in alongside some of the advantages of modelling over laboratory experiments.

6.2 Density

The change in simulated density for both HLi and FLi glasses is shown in **Figure 6.1** (see **Section 3.7.8** for compositions). **Figure 6.1** also shows the starting density taken from laboratory results (see **Section 4.2**).

The densities for both the HLi and FLi MD glasses increase linearly with increasing ZrO_2 at a

[1] The compositions used in this chapter are those of the as-batched form. For this reason there will be small deviations in composition from MD glass to laboratory glasses. This issue will be highlighted in the text where relevant.

similar rate of change as the initial laboratory densities. However, there is a consistent difference between the MD and laboratory densities of ca. 0.17 gcm^{-3} HLi and ca. 0.18 gcm^{-3} for the FLi glass. The difference is approximately the same as that seen for the glasses in **Section 5.7** for equivalent *R* values. The change in density with increasing ZrO_2 for the laboratory and simulated glasses shows good agreement. This indicates that the difference in densities between the simulated and laboratory glasses is due primarily to base glass density; changes in density with ZrO_2 content in laboratory glasses are reproduced well in simulated glasses.

The density for the FLi glasses is consistently higher than that for the HLi glasses, this effect is discussed in **Section 4.2**.

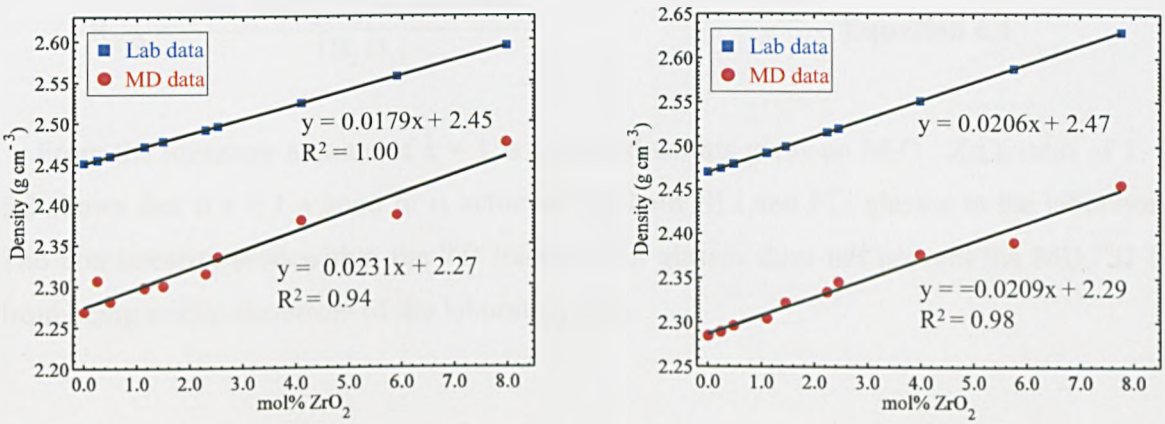

Figure 6.1: Relationship between simulated density and laboratory density (2σ).

6.3 Boron environment

The environment of B within the HLi and FLi glasses varies significantly with changing ZrO_2 content (see **Figure 6.2a**). It would be expected that increasing ZrO_2 within an alkali borosilicate glass would lead to a decrease in ^{IV}B fraction due to the requirement for charge balancing of the Zr^{4+} ion. However, as was shown in **Chapter 4** this is not necessarily the case. There is a non-linearity in the laboratory determined trend in ^{IV}B fraction with ZrO_2 content, showing an initial increase in ^{IV}B fraction at low ZrO_2 levels.

The results from MD modelling go some way to supporting the aforementioned laboratory findings and give a clearer picture (see **Figure 6.2b**). For the FLi glasses, at low ZrO_2 contents there is an increase in ^{IV}B with increasing ZrO_2 content and then, as ZrO_2 increases to >2 mol%, the ^{IV}B fraction decreases approximately linearly. For the HLi glass the result is not so clear. The

noise within the data suggests two possible trends (see **Figure 6.2a**), either a linear decrease in ^{IV}B with increasing ZrO_2 or an initial increase then a decrease at ZrO_2 content >1 mol%; similar to that seen in FLi glasses. The difference between HLi and FLi indicates that the composition of the base glass has an important effect on this trend and is discussed in more detail below.

In **Figure 6.3** the trends in ^{IV}B fractions for HLi and FLi are placed alongside those of the ^{IV}B fraction laboratory data with a recalculated R value for the ZrO_2 bearing glasses (see **Equation 6.1**). Care must be taken here as the laboratory data is for glasses where $K = 3.0$ and MD glasses have K=3.27, for this reason the Dell Bray model is expressed for $K = 3.27$, however, there is expected to be relatively little variation between $K = 3.00$ and $K = 3.27$.

$$R_{ZrO_2} = \frac{([Na_2O]+[Li_2O]-x[ZrO_2])}{[B_2O_3]} \qquad \textbf{Equation 6.1}$$

From the literature a value of $x = 1$ is expected as this gives an $M_2O : ZrO_2$ ratio of 1. **Figure 6.3** shows that if $x = 1$ a good fit is achieved for both HLi and FLi glasses to the laboratory data. The non-linearity seen within the ^{IV}B fraction FLi glasses does not prevent the MD ^{IV}B fraction from being within the errors of the laboratory data.

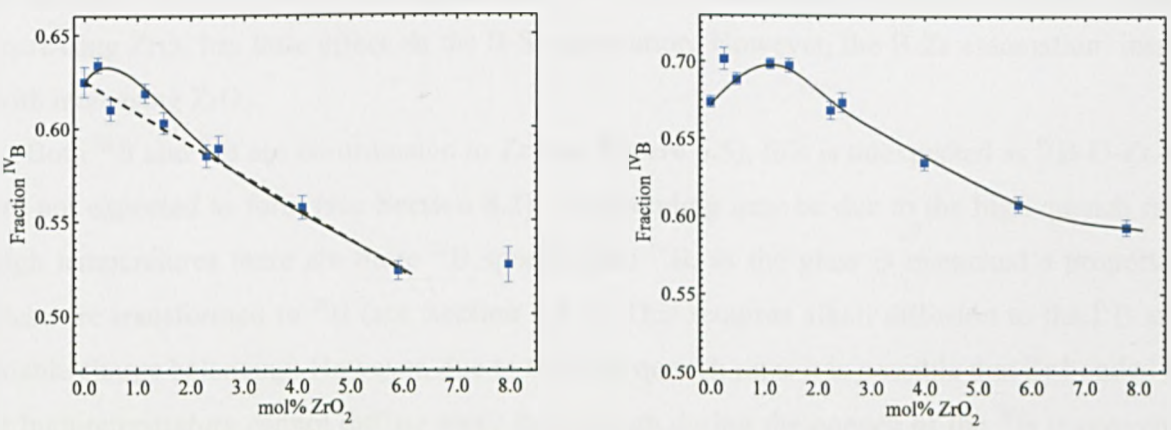

Figure 6.2: Change in simulated ^{IV}B fraction with increasing ZrO2 (2σ). Lines are as a guide to the eye only.

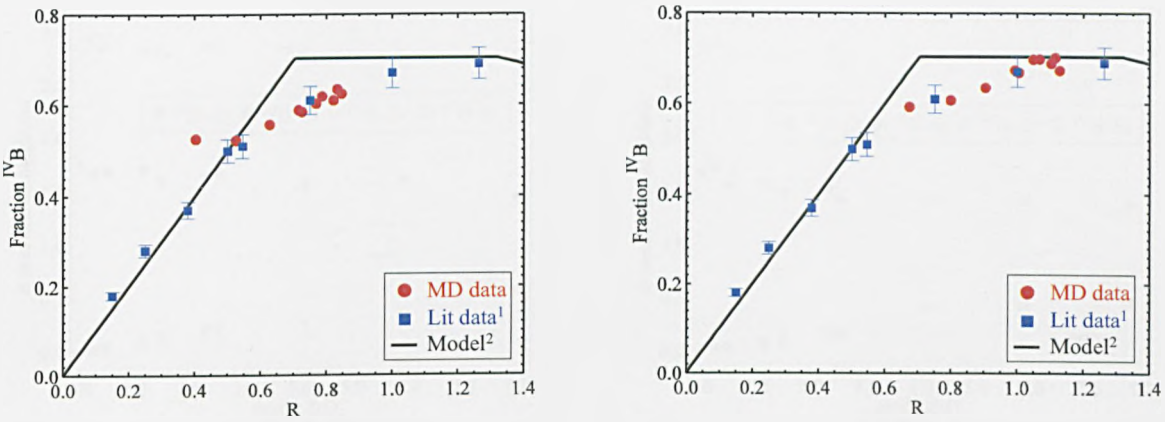

Figure 6.3: Relationship between simulated ^{IV}B fraction and laboratory ^{IV}B fraction with recalculated *R* values for varying ZrO_2 (see text for details) (2σ for simulation data). [1](Rodderick *et al.* 2001)(±5 %), and [2](Dell *et al.* 1983) with $K = 3.27$ (2σ).

6.4 Next nearest neighbour environment of boron

The next nearest neighbour environment of boron is dependent on the nearest neighbour co-ordination of B. **Figure 6.4** shows that for both HLi and FLi glasses there is a propensity for ^{IV}B to associate with Si over ^{III}B. It is also seen that ^{III}B is more likely to associate with Zr than ^{IV}B. Increasing ZrO_2 has little effect on the B-Si association. However, the B-Zr association increases with increasing ZrO_2.

Both ^{III}B and ^{IV}B are co-ordinated to Zr (see **Figure 6.5**), this is unexpected as ^{IV}B-O-Zr bonds are not expected to form (see **Section 8.2**). This bonding may be due to the high quench rate. At high temperatures there are more ^{III}B species than ^{IV}B, as the glass is quenched a proportion of these are transformed to ^{III}B (see **Section 6.9.2**). This requires alkali diffusion to the ^{IV}B sites to enable charge balancing. However, due to the high quench rates it is possible that Zr bonded to ^{III}B at high temperature cannot diffuse away fast enough during the quench as the ^{III}B is converted to ^{IV}B. This would leave some Zr bonded to ^{IV}B species. This would not be seen in laboratory data where glasses are cooled at a much lower quench rate.

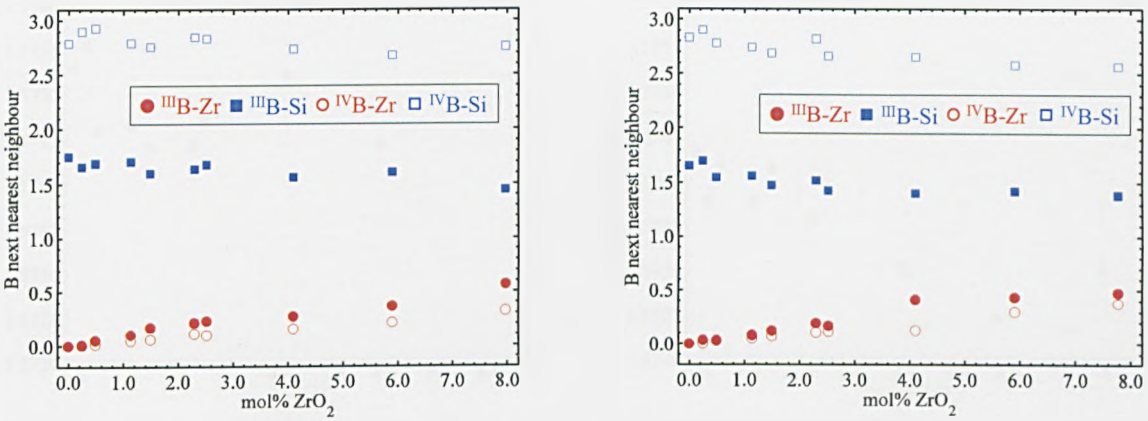

Figure 6.4: Variation in B environment depending on B co-ordination (2σ).

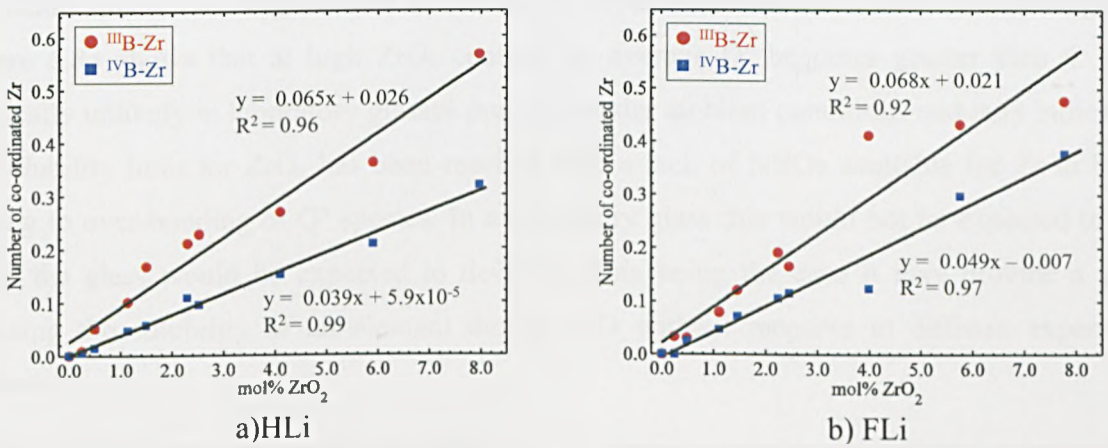

Figure 6.5: Co-ordination of ^{IV}B and ^{III}B to Zr. (2σ).

6.5 Silicon environment

The co-ordination of Si within all glasses is 4.00, as would be expected from the literature (Shelby 2005, see **Section 2.2**). As seen in **Section 5.8** a decrease in Si-O bond length suggests an increasing number of NBOs. **Figure 6.6** shows that for the HLi glass the change in Si-O bond length is very small with increasing ZrO_2 content and that there is no clear trend. For the FLi glasses there is a change in Si-O bonds length indicating that the environment of the $[SiO_4]^{4-}$ tetrahedra is changing to a much greater extent. This is explored in more detail below.

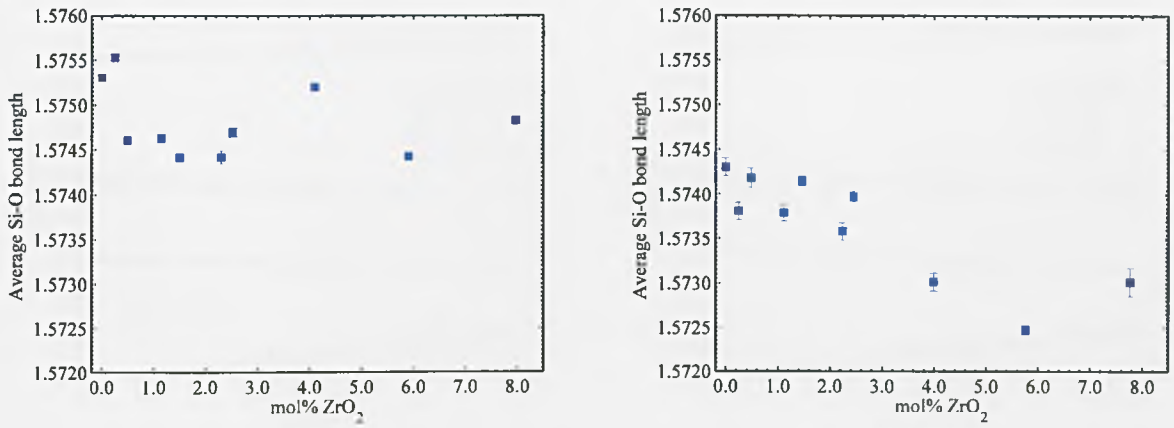

a) HLi b) FLi

Figure 6.6: Change in Si-O bond length with increasing ZrO_2 content (2σ).

The next nearest neighbour co-ordination is more complex; increasing ZrO_2 gives higher Q^n (see **Figure 6.7**). If this increase is broken down into the different contributions to the Si co-ordination sphere (see **Figure 6.8**) increasing Zr replaces Si and B as next nearest neighbours. **Figure 6.8a** shows that at high ZrO_2 content the average Q^n becomes greater than 4. This is physically unlikely in laboratory glasses prepared under ambient conditions and may indicate that the solubility limit for ZrO_2 has been reached with a lack of NBOs available for Zr to bond to leading to over-bonding of Q^n species. In a laboratory glass this would not be expected to occur, rather the glass would be expected to devitrify. This being the case it may provide a way of assessing the solubility of an element though MD without recourse to difficult experimental methods.

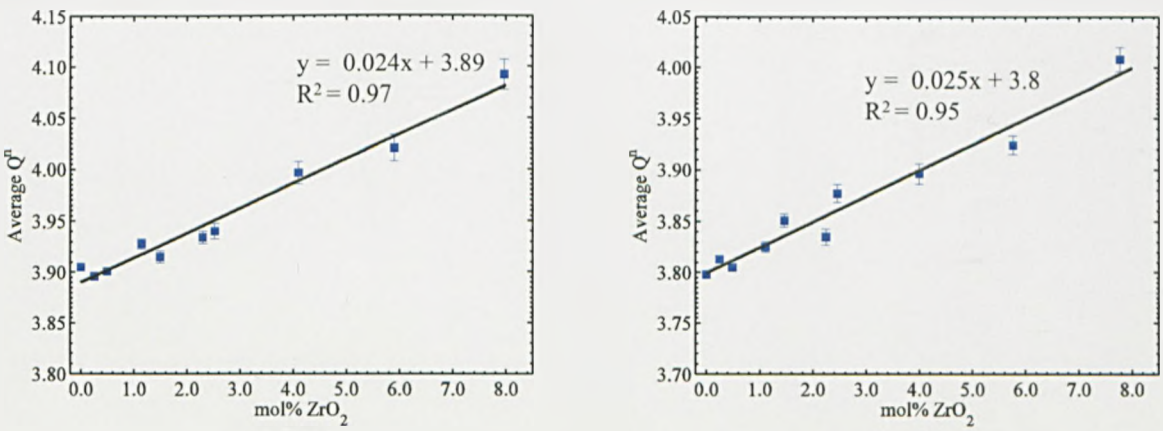

a) HLi b) FLi

Figure 6.7: Change in average Q^n with increasing ZrO_2 content (2σ).

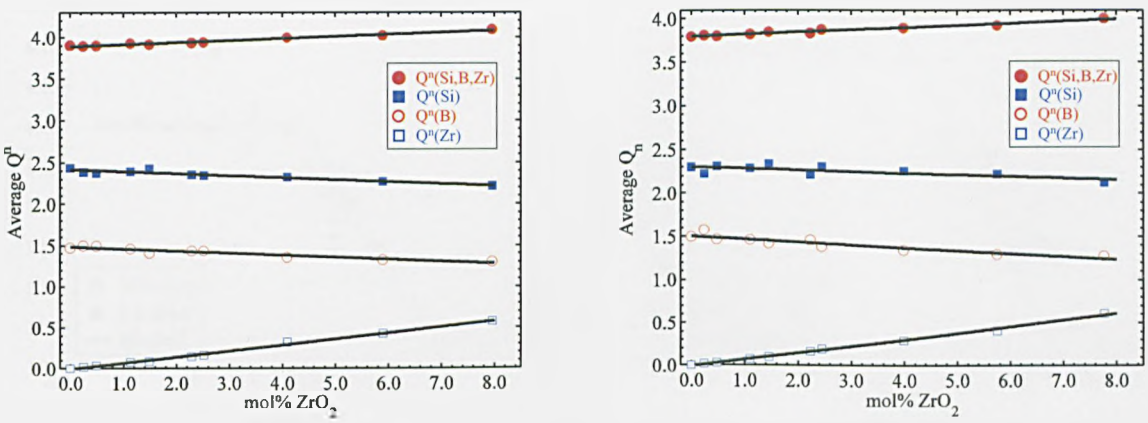

a) HLi b) FLi

Figure 6.8: Change in average Q^n with increasing ZrO_2 content (2σ).

The average Q^n values can also be compared to those taken for the *NPT* alkali addition glasses in **Chapter 5**. This can be achieved in the same way as for the ^{IV}B fraction above with a recalculation of R as shown in **Equation 6.1**. When mapping onto average Q^n there is no experimental data and so the average Q^n values from *NPT* glasses (see **Section 5.5**) are used. If a value of x=1 is used (as for the ^{IV}B fraction data above) a poor fit to the *NPT* glass Q^n average is achieved but a good fit to the Dell-Bray model is achieved (see **Figure 6.9**). If a value of $x \approx 1.5$ for the FLi glasses and $x \approx 2.0$ for the HLi glasses are used (values derived from trail and error to give the best fit) a better fit to the *NPT* glass Q^n average is achieved (see **Figure 6.10**). This difference indicates that the silicate network from the *NPT* MD simulations may not accurately reproduce a laboratory silicate network.

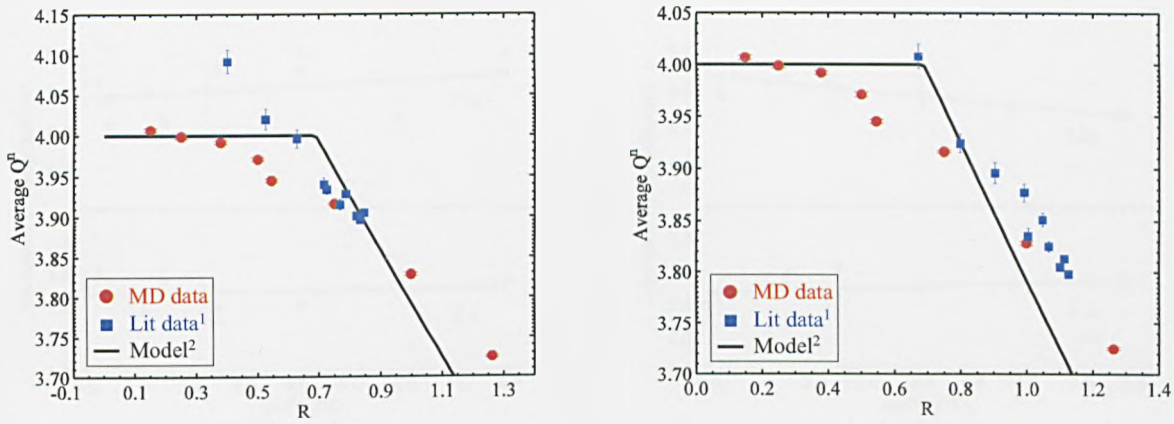

a) HLi b) FLi

Figure 6.9: Change in Q^n average with change in recalculated R (2σ). a) HLi ($x \approx 1$), and b) FLi ($x \approx 1$). [1](Rodderick *et al.* 2001) (±5 %), and [2](Dell *et al.* 1983).

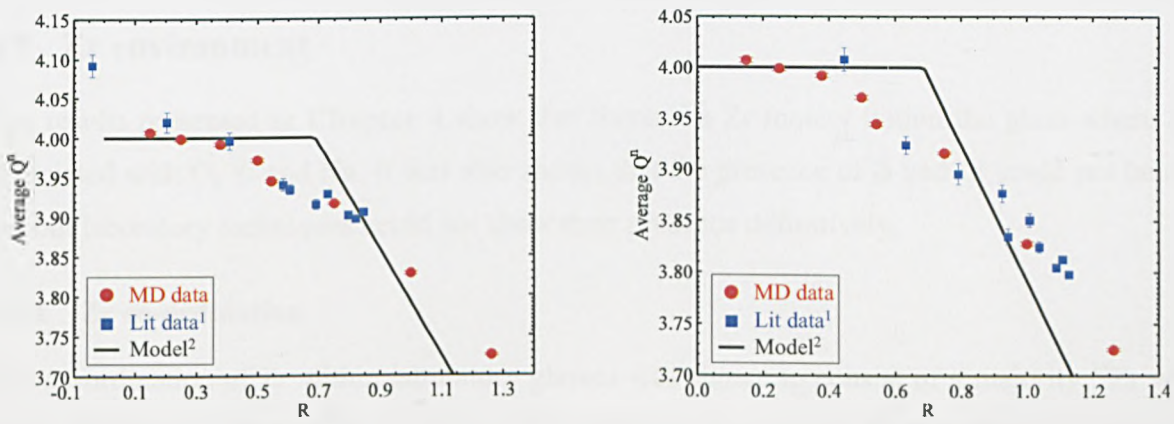

a) HLi b) FLi

Figure 6.10: Change in Q^n average with change in recalculated R (2σ). a) HLi ($x \approx 2$), and b) FLi ($x \approx 1.5$). [1](Rodderick *et al.* 2001) (±5 %), and [2](Dell1 *et al.* 983).

6.6 Alkali environment

The alkali environment in these glasses is very similar to that seen in the *NPT* glasses (see **Chapter 5).** Where the Li co-ordination was ca. 3.5 and the Na co-ordination ca. 8.6. This is a slightly larger than expected value for Na (6-8) and slightly smaller than expected value for Li (4). There is little change in alkali co-ordination with increasing ZrO_2 this may be because alkali ions associated with ZrO_2 are a small fraction of the total alkali ions in the glasses (see **Figure 6.11**).

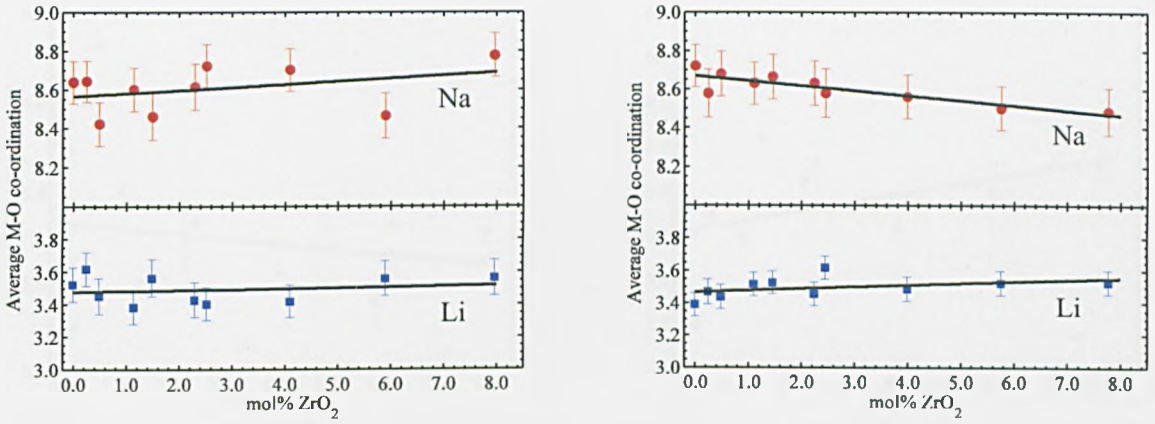

a) HLi b) FLi

Figure 6.11: Change in alkali co-ordination with increasing ZrO_2 content (2σ).

6.7 Zr environment

The results presented in **Chapter 4** show that there is a Zr moiety within the glass where Zr is associated with O, Si and Na. It was also shown that the presence of B and Li could not be ruled out but laboratory techniques could not show their presence definitively.

6.7.1 Zr co-ordination

The co-ordination of Zr within laboratory glasses was shown to consist of a majority ^{VI}Zr with a small fraction of ^{VII}Zr (or ^{VIII}Zr). Within the simulations the average Zr co-ordination was ca. 5.8 with the majority being 6 co-ordinate (see **Figure 6.13).** This co-ordination number is slightly less than that from laboratory values (see **Section 4.4.2**). The small numbers of Zr atoms within these simulated glasses makes the statistics very poor for these co-ordination values.

There is little variation in average Zr-O co-ordination with increasing ZrO_2 (see **Figure 6.12**); that which there is may be due to the low numbers of Zr atoms in the simulations and so low statistical reliability. The distribution of Zr co-ordinations is similar for all the glasses, an example can be seen in **Figure 6.13**.

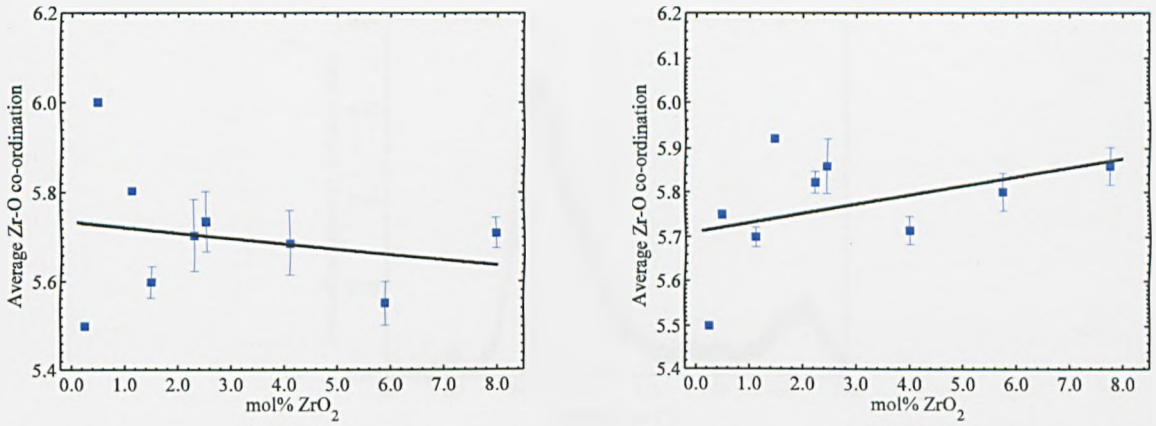

Figure 6.12: Change in Zr co-ordination with increasing ZrO_2 content (2σ). Lines are as a guide for the eye only.

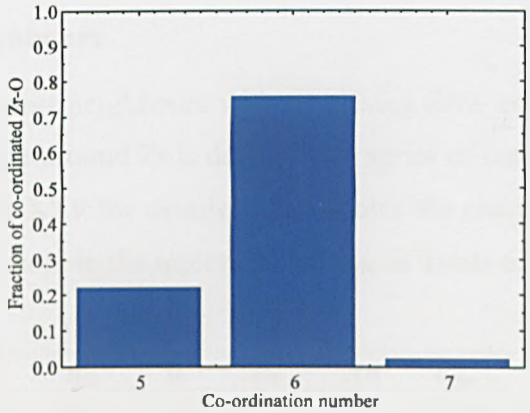

Figure 6.13: Typical distribution of Zr-O coordination FLi-H.

A typical O-Zr-O bond angle distribution is shown in **Figure 6.14**. For a regular polyhedron a O-Zr-O bond angle of 90° and 120° (for 5 co-ordinate), and 90° (for 6 co-ordinate) would be expected. The main peak is at ca. 85° showing that the environment is close to octahedral (especially as there is only a small contribution at 120°). If the co-ordination environment was a regular octahedral environment bonds at 180° would also be expected (2 x 90°). **Figure 6.14** shows some O-Zr-O bond angles at 160-170° but none at 180°. This indicates a distorted octahedral environment for the majority of the Zr atoms.

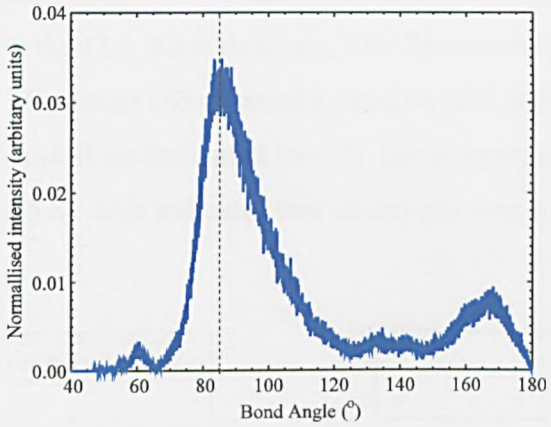

Figure 6.14: Typical O-Zr-O bond angle distribution.

6.7.2 Zr next nearest neighbours

The variation in Zr next nearest neighbours with increasing ZrO_2 content can be seen in **Figure 6.15**. The co-ordination sphere around Zr is defined as a series of cut-offs for each atom pair (e.g. Zr-O, Zr-Na etc. see **Section 3.7.9** for details). This allows the characterisation of an average Zr moiety. The number of each atom in the moiety are shown in **Table 6.1** for HLi and FLi.

	O	σ_O	Si	σ_{Si}	B	σ_B	Na	σ_{Na}	Li	σ_{Li}	Zr	σ_{Zr}
HLi	5.70	0.16	3.78	0.41	2.07	0.51	2.71	0.74	1.08	0.54	0.23	0.21
FLi	5.80	0.08	3.69	0.17	2.10	0.13	2.35	0.27	2.08	0.30	0.39	0.28

Table 6.1: Average Zr environment for glasses containing Zr.

The number of co-ordinating atoms is similar for the HLi and FLi glasses except that there is an increased number of Na ions for HLi over FLi, there is also an increased number of Li ions in the FLi glasses. The presence of less Li in the HLi Zr environment is due to the lower number of Li in the glass. The extra Na may be present to compensate for this. The total number of alkali ions is ca. 3.79 for HLi glasses and ca. 4.43 for FLi glasses. However, it is not clear whether the alkali ions are present to provide charge compensation for the Zr or the co-ordinating Si and B atoms.

The standard deviation of the values for all the elements in the environment for the HLi glasses is much higher than the FLi. This indicates that there is a much larger variation in the glass environment with addition of ZrO_2 in the HLi than FLi glasses.

Figure 6.15 shows the change in Zr-Si and Zr-B in the HLi glasses at low ZrO_2 content reflects

that seen in the ^{IV}B fraction in the HLi glasses. It might be expected that the change in Zr environment might occur in the FLi, but it does not. The Zr environment in the FLi glasses varies little with increased ZrO_2. This result seems counter intuitive and is difficult to explain.

The total number of Si and B co-ordinated to a Zr ion is approximately equal to the average number of oxygen ions (ca. 5.8). This indicates that all oxygen ions on the Zr ions are BO.

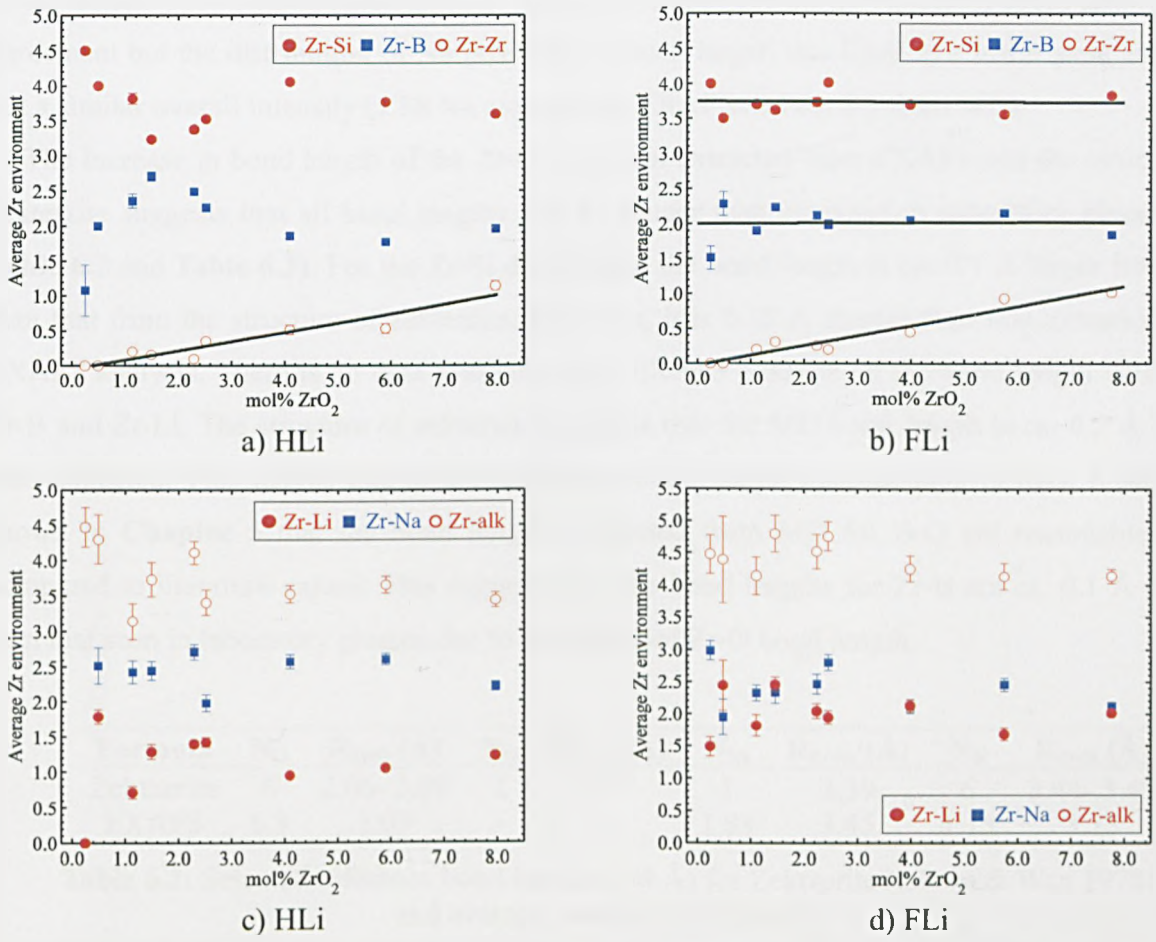

Figure 6.15: Variation of Zr environment with increasing ZrO_2 content (2σ). Lines are as a guide to the eye only.

6.7.3 Comparison with XAS

The magnitude FT plot that is generated from EXAFS analysis is not a simple RDF since there are many other contributions such as phase shifts and multiple scattering effects (see **Section 3.5.2**). For this reason it is not possible to directly compare a $g(r)$ and an EXAFS magnitude FT plot. However, the results of EXAFS analysis (see **Section 3.5.2**) can be represented as a modified $g(r)$

with distributions assumed to be Gaussian. This allows EXAFS and MD data to be compared on the same plot (see **Appendix F** for details).

Figure 6.16 shows the $g(r)$ for all the Zr-X pairs within the FLi-G glass and EXAFS data (see **Table 6.2**) for plotted for the Fli-4 (equivalent glasses). B, Li, and Zr data are not available from the EXAFS fits and so has not been included. The agreement between the EXAFS and MD data for the Zr-O distributions agrees well with a slightly longer bond distance (ca. 0.1 Å), and slightly lower intensity for the simulated glasses. The bond lengths for the Zr-Na distributions shows good agreement but the distribution of Na positions is much larger, this leads to a lower peak intensity but a similar overall intensity (1.88 Na atoms from EXAFS and ca. 2.5 from MD)

The increase in bond length of the Zr-O over than extracted from EXAFS and the structure of zekterzite suggests that all bond lengths will be longer than expected in laboratory glasses (see **Table 6.2** and **Table 6.3**). For the Zr-Si distribution the bond length is ca. 0.1 Å larger from MD than that from the structure of zekterzite. However, it is 0.18 Å shorter than that extracted from EXAFS analysis. There is no data available from EXAFS analysis on the bond length values for Zr-B and Zr-Li. The structure of zekterzite suggests that the MD bond length is ca. 0.2 Å longer than expected. This maybe due to the method of bond length measurement in MD. It has been shown in **Chapter 5** that the bond lengths extracted from MD for B-O are reasonable when compared to literature values. This suggests that the bond lengths for Zr-B are ca. 0.1 Å greater than that seen in laboratory glasses due to the extended Zr-O bond length.

Formula	N_O	$R_{Zr\text{-}O}$ (Å)	N_{Li}	$R_{Zr\text{-}Li}$ (Å)	N_{Na}	$R_{Zr\text{-}Na}$ (Å)	N_{Si}	$R_{Zr\text{-}Si}$ (Å)
Zektzerite	6	2.06- 2.09	2	2.97	1	3.39	6	3.44- 3.49
EXAFS	6.3	2.09	-	-	1.88	3.45	1.15	3.73

Table 6.2: Selected reference bond lengths (<4 Å) for Zektzerite (Ghose & Wan 1978) and average results from EXAFS.

	O	σ_O	Si	σ_{Si}	B	σ_B	Na	σ_{Na}	Li	σ_{Li}
HLi	2.17	0.69	3.56	0.02	3.32	0.05	3.64	0.07	3.27	0.04
FLi	2.18	0.01	3.55	0.02	3.31	0.03	3.69	0.07	3.30	0.10

Table 6.3: Average bond lengths (Å) in Zr environment for glasses containing Zr.

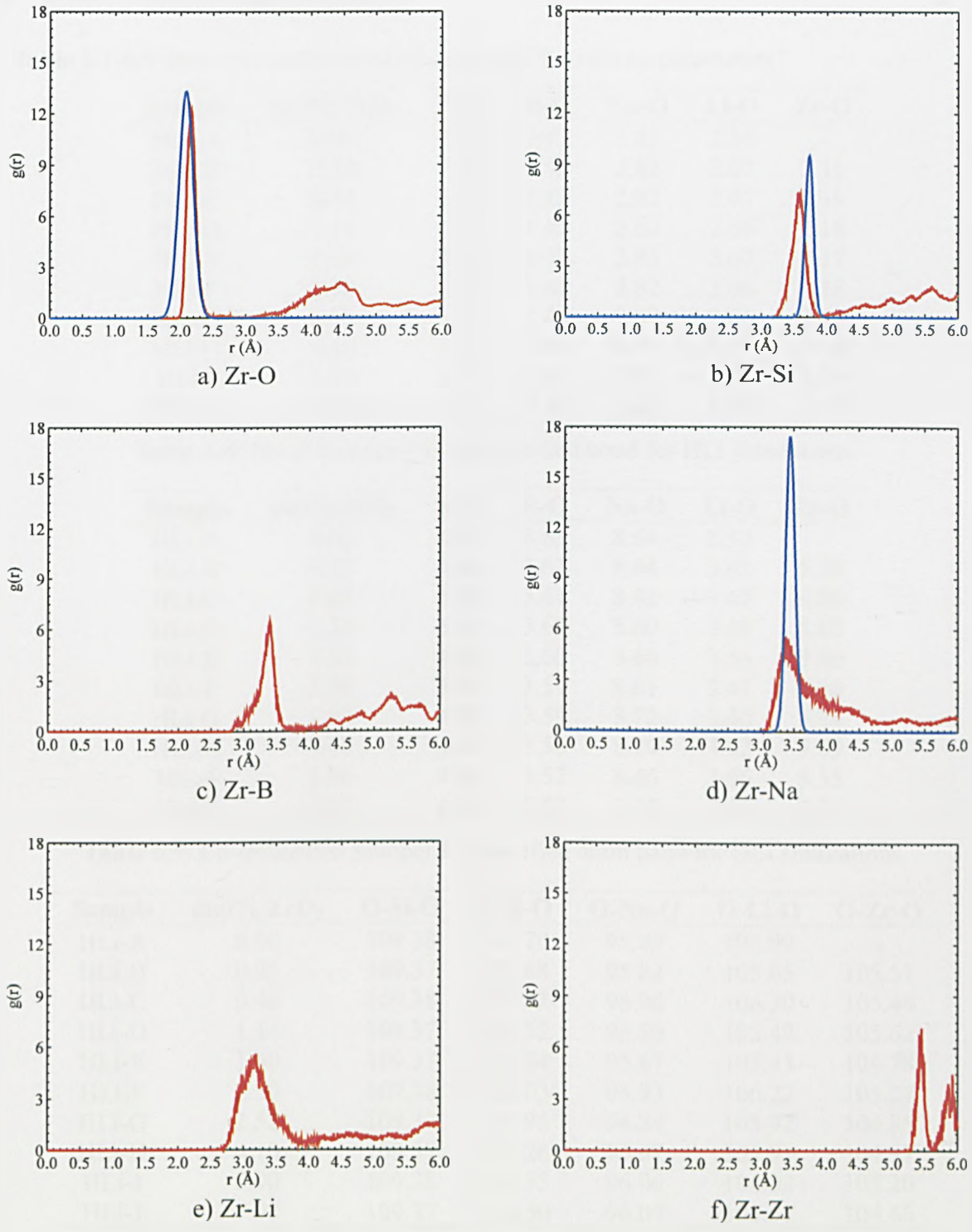

Figure 6.16: Deconvoluted combined $g(r)$ for Zr pairs, where red shows MD result and blue shows data extracted from EXAFS results.

6.8 Glass structure parameters

Table 6.1-6.9 show the cation-anion relationships for various parameters.

Sample	mol% ZrO_2	Si-O	B-O	Na-O	Li-O	Zr-O
HLi-A	0.00	1.58	1.42	2.83	2.05	-
HLi-B	0.25	1.58	1.42	2.82	2.07	2.15
HLi-C	0.49	1.57	1.42	2.82	2.07	2.19
HLi-D	1.14	1.57	1.42	2.82	2.06	2.18
HLi-E	1.50	1.57	1.42	2.83	2.07	2.17
HLi-F	2.30	1.57	1.42	2.82	2.06	2.18
HLi-G	2.52	1.57	1.42	2.82	2.06	2.18
HLi-H	4.10	1.58	1.41	2.81	2.07	2.18
HLi-I	5.90	1.57	1.41	2.81	2.07	2.16
HLi-J	7.97	1.57	1.41	2.82	2.08	2.18

Table 6.4: Bond distance (Å) for specified bond for HLi simulations.

Sample	mol% ZrO_2	Si-O	B-O	Na-O	Li-O	Zr-O
HLi-A	0.00	4.00	3.63	8.64	3.52	-
HLi-B	0.25	4.00	3.63	8.64	3.62	5.50
HLi-C	0.49	4.00	3.61	8.42	3.45	6.00
HLi-D	1.14	4.00	3.62	8.60	3.38	5.80
HLi-E	1.50	4.00	3.60	8.46	3.56	5.60
HLi-F	2.30	4.00	3.59	8.61	3.43	5.70
HLi-G	2.52	4.00	3.59	8.72	3.40	5.74
HLi-H	4.10	4.00	3.56	8.70	3.42	5.69
HLi-I	5.90	4.00	3.52	8.46	3.56	5.55
HLi-J	7.97	4.00	3.53	8.78	3.56	5.71

Table 6.5: Co-ordination number for specified atom pairs for HLi simulations.

Sample	mol% ZrO_2	O-Si-O	O-B-O	O-Na-O	O-Li-O	O-Zr-O
HLi-A	0.00	109.38	111.70	95.89	105.99	-
HLi-B	0.25	109.37	111.68	95.82	105.65	105.51
HLi-C	0.49	109.38	111.82	95.90	106.30	105.40
HLi-D	1.14	109.37	111.72	95.80	105.49	105.62
HLi-E	1.50	109.37	111.84	95.67	105.43	104.78
HLi-F	2.30	109.38	112.03	95.93	106.22	105.27
HLi-G	2.52	109.37	111.95	96.29	105.92	104.85
HLi-H	4.10	109.37	112.26	96.07	105.91	104.97
HLi-I	5.90	109.38	112.55	96.06	104.02	105.20
HLi-J	7.97	109.37	112.50	96.09	105.57	104.66

Table 6.6: Bond angles (°) for specified bond for HLi simulations.

Sample	mol% ZrO_2	Si-O	B-O	Na-O	Li-O	Zr-O
FLi-A	0.00	1.57	1.43	2.82	2.03	-
FLi-B	0.24	1.57	1.43	2.83	2.05	2.16
FLi-C	0.48	1.57	1.43	2.82	2.04	2.16
FLi-D	1.11	1.57	1.43	2.82	2.04	2.18
FLi-E	1.46	1.57	1.43	2.82	2.06	2.18
FLi-F	2.24	1.57	1.43	2.83	2.05	2.18
FLi-G	2.45	1.57	1.43	2.82	2.06	2.18
FLi-H	3.99	1.57	1.42	2.82	2.06	2.18
FLi-I	5.75	1.57	1.42	2.81	2.06	2.18
FLi-J	7.77	1.57	1.41	2.82	2.07	2.18

Table 6.7: Bond distance (Å) for specified bond for FLi simulations.

Sample	mol% ZrO_2	Si-O	B-O	Na-O	Li-O	Zr-O
FLi-A	0.00	4.00	3.67	8.72	3.39	-
FLi-B	0.24	4.00	3.73	8.58	3.47	5.50
FLi-C	0.48	4.00	3.69	8.68	3.44	5.75
FLi-D	1.11	4.00	3.70	8.63	3.52	5.70
FLi-E	1.46	4.00	3.70	8.66	3.53	5.92
FLi-F	2.24	4.00	3.70	8.63	3.46	5.82
FLi-G	2.45	4.00	3.67	8.58	3.62	5.86
FLi-H	3.99	4.00	3.64	8.56	3.49	5.72
FLi-I	5.75	4.00	3.61	8.50	3.52	5.80
FLi-J	7.77	4.00	3.59	8.49	3.53	5.86

Table 6.8: Co-ordination number for specified atom pairs for FLi simulations.

Sample	mol% ZrO_2	O-Si-O	O-B-O	O-Na-O	O-Li-O	O-Zr-O
FLi-A	0.00	109.37	111.34	96.14	106.95	-
FLi-B	0.24	109.37	110.96	95.74	105.66	106.65
FLi-C	0.48	109.38	111.21	95.59	106.39	105.93
FLi-D	1.11	109.38	111.17	96.19	106.15	104.93
FLi-E	1.46	109.37	111.16	96.03	105.26	104.76
FLi-F	2.24	109.37	111.33	95.79	106.62	104.35
FLi-G	2.45	109.37	111.28	95.85	106.25	105.03
FLi-H	3.99	109.38	111.64	95.83	105.87	104.86
FLi-I	5.75	109.38	111.82	96.03	105.65	105.02
FLi-J	7.77	109.38	111.97	95.94	104.57	104.52

Table 6.9: Bond angles (°) for specified bond for FLi simulations.

6.9 Effect of high temperature on glass

6.9.1 Co-ordination of Zr

The co-ordination of Zr within these glasses changes very little with increasing temperature (see

Figure 6.17). The variation in Zr-O co-ordination increases with increasing temperature.

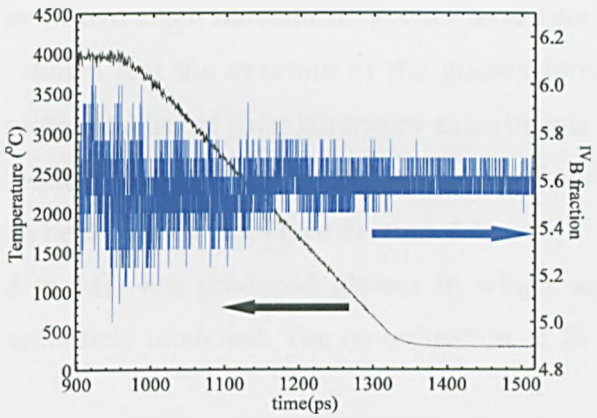

Figure 6.17: Change in Zr-O co-ordination and temperature with time.

6.9.2 Environment of B

A key advantage of using borosilicate glasses over silicate glasses is that the co-ordination environment of B changes with temperature (see **Section 2.2.1**) with more ^{III}B at high temperature giving a less polymerised network and so lower viscosity. This allows relatively low temperature processing of the glass.

Figure 6.18 shows the effect of temperature in the simulations. Although the temperature of the "melt" is much greater than that used in the laboratory the co-ordination clearly increases with decreasing temperature.

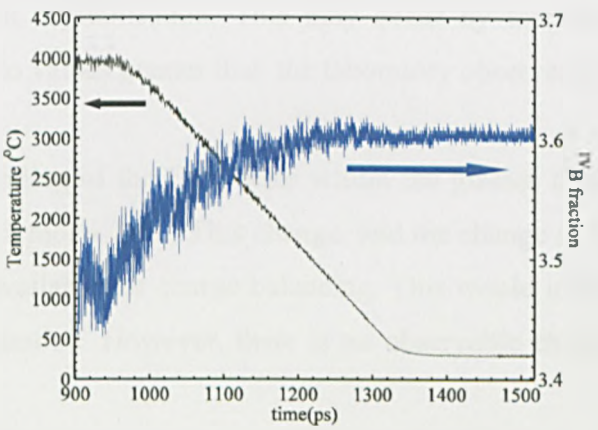

Figure 6.18: Change in B-O co-ordination and temperature with time

6.10 Chapter summary

The changes in the structure of two alkali borosilicate glasses have been examined with changing ZrO_2 content. It has been shown that the structure of the glasses formed from MD simulation matches well with the structure established from laboratory experiments. This allows more details of the glass structure to be established. The number and location of B and Li in the Zr moiety have been shown which could not be shown by XAS (see **Section 4.4**).

The rapid quench used in MD has produced glasses in which some laboratory discerned structural aspects are not accurately modelled. The co-ordination of Zr-O-^{IV}B is not expected in these glasses.

The polymerisation of the silicate network within both the HLi and FLi glasses increases with increasing mol% ZrO_2. This is due to the formation of Q^n(Zr) units. In the HLi glasses at high mol % ZrO_2 the silicate tetrahedra become over bonded with average $Q^n > 4$. There are several possible explanations of this:

1. The rapidity of the quench giving a high temperature structure which may allow overly co-ordinated silicate tetrahedra;
2. The low density of the glasses means that the Q^n units are not confined as they would be within a more dense glass. This allows the formation of higher than Q^4 species;
3. The solubility limit of the ZrO_2 within these alkali borosilicate glasses has been reached. In a laboratory glass this would lead to devitrification of the glass with the formation of Zr bearing crystals. However, the high cooling rate in borosilicate glasses makes crystal formation unlikely. Thus, the glass structure must adapt to accommodate extra ZrO_2 without crystallisation. This may occur by increasing the co-ordination of silicate tetrahedra to values greater than the laboratory observed 4.

Alongside the over bonding of the Q^n species within the glasses there is also a change in the trend in ^{IV}B fraction at high mol% ZrO_2. This change, and the change in Q^n, suggests that there are no longer enough alkali available for charge balancing. This would indicate that the ZrO_2 can no longer find alkali compensation. However, there is no observable change in the environment of the Zr at this ZrO_2 level.

If the solubility limit has been reached approximate solubility values can be extracted from and for the FLi and HLi glasses. Although more data points would be needed to get exact values it is clear that for the HLi glasses the solubility limit is between 5.9 and 8 mol% which is

equivalent to between 10 and 15 wt%. However, the deviation from the expected trend occurs closer to the lower limit of these values suggesting a solubility of ca. 11 wt% in the HLi glass. In the FLi glass the deviation has only just begun at 7.8 mol% which is equivalent to 15 wt%. These values are consistent with those shown in **Table 2.3**. Laboratory glasses were only produced up to ZrO_2 of ca. 4 mol% (ca. 8 wt%) due to the high melting temperatures required (see **Section 3.1.1**). The solubility in the FLi glass is higher than that in the HLi glass which is expected due to the higher alkali content of the FLi glass.

As calculated from the ^{IV}B fraction **Figure 6.3** has shown that the addition of one mole of ZrO_2 to the FLi and HLi glasses removes 1 mole of M_2O (where M represents Na or Li) from the glass network. From the Q^n average two different results have been achieved (see **Figure 6.9** and **Figure 6.10**). An x value of 1 produces a good fit to the Dell-Bray model whereas a value of x between ca. 2 (FLi) and ca. 1.5 (HLi) produces a good fit to *NPT* glass Q^n average.

This indicates that the number of moles of alkali oxide required to charge compensate the addition of ZrO_2 is between 1 and 2. Laboratory experimental evidence from Watson (Watson1979) suggests that 2 moles of M_2O (where M represents Na or K) are required to charge balance one mole of ZrO_2. However, these glasses where formed under unusual conditions (see **Section 2.4.1**). Other laboratory evidence under more standard conditions shows that only 1 mole of alkali oxide is required (see **Section 2.4.1**)(Ellison & Hess 1994a). This is discussed more in **Chapter 8.**

7 Structure and Properties of U within a Borosilicate Waste Glass

7.1 Introduction

This Chapter presents the results of an investigation into the structure and properties of glasses bearing UO_3 and other elements of importance to the HAST waste stream (see **Section 2.1.3**). The motivation here is to study the fundamental effects of this waste stream on the structure of an alkali borosilicate glass, and its effect on various properties. The eventual aim being a more complete understanding of the system and so improved vitrification possibilities.

The composition of this waste stream is unusual due to the high U, Al, Fe and Cr content (see **Appendix B**). The difficulties involved in a complete study of a waste stream of this complexity means this work only deals with a simplified waste stream. It will concentrate on the effect of U on glass properties with the effect of Cr, Fe on redox also being shown. Al has not been investigated as its effect on glass structure and properties has been well characterised (Volf 1984). This chapter is set out in a similar manner to **Chapter 5** where initially physical, and structural (including redox) properties are presented followed by the results of limited durability studies. At the end there is a discussion of the results presented, with further discussion in **Chapter 8** of how the results correspond to those from other chapters. An up-to-date literature review for the effect of U, Cr and Fe on these glasses is presented in **Section 2.4**. A full list of the compositions studied can be found in **Table 3.4** and **Appendix B**. The composition of the base glass used here is the same as that used for the FLi series in the ZrO_2 glasses (**Chapter 4** and **6**) allowing direct comparison.

7.2 Density

The increase in density with addition of UO_3 is to be expected due to the high Relative Atomic Mass (RAM) of U. **Figure 7.1** shows that addition of UO_3 to the glass gives a linear increase in

density. The change in density is significant, a similar plot for ZrO_2 additions (see **Figure 4.1**) gives a line of best fit with equation y = 0.021x + 2.47. This shows that although the atomic weight of UO_3 (ca. 271 $gmol^{-1}$) is only 2.2 times greater than that for ZrO_2 (ca .123 $gmol^{-1}$) the rate of increase in density is 3 times greater. This suggests that the addition of ZrO_2 to the glass has the effect of rearranging the glass structure more than UO_3 giving a lower density increase per ZrO_2 addition.

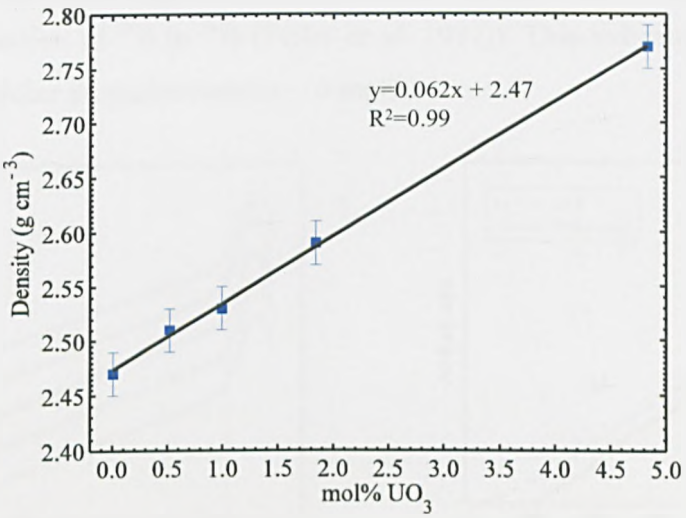

Figure 7.1: Density of glass with increasing UO_3 content.

7.3 Thermomechanical properties

The equipment available for analysis of T_g and other thermal properties of UO_3 bearing glasses did not allow DTA data to be collected, due to the potential for radioactive contamination (see **Section 3.2**). However, the use of dilatometry allowed T_g values to be obtained for UO_3 bearing glasses. Dilatometric data were collected and analysed as set out in **Section 3.6.1**. At least two specimens of each sample were measured (see below) and averaged. The nature of the glass transition allows T_g generated from dilatometry to be directly compared to that from DTA. To confirm this DTA and dilatometry data for U-0 glass (a non active glass - see **Figure 7.2a**), give values for T_g of 508 °C and 508 °C (± 1 °C) respectively. A stack plot of data collected for glasses with different UO_3 contents is shown in Figure **7.2b.**

T_g appears to decrease with increasing UO_3 content, although the absolute decrease is relativity small (ca. 10 °C) (see **Figure 7.3**). This effect is also seen in values for the dilatometric softening

point. Dilatometric softening point is an indication of viscosity, the small changes seen in these data (ca. ± 25 °C) support viscosity data presented by Jantzen (Jantzen2005) which show minimal changes with increasing UO_3.

In a silicate glass a decrease in T_g would normally be expected with addition of a modifier to the glass due to the decrease in network connectivity. In a borosilicate glass the situation is more complex due to changes in the B co-ordination (Feller *et al.* 1997). However, taking the composition of the base glass into consideration, an increase in alkali should lead to an increase in T_g (due to transformation of ^{III}B to ^{IV}B (Feller *et al.* 1997)). This indicates that the effect of UO_3 may not be as a modifier at concentrations < 5 mol%.

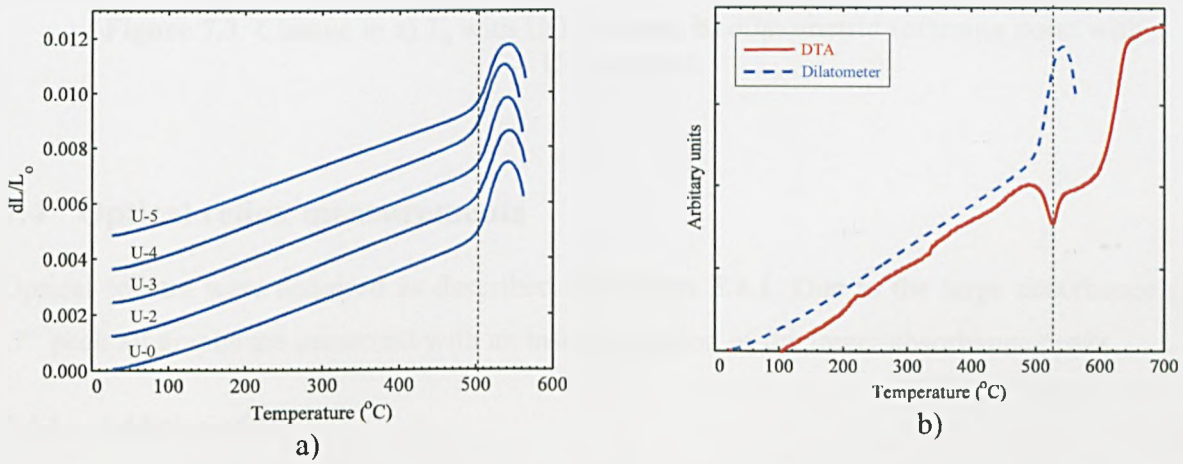

Figure 7.2: a) Stack plot of dilatometry trace from each sample. b) Plot showing dilatometry trace and the DTA trace for the base glass to show similarity. Lines are draw as a guide for the eye only.

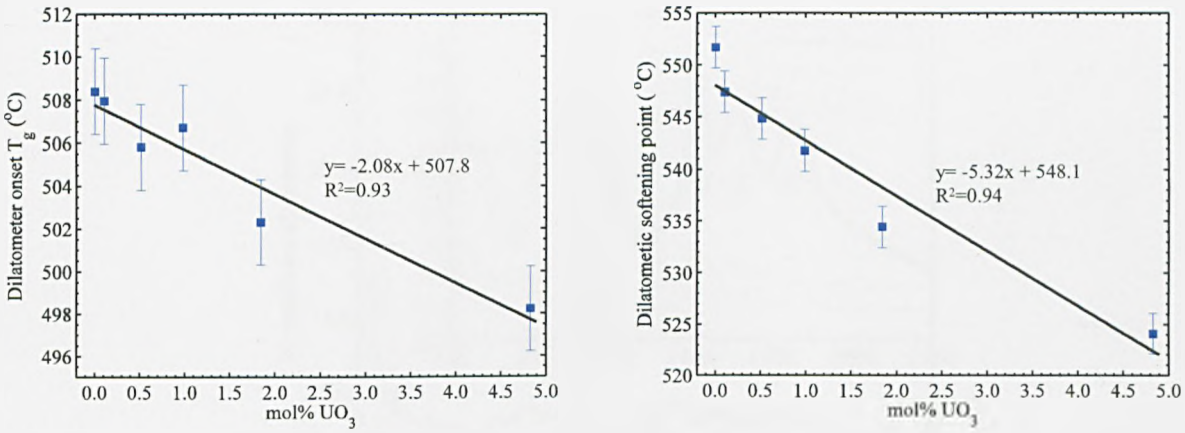

Figure 7.3: Change in a) T_g with UO_3 content, b) dilatometric softening point with UO_3 content.

7.4 Optical redox measurements

Optical spectra were acquired as described in **Section 3.4.1**. Due to the large absorbance of the U^{6+} peak all graphs are presented with an inset expansion of the lower absorbance peaks.

7.4.1 Addition of U

U has three common valence states in alkali (boro)silicate glasses, U^{6+}, U^{5+}, and U^{4+}. In the glasses melted under an air atmosphere only U^{6+} and U^{5+} are present, however, with addition of a small amount of carbon to the melt a much reduced glass was produced with all 3 valence states present (see **Figure 7.4**).

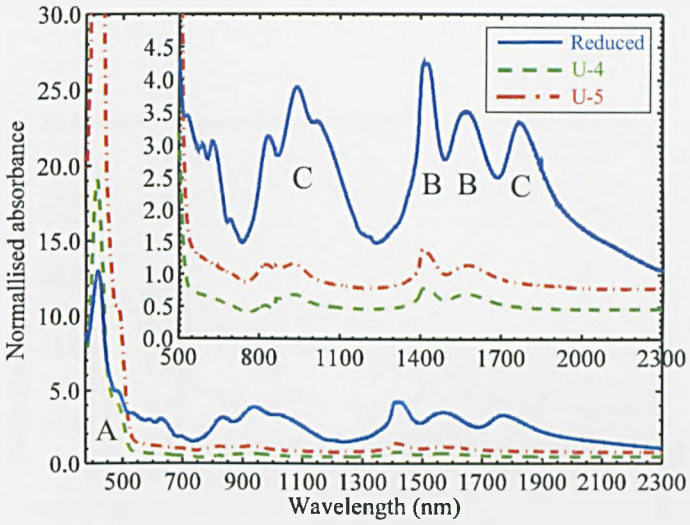

Figure 7.4: Optical spectra with increasing UO_3 content. Presence of carbon (reducing agent during melting) in sample gives more reduced phases. The letters in the figure indicate: A : U^{6+}, B : U^{5+} and C : U^{4+}.

7.4.2 Addition of U and Fe

The two common valence states of Fe in alkali borosilicate glasses are Fe^{2+} and Fe^{3+}. In this study, glasses with only Fe present showed both Fe^{2+} and Fe^{3+} were present. With addition of U to a Fe bearing glass no changes in the Fe optical spectra were observed (see **Figure 7.5**). The spectra that are produced appear to be a sum of the U and Fe spectra with no observable interaction between the redox couples. In order to confirm this, spectra for glasses containing U and Fe separately were summed and plotted to compare with a glass containing both U and Fe (see **Figure 7.6**). This shows that the Fe optical spectrum is indeed invariant with U addition. The vertical shift in the spectra is likely to have caused the difference in refractive index of the glasses not being taken into account when reflection losses were calculated.

The similarity of the two curves shown in **Figure 7.6** indicates that the following redox couples are present and that they either do not interact during cooling (as set out in **Section 2.3**) or interact in such a way as to give no observable change in redox:

$$4U^{6+}_{(melt)} + 2O^{2-}_{(melt)} \rightleftharpoons 4U^{5+}_{(melt)} + O_{2(melt)}$$
$$3Fe^{3+}_{(melt)} + 2O^{2-}_{(melt)} \rightleftharpoons 3Fe^{2+}_{(melt)} + O_{2(melt)} \qquad \textbf{Equation 7.1}$$

An attempt to confirm this with Mössbauer spectroscopy was unsuccessful as the level of Fe^{2+}

was not high enough (<< 5 % of the overall iron content) to be resolved using Mössbauer spectroscopy.

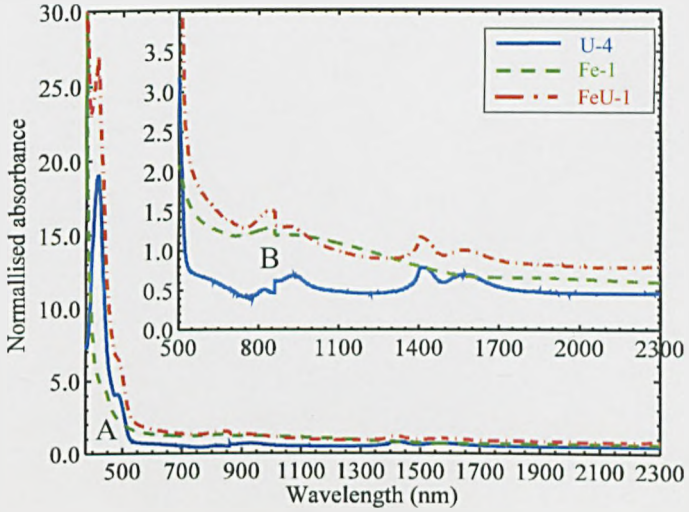

Figure 7.5: Optical spectrum of glass with added U, and Fe. Labelled features are A: Fe^{3+} and B: Fe^{2+}.

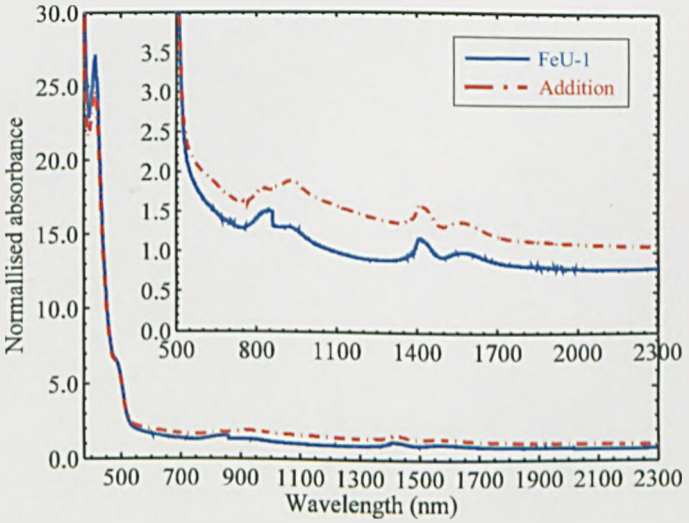

Figure 7.6: Difference between the FeU-1 spectra and a combined spectra of the individual U-4 and Fe-1 spectra.

7.4.3 Addition of U and Cr

The two most common valence states of Cr within an alkali borosilicate glass are Cr^{3+} and Cr^{6+}. In this study all glasses showed the presence of Cr^{3+} (see **Figure 7.7**), the presence of Cr^{6+} is difficult to ascertain due to the proximity of the Cr^{6+} absorption band to the UV edge. However, its

presence is confirmed using XANES in **Section 7.7**. The presence of a higher valence state can also be inferred from the ability of Cr to oxidise both Fe and U within the glasses (shown in **Figure 7.7** and **Figure 7.8**). This indicates that the following redox equilibria move to the right hand side:

$$3U^{5+}_{(melt)} + Cr^{6+}_{(melt)} \rightleftharpoons 3U^{6+}_{(melt)} + Cr^{3+}_{(melt)}$$
$$3Fe^{2+}_{(melt)} + Cr^{6+}_{(melt)} \rightleftharpoons 3Fe^{3+}_{(melt)} + Cr^{3+}_{(melt)}$$

Equation 7.2

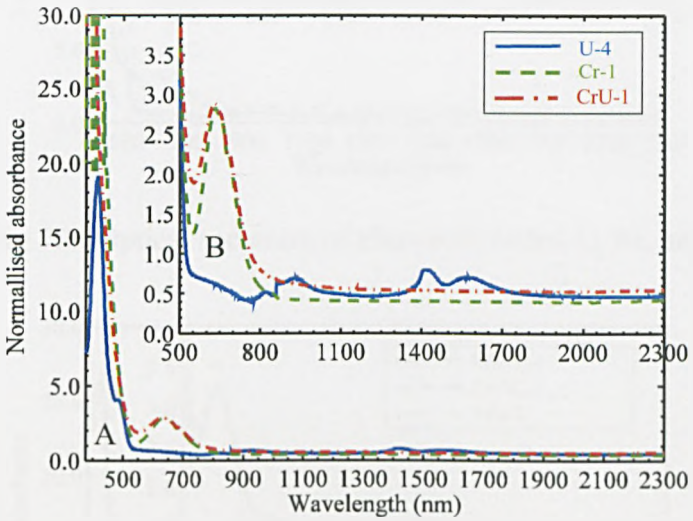

Figure 7.7: Optical spectrum of glass with added U, and Cr. Letters in figure indicate: A : Cr^{6+} peak and B : Cr^{3+}.

7.4.4 Multiple additions

The addition of Cr, Fe and U to a glass makes the analysis of the redox reactions disproportionately more complex[1]. The results presented so far show that Cr fully oxidised both U and Fe in the glass (see **Equation 7.2**). This also appeared to be the case in glasses where Fe, U, and Cr were all present. This is shown in **Figure 7.8** where addition of Cr to a glass with both Fe and U present produced only U^{6+} and Fe^{3+}. However, if the concentration of Cr is reduced the presence of U^{5+} could be shown but without the presence of Fe^{2+}. This is shown in **Figure 7.9** where the two peaks that are indicative of U^{5+} begin to reappear. This indicates that that Fe^{2+} preferentially oxidises over U^{5+} as suggested by Schreiber *et al.* (1984a), and discussed in **Section**

[1] The presence of two redox couples in a glass presents the possibility for one multi-element redox equilibrium; the presence of two redox couples gives the possibility for up to three separate interactions; four couples six equilibria; five couples ten equilibria etc.

2.4.2.

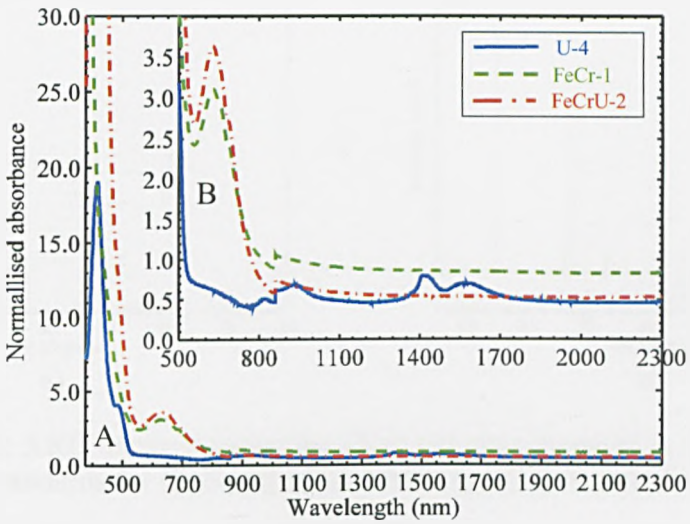

Figure 7.8: Optical spectrum of glass with added U, Fe, and Cr.

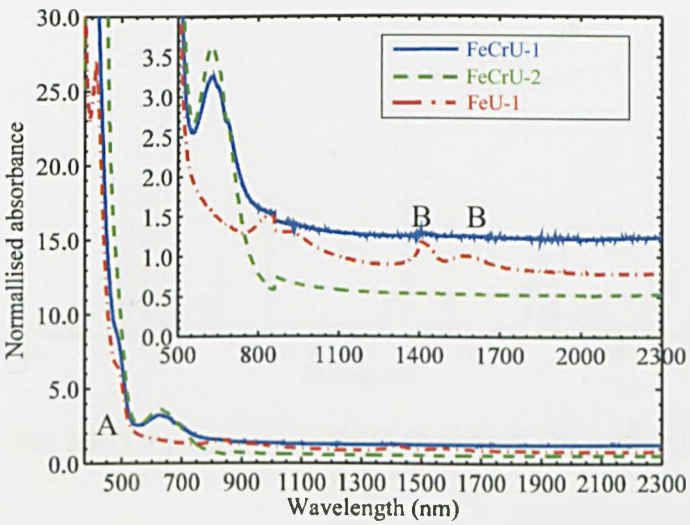

Figure 7.9: Optical spectra showing the reappearance of U^{5+} (B), without the reappearance of Fe^{2+}, with reduced Cr levels.

7.5 Formation of alkali uranates

The XRD patterns for the alkali uranates can be seen in **Figure 7.10**. There is a strong similarity between $Na_2U_2O_7$ and $Li_2U_2O_7$ which is expected due to both phases having essentially identical structures. No reliable ICD cards exist for $Li_2U_2O_7$. However, a reliable ICDS card for $Na_2U_2O_7$ exists ([43-347]) and is shown over laid with XRD spectrum in **Figure 7.11**.

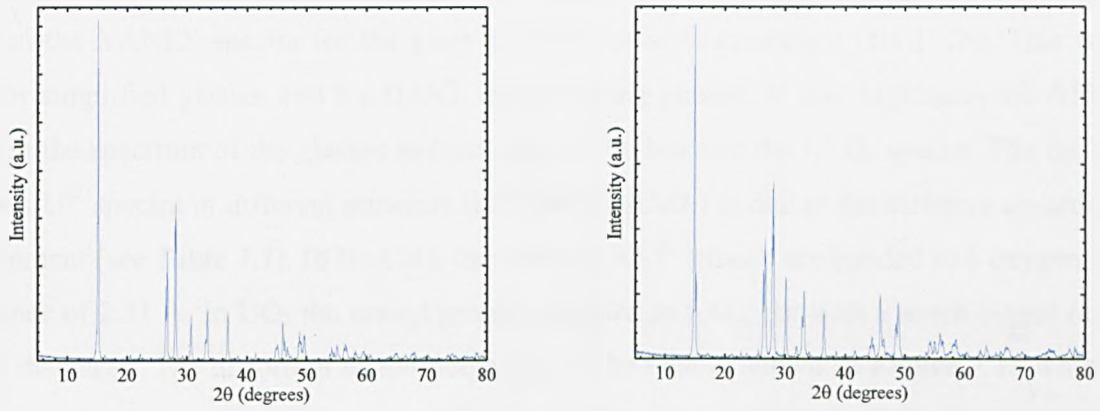

Figure 7.10: XRD traces showing the alkali uranates prepared in this project to act as standards for XAS and MAS-NMR. a) $Li_2U_2O_7$ and b) $Na_2U_2O_7$.

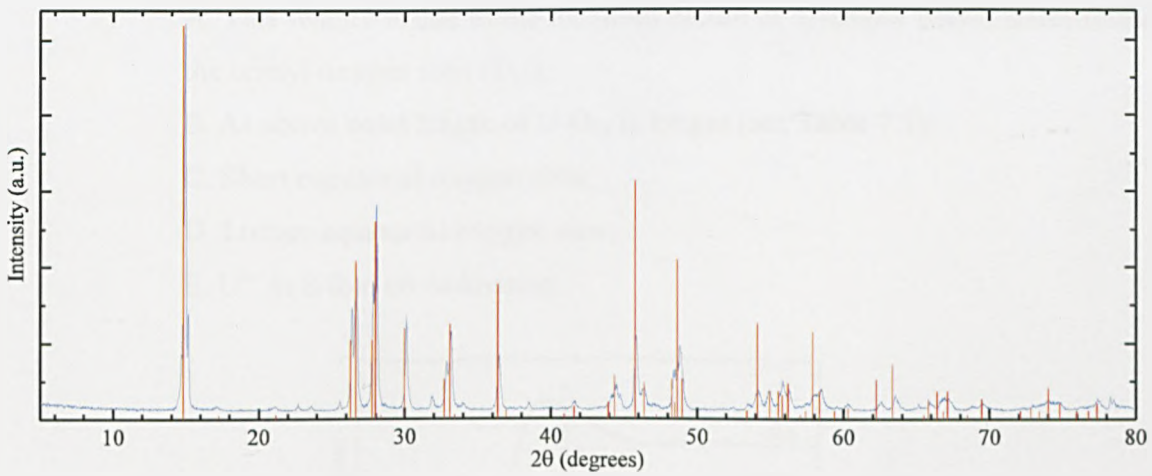

Figure 7.11: XRD trace showing $Na_2U_2O_7$ with ICDS pattern [43-347].

7.6 XAS at the U L_{III}-edge

7.6.1 Pre-edge and XANES

The complex nature of the pre-edge and XANES processes makes deconvolution of XANES experimental data, in a similar manner to EXAFS (see **Section 7.6.2**), very difficult for chemically complex systems. However, comparison between pre-edge and XANES spectra may show differences in local co-ordination very effectively. The electronic nature of this region allows certain assignments to be made which also aid understanding of the local co-ordination.

Comparison of a typical glass and a selection of standards (**Figure 7.12**) shows the similarity between the XANES spectra for the glass and that for sodium uranate ($Na_2U_2O_7$). This was the case for simplified glasses and for HAST waste bearing glasses. It also highlights the difference between the spectrum of the glasses and not only $U^{4+}O_2$ but also the $U^{6+}O_3$ spectra. The difference between U^{6+} spectra in different minerals (UO_3 and $Na_2U_2O_7$) is due to the different co-ordination environment (see **Table 7.1**). In $Na_2U_2O_7$ the uranyl $[UO_2]^{2+}$ groups are bonded to 6 oxygen ions at a distance of 2.31 Å. In UO_3 the uranyl group is bonded to 5 O_{eq} but with a much bigger range of longer distances. The distortion of the polyhedra in the UO_3 is shown in **Figure 7.13** which also shows the structure of $Na_2U_2O_7$. The distortion in the UO_3 polyhedra may be due to the lack of charge compensating ions within the network. The difference between UO_3 and $Na_2U_2O_7$ is also seen in **Section 7.6.2** with EXAFS data). Various features in the spectra have been assigned in the literature (Petiau *et al.* 1986, Farges *et al.* 1991):

A. This feature is due to the localised nature of 5*f*-empty bound states related to the uranyl oxygen ions (O_{Ur});

B. As above bond length of U-O_{Ur} is longer (see **Table 7.1**);

C. Short equatorial oxygen ions;

D. Longer equatorial oxygen ions;

E. U^{4+} in 8-fold co-ordination.

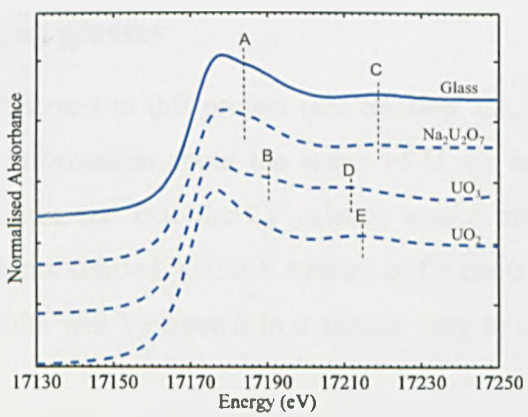

Figure 7.12: XANES data for glasses showing similarity between glass U L_{III}– XANES and sodium uranate U L_{III}– XANES.

Formula	N_O	$R_{U\text{-}Our}$ (Å)	N_O	$R_{U\text{-}Oeq}$ (Å)	N_U	$R_{U\text{-}U}$ (Å)	N_{Na}	$R_{U\text{-}Na}$ (Å)
UO_3	2	1.80-1.85	5	2.19-2.56	2	3.69	-	-
$Na_2U_2O_7$	2	1.92	6	2.31	5	3.93	6	3.73

Table 7.1: Selected reference bond lengths (<4 Å) for standards used in XAS experiments (Fletcher1996). Bracketed numbers are number of atoms of specified elements within distance range (Siegel *et al.* 1966, Kovba *et al.* 1958).

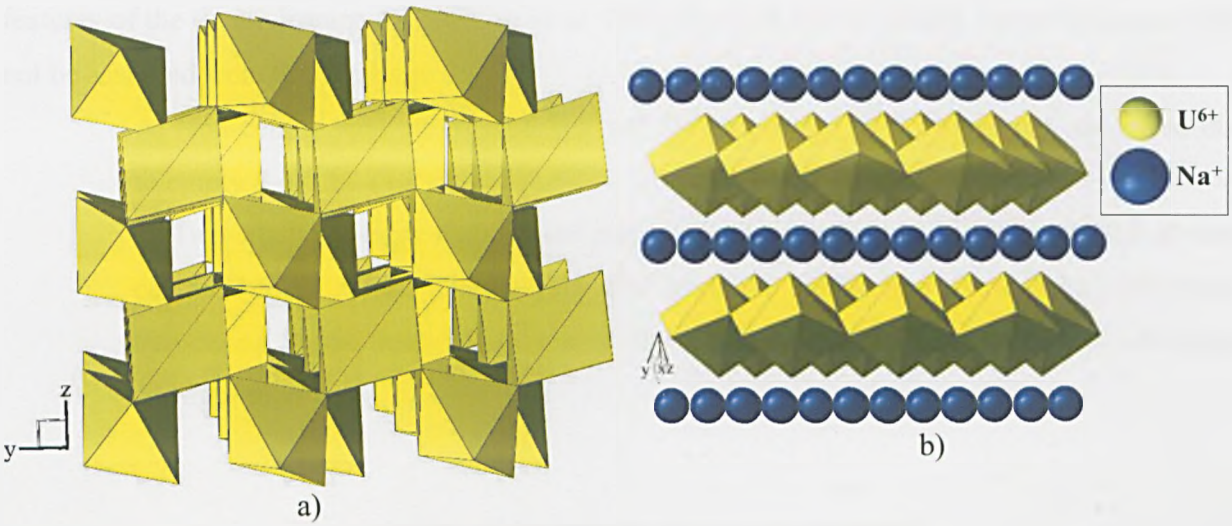

Figure 7.13: Crystal structures of a) UO_3 and b) $Na_2U_2O_7$. UO_7 and UO_8 polyhedra are shown respectively (Seigel1966, Kovba1958).

7.7 XAS of Cr containing glasses

The HAST waste streams of interest to this project (see **Section 2.1.3**) are high in U, Cr and Fe. Optical data provided some information about the redox of U, Cr and Fe within the glass (see **Section 7.4**). These results indicated that the Cr valence was a mixture of Cr^{3+} and Cr^{6+}. To examine this result in more detail limited XANES spectra of Cr containing glasses were acquired (see **Figure 7.14**). These results will be treated in a similar way to the U XANES (see **Section 7.6.1**).

Comparison of the Cr^{3+} and Cr^{6+} standards and the glass spectra showed that in the glasses examined Cr is present in a mixed valence state with both Cr^{3+} and Cr^{6+}. Using linear combination analysis (LCA) an approximation of the amounts of each valence state can be made: ca. 35 % Cr^{6+} and 65 % Cr^{3+} (± 5 %)).

With addition of 2 mol % Fe there was a small reduction in the Cr^{6+} peak indicating oxidation of the Fe as observed in the optical spectroscopy results. Using LCA again, ca. 30 % $Cr^{6+}$and 70

% Cr^{3+} (± 5 %) was found. Unfortunately, no U bearing samples could be examined; however, the similar redox activity of Fe and U suggests U may indeed reduce, supporting the results seen in **Section 7.4**.

Information about the structural environment of Cr within the glass can be gained from the XANES spectra. The various features of the spectra in **Figure 7.14** can be assigned to electronic features of the Cr environment (Peterson *et al. 1*997, Berry & O'Neil 2004), however, some could not be assigned from the literature:

A. Non-centrosymmetric tetrahedral $Cr^{6+}O_4$ species (1*s* to 3*d* transition, enhanced due to empty d-orbital ($3d^0$));

B. Two small pre-edge features are present due to octahedral Cr^{3+} at ca. 5990.5 eV and ca. 5993.5 eV. These features are due to 1s to $3d(t_{2g})$ and 1*s* to $3d(e_g)$ electronic transitions, respectively. They are of low intensity due to stability of $3d^3$ electronic configuration.

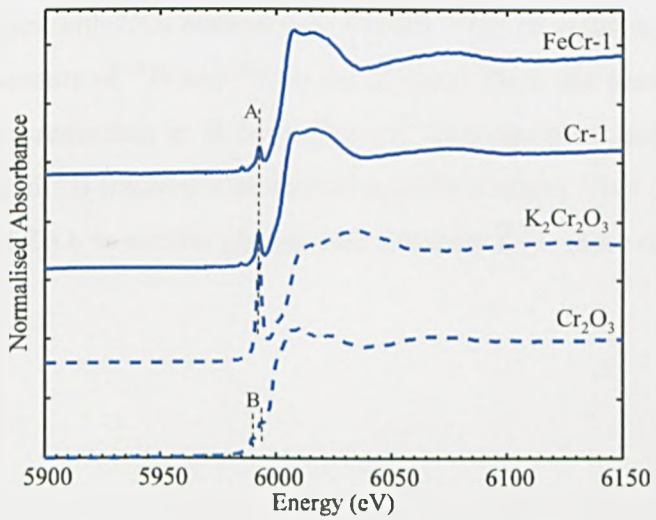

Figure 7.14: XANES data showing the presence of Cr^{6+} in glasses containing only Cr and glasses with addition of Fe.

7.8 MAS-NMR results

Presented below are the results of the analysis of various MAS-NMR spectra collected on U containing glasses. An attempt was also made to collect MAS-NMR spectra from glasses with Cr

present, however, due to the paramagnetic[1] nature of Cr^{3+} the spectra underwent paramagnetic broadening and so were unsuitable for analysis. The author is also aware that the presence of a small amount of the paramagnetic U^{5+} within the glasses may also broaden spectra; however, no such effect was not observed. Data collection and analysis were carried out as described in **Section 3.4.2**. The results for each isotope will be set out in turn with a summary at the end of this chapter.

7.8.1 ^{11}B MAS-NMR data

The primary information available from analysis of ^{11}B MAS-NMR spectra is that of B co-ordination. It is assumed that the co-ordination of boron is either ^{IV}B or ^{III}B. The spectra collected in this study are shown in **Figure 7.15**. Four peaks were fitted under each spectrum as shown in **Figure 7.16** and **Section 3.4.2**; two peaks each to represent ^{IV}B and two peaks to represent ^{III}B.

The chemical shifts of the ^{IV}B peaks appears invariant with UO_3 content; however, there is a small initial increase in ^{III}B peak chemical shift with a decrease at higher UO_3 content (see **Figure 7.17**). This maybe due to the difficulties fitting this type of spectra with four peaks. The relative areas of the peaks changes with UO_3 content (see **Figure 7.19**). It is the area under the peaks that provides the relative amounts of ^{IV}B and ^{III}B in the glasses. Thus, the increase in the intensity of the ^{III}B peaks indicates a reduction in B co-ordination. This has been quantified in **Figure 7.18** which shows a decrease in ^{IV}B fraction with increasing UO_3 content. This trend is different to that seen with the addition of ZrO_2 to similar glasses (see **Chapter 8** for more discussion).

[1] The presence of a localised unpaired electron (e.g. Cr^{3+} - $[Ar].3d^1.4s^2$) causes an additional magnetic field at the nucleus giving broadening. Also, for this reason no data for glasses with Fe present were acquired (Fe^{2+} $[Ar].3d^5.4s^1$) (Mackenzie & Smith 2002).

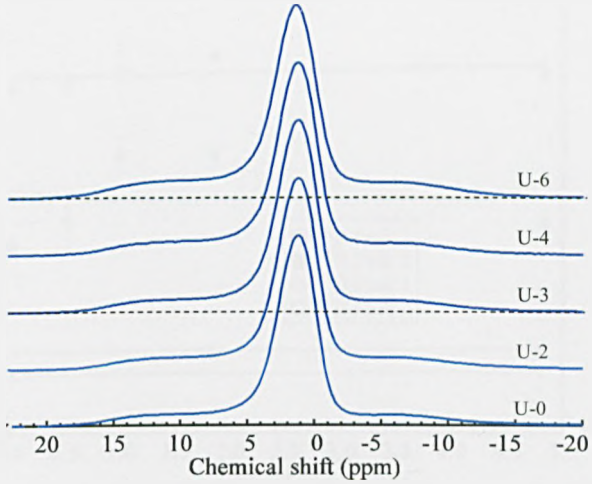

Figure 7.15: Stack plot of ^{11}B spectra showing decrease in ^{IV}B fraction (central peak) with increasing U content.

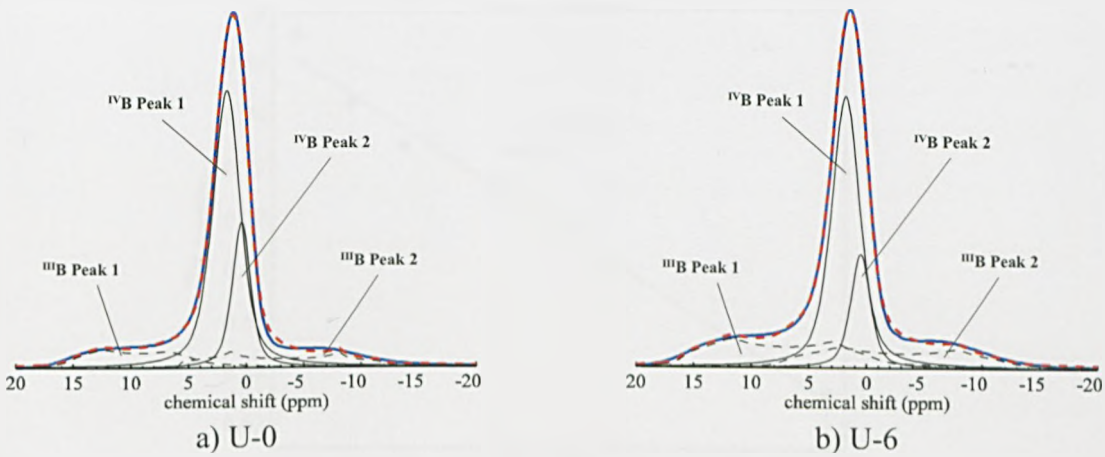

Figure 7.16: Example fits of ^{11}B MAS-NMR spectra.

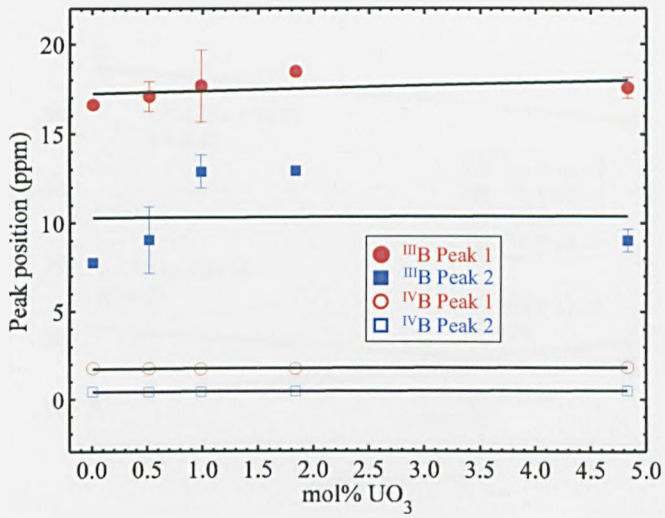

Figure 7.17: Peak positions for ^{11}B MAS-NMR spectra with increasing UO_3 content.

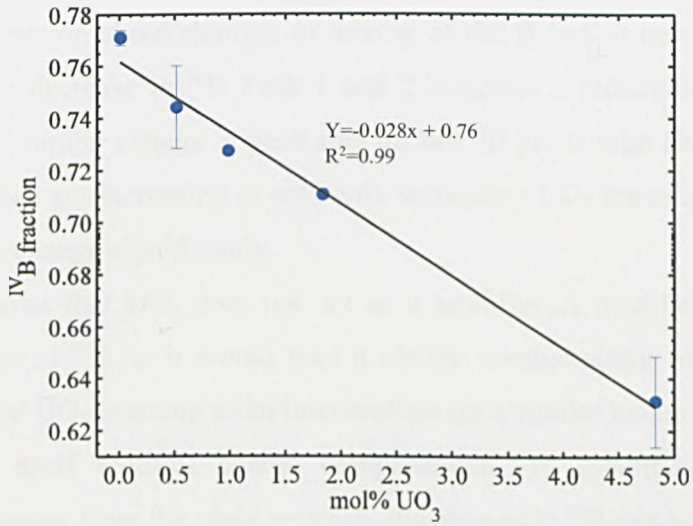

Figure 7.18: Decrease in ^{IV}B fraction with addition of UO_3

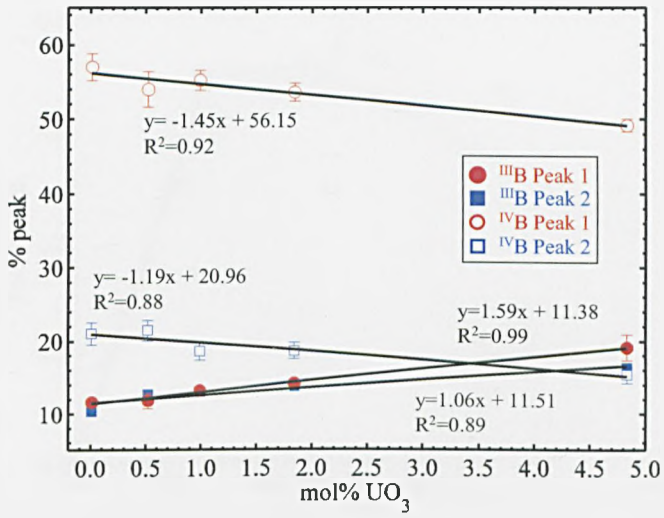

Figure 7.19: Trends in ^{11}B MAS-NMR peak areas with increasing UO_3 content.

A secondary source of information is the relative areas under the fitted peaks (see **Figure 7.19**). This can give information about changes in mixing of the B and Si networks (see **Section 3.4.2** and **Table 3.8**). The decrease in ^{IV}B Peak 1 and 2 indicates a reduction in both ^{IV}B units with increasing UO_3. The similar change in peak area for the ^{III}B peaks with UO_3 addition suggests that although the ^{III}B peaks are increasing in area with increasing UO_3 the average environment of the ^{III}B species does not change significantly.

Figure 7.18 shows that UO_3 does not act as a modifier. A modifier would be expected to increase the fraction of ^{IV}B as it would take a charge compensating role. The decrease in ^{IV}B fraction indicates that UO_3 is acting as an intermediate (in a similar manner to ZrO_2 (see **Chapters 4** and **6**) and so itself requires charge compensation. To establish what level of charge compensation it removes from the glass network, the change in ^{IV}B can be plotted as a function of modified *R*:

$$R_{ZrO_2} = \frac{([Na_2O]+[Li_2O]-x[ZrO_2])}{[B_2O_3]} \qquad \textbf{Equation 7.3}$$

with $x = 2$ **Figure 7.20** shows that the addition of UO_3 removes ca. 4 alkali ions (2 moles of alkali oxide) from the glass network.

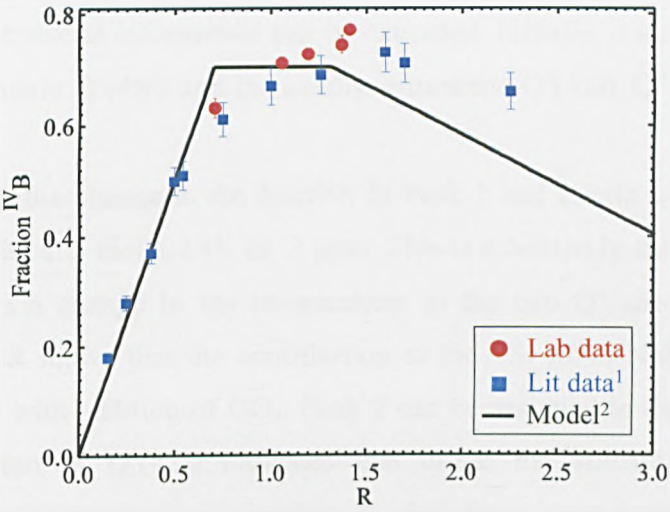

Figure 7.20: Fraction ^{IV}B of literature data (Rodderick2001) with laboratory data rescaled onto the R-axis with $x = 2$ (see).

7.8.2 ^{29}Si MAS-NMR data

The line shapes of the ^{29}Si MAS-NMR spectra are dependent on the degree and nature of the bonding between silicate tetrahedra (**Section 3.4.2**). This effect can be quantified if the chemical shifts and shape of the spectra are examined. **Figure 7.21** shows that the chemical shift becomes more positive with increasing UO_3 content. This effect is generally caused by (Mackenzie2002) (see **Table 3.7**):

1. decreasing electronegativity of the surrounding groups;
2. increasing Si-O bond length;
3. decreasing mean T-O-T bond angle (where T denotes the tetrahedral atom).

In order to quantify this effect and to extract the cause of the chemical shift two peaks are fitted under each spectrum (see **Section 3.4.2** and **Figure 3.11**). **Figure 7.22** shows the chemical shift of the fitted peaks with increasing UO_3. This result is discussed in more detail below.

Analysis of the deconvolution of these spectra is more complex than that for ^{11}B MAS-NMR. As shown in **Section 3.4.2** and **Table 3.7** in a simple alkali borosilicate glass the relative proportions of Q^4 and Q^3 can be estimated. However, with addition of U the situation becomes more complex. The possible presence of Q^n(U) species of unknown peak position makes analysis

difficult. The analysis technique used in **Section 4.6.2** showed that if an assumption is made as to what units are present, useful information can be extracted. Initially, it must be assumed that only the spherically symmetric $Q^4(4Si)$ and the axially symmetric $Q^3(3Si)$, $Q^4(1B)$ and $Q^4(1U)$ groups are present.

Figure 7.23 shows the change in the fraction of Peak 1 and 2 with increasing UO_3. For both peaks the change with ca. 5 mol% UO_3 ca. 3 ppm. This is a relatively small shift which indicates that although there is a change in the environment to the two Q^n species the effect is small. However, **Figure 7.23** shows that the contribution to the ^{29}Si MAS-NMR spectra from Peak 2 changes significantly with addition of UO_3. Peak 2 can be assigned to the $Q^4(4Si)$ groups within the glass. A reduction in $Q^4(4Si)$ indicates that either the silicate network is becoming deploymerised with an increase in Q^3 species. Or that there is an increase in $Q^4(U)$ or $Q^4(B)$ species. The results of ^{11}B MAS-NMR suggest that there is little change in mixing of the silicate and borate networks and so it is unlikely that there is an increase in $Q^4(B)$. ^{11}B MAS-NMR results also suggests that the addition of UO_3 tends to reduce the alkali available for charge compensation. Thus, unless the addition of UO_3 effects the borate and silicate networks differently, the $Q^4(U)$ is becoming dominant. The possibility of differential effects on the borate and silicate network cannot be confirmed without further work; however, it is considered unlikely and it is suggested that $Q^4(U)$ species are increasing within the glass with increasing UO_3 content.

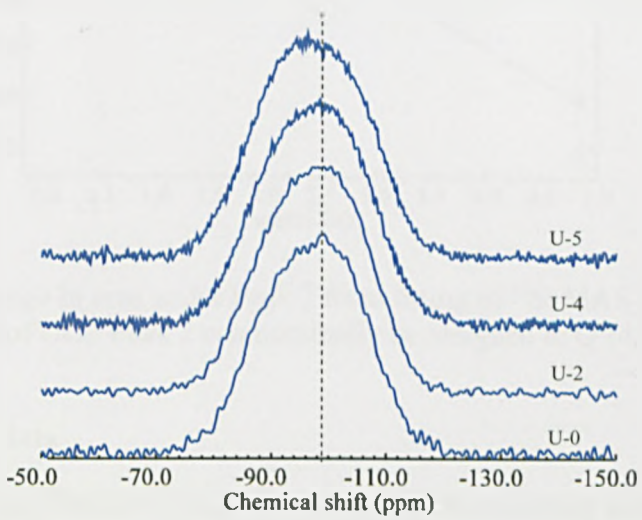

Figure 7.21: Stack plot of ^{29}Si MAS-NMR results. Shows change in peak position and shape with increasing UO_3 content.

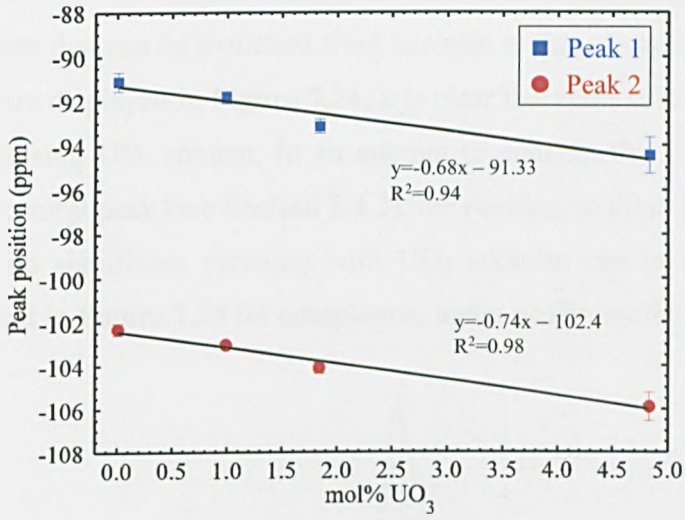

Figure 7.22: Decrease in chemical shift the two peaks under the main peak (peak 1 and 2) of the ^{29}Si spectra.

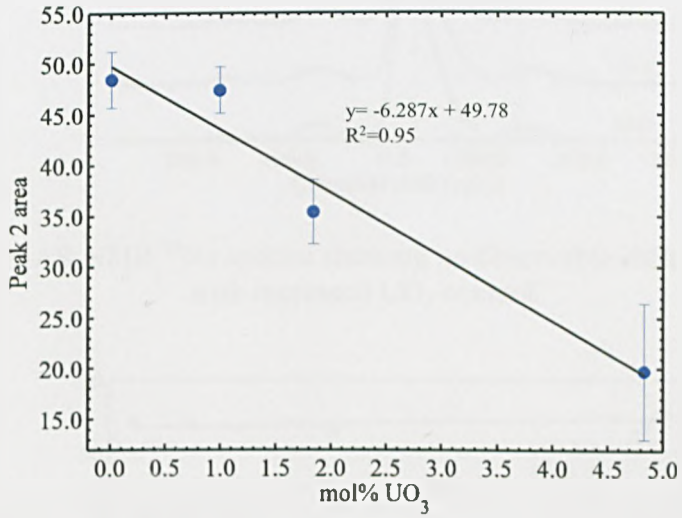

Figure 7.23: Change in area under Peak 2 from fitting of ^{29}Si MAS-NMR spectra with additions of UO_3. Peak 2 can nominally be assigned to Q^4(4Si) species.

7.8.3 ^{23}Na MAS-NMR data

The primary contribution to ^{23}Na MAS-NMR spectra is the co-ordination number of the Na within the glass. In principle these spectra should be capable of distinguishing between Na ions which are associated with NBOs and those charge compensating tetrahedral boron sites. However, ^{23}Na has I = 3/2 and suffers from quadruple broadening and so the two (or more) discrete resonances cannot be resolved. This effect, and the large number of different environments for Na in glasses,

mean that it is very difficult to assign co-ordination numbers to signals from glasses. Thus, the most useful information that can be extracted from analysis is that of chemical shifts. To this end the spectra collected are displayed in **Figure 7.24**, it is clear that there is no discernable change in the spectra with increasing UO_3 content. In an attempt to confirm this observation three peaks were fitted under the central peak (see **Section 3.4.2**), the position of these three peaks is shown in **Figure 7.26**, where no significant variation with UO_3 addition can be resolved. The relative intensities are presented in **Figure 7.25** for completion, again no discernible trend is observed.

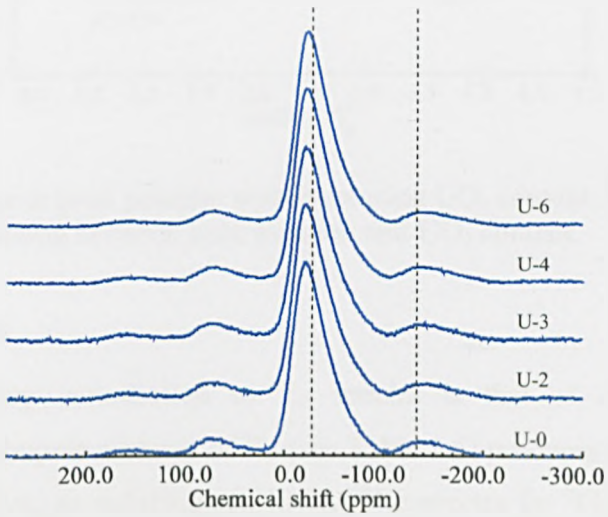

Figure 7.24: MAS-NMR ^{23}Na spectra showing no observable shift in peak positions with increased UO_3 content.

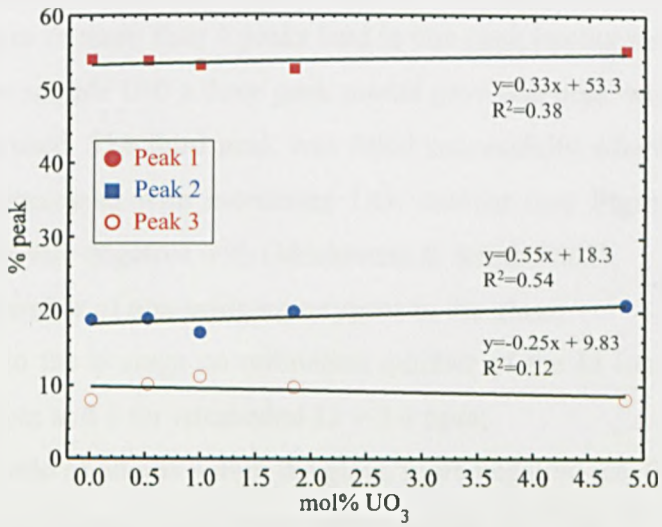

Figure 7.25: Change in area of fitted peaks with increasing UO_3 content.

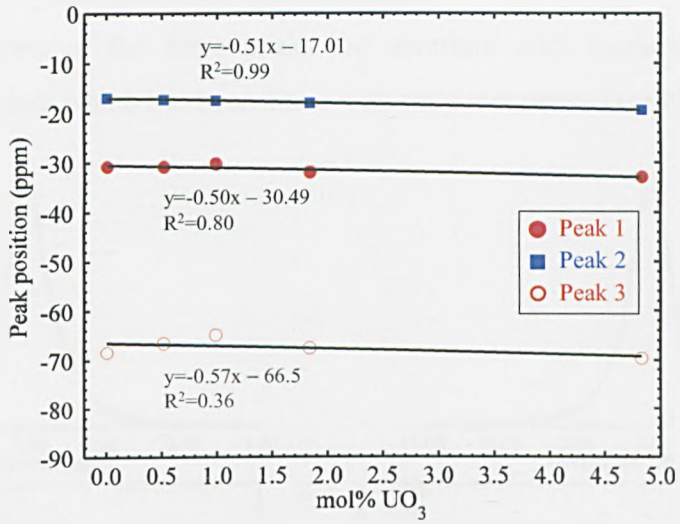

Figure 7.26: Change in peak position with increasing UO_3 content. Shows limited variation between peak position and UO_3 content.

7.8.4 ^{7}Li MAS-NMR data

Similar to ^{23}Na the primary contribution to ^{7}Li spectra is that of co-ordination number. Unfortunately, the high quadrupole moment of ^{7}Li (see **Table 3.6**) produces relatively broad bands from non-symmetrical Li sites, so reducing sensitivity. The spectra for ^{7}Li (**Figure 7.27**) show a central peak with a clearly increasing second side peak at more negative chemical shift (highlighted by the dashed line) with increasing UO_3 content. In order to quantify this shoulder peak an attempt was made to fit one, two and three Lorentzian peak models to each spectrum (see **Figure 7.27**). Attempts to fit more than 4 peaks lead to one peak having near zero intensity and so these were rejected. For sample U-0 a three peak model gave one peak with zero intensity and so a two peak model was used. The third peak was fitted successfully where UO_3 was present, the intensity of this peak increased with increasing UO_3 content (see **Figure 7.29**). The isotropic chemical shift becomes more negative with (Mackenzie & Smith 2002):

1. Decreasing number of non-bridging oxygens in the glass;
2. An increase in the average co-ordination number of the Li ion, δ for octahedral Li = -0.1 to -0.6 ppm and δ for tetrahedral Li = 2.4 ppm;
3. The relative ratio of alkalis within the glass, more negative (ca. 0.4 ppm max shift) with decreasing $Na_2O/[Na_2O+Li_2O]$ (same effect as seen for ^{23}Na).

This is in contrast to the ^{23}Na data which shows no resolvable shift with increasing UO_3 content. It is possible that ^{23}Na is less sensitive to the effects of UO_3 or the additions have greater

effect on the co-ordination environment of Li than Na.

The relative positions of the three peaks are invariant with increasing UO_3 content, but different for the base glass which has been fitted with only two peaks (see **Figure 7.30**).

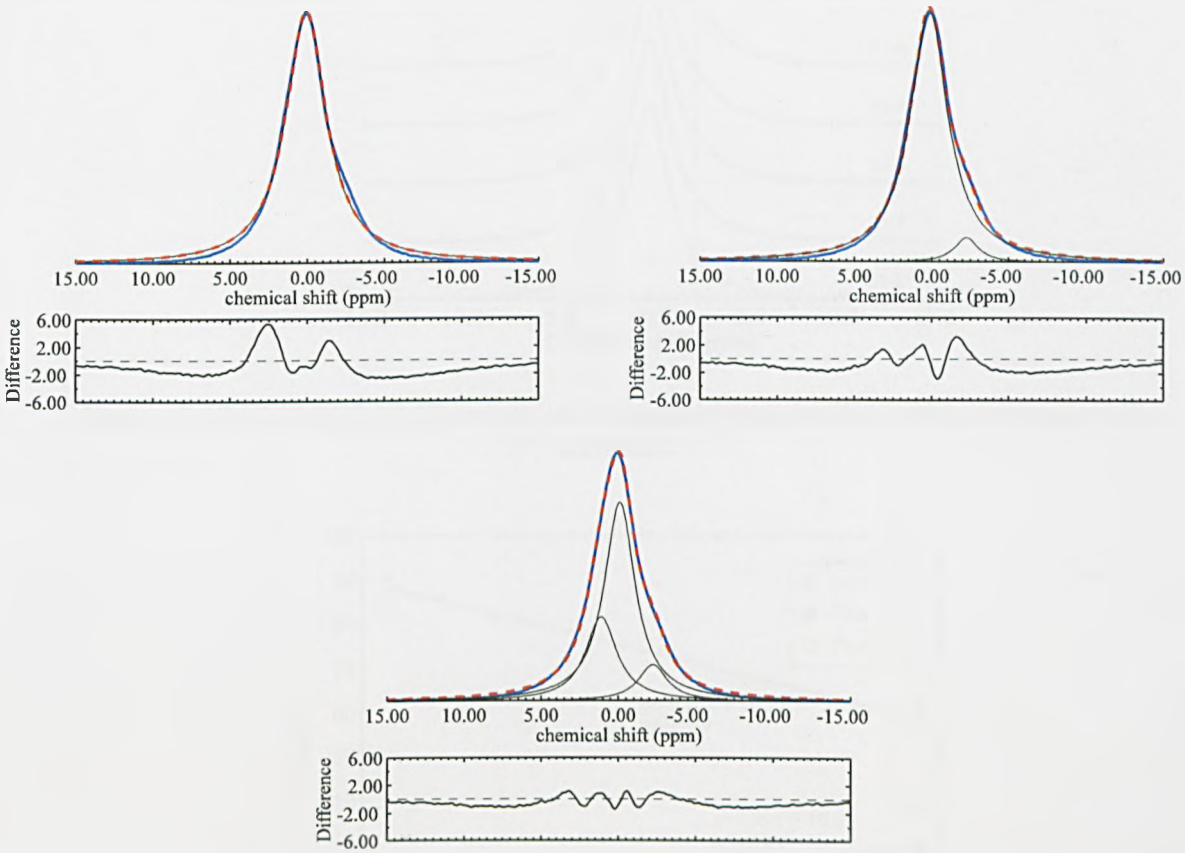

Figure 7.27: ^{7}Li spectra showing the different fits possible on U-3 sample.

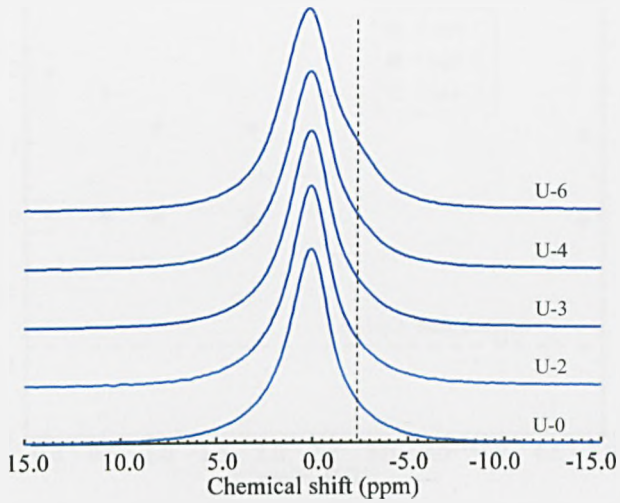

Figure 7.28: ^{7}Li MAS-NMR spectra showing side peak increase with increasing UO_3 additions.

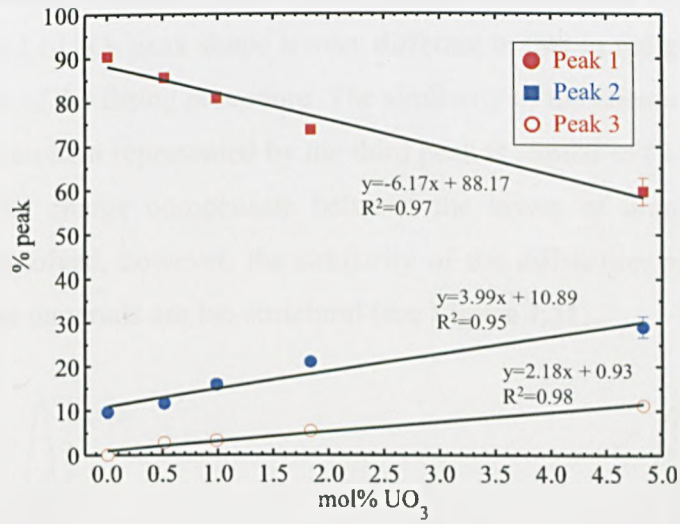

Figure 7.29: Change in ^{7}Li MAS-NMR peak area with increasing UO_3 content.

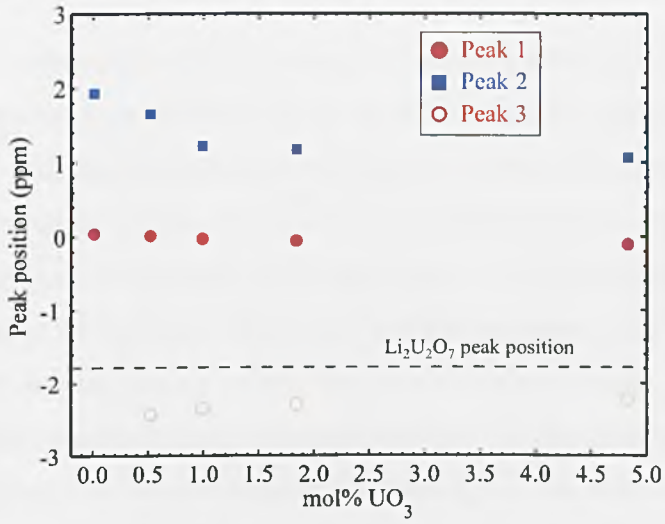

Figure 7.30: Shift in peak position with increasing UO_3 content. Peak 3 is not present in sample at zero mol % UO_3.

^{7}Li MAS-NMR spectra for $Li_2U_2O_7$, shows that the chemical shift for $Li_2U_2O_7$ is similar to that for the 3rd peak but the $Li_2U_2O_7$ peak shape is very different to that in the glass (see **Figure 7.31**). This may be a function of the fitting procedure. The similarity of the chemical shift would indicate that the chemical environment represented by the third peak is similar to $Li_2U_2O_7$. In this structure, Li^+ ions are present to charge compensate between the layers of uranyl species. The exact structure has not been solved, however, the similarity of the diffraction patterns of $Li_2U_2O_7$ and $Na_2U_2O_7$ suggests these materials are iso-structural (see **Figure 7.11**).

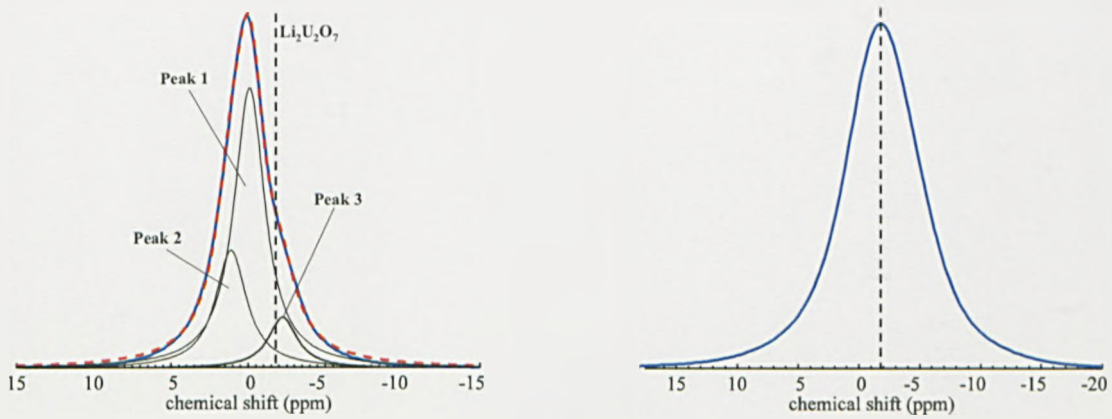

Figure 7.31: MAS-NMR ^{7}Li spectra for a) U-6 glass with fitted curves, with line indicating chemical shift for $Li_2U_2O_7$. b) ^{7}Li MAS-NMR spectra for $Li_2U_2O_7$.

7.8.5 Sodium glasses

In **Section 7.8.3** it was shown that with increasing UO_3 content there was no resolvable change in the MAS-NMR ^{23}Na spectra (see **Section 7.8.3**). To investigate this effect more thoroughly two glasses were produced with equimolar alkali additions but where the only alkali present was Na (see **Table 3.4**). One of these glasses had no UO_3 present, the other with ca. 1.8 mol% UO_3. **Figure 7.32** shows that there is negligible difference in the ^{23}Na MAS-NMR peak chemical shifts and shape between these two glasses. This would indicate either a different U incorporation mechanism occurs in Li bearing glasses or that ^{23}Na MAS-NMR is not able to resolve changes.

In **Section 7.8.4** it was shown that the chemical shift for ^{7}Li MAS-NMR trended towards that of $Li_2U_2O_7$ with increasing UO_3 content. **Figure 7.32** shows the ^{23}Na MAS-NMR spectrum for the crystalline phase $Na_2U_2O_7$ (believed to be iso-structural to $Li_2U_2O_7$). This spectrum is coincident with the main peak produced by the spectra of the glass samples. This overlap may prevent changes in the Na environment towards the structure of $Na_2U_2O_7$ from being observed in the glass spectra.

^{11}B MAS-NMR carried out on the same samples indicated that the effect of U on the bulk network is similar to that in Li bearing glasses (see **Figure 7.33** and **Figure 7.34**). The difference in ^{IV}B fraction between Na and Na-Li containing glasses is expected from the literature. Du *et al.* (2003a) showed that Li tends to form Q^3 species more readily in alkali borosilicate glasses than ^{IV}B thus reducing the overall ^{IV}B fraction compared to a Na only glass.

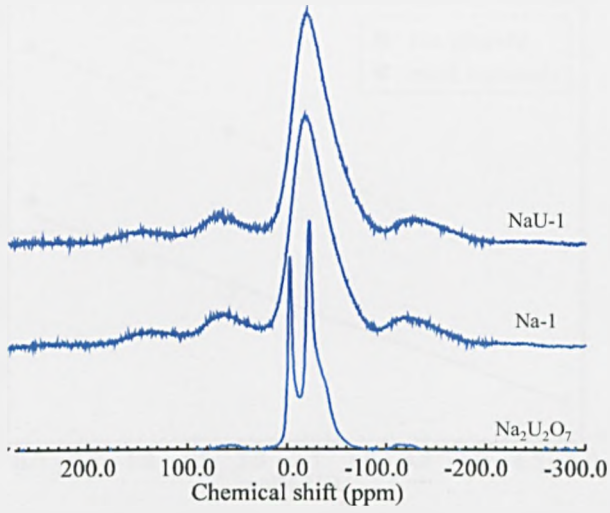

Figure 7.32: MAS-NMR ^{23}Na spectra for Na glasses and standard. Showing the similarity between Na base glass with, and without, UO_3, and that $Na_2U_2O_7$ is unlikely to be present.

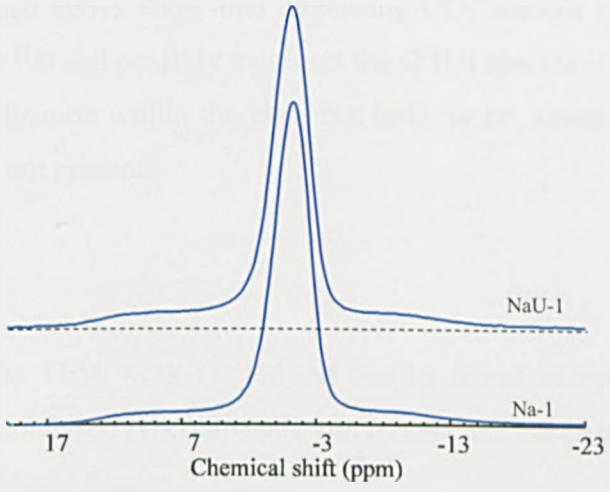

Figure 7.33: MAS-NMR ^{11}B spectra for Na glasses. Showing increase in ^{III}B region with increasing UO_3 content.

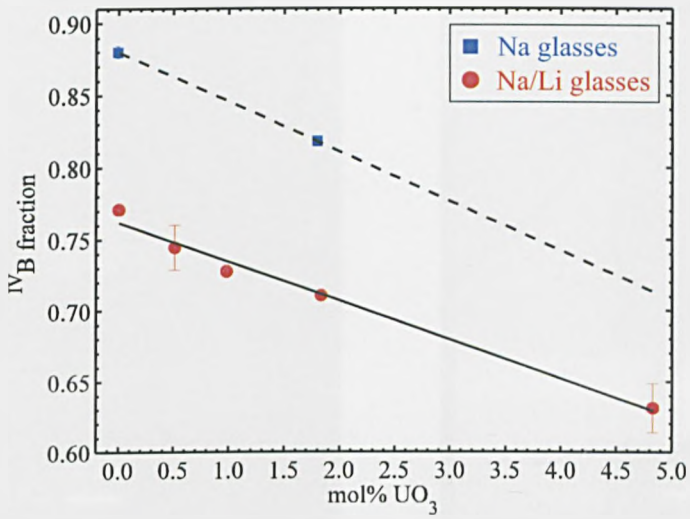

Figure 7.34: Results of analysis of ^{11}B spectra showing change in ^{IV}B fraction with UO_3 additions. Na glasses show same trend as Na/Li glasses.

7.8.6 Summary

MAS-NMR results presented above show that increasing UO_3 content in an alkali borosilicate glass decreases the fraction ^{IV}B and possibly increases the Q^4(U) species in the glass. There is also a clear change in Li co-ordination within the glass but little, or no, observable change in Na co-ordination even when Li is not present.

7.9 TEM

Experimental details for the TEM work carried out can be found in **Section 3.3.2**. The initial results show that the glass analysed (U-5) appears amorphous and homogeneous when examined under TEM (see **Figure 7.35** and **Figure 7.36**).

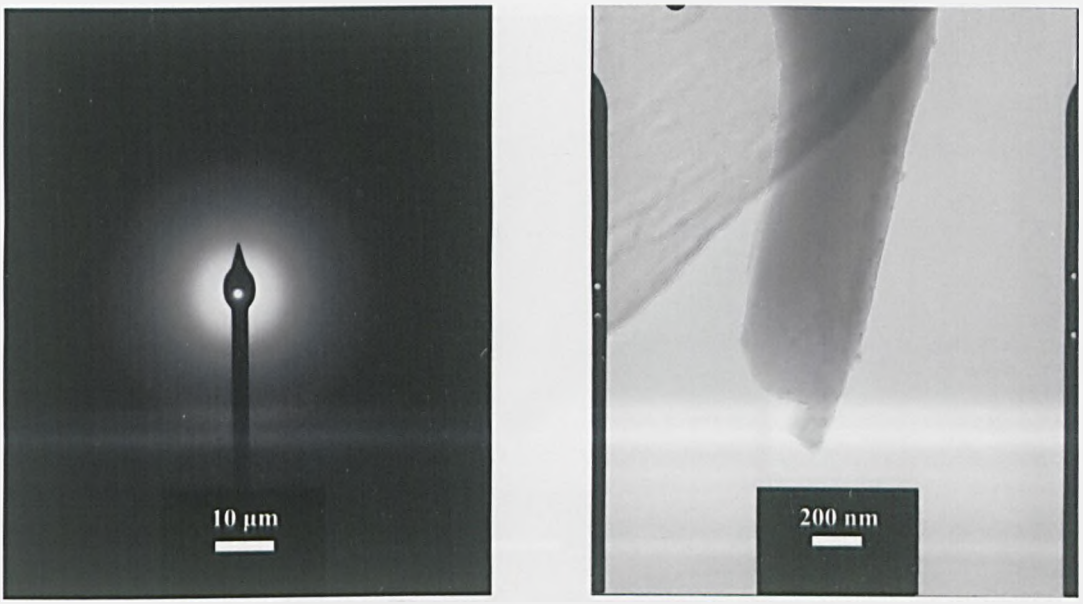

a) b)

Figure 7.35: a) Electron diffraction pattern showing amorphous nature of the glass, b) Showing glass is homogeneous.

The high energy of the electrons incident on the glass samples and the ionic nature of the alkali bonding to the glass network means that alkali ions are relatively mobile under irradiation by negatively charged electrons. It can be seem from the EDS mapping (see **Figure 3.37**) that this beam damage causes migration of the light sodium (and presumable lithium which could not be resolved using EDS mapping) ions from that region. This makes it very difficult to produce images with high resolution and high magnification that are representative of an undamaged glass.

The EDS scans shown in **Figure 7.38** and other EDS scans collected show that the glass is homogeneous with no detectable impurity elements.

The only crystalline phase found within the glass was a Y-Ti phase which is an inclusion from unknown origin (possibly an impurity within the UO_3) (see **Figure 7.39** and **Figure 7.40**).

Figure 7.36: Picture showing amorphous sample on edge of carbon film, picture is taken before beam damage was apparent.

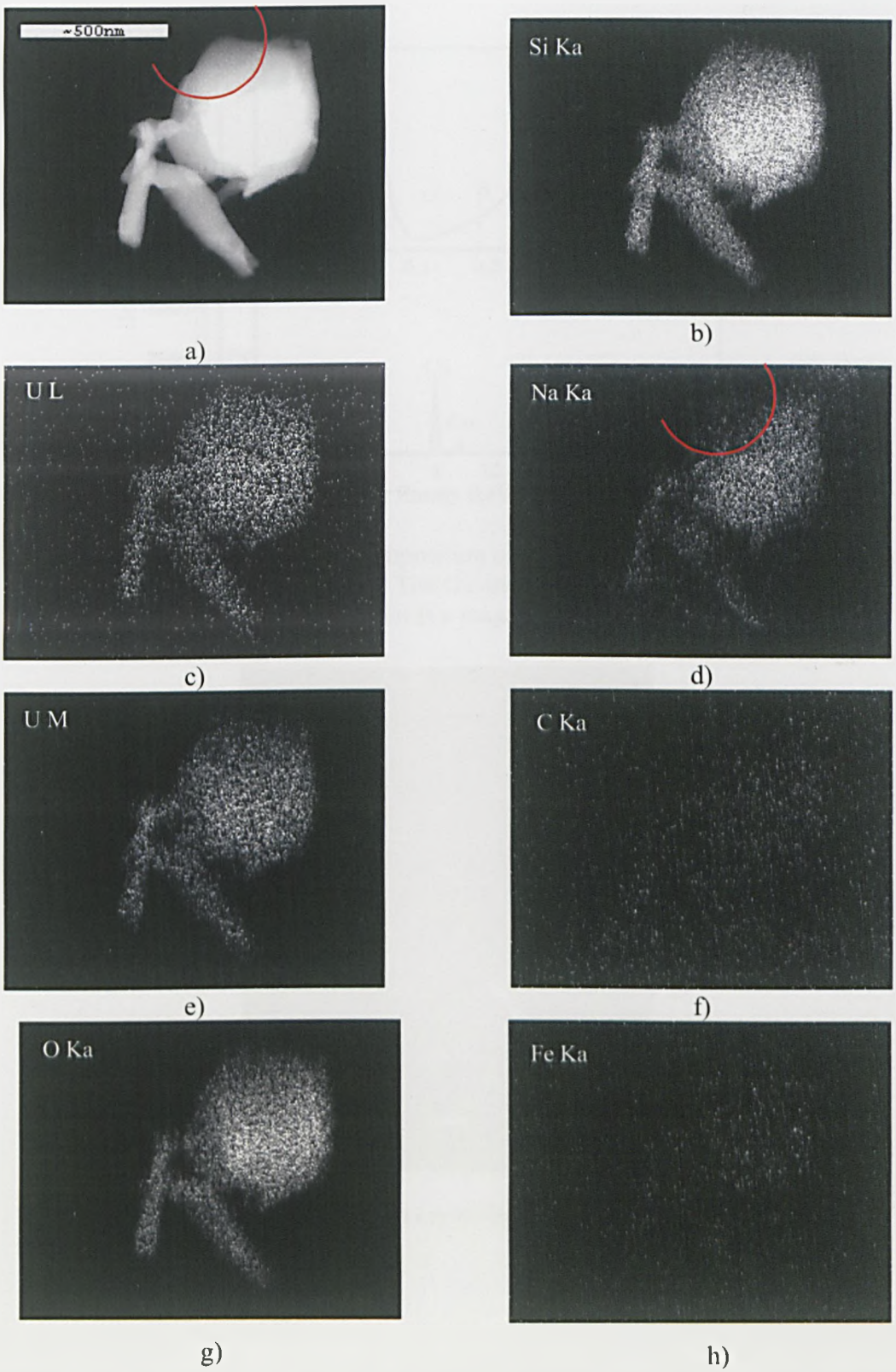

Figure 7.37: Scanning EDS images for various elements. Area marked with red curve shows beam damaged area.

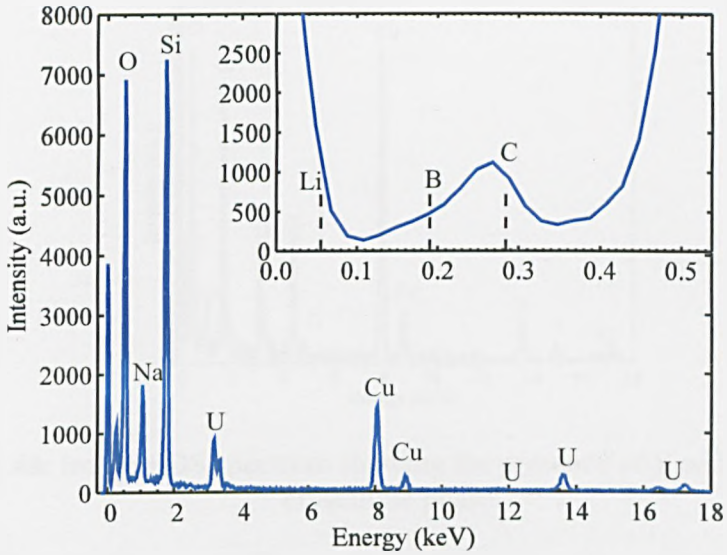

Figure 7.38: EDS trace showing composition of the glass, Li, B and C do not give a signal due to their very low energy. The Cu and C background from the mounting and are not part of the glass. Inset is a magnification of low energy region.

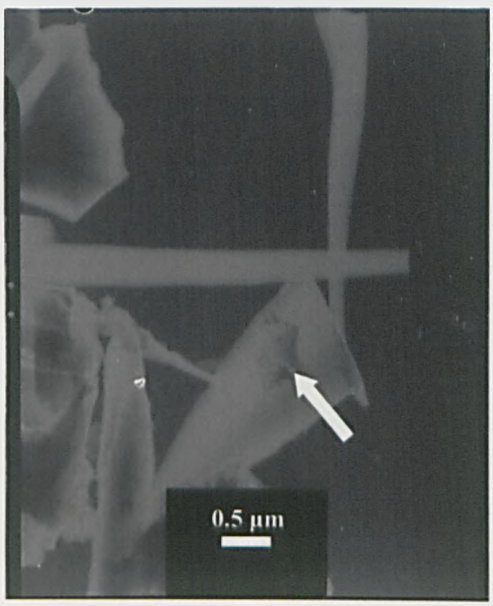

Figure 7.39: Image showing a crystalline inclusion within the glass.

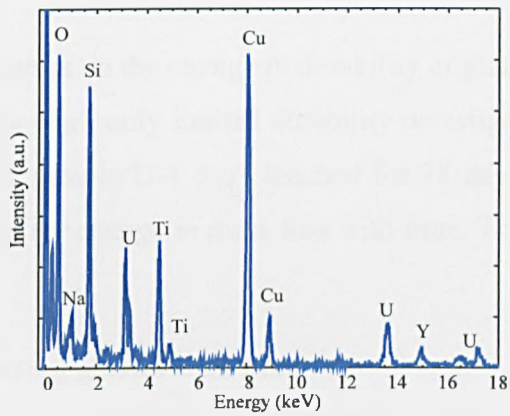

Figure 7.40: Image EDS spectrum showing the presence of Y and Ti within the crystalline phase.

In order to confirm the amorphous nature and homogeneity very high magnification images were taken (see **Figure 7.41)**. **Figure 7.41a** is at a magnification which would show the presence of lattice fringes if they were present. The slight granular nature of **Figure 7.41a** is believed to be due to the constructive and destructive and interference effects of the electron beam within the microscope. The homogeneous nature of the glasses seen under high resolution TEM indicate that there is no clustering of U atoms at length scales greater than ca. 1 nm.

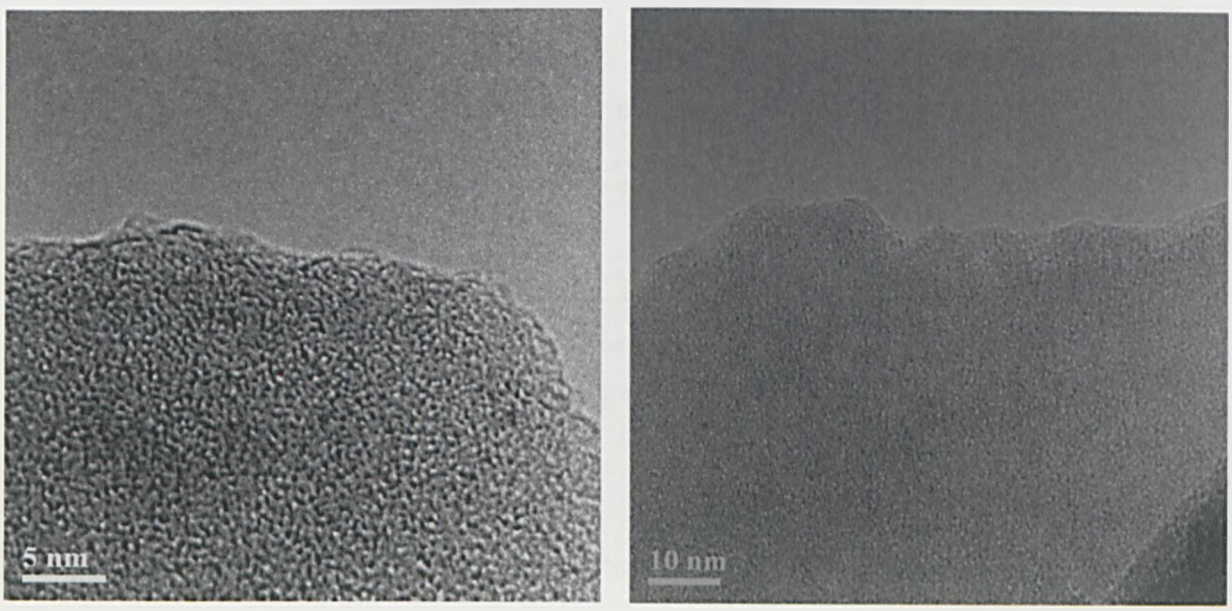

a) b)

Figure 7.41: High magnification image (U-6) glass.

7.10 Durability

A discussion of previous literature on the change in durability of glasses with addition of UO_3 was given in **Section 2.4.2**. In this work only limited durability investigation was undertaken for UO_3 in glasses. Two specimens of sample U-4 were leached for 28 day as described in **Section 3.6.** **Figure 7.42** shows the results for change in mass loss with time. The results are discussed below and in **Chapter 8**.

7.1.1 Leaching of UO_3 bearing glasses with time

The results shown in **Figure 7.42** show that mass loss increases with time for most elements within all samples. However, the leaching of uranium appears to decrease with time, having reach the maximum after only 3 days. This indicates that U is precipitating out of solution, forming some solid or colloidal phase within either the solution or on the glass itself.

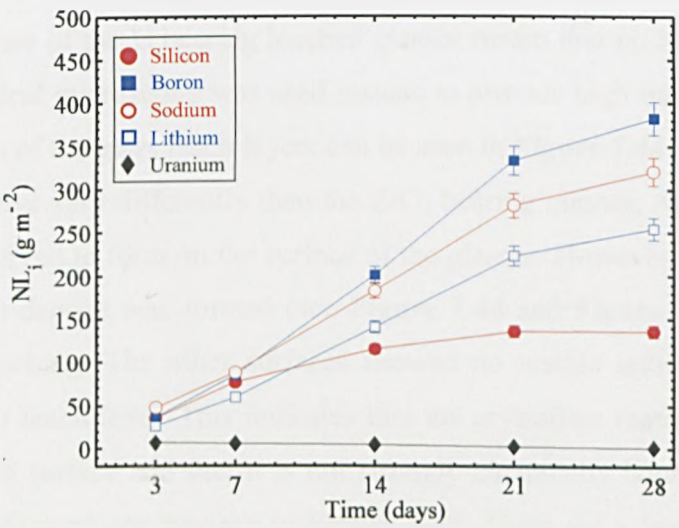

Figure 7.42: Durability of a uranium bearing glass with time (U-4) (± 5%)

7.1.2 Leaching of UO_3 bearing glasses – pH

Figure 7.43 shows that the pH of the the leachate solution from uranium bearing glasses increases with increasing time. The pH values are approximately the same as those for the FLi ZrO_2 glass series (see **Section 4.7.3**).

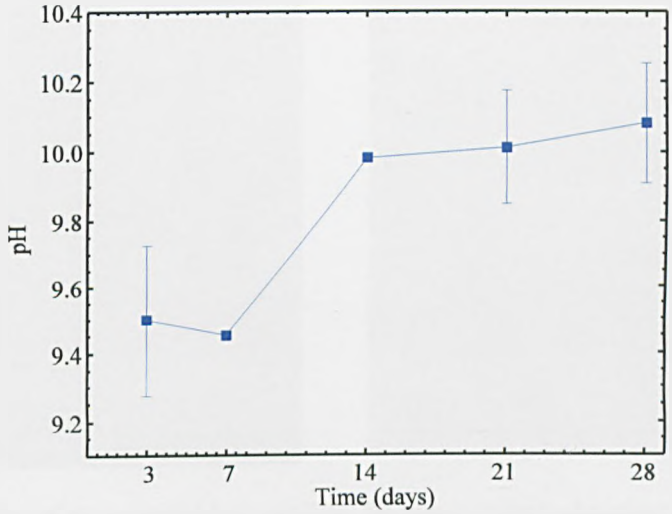

Figure 7.43: Change in pH with a) time for selected sample compositions.

7.1.3 Secondary phases formed

The radioactive nature of the U bearing leached glasses meant that no SEM was possible for any of the samples. Optical microscopy was used instead to provide high magnification images of the leach layers. Images of the glass leach layers can be seen in **Figure 7.44**. These show that the UO_3 bearing glasses behave very differently than the ZrO_2 bearing glasses. At no time during leaching was a gel layer observed to form on the surface of the glasses. However, on the top surface of the glasses a crystalline deposit was formed (see **Figure 7.44** and **Figure 7.46**) which increased in size with longer leaching. The other surfaces showed no visible indication of the presence of crystalline phases or leach layer. This indicates that the crystalline material has reprecipitated on to the only available surface and that it is not strongly chemically bound to the glass. An XRD trace of the phases formed can be seen in **Figure 7.45**. There are a large number of difficult to distinguish phases present. Among them may be sodium and lithium uranates, uranium borate, hydrated sodium uranyl silicates and hydrate a uranium oxide (studtite).

Visual inspection also showed the presence of suspended gel like particles in the leachate after only short periods of time (**Figure 7.44a**). These particles would not have passed through the filters used to extract leachate for testing and so would not appear in leachate analysis. Such suspended particles have been seen previously by Buck *et al.* (1999) who saw hydrated potassium uranyl silicate (Weeksite) compound within the leachate of full scale waste glasses from Savannah River.

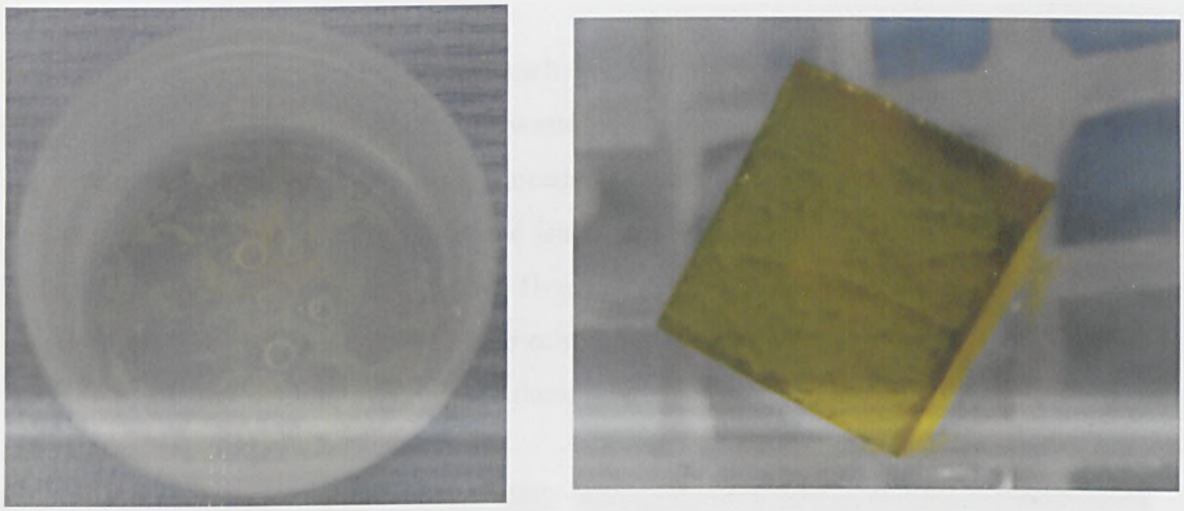

Figure 7.44: Images of a) the leaching pot (ca. 50 mm across) showing yellow colloidal phase and b) glass monolith (ca. 1 cm across) showing white material deposited on the top surface.

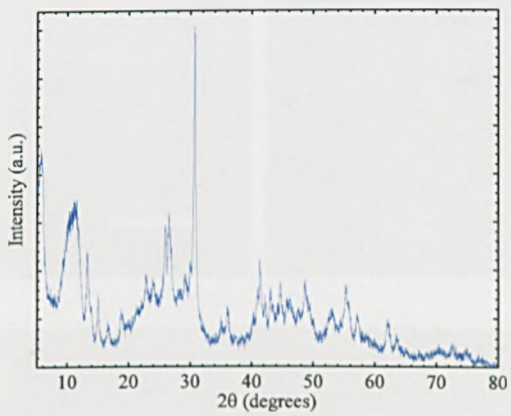

Figure 7.45: White phase that formed on the surface on the uranium bearing glasses. This phase formed after only 3 days.

The lack of observable leach layer formation suggests that addition of UO_3 to the glass may cause destabilisation of the leach layer. An explanation of this may be seen if the structures of the crystalline compounds of U are examined. In general the presence of an alkali or alkaline earth cation is required to charge balance uranyl oxygen ions. The only alkalis available within the glass are Na and Li and these elements are not retained in the leach layers. Charge compensation has also been shown to come from 4 co-ordinated boron (see **Section 8.2**) for example the mineral uranium borate $(U(BO_3)_2$, however B is also not held in the leach layer. Some phases also form using water ions (hydrogen bonds) in a charge compensating role (e.g. coffinite $U(SiO4)_1$.

$_x(OH)_{4x}$).

In order to reduce this effect elements such as Mg may be added to the glass. Mg is often stabilised within the leach layer or nuclear waste glasses and may be able to stabilise the uranyl species within the leach layer. More work is needed to establish this possibility.

The lack of leach layer formed during the leaching of the uranium containing glass examined here means that no passivating layer forms. Hence, there is no diffusion barrier for alkali, boron and silicon ions. The colloids formed in the solution may act as a "sink" for the other elements (see **Section 2.2.2** for details) providing the thermodynamic potential for the removal of elements from the glass.

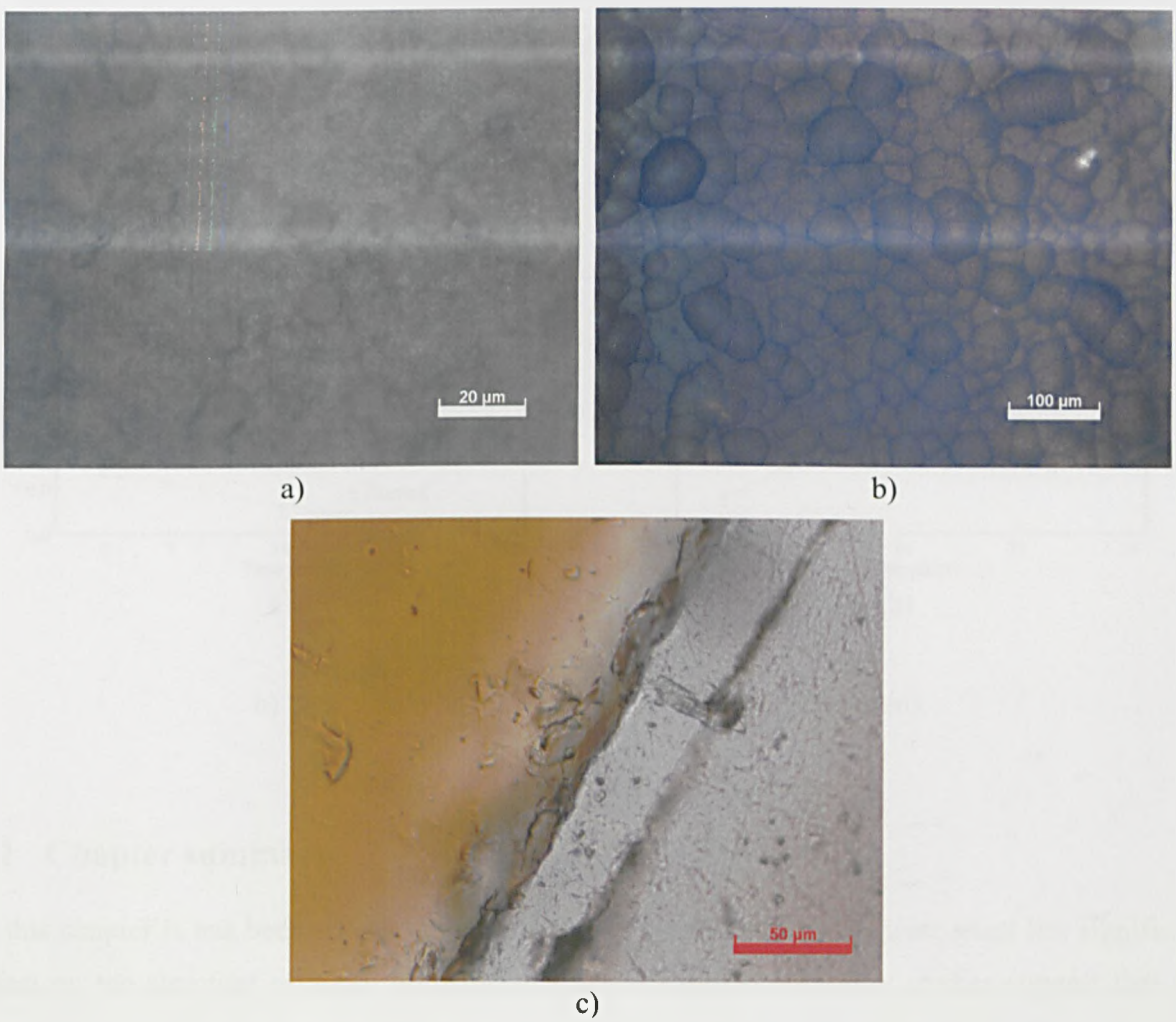

a) b)

c)

Figure 7.46: Optical microscopy [U-6] of a) surface of the white crystalline deposit and the surface under the deposit and b) cross section showing (left to right) glass, deposit, and epoxy resin (NB no leach layer is seen).

In order to investigate the composition of the colloids two sets of leachates were analysed using ICP (see **Section 3.4.3**) one set had been treated as all other samples in this study, and was filtered (see **Section 3.6.3**). The other set had not been filtered. The results for the filtered and non-filtered, within error, for B, Na, and Li were the same. However, for U and Si there was a significant difference between filtered and non-filtered. **Figure 7.47** shows that filtering removes significant quantities of U and some Si from the leachate, although for the Si the difference is still within errors. This suggests that the U is forming hydrated uranyl colloid phases (and perhaps some hydrated uranyl silicates) within solution. It is suggested that it is formation of this phase that is driving leaching of the glasses. The main hydrolyzed species of UO_2^{2+} at 25°C are UO_2OH^+, $(UO_2)_2(OH)_2^{2+}$ and $(UO_2)_3(OH)_5^+$, at higher temperatures the monomer is most stable (Cotton *et al.* 1999).

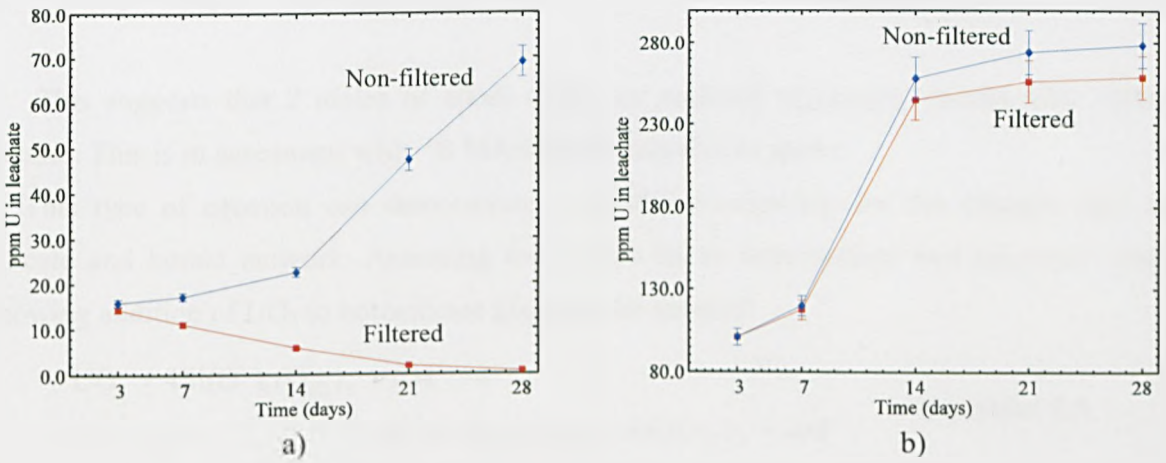

Figure 7.47: Concentration (ppm) of a) U and b) Si in a filtered and non-filtered leachate (±5 ppm).

7.2 Chapter summary

In this chapter is has been shown that addition of U to an alkali borosilicate glass has significant effect on the structure of alkali borosilicate glasses. Limited durability studies suggest that the presence of UO_3 weakens the gel layer which may lead to increased leaching. More work is needed to confirm this. The effect of UO_3 addition on the physical properties of the glasses appears mixed.

7.2.1 Structure

The decrease in ^{IV}B fraction indicates that UO_3 requires charge compensation. From **Figure 7.20,** 2 moles of alkali oxide are required to charge compensate UO_3 within the borosilicate glass. From ^{29}Si MAS-NMR it is suggested that either there is an increase in Q^3 species or an increase in $Q^4(U)$ species. More work is required to better analyse the ^{29}Si MAS-NMR spectra. ^{29}Si MAS-NMR spectra for uranyl silicate crystalline materials need to be obtained to find chemical shifts for $Q^4(U)$, Q4(2U 2Si) etc. This would allow more complete deconvolution of the spectra.

The similarity of the XANES spectrum for $Na_2U_2O_7$ and that for a typical glass indicates that average number of equatorial oxygen ions is 6 for the glasses. The number of alkali ions that are theoretically required for charge compensation of UO_3 in the form of a uranyl group with 6 O_{eq} can be shown with some a simple oxygen balancing equation.

$$UO_3 + 2M_2O \rightarrow U(=O)_2(O_{1/2})_6 + 4M^+ \qquad \textbf{Equation 7.4}$$

This suggests that 2 moles of alkali oxide are required to charge balance UO_3 within the glasses. This is in agreement with ^{11}B MAS-NMR data shown above.

This type of equation can demonstrate a possible mechanism for the changes seen in the silicate and borate network. Assuming the U acts as an intermediate two simplistic reactions showing addition of UO_3 to borosilicate glass can be derived:

$$UO_3 + 4Si(O^-)_1(O_{1/2})_3 + 4M^+ \rightarrow U^{6+}(=O)_2(O_{1/2})_6 + 4Si(O_{1/2})_4 + 4M^+ \qquad \textbf{Equation 7.5}$$

$$UO_3 + 4B^{3+}(O_{1/2})_4 + 4M^+ \rightarrow U^{6+}(=O)_2(O_{1/2})_6 + 4B(O_{1/2})_3 + 4M^+ \qquad \textbf{Equation 7.6}$$

The change in ^7Li spectra indicate that the addition of UO_3 significantly changes the environment of the Li ion. There is no direct evidence of changes in the ^{23}Na spectra but the lack of change in the monoalkali (Na glasses) (see **Figure 7.33**) indicates that either a different structure is present with Li (giving a large change in the Li environment) or that, more likely, ^{23}Na MAS-NMR is insensitive to the change. The similarity between the XANES spectra for the layered alkali uranates and the glasses may indicate that the $[UO_2]^{2+}$ may form similar groups within the glass (see **Figure 7.12**). This is supported by the ^7Li MAS-NMR peak shift which shows a new peak at a peak shift similar to that of $Li_2U_2O_7$ (see **Figure 7.31**).

The similarity in environment of U in layered alkali uranates and that in the glasses studied here indicates a possible structural model. The similarity between the structure of the alkali uranates and the alkali channels proposed by Greaves *et al.* (1981) indicates that U maybe present in these channels. This would allow U to fill up interstitial holes within the glass network, this would lead to the large increase in density seen in **Section 7.2**. This possibility is discussed more in **Chapter 8.**

7.2.2 Redox

The results shown from XANES, EXAFS and optical spectroscopy are all consistent with U being present in the glass as predominantly U^{6+} in the uranyl form $[UO_2]^{2+}$.

Optical spectroscopy data have shown that there is a small amount of U^{5+} present in the glass. An attempt was made to quantify this level with EELS (Electron Energy Loss Spectroscopy) but change in redox with beam damage and the limited access time available to the microscope made this difficult. For this reason, the results are not shown.

The interactions that U, Cr and Fe were found to undergo are shown to be as follows:

- U and Fe, no observable interaction;
- U and Cr, $3U^{5+}_{(melt)} + Cr^{6+}_{(melt)} \rightleftharpoons 3U^{6+}_{(melt)} + Cr^{3+}_{(melt)}$;
- Fe and Cr, $3Fe^{2+}_{(melt)} + Cr^{6+}_{(melt)} \rightleftharpoons 3Fe^{3+}_{(melt)} + Cr^{3+}_{(melt)}$.

This result is as expected if the relative redox potential of U, Fe and Cr are taken into account (see **Figure 7.48**). At an atmospheric $-\log fO_2$ (ca. 0.7) it is clear that the Cr will oxidise both U and Fe. Also, the close proximity of U and Fe would indicate limited interaction.

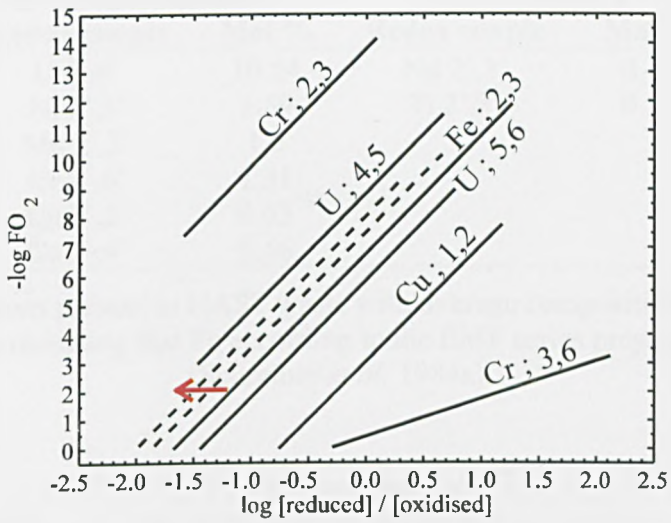

Figure 7.48: Change in redox of various multivalent ions with oxygen fugacity. Dashed lines indicate increasing Fe_2O_3 content (1wt%, 5wt%, and 10wt% increasing with arrow). After Schreiber *et al.* (Schreiber *et al.* 1984).

The high Cr content of the simplified HAST waste glass and the highly oxidising nature of the Cr^{6+} ion indicates that all of the U present in the glasses will be present as U^{6+}. It also suggests that all the Fe will be present at Fe^{3+}. As a result the majority of the Cr will be present as Cr^{3+}. **Table 7.2** shows the ions redox couples present in the HAST waste streams which are more, or less oxidising than Fe^{2+}/Fe^{3+} couple. This table shows that the glass is highly oxidising and will give U^{6+} and Fe^{3+} as the major redox states. The presence of Fe^{3+} has a significant effect on the processing properties of the glass changing viscosity and melting temperature (see **Section 2.4.4**). The presence of Cr^{3+} is undesirable as it can lead to spinel formation (see **Section 2.4.3)** which can adversely effect durability due to segregation of elements which can improve glass durability (e.g. Al). Formation of spinels can also adversely effect melter operation due to the formation of a high density "heel" in the bottom of the melter as a result of settling of the high density crystalline phases.

More oxidising than Fe		Less oxidizing Fe	
Redox couple	**Mol %**	**Redox couple**	**Mol %**
$U^{5+},^{6+}$	10.54	$Nd^{2+},^{3+}$	0.47
$Ni^{2+},^{3+}$	1.59	$Ti^{2+},^{3+}$	0.16
$Mn^{2+},^{3+}$	1.5		
$Cr^{3+},^{6+}$	1.31		
$Cu^{1+},^{2+}$	0.63		
$Ce^{3+},^{4+}$	0.56		

Table 7.2: Cations present in HAST waste with average composition (mol%) which are more or less oxidising that Fe according to the EMF series presented by Schreiber (Schreiber *et al.* 1984a).

7.2.3 Durability

Only limited investigations into the durability of alkali borosilicate glass with addition of UO_3 were carried out in this work. UO_3 appears to have a detrimental effected on the leach layer of the glasses.

It is proposed that the presence of UO_3 within the glass and during leaching prevents or inhibits the formation of the gel layer. It would be expected that U is integrated into the leach layer in a similar way to Zr, however, U (and possibly Si) form hydrated colloidal phases within the leachate. The formation of colloidal phases is a potentially significant problem as would act as a "sink" phase, removing U from solution and so providing a driving force for more U leaching.

8 Discussion

8.1 Introduction

Initial discussions have been presented at the end of each of the results chapters in this work (see **Chapters 4, 5, 6** and **7**). In this Chapter a concluding discussion of all the results in this work is presented. Ideas and results will be brought together to allow comparison between ZrO_2 additions and UO_3 additions and their effect on glass structure and physical properties. Also, discussion on the agreement between MD simulations and laboratory determinations of glass structure is presented with a consideration of what can be learnt from using both these techniques in combination.

The development and presentation of theories and ideas on experimental evidence must always be approached with care. The nature of a scientific theory or idea means that it can only ever be valid within certain boundaries and under a certain set of circumstances. Thus, it is important to be aware of these boundaries as extrapolation of a theory outside a known set of boundaries may lead to an incorrect conclusion. It is also important that all supporting and detracting evidence is considered.

This Chapter will begin with a discussion of glass structure relating to Zr and U in terms of bond valence. This will be presented with reference to the literature discussed in **Chapter 2** and set in the context of the the present knowledge of glass structure and properties.

8.2 Bond valence

Before discussing the possible structural environments for U and Zr in alkali borosilicate glasses it is useful to examine which environments are likely, and which are unlikely, to occur. A discussion of glass structure was presented in **Section 2.2**.

The use of bond valence (BV) values (see **Appendix A**) provides an insight to the validity of certain structural arrangements. Although originally designed for crystalline materials, BV

concepts still have relevance for glasses. For the purpose of this project a simplified form of the Pauling bond valence model will be used (Pauling 1929). That is: the sum of the bond valences relating to a bridging oxygen must be close to the theoretical value of 2.0 valence units (vu[1]) (Brown2002). The bond valence will be calculated with the following equation (Brese & O'Keeffe 1991):

$$v_{iO}=\exp[(R_{iO}-d_{iO})/b] \qquad \textbf{Equation 8.1}$$

where v_{iO} is the valence of the bond between cation i and oxygen, R_{iO} is the bond valence parameter for oxides of cation i, d_{iO} is the cation i - oxygen bond length (Å), and b is a constant generally taken as 0.37 Å (Brese & O'Keeffe 1991), for uranium valence calculations alternative values for R_{iO} *and* b are taken from Burns *et al.* (Burns *et al.* 1997) (see **Table 10.1**).

When calculating BV, values of d_{iO} are taken either from experimental data presented by the author or by addition of the ionic radii of the cation of interest (of known co-ordination number and valence) to that of $^{III}O^{2-}$ (1.36 Å), with ionic radii obtained by Shannon (Shannon 1976, Ellison & Hess 1994).

For an unstrained structure the total bond valence should be within ±0.05 vu of 2.0 vu. Structures with BV outside this range can exist but are generally strained and potentially unstable (Brown 2002). For example, using the values set out in **Table 8.1**, a BO (Si-O-Si) gives a total bond valence of 2.02 vu which is with ±0.05 vu of 2.0 vu. The BV values shown in **Table 8.1** and **Table 8.2** are used here to calculate possible structural arrangements around U and Zr atoms.

The analysis presented below can only be used as a guide to what environment is possible under bond valence rules, it does not necessarily follow that this environment will occur, only that it is 'chemically sensible'.

Cation	d_{iO}	v_{iO}	Cation	d_{iO}	v_{iO}
$^{IV}Si^{4+}$	1.62	1.01	$^{VI}Na^{+}$	2.38	0.21
$^{III}B^{3+}$	1.37	1.00	$^{IV}Li^{+}$	1.95	0.27
$^{IV}B^{3+}$	1.47	0.77			

Table 8.1: Bond lengths (Å) and bond valences for a selection of cations. Bond length (d_{iO}) calculated as sum of ionic radii. R_{iO} (used to calculate v_{iO}) values taken from (Brown 2007) see **Table 10.1**.

[1] vu = valence unit. One valence unit is equal to the charge of one electron or the flux generated by the charge of one electron (Brown 2002).

Cation	d_{iO}	v_{iO}	Cation	oxygen	d_{iO}	v_{iO}
$^{VI}Zr^{4+}$	2.08 (2.09)	0.66 (0.65)	U^{6+}	O_{Ur}	(1.92)	(1.27)
$^{VII}Zr^{4+}$	2.14	0.56	U^{6+}	O_{eq}	(2.31)	(0.59)
$^{VIII}Zr^{4+}$	2.20	0.48				

Table 8.2: Bond lengths (Å) and bond valences for a selection of cations. Bond length (d_{iO}) calculated as sum of ionic radii . R_{iO} (used to calculate v_{iO}) values taken from (Shannon1976). Values in parentheses are taken from experimental values presented in this thesis.

8.2.1 Zirconium

The environment around Zr was discussed in **Chapters 4 and 6**. Both laboratory evidence presented here, and literature data, show the presence of ^{VI}Zr with alkali and / or Si ions cations as next nearest neighbours. Evidence is also shown for the presence of higher co-ordinated ^{VII}Zr and ^{VIII}Zr and these will also be considered. Simulation data presented in this work shows the presence of B and Li. The values for bond valence sums of relevance to the discussion below can be found in **Table 8.3**.

The presence of Si as a next nearest neighbour to Zr would indicate ^{VI}Zr-O-^{IV}Si bonds giving a BV, for this arrangement, of 1.66 vu. This value is much less than 2.00 vu and so this bond requires a contribution from an alkali cation for charge compensation. Thus, ^{VI}Zr-O-^{IV}Si + ^{IV}Li = 1.93 vu and ^{VI}Zr-O-^{IV}Si + ^{VI}Na = 1.87 vu indicating that ^{IV}Li is marginally the preferred charge balancing cation as the resulting BV is closer to 2.00. The presence of ^{VI}Zr-O-^{III}B bonds gives a BV for the oxygen of 1.65 vu and for ^{VI}Zr-O-^{IV}B a BV of 1.42 vu. This indicates, again, that a contribution from alkali ions is required for charge compensation. In fact, it indicates that ^{III}B is more likely to bond to ^{VI}Zr than ^{IV}B as a lower contribution from the alkali ions is required to increase the value of the oxygen BV to ca. 2. Based on the BV model presented above each ^{VI}Zr ion requires ca. 2.1 alkali ions to charge balance 6 bridging oxygen ions to either ^{IV}Si or ^{III}B.

The co-ordination of ^{VII}Zr requires a larger contribution from alkali ions for charge balancing than ^{VI}Zr due to the low BV of ^{VII}Zr (see **Table 8.2** and **Table 8.3**). For silicate bonding more than one alkali ion contribution is required: ^{VII}Zr-O-^{IV}Si + 2(^{IV}Li) = 2.11 vu and ^{VII}Zr-O-^{IV}Si + 2(^{VI}Na) = 1.99 vu. This is also the case for the borate bonding: ^{VII}Zr-O-^{III}B gives 1.55 vu and ^{VII}Zr-O-^{IV}B 1.32 vu in this case it is even more difficult to achieve charge compensation (see **Table 8.3**). This indicates that a ^{VII}Zr species requires ca. 3.1 alkali ions to charge balance 7 bridging oxygen ions to either Si or ^{III}B.

For ^{VIII}Zr the low BV may be too low to consider alkali charge compensation. From **Table 8.3** it

can be shown that ^{VIII}Zr requires contribution from ca. 4.1 alkali ions to charge balance 8 bridging oxygen ions to either Si or ^{III}B. For this reason, Zr-O-Zr bonding may occur. For example 2(^{VIII}Zr)-O-^{IV}Si gives a bond valence of 1.96 vu (as is seen in zircon **Figure 8.1**). Work by Watson (1979) showed that for highly polymerised glasses there was a propensity for zircon crystallisation. Work by Farges *et al.* (Farges1991) suggests the presence of zircon like units in highly polymerised aluminosilicate glasses with the presence of Zr-O-Zr bonds. The bond valence model presented gives a good model for the propensity of zircon crystallisation from highly polymerised glasses and also the low solubility of ZrO_2 in such glasses.

Species	BV (vu)	Charge comp.	BV (vu)
^{VI}Zr-O-^{IV}Si	1.66	^{VI}Na	1.87
		^{IV}Li	1.93
^{VI}Zr-O-^{III}B	1.65	^{VI}Na	1.86
		^{IV}Li	1.92
^{VI}Zr-O-^{IV}B	1.42	2(^{VI}Na)	1.84
		2(^{IV}Li)	1.96
^{VII}Zr-O-^{IV}Si	1.57	2(^{VI}Na)	1.99
		2(^{IV}Li)	2.11
^{VII}Zr-O-^{III}B	1.56	2(^{VI}Na)	1.98
		2(^{IV}Li)	2.10
^{VII}Zr-O-^{IV}B	1.33	3(^{VI}Na)	1.96
		2(^{IV}Li)	1.87
^{VIII}Zr-O-^{IV}Si	1.49	2(^{VI}Na)	1.91
		2(^{IV}Li)	2.03
^{VIII}Zr-O-^{III}B	1.48	2(^{VI}Na)	1.90
		2(^{IV}Li)	2.02
^{VIII}Zr-O-^{IV}B	1.25	4(^{VI}Na)	2.09
		3(^{IV}Li)	2.06
(2^{VI}Zr)-O-^{IV}Si	2.31		
(2^{VI}Zr)-O-^{III}B	2.3		
(2^{VI}Zr)-O-^{IV}B	2.07		
(2^{VII}Zr)-O-^{IV}Si	2.13		
(2^{VII}Zr)-O-^{III}B	2.12		
(2^{VII}Zr)-O-^{IV}B	1.89		
(2^{VIII}Zr)-O-^{IV}Si	1.97		
(2^{VIII}Zr)-O-^{III}B	1.96		
(2^{VIII}Zr)-O-^{IV}B	1.73	^{VI}Na	1.94
		^{IV}Li	2.00

Table 8.3: Bond valence values for species of relevance to this work.

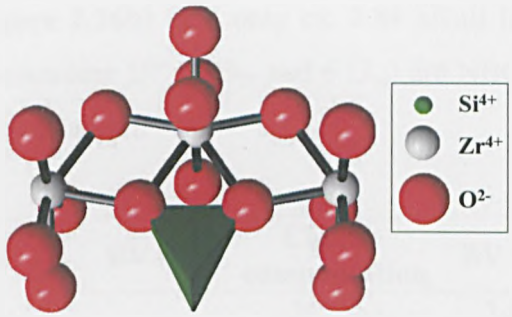

Figure 8.1: Bonding of ^{VIII}Zr units in zircon to silicate tetrahedra (in green).

8.2.2 Uranium

The structural environment around U in an alkali borosilicate glass was discussed in **Chapter 7**. The results presented in this thesis are consistent with literature data that demonstrates the presence of uranyl (UO_2^{2+}) species as dominant in alkali borosilicate glasses. Beyond the first uranyl (and equatorial) oxygen shell, little is known of the structure around the U atom. The values for bond valence sums of relevance to the discussion below can be found in **Table 8.4**.

The two types of U-O bond around the U give different v_{io} values, with the uranyl oxygen ions giving a BV of 1.27 vu indicating that they require contributions from approximately three alkali ions to stabilise (e.g. $U_{ur}{=}O^{-2}$ $3(^{VI}Na^{+})$ = 1.90 vu). It is unlikely that Si or ^{III}B will bond to the uranyl oxygen ions as it would lead to over bonding (see **Table 8.4**). However, ^{IV}B may bond to O_{Ur} (see **Table 8.4**).

The equatorial oxygen ions (O_{eq}) around the uranyl group are available for bonding to the silicate or borate network. If Si or B is directly bonded to the O_{eq} the BV values on the oxygen ion would be: U-O-^{IV}Si = 1.6 vu; U-O-^{III}B = 1.59 vu; and U-O-^{IV}B = 1.36 vu. To stabilise this bond a contribution from 1 - 2 alkali cations is required: e.g. U-O-^{IV}Si + 2(^{VI}Na) = 2.02 vu. ^{IV}B seems less likely to bond to U as it would require contributions from 2 - 3 alkali ions; U-O-^{IV}B + 3(^{VI}Na)= 1.96 vu (see **Table 8.4**).

The possibility for U-O-U (1.18 vu) bonding is also present, but this requires either contributions from 3 - 4 alkali ions (U-O-U + 3(^{IV}Li) = 1.99 vu). Thus, a more likely arrangement is the presence of 2(U)-O-U bonding (1.77 vu) which requires just one alkali ions to charge balance.

Assuming the absence of any U-O-U linkages the number of alkalis required to charge compensate a U^{6+} ion with 2 uranyl oxygen ions (as NBO) and 6 O_{eq} (as BO to either ^{IV}Si or ^{III}B) is ca. 3.89 alkali cations. If all the O_{eq} were linked to other uranyl goups (i.e. U_{eq}-O-U_{eq}) (seen in

structure of alkali uranates - **Figure 2.16b**) then only ca. 2.84 alkali ions are required. If it is assumed that all oxygen ions surrounding U^{6+} (2 O_{Ur} and 6 O_{eq}) are NBO then ca. 9.9 alkali ions would be required for charge compensation.

Species	BV (vu)	Charge compensation	BV (vu)
U_{Ur}-O^{2-}	1.27	3(^{VI}Na) 3(^{IV}Li)	1.90 2.08
U_{Ur}-O-^{IV}Si	2.28		
U_{Ur}-O-^{III}B	2.27		
U_{Ur}-O-^{IV}B	2.04		
U_{eq}-O-^{IV}Si	1.6	2(^{VI}Na) 2(^{IV}Li	2.02 2.14
U_{eq}-O-^{III}B	1.59	2(^{VI}Na 2(^{IV}Li	2.01 2.13
U_{eq}-O-^{IV}B	1.36	3(^{VI}Na) 2(^{IV}Li)	1.99 1.9
U_{eq}-O-U_{eq}	1.18	4(^{VI}Na) 3(^{IV}Li)	2.02 1.99
($2U_{eq}$)-O-^{IV}Si	2.19		
($2U_{eq}$)-O-^{III}B	2.18		
($2U_{eq}$)-O-^{IV}B	1.95		
($2U_{eq}$)-U_{eq}	1.77	^{VI}Na ^{IV}Li	1.98 2.04

Table 8.4: Bond valence values for species of relevance to this work.

8.2.3 Summary

The above bond valence sums show that the structural model ZrO_2 shown in **Chapters 4** and **6** is chemical sensible. With the requirement for charge balancing with alkali when bonding to either the silicate or the borate network.

For U the bond valence modelling shows that both the O_{Ur} and the O_{eq} require charge balancing to bond to the silicate, borate or uranate networks. This would indicate that the role of U is similar to that of ZrO_2, acting as an intermediate; however, it requires more alkali ions for charge balancing. The number of alkali ions required to charge balance a ^{VI}Zr ion within the glass network is ca. 2. This analysis supports the analysis shown below in **Equation 8.2**. The number of alkali ions required to charge balance the U^{6+} ion with BO is 3.89 which is very similar to that seen in **Equation 8.5** with 6 O_{eq} where 4 alkali ions are required. If clustering of the uranyl species (i.e. formation of 2(U_{eq})-U_{eq} bonds) a minimum of 2.8 alkali ions are required.

8.3 Vitrification of high ZrO_2 waste streams

There are several problems encountered in the vitrification of waste streams high in ZrO_2 (see **Section 2.4.1**). The most significant of these is the low solubility of ZrO_2 in waste glasses, its tendency to devitify the glass, and the high viscosity it produces on addition to alkali borosilicate glasses.

Work by Watson (Watson 1979) showed that the level of alkali ions within a silicate glass has a direct link to the solubility of ZrO_2. The results presented in **Chapter 4** and **6** show that this is also the case in borosilicate glasses and quantification of this effect is shown. Knowledge of this ratio allows, in principle, any amount of ZrO_2 with an appropriate quantity of M_2O to be added to an alkali borosilicate glass with guaranteed complete solution of the ZrO_2[1]. The effect of such a relationship on processing properties will be discussed below.

8.3.1 The structural role of Zr in the glass structure

The combined use of laboratory and Molecular Dynamics (MD) experiments has allowed the environment of Zr to be defined within a glass. The majority of Zr atoms within the alkali borosilicate glasses investigated here have 6 oxygen ions in the first co-ordination shell. The next nearest neighbours are then thought to be Si and ^{III}B (less likely ^{IV}B). Within this shell there must also be at least 2 alkali ions to provide charge compensation.

A schematic of a possible atomic arrangement is shown in **Figure 8.2** which shows the ^{VI}Zr with BOs to Si and ^{III}B. Alkali ions are present to demonstrate change balancing.

[1] This is based on a consideration of structure, but the kinetics may be slow.

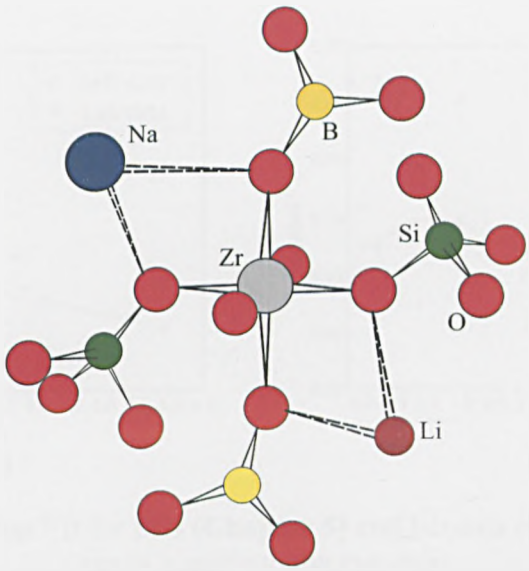

Figure 8.2: Proposed structure of atoms around the Zr atom. The sodium ions are included in a charge balancing role. For clarity not all Zr co-ordinated oxygens are shown as BO, in a glass all Zr co-ordinated oxygens would be BO.

8.3.2 Effect of Zr on bulk glass structure

The non-linear change in ^{IV}B fraction with increasing ZrO_2 for HLi and FLi glasses is seen from both ^{11}B MAS-NMR data (see **Section 4.6.1**) and, in more detail, from MD simulations (see **Section 6.3**). Results from both the MAS-NMR and MD show a similar trend; however, the effect is more pronounced in the laboratory glasses (see **Figure 8.3**). There are several possible explanations for this:

1. Differences in composition between laboratory and simulated glasses;
2. In **Section 4.8.1** it was proposed that the increase in ^{IV}B fraction is due to small scale phase separation. If this is the case, the quench rate of the simulated glasses is much higher than that of the laboratory glasses and so the level of phase separation will be much reduced in the MD glass. This is discussed in more detail below;
3. There is an increase in the average Zr co-ordination in the laboratory glasses (ca. 6.3) over that seen in the MD glasses (ca. 5.8), this may increase the effect of changing ^{IV}B fraction.

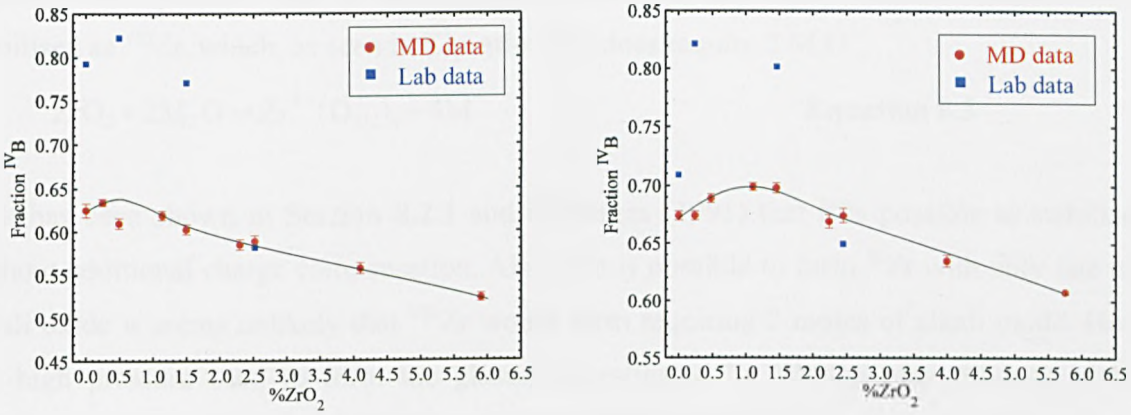

a) HLi b) Fli

Figure 8.3: Fraction ^{IV}B for MD (**Chapter 5**) and lab data (**Chapter 6**). Lines are as a guide to the eye only.

Addition of ZrO_2 would be expected to remove alkali oxide from its charge compensating role in the borate network and so decrease ^{IV}B fraction. However, in the FLi and HLi glasses the ^{IV}B fraction initially increases.

The ratio of alkali oxide to ZrO_2 required to achieve charge compensation is an important value when developing glass compositions for vitrification of high ZrO_2 waste streams. From ^{11}B MAS-NMR and MD it has been shown that at least 1 mole of alkali oxide is required per mole of ZrO_2. ^{29}Si MAS-NMR and MD modelling has shown that there are significant changes in the silicate network with ZrO_2 addition. Although difficult to quantify from MAS-NMR the MD and MAS-NMR evidence suggests an increase in $Q^4(Zr)$. Evidence from MD is conflicting, from changes in ^{IV}B fraction only 1 mole of alkali oxide is required for change compensation. However, from Q^n average 1.5-2 moles are required. A simple charge balancing equation suggests that only one mole of alkali oxide is required which is supported by the bond valence calculations shown in **Section 8.2**:

$$ZrO_2 + M_2O \rightarrow Zr^{4+}(O_{1/2})_6 + 2M^+ \qquad \textbf{Equation 8.2}$$

This suggests that either more alkali oxide is required to charge balance ZrO_2 than simple charge balancing rules (and bond valence rules) indicate or the simulation average Q^n data (or analysis there of) is misleading. Previous studies from the literature have given ratios of 1:1 and 2:1 M_2O : ZrO_2 (see **Section 2.4.1**). The value of 2:1 was suggested by Watson (Watson 1979)

however, it is possible that in these glasses (produced at 2 kbar) Watson measured Zr being stabilised as ^{VIII}Zr, which, as seen in **Equation 8.3** does require 2 M_2O.

$$ZrO_2+2M_2O\rightarrow Zr^{4+}(O_{1/2})_8+4M^+ \qquad \textbf{Equation 8.3}$$

It has been shown in **Section 8.2.1** and by Farges (1991) that it is possible to stabilise ^{VIII}Zr without additional charge compensation. Also, if it is possible to form ^{VI}Zr with only one mole of alkali oxide it seems unlikely that ^{VIII}Zr would form requiring 2 moles of alkali oxide. However, the high pressure used to form the glasses investigated by Watson may produce higher co-ordination environments for Zr as higher co-ordination numbers are typically favoured at higher pressures.

The conclusion of this analysis is that, although only one mole of alkali oxide is strictly required to charge compensate ZrO_2, there is some evidence that more than one mole of alkali oxide is required for the stabilisation of ^{VI}Zr within a (boro)silicate glass. If this is the case one possibility is that the extra alkali oxide is required to relax the network around the Zr to allow the presence of a 6 co-ordinate bridging species.

Another possibility is the presence of NBOs on the Zr atom (see **Equation 8.4**). Evidence from MD suggests that all oxygen ions on the Zr are BO. However, if this is incorrect and there are NBOs it would take the presence of only two NBOs to give a M_2O : ZrO_2 of 2:1 as shown by Watson (1979).

$$ZrO_2+2M_2O\rightarrow Zr^{4+}(O_{1/2})_4(O^-)_2+4M^+ \qquad \textbf{Equation 8.4}$$

8.3.3 Effect of Zr on durability

It is has been shown above that there is a non-linearity in the fraction of ^{IV}B with increasing ZrO_2 for the FLi and HLi glasses. A similar non-linearity can be seen in the durability data presented in **Chapter 4** (see **Figure 8.5**). It is generally accepted that increasing ^{IV}B increases durability of alkali borosilicate glasses due to increased network polymerisation (Marples 1988). However, in these glasses this concept is challenged by two observations:

1. Increasing ZrO_2 content in both FLi and HLi glasses leads to an overall increase in durability but a decrease in ^{IV}B;
2. The initial small increase (at low ZrO_2 contents) in ^{IV}B in the glasses leads to a decrease in durability.

These two observations suggest that the effect of large additions of ZrO_2 to a glass has a greater effect on durability than the fraction ^{IV}B. In addition the low ZrO_2 glasses, there is a more complex mechanism occurring.

A possible mechanism for this process is suggested in **Section 4.8.2**. The effect of decreasing durability at low ZrO_2 contents within an alkali borosilicate glass has been observed before within a sodium borosilicate glass by Lobanova *et al.* (Lobanova2002) (see **Section 2.4.1**). The composition of this glass in terms of *R* and *K* can be seen in **Figure 8.4**. The presence of the Lobanova glass composition lies between HLi and FLi. This suggests the same effect may be occurring in the Lobanova glass as in the FLi and HLi glasses.

The mechanism suggested by Lobanova *et al.* and Sicard *et al.* (Sicard2004) is based on leach layer morphology as described in **Section 2.4.1**. The work here in no way invalidates this model. However, it does suggest that the mechanism may be more complex and that the effect of glass structure on durability must be considered.

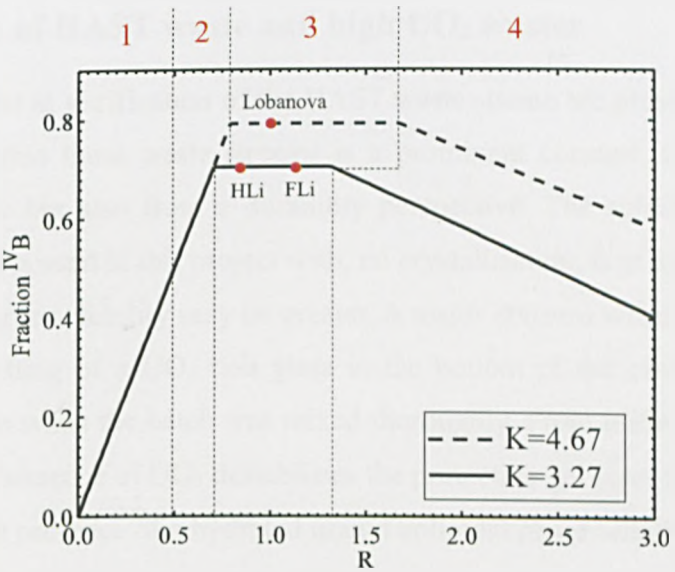

Figure 8.4: Compositions of the glasses used in this structure superimposed on Dell Bray model (Dell1983) for ^{IV}B fraction (see **Table 4.7**).

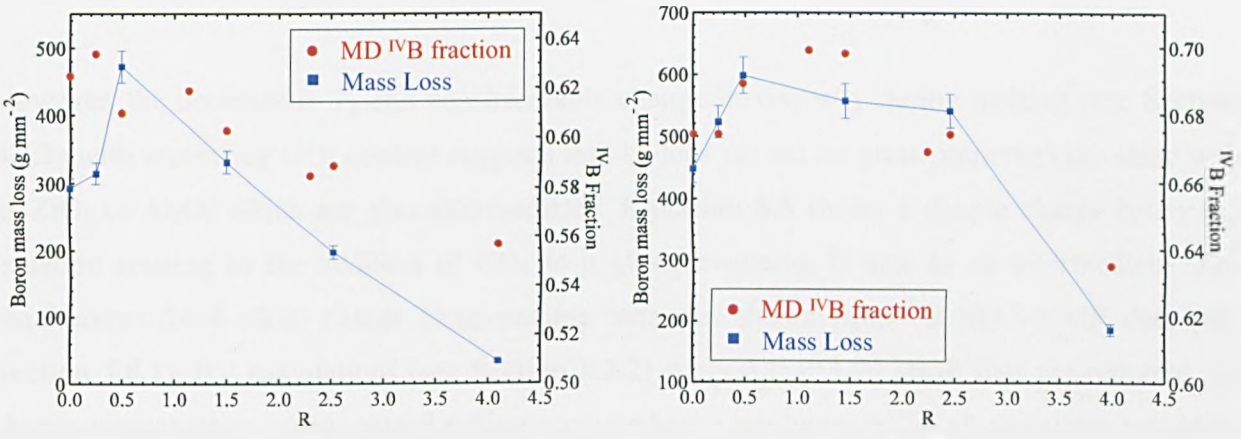

Figure 8.5: Change in boron mass loss with mol% Zr with change in ^{IV}B fraction measured from MD simulations. Lines drawn to guide the eye.

8.4 Vitrification of HAST waste and high UO_3 wastes

The problems inherent in vitrification of the HAST waste stream are presented in **Chapter 2**. The high levels of U within these waste streams is a prominent concern, initially from a uranium solubility perspective but also from a durability perspective. The solubility of UO_3 within the alkali borosilicate glass used in this project with, no crystallisation, is at least ca. 4.8 mol% (ca. 20 wt%); however, the true solubility may be greater. A major concern when melting of UO_3 bearing glasses is that of settling of a UO_3 rich glass in the bottom of the crucible which occurred in laboratory melts even when the batch was mixed thoroughly. From initial durability studies there is a concern that the presence of UO_3 destabilises the protective gel layer that forms on the surface of the glass. Also, the presence of a hydrated uranyl colloidal phase within the leachate may act as a "sink" phase.

The redox of ions within a HAST waste bearing glass has been shown to be highly oxidised due to the significant presence of Cr^{6+} (which itself is reduced).

8.4.1 Effect of U on bulk glass structure

There has been discussion within the literature as to whether U acts as a modifier or an intermediate within alkali (boro)silicate glasses. This work has shown that U acts more as an intermediate than a modifier. This is shown by:

1. a decrease in ^{IV}B fraction;

2. the possible formation of Q^4(U) species.

However, the decrease in T_g and no observable change in viscosity during melting (see **Section 3.1.2**) with increasing UO_3 content suggests that U does not act on glass properties the same way as ZrO_2 or Al_2O_3 which are also intermediates. **Equation 8.5** shows a simple charge balancing equation relating to the addition of UO_3 to a glass, assuming U acts as an intermediate. The requirement for 4 alkali charge compensating ions was shown from ^{11}B MAS-NMR data (see **Section 7.8.1**). BV calculations (see **Section 8.2.2**) suggest that 3.89 alkali ions are required for charge compensation unless uranyl rafting occurs where a minimum of 2.8 alkali cations would be required depending on the level of rafting.

$$UO_3 + 2Na_2O \rightarrow U(=O)_2(O_{1/2})_6 + 4M^+ \qquad \textbf{Equation 8.5}$$

Section 8.3.1 above shows that using a similar argument based on charge balanced equations, ^{11}B MAS-NMR results, and BV calculations the addition of UO_3 requires more charge compensating alkali ions as an equal addition of ZrO_2. For the addition of 1 mole of UO_3 to alkali borosilicate glasses it has been shown that ca. 2 moles of alkali oxide are required.

The differences in the number of alkalis required for charge compensation highlights the difference between the structural role of UO_3 and ZrO_2 within the glass network. Whereas addition of ZrO_2 tends to increase T_g, viscosity, and, at high additions, increase durability, addition of UO_3 decreases T_g, gives little observable change in viscosity, and has a deleterious effect on leach layer stability.

The structural role of ZrO_2 has been elucidated in **Section 8.3.1** showing ^{VI}Zr directly bonding to the glass network with 6 BO to Si and B. BV calculations in **Section 8.2.2** show that O_{Ur} is unlikely to bond to the glass network and requires charge compensation. However, BV calculations show that O_{eq} are able to bond to the glass network in a similar way to ^{VI}Zr.

From the results presented in this work the most likely model for the role of U within the glass network involves association with the alkali channels. Work by Greaves *et al.* (Greaves 1989) suggested U sat within the alkali channels acting as a modifier. In this work it has been shown that U acts as an intermediate within the glass requiring charge compensation from ca. 4 alkali ions. **Figure 8.6** shows a potential model for the speciation of U within these glasses showing the 6 O_{eq} bonding to the glass network the O_{Ur} being charged balanced in a similar way to that seen in alkali uranates. To simplify the diagram not all charge compensating cations are shown.

This model is supported by evidence from XANES and ^{7}Li MAS-NMR which shows a uranate like environment within the glass. Also, the requirement for charge compensating cations was shown by with ^{11}B MAS-NMR and BV calculations. This suggests that a similar structural model to that seen for ^{VI}Zr, with a bond to the glass network.

The contradictions to this model can be seen in the physical properties produced by the addition of UO_3. A model with 6 bonds to the glass network in this manner would be thought to increase properties such as T_g and viscosity (is a similar way to that for ZrO_2 additions) due to increased network polymerisation. However, the addition of UO_3 to the glass produces a small decrease in T_g and little observable change in viscosity (especially when compared to ZrO_2 at similar concentrations). This may be due to the low relative bond strength of U within these glasses. Using BV as a measure of bond strength U-O_{eq} bonds are weak (0.59) compared to ^{VI}Zr-O (0.65) and network Si-O, B-O bonds (see **Table 8.1**). This would allow easier bond breaking and so may reduce T_g *etc.*

Evidence from ^{29}Si MAS-NMR can be interpreted to support or contradict the structural model set out above. The presence of increasing Q^4(3Si,1U) species would support the model proposed, however, increasing Q^3 species would contradict the model, suggesting a more modifier like environment.

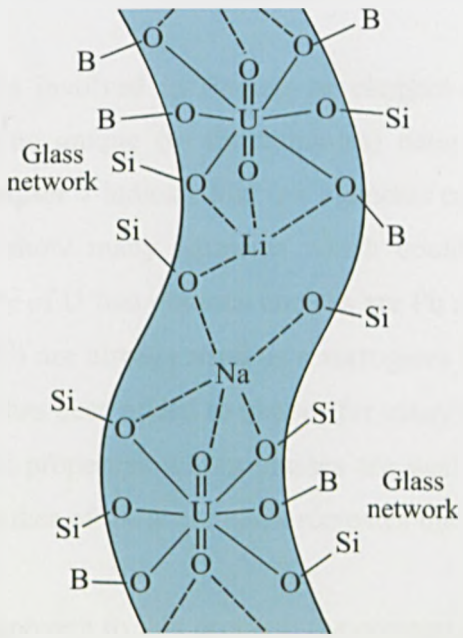

Figure 8.6: 2D schematic showing the possible structure of uranium within the alkali channels of an alkali borosilicate glass. Dashed lines indicate charge compensation (more ionic) and solid lines indicate a BO (more covalent). See text for details.

8.4.2 Surrogate for U^{6+} in glass

The radioactive and toxic nature of U, and other radioactive isotopes of concern to the nuclear vitrification industry, means that ways of gaining an understanding of how these elements interact within the vitrification process without actually using these elements is of great importance. There are two main ways of achieving this:

1. **Use of modelling:** results from this work on ZrO_2 additions to glass (and previous (Delaye & Ghaleb 1996b, Liu *et al.* 2001)) shows that it is possible to model many aspects of glass structure with computer simulation. Other forms of modelling using empirical equations have also been used (e.g. Jantzen 2005), this is discussed more in **Section 8.6**;
2. **Use of surrogate:** laboratory experiments using an element with similar properties to the radioactive element of interest. These properties can be considered dependent on:
   a. Atomic weight, important as radioactive elements are often of high atomic number leading to the components of the melt sinking within melter producing an inhomogeneous product. (e.g. Hf used as a surrogate for Pu);
   b. How an element interacts with the glass network and affects the redox of other elements within the glass has an effect on viscosity, pouring characteristics, product durability etc. (e.g. Ce used as a surrogate for the redox couple for Pu).

For uranium the difficulties involved in finding an element of similar weight and similar properties are considerable. The unique (to the actinides) nature of the uranyl bond and the properties demonstrated in **Chapter 7** indicate that few elements can have appropriate properties.

Table 8.5 and **Table 8.6** show many elements which could be considered as a possible surrogate for U. For the density of U two obvious choices are Pb and W. Tungsten/cobalt (W/Co) fragments (density ~14.5 gcm^{-3}) are already used as a surrogates for U metal (density 19 gcm^{-3}) (Schmidt & Elmore 2002). Pb has been added to glasses for many years to increase density and to increase working range and its properties within glasses are well understood (Varshneya 1994). However, it is believed that neither of these elements recreates the effect of U on the properties of alkali borosilicate glass.

To gain a more chemical approach to this problem the concept of field strength (see **Footnote on page 25**) can be used. Additions to oxide glasses are often classified using the terms network modifier, intermediate and network former (see **Section 2.2**). These classifications are often defined using field strength values. The values for some elements (and species) of interest are

shown in **Table 8.5**. With addition of U there are two types of bonding to consider, the first is to the O_{ur} which gives uranium a field strength of 1.24 (indicating an intermediate like status), the second type of bonding is to the $[UO_2]^{2+}$ ion itself which has an estimated field strength of ca. 0.60 again suggesting an intermediate type role. This conclusion is supported by MAS-NMR results presented in **Chapter 7** which suggest that UO_3 has an intermediate like nature. From **Table 8.5** and **Table 8.6** Mn^{2+} may be a good surrogate for the $[UO_2]^{2+}$ ion but clearly not for the U-O_{Ur}. More measurements of properties relating to processing parameters are needed with these glasses to choose a surrogate for density and processing properties.

Another aspect of U within the glass that is important to measure is that of redox. The results in **Chapter 7** show that the U^{6+}/U^{5+} redox couple for uranium can be modelled using the Fe^{2+}/Fe^{3+} couple. Although the redox states are different, results from **Chapter 7** show that the relative ratio of the two redox couples are similar and are affected by compositional changes (and atmospheric changes (Schreiber 1984a)).

Ion	Classification	Atomic mass	Field strength	CN[a]
W	F	183.84	1.56	6
Si	F	28.09	1.52	4
B	F	10.81	1.60	3
B	F/I	10.81	1.39	4
U	I	238	1.24	2
Al	I	26.98	0.98	4
Zr	I	91.22	0.92	6
[b]UO_2^{2+}	I/M	270.00	0.60	4
Mn	I/M	54.94	0.49	4
Fe	I/M	55.85	0.44	6
Ca	M	40.08	0.36	6
Pb	M	207.20	0.28	8
Ba	M	137.30	0.26	8
Li	M	6.94	0.26	4
Na	M	22.99	0.18	6

Table 8.5: Elemental information for $[UO_2]^{2+}$, various possible surrogate elements, and other elements of interest to this project.
[a] Most frequency observed co-ordination number (CN) in glass,
[b] CN taken assuming 4 O_{eq} however, radius for $[UO_2]^{2+}$ taken as radius of U^{6+}(6 co-ordinate) (Shannon 1976). Other information from (Webelements 2007)

Ion	Oxide density	Oxide melting temp. (°C)	Valence	Ionic radius (Å)[a]	R = d(M-O) Å, 298K [b]
W	7200	1473	6	0.6	1.96
Si	2533	2590	4	0.26	1.62
B	2550	450	3	0.01	1.37
B	2550	450	4	0.11	1.47
U	7300	1150	6	0.76	(2.20)
Al	4000	2054	3	0.39	1.75
Zr	5680	2677	4	0.72	(2.09)
Mn	5370	1785	2	0.66	2.02
[c]UO_2^{2+}	-	-	2	0.73	(1.82)
Fe	6000	1370	2	0.78	2.14
Ca	3340	2900	2	1.00	2.36
Pb	9350	888	2	1.29	2.65
Ba	5720	1973	2	1.42	2.78
Li	2013	1570	1	0.59	1.95
Na	2270	1132	1	1.02	2.38

Table 8.6: Elemental information for $[UO_2]^{2+}$, various possible surrogate elements, and other elements of interest to this project. [a] Radii from (Shannon 1976), [b] Sum of ionic radius and radius for 3-coordinated oxygen (1.36 Å), except for values in parentheses which are experimental results from this work, [c] CN taken assuming 4 O_{eq} however, radius for $[UO_2]^{2+}$ taken as radius of U^{6+}(6 co-ordinate). Other information from (Webelements 2007).

8.4.3 U and durability

Only limited studies have been carried out on the effect of U on durability. However, it has been shown that UO_3 destabilises the leach layer that was shown to form on similar glasses in **Section 4.7**. The formation of a leach layer has been shown to decrease the leach rate of alkali borosilicate glasses by acting as a passivating layer reducing ionic exchange between alkali ions and water and reducing diffusion of other ions into the leachate. Thus, a spalling of this leach layer may lead to an increase in leaching.

The presence of colloidal U (and possibly Si) species within the leachate may act as a "sink" for U, providing a driving force for removal of U from the glass and so degradation of the glass network. However, this does not explain why the leach layer is destabilised.

The reduction in stability of the leach layer with addition of UO_3 is a major concern for the immobilisation of high UO_3 contain wastes. Further work is needed to reduce the effect of leach layer destabilisation, one possibility may be charge compensation of UO_3 with the presence Al or Mg within the leach layer which are already known to stabilise the leach layer (Godon *et al.* 2003).

8.5 Bond valence and charge compensation

It has been shown above that Zr makes use of alkali oxide in the base glass for charge compensation. This alkali oxide is taken from its role in charge compensating ^{IV}B and Q^3 species. The results presented in this work indicates that it is preferential for these alkali ions to be associated with the Zr than with ^{IV}B or Q^3.

It is well documented (see **Section 2.4.1)** that in aluminosilicate glasses charge compensation of Al tetrahedra occurs before ^{III}B transforms to ^{IV}B (Cormier2000) or Q^4 species transform to Q^3 (Watson 1979). It was also shown in **Section 2.4.1** that the solubility of Zr is highly dependent on the Al / alkali ratio, indicating that Al must be charge compensated before charge compensation is available to stabilise ^{VI}Zr. This indicates an order for charge compensation preference where the highest preference is for Al and the least preference is for Q^3 ($Al>Zr>B>Q^3$). This scheme can be thought about in terms of stabilisation. Charge compensation of Al stabilises the Al from ^{VI}Al to ^{IV}Al. For Zr the alkali oxide stabilises the ^{VIII}Zr by transformation to ^{VI}Zr, since the stabilities (solubilities) of ^{VI}Al and ^{VIII}Zr are low.

Using this information, and considering the stability in terms of bond valence, a simple theoretical model can be proposed. The difference between the bond valence of a co-ordination number stable in the glass without alkali charge compensation (e.g. ^{III}B) and the bond valence of the charge compensated environment (e.g. ^{IV}B) is taken. This gives the values shown in **Table 8.7**. A similar calculation can be performed for the Q^n species and for $^{III}B(O_{1/2})_2(O^-)$ (see **Table 8.1** and **Table 8.2**).

Order	Species	BV difference	Difference between
1	^{IV}Al	-0.22	^{VI}Al and ^{IV}Al
2	^{VI}Zr	-0.18	^{VIII}Zr and ^{VI}Zr
3	^{VII}Zr	-0.08	^{VIII}Zr and ^{VII}Zr
4	^{IV}B	0.24	^{III}B and ^{IV}B
5	Q^3	0.25	Q^4 and Q^3
6	$^{III}B(O_{1/2})_2(O^-)$	0.34	^{III}B and $^{III}B(O_{1/2})_2(O^-)$
7	Q^2	0.49	Q^4 to Q^2

Table 8.7: Relative priority of charge compensation within the glasses studied in this project. The presence of Al is as a reference, data from the literature suggests Al is charge compensated before B, Si, and Zr .

If the species are placed in order of descending BV difference (or stabilisation) it can be seen that the order agrees with that set out above and that seen in this work, with Al being the most in need of stabilisation and $^{III}B(O_{1/2})_2(O^-)$ and Q^2 the least. Charge compensation of ^{III}B to ^{IV}B occurs

initially before that for Q^4 to Q^3 but then after only a small alkali addition they occur together. **Table 8.7** also puts the formation of ^{III}B with a NBO after the formation of Q^3 which is supported experimentally in the literature (Dell *et al.* 1983). This concept of bond valence stabilisation allows the charge compensation order for any element in a glass to be predicted. It is not known what the effects of redox state and base glass composition are on this concept.

An attempt has been made to represent this order schematically in **Figure 8.7**. It has been assumed that the distribution of charge compensation is Gaussian – there is no direct experimental evidence for this. However, the change in ^{IV}B fraction seen in the FLi glasses where initially ^{IV}B were created, where current theory suggests no $^{III}B(NBO)$ are present, suggests that the distribution of charge compensated sites is statistical and not an "either/or" process. This effect is also thought to occur in Q^n species distributions where with increasing alkali Q^4 transforms to Q^3, then Q^3 transforms to Q^2, with an equilibrium being achieved between the different species.

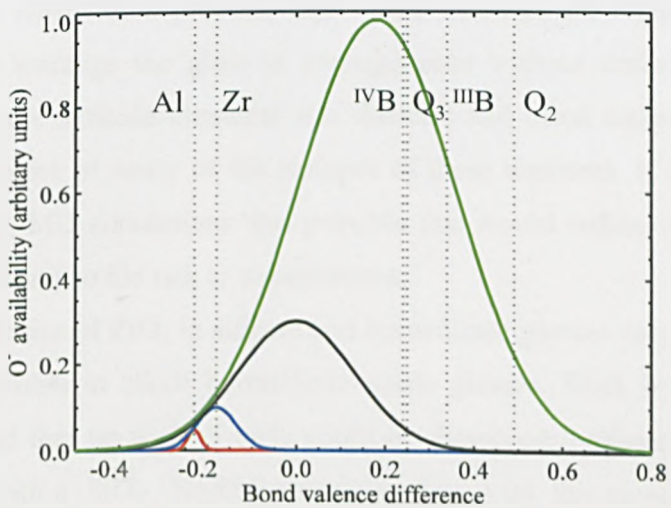

Figure 8.7: Schematic showing possible distribution of O^- availability in an glass containing SiO_2, B_2O_3, Al_2O_3 and ZrO_2. Each curve represents a different concentration of alkali oxide, with the area under the curve being proportional to the concentration.

Unfortunately, it is not possible to place U^{6+} within **Table 8.7** as it currently stands as no environment is known that does not require charge compensation. Indeed, U^{6+} is known to have low solubility in highly polymerised glasses (Domine & Velde 1985, Farges *et al.* 1992).

8.6 Property prediction through the use of MD simulation

The possibility of property prediction though the use of molecular dynamics has been demonstrated in the **Section 6.10**. The apparent close relationship between ^{IV}B fraction and durability is a fascinating insight into the power of MD modelling for glass science.

MD modelling provides the exact position of every atom in the simulated glass, this allows very accurate structural characterisation. This characterisation can then be fed into pre-existing models for the relationship between properties and structure. One such model is the US DOE viscosity model (Jantzen 2005) which is based on a calculation of NBO within a glass. The number of NBO can be extracted from a simulation structure and fed into this model to reduce costly laboratory experiments (e.g. NMR) required to quantify the number of NBOs. Also, properties of U and Pu bearing glass simulations could be gathered leading to a much safer way of achieving laboratory experiments with these difficult materials (Jantzen 2005).

Another property of importance to the nuclear industry is that of in-glass solubility. In order to achieve an efficient vitrification process, high waste loadings are required. It is important that even at high waste loadings the glass is homogeneous without undissolved batch. Producing solubility limits for the actinide elements is a difficult and often dangerous process due to the highly radioactive nature of many of the isotopes of these elements. If a method of establishing solubility limits from MD simulations was possible this would reduce the number of laboratory experiments required and so the risk to experimenter.

Laboratory solubilities of ZrO_2 in silicate and borosilicate glasses vary greatly. **Table 2.3** states that 5-15 wt% is soluble in alkali borosilicate waste glasses. Work by Wang *et al.* (2002) on silicate glasses found that up to 23.5 wt% could be dissolved; however, the compositions used were high in alkali with a $SiO_2 : Na_2O$ molar ratio of ca. 1.84, this compares to a $[SiO_2 + B_2O_3] : [Na_2O + Li_2O]$ ratio of ca. 3.89 for the BNFL base glass composition (FLi-0).

This indicates that the solubility of ZrO_2 predicted by MD gives values which are of a reasonable magnitude when compared to laboratory values for the glass compositions studied here (ca. 6.0 and ca. 7.8 wt% for HLi and FLi glasses respectively) and show the effect of increased alkali addition with FLi having higher solubility than HLi. More work is required to extract accurate solubility data with more glass melts in region of the suspected solubility limit.

Above, it has been shown that information can be gained on laboratory and industrial glass properties from interrogation of the structure of simulated glasses. Another approach, not taken within this work, is that of direct experimentation on simulated structures to extract physical

properties such as viscosities and crack resistance. These processes are complex and difficult to achieve but are possible for simple systems (Allen & Tildesley 1987).

9 Conclusions

9.1 Vitrification of ZrO_2 bearing wastes

In this work two simplified waste glasses were taken and to each glass increasing amounts of ZrO_2 were added. Various structural and physical properties of these glasses were then analysed. The aim was to improve the possibilities for vitrifying high ZrO_2 waste streams though gaining a greater understanding of the role of ZrO_2 in an alkali borosilicate glass.

The most important result from this work, from a processing aspect, is the requirement for charge compensation of ZrO_2 in alkali borosilicate glasses. This work showed that at least ca. 1 mole of alkali oxide is required for charge compensating one mole of ZrO_2 in alkali borosilicate glasses. The weight of evidence presented in this work suggests that only 1 mole of alkali oxide is required. This result is expanded on in **Section 9.4.2**.

The combined use of laboratory and Molecular Dynamic (MD) experiments has allowed the environment of Zr to be defined within a glass. The majority of Zr atoms within the alkali borosilicate glasses investigated here have 6 oxygen ions in the first co-ordination shell. The next nearest neighbours are then thought to be Si and ^{III}B (less likely ^{IV}B). Within this shell there must also be at least 2 alkali ions to provide charge compensation.

The effect of ZrO_2 addition on the bulk structure of alkali borosilicate glasses has been elucidated with MD and laboratory experiments. It has been shown that low level additions of ZrO_2 (< 0.5 mol%) increases the ^{IV}B fraction in the glass. At higher ZrO_2 additions the ^{IV}B fraction decreases. A similar trend is observed in the durability of these glasses. With initially a decrease in durability at low ZrO_2 content then an increase in durability at higher ZrO_2 contents. The fact that these two observations occur over the same compositional ranges suggests that the initial increase in ^{IV}B fraction somehow acts to decrease the durability of the glass. A mechanism has been put forward (see **Section 4.8.2**) that additions of ZrO_2 to an alkali borosilicate glass cause phase separation with formation of ^{IV}B and alkali rich regions that are more easily leached. At low ZrO_2 concentrations these regions decrease durability. With increased ZrO_2 concentrations the increased

hydrolytic stability of Si-O-Zr (and ^{III}B-O-Zr) become the governing factor and the glasses become more durable.

9.2 Vitrification of UO_3 bearing wastes

This work has shown that UO_3 has a high solubility in (ca. 4.8 mol%, ca. 20 wt%) in alkali borosilicate glasses, this potentially allows for efficient vitrification of UO_3 bearing wastes.

It has been shown in **Chapter 7** that in the glasses studied here U is primarily present as U^{6+} within a uranyl species. The environment of the uranyl species is difficult to define but it is believed to be similar to that seen in alkali uranates and involves association with the alkali channels in the glass.

The effect on bulk glass structure has be elucidated showing that addition of UO_3 to a glass requires charge compensation in a similar manner to ZrO_2, but with 2 mole of alkali oxide per mole of added UO_3. This has been shown from ^{11}B MAS-NMR and BV calculations. The effect on the silicate network has not been fully elucidated. It is proposed that U acts as an intermediate within the glass network. It is thought that UO_3 sits in interstices of the glass network related to the alkali channels. This requires little structural rearrangement of the glass and so allows for high solubility. This is unlike ZrO_2 which requires a large amount of structural rearrangement for the Zr moiety to form as discussed above.

In leach tests, U has been shown to readily leach from the glasses studied here and to form hydrated uranyl colloidal phases within the leachate solution. These phases may act as a "sink" driving more and more uranium to leach into solution and so increasing leaching rate of the glass. It is also seen that the presence of U within the glass prevents, or hinders, the formation of a gel layer on the glass surface. This prevents the passivating effect of a leach layer and also increases leaching from the glass.

9.3 The use of molecular dynamic modelling of glass

Molecular Dynamic modelling has been a controversial technique for exploring the structure of glasses. It has many advantages over laboratory techniques as it gives knowledge of the exact position of every atom within the atomic arrangement. However, the fast cooling rate and high temperatures involved (**Table 2.7**) produce controversy over how well the atomic arrangement produced though MD represents an laboratory or commercial glass.

This work has showed that modelling can produce an atomic arrangement representative of the British nuclear waste glass. It has been shown that the MD glass reproduces certain structural features of the laboratory glasses. The reproduction of ^{IV}B fraction and the distribution of Q^n species holds well to that seen in laboratory glasses.

The fast cooling rate of simulated glasses has been shown to hinder the agreement between laboratory and MD glasses. In the ^{IV}B fraction for ZrO_2 bearing glasses the change in ^{IV}B fraction in laboratory glasses is more significant that that seen in MD glasses. It is believed that this is due to small scale phase separation in the glasses which the fast cooling rate under MD cannot accurately reproduce.

Another difficulty with MD glasses is that the system size is small. The computational time taken to simulate systems with more than 3000 atoms makes it difficult without access to very powerful computers. With additions of only small amounts of ZrO_2 to a glass the number of Zr atoms can be as low as unity. This makes the sampling of different possible Zr environments limited.

In the simulations presented in this work there are regions where the simulation structure and laboratory expected structure are not the same. These regions are as interesting as the regions of agreement. The possibility to predict solubility limits for elements within glasses for the point at which expected structure and actual structure misalign is of great importance. Within a laboratory glass once the solubility of an element within a glass is reached the result is often either non-solution (i.e. undissolved batch) or crystallisation on cooling. Neither of these process is possible within these simulations. The time required for devitrification is much longer than the time of the simulations and the method of glass production does not allow for the concept of "undissolved batch". This being the case, in simulations at reaching the solubility limit the structure would start to behave in a different manner than expected. This can be observed in the glass structures, however, it relies on accurate simulation.

This ability to predict the solubility of an element without undertaking experimental work would be of great advantage when dealing with highly radioactive elements such as Pu for which solubility studies in glasses is very difficult due to the dangers involved.

9.4 Controlling glass composition to control properties

The relationship between glass composition and properties is a key aspect of our understanding of

nuclear waste glasses. Processing conditions, durability, and waste loading must all be controlled within nuclear waste glasses. A major factor in the control of these properties is composition. The control (and ideally prediction) of properties from composition has been the aim for glass scientists for many years (see **Section 2.2**). From the results presented in this work certain aspects can be drawn which shed light on this subject.

9.4.1 Redox

The control of the valence state of elements within a glass is key to many aspects of nuclear waste. For each element:

1. The properties it imparts to the glass are often dependent on redox, for example iron where Fe^{3+} generally acts as a modifier decreasing viscosity whereas Fe^{2+} acts as an intermediate and so increases viscosity;
2. The solubility of the element is often controlled by redox, for example Pu;
3. The amount and nature of devitrification of a glass is often controlled by redox. For example, whereas Cr^{3+} under certain conditions forms spinels, Cr^{6+} tends to avoid crystallisation.

In the HAST waste stream glasses that have been looked at in this work, the most abundant elements which have a significant effect on redox are Cr, U and Fe. It has been shown in **Chapter 7** that the Cr content is the deciding factor that defines the redox of the elements within the glass. This is due to the high redox potential of the Cr^{3+}/Cr^{6+} couple. The redox of the U and Fe are oxidised to U^{6+} and Fe^{3+}. This means that the Fe^{3+} is in a tetrahedral co-ordination which requires charge compensation and so increases viscosity and durability.

9.4.2 Charge compensation

A scheme for predicting the relative propensity for the requirment of charge compensating alkali ions was set out in **Section 8.2**. Although the model presented is not complete it gives the possibility for controlling of the solubility and speciation of many elements within an alkali borosilicate glass. In a waste of known composition where the number of alkali ions required to charge compensate each element is known the solubility and in many cases speciation of all the elements can be predicted.

This control of solubility and speciation would not be simple but could theoretically have many advantages allowing reduced crystallisation within the glass and allowing an increased waste

loading. However, the model is not complete and the exact quantities of alkali required for each element has not be calculated.

The change in durability of Zr bearing glasses with increased ^{IV}B fraction highlights the importance of controlling speciation of elements within nuclear waste glasses. For ZrO_2 it appears that 1 mole of alkali oxide is required for charge compensation, for UO_3 2 moles. This indicates that addition of 1 or 2 moles of alkali oxide allows a further mole of ZrO_2 or UO_3 to be dissolved respectivly. However, the effect of these additions on processing properties must also be considered. Whereas addition of ZrO_2 significantly increases viscosity and so alkali addition would improve this problem. Addition of UO_3 has little observable effect on viscosity and so addition of extra alkali oxide would decrease viscosity. Also, the deleterious effect leach layer stability of UO_3 addition may be exacerbated by addition of extra alkali.

9.5 Summary

1. The effect of ZrO_2 on durability is a complex function of composition. In the glasses studied here low concentrations of ZrO_2 decrease durability of the glass, high concentrations increased durability. It is believed that this is due to an increase in ^{IV}B fraction, and phase separation of a high ^{IV}B and alkali region, within the glass which is thus more easily leached. At high ZrO_2 concentration the durability increases due to the increased hydrolytic stability the presence of Zr gives to the silicate (and ^{III}B) network;
2. UO_3 acts on the glass network as an intermediate, decreasing ^{IV}B fraction. However, addition of UO_3 decreases leach layer stability. A model for the structural role of U has been proposed;
3. Molecular dynamic modelling can give key insights into the structure of alkali borosilicate glasses. It has been shown to accurately reproduce many structural aspects of nuclear waste glass structure. It has been shown that it may be possible to predict solubility limits of elements within glasses from MD simulations. Most important of all MD simulation allows a complete structural analysis which, if carefully handled, can give a large amount of information on processing properties, durability and waste loadings.

9.6 Further work

The work done during this study highlights the need for more fundamental research into the area

of analysis of the relationship between glass structure and properties. There are several questions raised which need expanding upon.

1 Further investigation into the presence, and if present, the extent of phase separation caused by the addition of ZrO_2. Also, some elucidation is required as to the mechanism by which ZrO_2 causes phase separation;

1.1 Investigation of boron co-ordination in the boron rich and boron deficient regions in a phase separated glass to confirm the hypothesis that a higher ^{IV}B will be present in the B rich region;

2 Investigation and quantification into the effect on viscosity of the glasses with UO_3 and ZrO_2 additions;

3 Detailed solubility study of ZrO_2 in alkali borosilicate glass to confirm solubility limits derived from MD simulations. Investigating solubility as a function of alkali addition, temperature and other additions as within a full scale glass;

4 Prediction of the order in which different elements are charge compensated within a glass is very important for modelling of glass structure and glass properties. The model presented in this work goes part way to presenting a way of predicting charge compensation order. However, more work is needed, and further laboratory quantitative work is required to confirm the model and to add a more quantitative aspect;

5 MD simulations of glasses with larger numbers of atoms, also with slower quench rates to see if the effect of phase separation possibly observed in the laboratory glasses can be more effectively reproduced;

6 Further MD studies in the use of 3-body-potentials for the Si-O-Si bond and whether this has effect on the results. Also looking at different pressures and the effect of this on B co-ordination;

7 Investigation into mechanism by which UO_3 additions destabalise the leach layer and what effect this has on the durability of the glasses. Also, an investigation in to how to stabilise U within the leach layer.

7.1 Is the deleterious effect of UO_3 on leach layer stability similar to the change in leach layer morphology seen by Lobanova *et al.* at low ZrO_2 contents (increased ^{IV}B fraction)?

10 Appendices

10.1 Appendix A – bond valence

10.1.1 Bond valence theory

Although based on observational and empirical concepts Pauling's theories (1929) have been shown to be accurate many times. In a recent paper Rossano *et al.* (2002) showed that an adaptation of the principal BV theory could be used to check the validity of MD simulations.

For the purposes of this project a much simplified form of the Pauling bond valence model will be used. That is: the sum of the bond valences relating to a bridging oxygen must be close to the theoretical value of 2.0 valence units (vu[1]) (Brown 2002). The bond valence will be calculated with the following equation (Brese & O'Keeffe 1991):

$$v_{iO} = \exp[(R_{iO} - d_{iO})/b] \qquad \textbf{Equation 10.1}$$

where v_{iO} is the valence of the bond between cation I and oxygen, R_{iO} is the bond valence parameter for oxides of cation i, d_{iO} is the cation i-oxygen bond length (Å), and b is a constant generally taken as 0.37 Å but for uranium valence calculations alternative values are taken from Burns *et al.* (1997).

When calculating bond valence, values of d_{iO} are taken either from experimental data presented by the author or by addition of the ionic radii of the cation of interest (of known co-ordination number and valence) to that of $^{III}O^{2-}$ (1.36 Å), with ionic radii obtained by Shannon (Shannon 1976, Ellison & Hess 1994a).

For an unstrained structure the total bond valence must be within ±0.05 vu of 2.0 vu. However, structures outside this range can exist but are strained and generally unstable (Brown 2002). For example a BO (Si-O-Si) gives a total bond valence of 2.02 which is close to 2.0. **Table 10.1** and **Table 10.2** show the values for bond valence that are used in this work.

[1] vu = valence unit. One valence unit is equal to the charge of one electron or the flux generated by the charge of one electron (Brown2002).

Cation	d_{iO}	v_{iO}	Cation	d_{iO}	v_{iO}
$^{IV}Si^{4+}$	1.62	1.01	$^{VI}Na^{+}$	2.38	0.21
$^{IV}Al^{3+}$	1.75	0.70	$^{IV}Li^{+}$	1.95	0.27
$^{III}B^{3+}$	1.37	1.00	Q^4	n/a	0.99
$^{IV}B^{3+}$	1.47	0.77	Q^3	n/a	0.74
$^{VI}Al^{3+}$	1.90	0.48	Q^2	n/a	0.50
			$^{III}B^{3+}(O_{1/2})_2(O^-)$	n/a	0.66

Table 10.1: Showing bond lengths and bond valences for a selection of cations. Bond length (d_{iO}) calculated as sum of ionic radii (Shannon 1976). R_{iO} (used to calculate v_{iO}) values taken from (Brown 2007).

Cation	d_{iO}	v_{iO}	Cation	oxygen	d_{iO}	v_{iO}
$^{VI}Zr^{4+}$	2.08 (2.09)	0.66 (0.65)	U^{6+}	uranyl	(1.82)	(1.56)
$^{VII}Zr^{4+}$	2.14	0.56	U^{6+}	equitorial	(2.2)	(0.77)
$^{VIII}Zr^{4+}$	2.20	0.48				

Table 10.2: Showing bond lengths and bond valence s for a selection of cations. Bond length (d_{iO}) calculated as sum of ionic radii (Shannon1976). R_{iO} (used to calculate v_{iO}) values taken from (Brown 2002). Values in brackets are taken from experimental values presented in this thesis.

10.2 Appendix B- Compositions

10.2.1 Base Glasses

	Half Lithia		Full Lithia	
	Wt %	Mol %	Wt %	Mol %
SiO_2	62.9	63.4	61.8	6.6
B_2O_3	23.0	20.0	21.9	18.6
Na_2O	11.4	11.1	11	10.5
Li_2O	2.7	5.5	5.3	10.5

Table 10.3: Composition of base glasses

10.2.2 Waste Streams

Oxide	High Zr (wt %)	Raw material
BaO	0.54	$BaCO_3$
CeO_2	0.84	CeO_2
Cr_2O_3	4.13	$Cr(NO_3)_3 \cdot 3.9H_2O$
Cs_2O	0.77	Cs_2CO_3
Fe_2O_3	6.37	Fe_2O_3
Gd_2O_3	1.67	Gd_2O_3
La_2O_3	0.42	La_2O_3
MoO_3	1.45	MoO_3
Nd_2O_3	1.36	Nd_2O_3
NiO	8.13	NiO
P_2O_5	0.04	H_3PO_4
Pr_6O_{11}	0.41	Pr_6O_{11}
RuO_2	0.79	RuO_2
Sm_2O_3	0.26	Sm_2O_3
SrO	0.28	$SrCO_3$
TeO_2	0.15	TeO_2
Y_2O_3	0.16	Y_2O_3
ZrO_2	72.22	ZrO_2

Table 10.4: High Zr waste composition (Matlack *et al.* 1999).

Waste composition	Magnox (wt%)	Oxide (wt%)	Blend (wt %)	Raw material used
Ag	0.13	0.14	0.14	Ag_2O
Al	13.93	0.05	3.24	Al_2O_3
Ba	2.91	4.85	4.41	$BaCO_3$
Ca	0.01	0.01	0.01	CaO
Cd	0.10	0.28	0.24	CdO
Ce	4.66	6.97	6.43	CeO_2
Cr	1.13	0.54	0.68	$Cr(NO_3)_3{\cdot}3.9H_2O$
Cs	5.93	7.40	7.06	Cs_2CO_3
Eu	0.21	0.41	0.37	Eu_2O_3
Fe	7.47	2.13	3.36	Fe_2O_3
Gd	2.41	14.76	11.91	Gd_2O_3
La	2.47	3.70	3.42	La_2O_3
Mg	17.14	0.01	3.94	MgO
Mn	0.10	0.05	0.06	MnO_2
Mo	6.53	9.83	9.07	MoO_3
Nb	0.04		0.01	Nb_2O_5
Nd	7.76	11.81	10.87	Nd_2O_3
Ni	0.87	0.36	0.48	NiO
P		0.10	0.08	H_3PO_4
P_2O_5	0.80	0.20	0.38	
Pd	2.41	3.45	3.21	PdO
Pm	0.21	0.13	0.15	Pm_2O_3
Pr	2.24	3.46	3.18	Pr_6O_{11}
Rb	0.66	1.02	0.94	Rb_2CO_3
Rh	1.18	1.29	1.26	Rh_2O_3
Ru	4.16	6.08	5.64	RuO_2
Sb	0.03	0.03	0.03	Sb_2O_3
Se	0.10	0.15	0.14	SeO_2
Si	0.25	0.03	0.08	SiO_2
Sm	1.65	2.35	2.19	Sm_2O_3
Sn	0.11	0.15	0.14	SnO_2
SO_4	0.34		0.08	$BaSO_4$
Sr	1.61	2.46	2.27	$SrCO_3$
Tb		0.01	0.01	Tb_4O_7
Tc	1.71	2.45	2.28	Tc_2O_7
Te	0.86	1.23	1.15	TeO_2
Y	0.86	1.34	1.23	Y_2O_3
Zn		0.12	0.09	ZnO
Zr	7.00	10.65	9.80	ZrO_2

Table 10.5: ISL reference stimulant waste compositions (Magrabi 1988). Blend composition taken as 25 wt% Magnox and 75 wt% Oxide.

Oxide	HAST A (wt%)	HAST B (wt%)	Oxide	HAST A (wt%)	HAST B (wt%)
Ag_2O	0	0	MoO_3	1.68	1.51
Al_2O_3	35.4	31.2	Na_2O	0	0
As_2O_3	0	0	Nb_2O_5	0.03	0.1
B_2O_3	0	0	Nd_2O_3	1.5	1.34
BaO	0.6	0.54	NiO	0.75	1.46
CdO	0.01	0.01	PbO_3	0.06	0.05
CeO_2	0.92	0.79	PO_4	0.19	0.27
Cl	0.19	0.18	Pr_6O_{11}	0.41	0.36
CoO	0.06	0.06	Rb_2O	0.15	0.13
Cr_2O_3	0.86	2.94	RuO_2	0.77	0.72
Cs_2O	0.91	0.84	Sb_2O_3	0	0
CuO	0.47	0.42	SeO_2	0.03	0.03
Eu_2O_3	0.02	0.02	SiO_2	1.6	1.44
F	0.14	0.12	Sm_2O_3	0.34	0.31
Fe_2O_3	13	17.5	SnO_2	0.09	0.08
Ga_2O_3	0.04	0.03	SrO	0.31	0.28
Gd_2O_3	0.01	0.01	TeO_2	0.2	0.18
GeO_2	0	0	TiO_2	0.12	0.11
In_2O_3	0	0	UO_2	30.9	18.7
Li_2O	0	0	WO_2	0.15	0.14
La_2O_3	0.46	0.41	Y_2O_3	0.18	0.16
MgO	5.3	15.5	ZnO	0	0
MnO_2	0.47	0.43	ZrO_2	1.66	1.65

Table 10.6: Composition of HAST wastes A & B).

Element	K-edge absorption		L_I		L_{II}		L_{III}	
	KeV	Å	KeV	Å	KeV	Å	KeV	Å
U	115.61	0.1072	21.76	0.5698	20.948	0.5919	17.17	0.7223
Gd	50.24	0.2468	8.376	1.480	7.930	1.563	7.243	1.712
Ce	40.44	0.3066	6.549	1.893	6.164	2.011	5.723	2.166
Mo	20.00	0.6200	2.866	4.327	2.625	4.723	2.520	4.920
Zr	18.00	0.6890	2.532	4.898	2.307	5.375	2.222	5.579
Ni	8.333	1.4880	1.008	12.30				
Fe	7.112	1.743						
Cr	5.989	2.070						
Si	1.839	6.742						
Al	1.560	7.950						

Table 10.7: Absorption edges for relevant elements (BMSC 2007).

10.3 Appendix C – Three body potential

In order to use the three body potential developed by Stillinger and Weber (1985) and used by various authors (Feuston & Garofalini 1988, Delaye & Ghaleb 1996) a potential function had to be added to list of inbuilt potentials and more importantly expressions had to be obtained for the atomic forces and these also coded into DL_POLY. The expression for the Potential energy is:

$$U(r_{ij}, r_{ik}, \theta_{ijk}) = \lambda_i \exp\left(\frac{\gamma_{ij}}{|r_{ij}| - r_{ci}} + \frac{\gamma_{ik}}{|r_{ik}| - r_{ci}}\right) \mathrm{x}(\cos(\theta_{ijk}) - \cos(\theta_0))^2 \qquad \textbf{Equation 10.2}$$

Where γ, λ, and r_{ci} are adjustable parameters, and other symbols are defined in **Figure 10.1**.

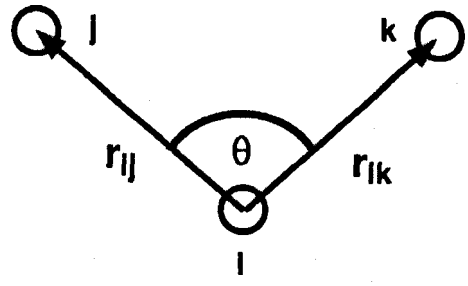

Figure 10.1: Naming convention for three atom potential

Defining the force vector f as:

$$f_i^{\alpha} = -\frac{\delta}{\delta r_i^{\alpha}} U(r_{ij}, r_{ik}, \theta_{ijk}) \qquad \textbf{Equation 10.3}$$

After differentiation this gives a force expression:

$$f_i^a = -\lambda_i \exp(z)(\cos\theta_{jik} - \cos\theta_o)\left[2\left(\frac{r_{ij}}{|r_{ij}||r_{ik}|} - \cos\theta_{ijk}\left(\frac{r_{ik}}{|r_{ik}|^2}\right)\right) - (\cos\theta_{jik} - \cos\theta_o)\frac{r_{ik}}{|r_{ik}|}\frac{\gamma}{(|r_{ik}| - r_{ci})^2}\right]$$

Equation 10.4

This equation was programmed into DL_POLY_2.14 in Fortran 77 code. The contribution to the pressure term, ω, was also added.

$$\omega = -(r_{ij} \bullet f_j^a + r_{ik} f_k^a)$$ **Equation 10.5**

Giving:

$$\omega = \lambda_i \exp(z)(\cos\theta_{jik} - \cos\theta_o)\left[(\cos\theta_{jik} - \cos\theta_o)\frac{|r_{ij}|\gamma}{(|r_{ij}| - r_{ci})^2} + (\cos\theta_{jik} - \cos\theta_o)\frac{|r_{ik}|\gamma}{(|r_{ik}| - r_{ci})^2}\right]$$

Equation 10.6

```
      elseif(ktyp.eq.6)then

      scrn=sw3(rab,rbc,prmtbp(kktbp,3),prmtbp(kktbp,4))
      pterm=scrn*vt6(cost,prmtbp(kktbp,1),prmtbp(kktbp,2))
      vterm=-pterm*prmtbp(kktbp,3)*((rbc/(rbc-prmtbp(kktbp,4)))**2
     x  +(rab/(rab-prmtbp(kktbp,4)))**2)
      gamma=-scrn*gt6(cost,prmtbp(kktbp,1),prmtbp(kktbp,2))
      gamsa=pterm*prmtbp(kktbp,3)/((rab-prmtbp(kktbp,4))**2)
      gamsc=pterm*prmtbp(kktbp,3)/((rbc-prmtbp(kktbp,4))**2)
      gamsb=0.d0
```

Figure 10.2: Small part of F77 code written for DL_POLY_2.14 to add Stillinger and Weber (1985) 3-body potential.

10.4 Appendix D – Chapter 4 - MAS-NMR analysis

Presented below are MAS-NMR spectra for all samples and isotopes used in this study. Each spectra has the fitted peaks shown and labelled. For a discussion of these results see **Chapter 4**.

10.4.1 ^{11}B MAS-NMR spectra

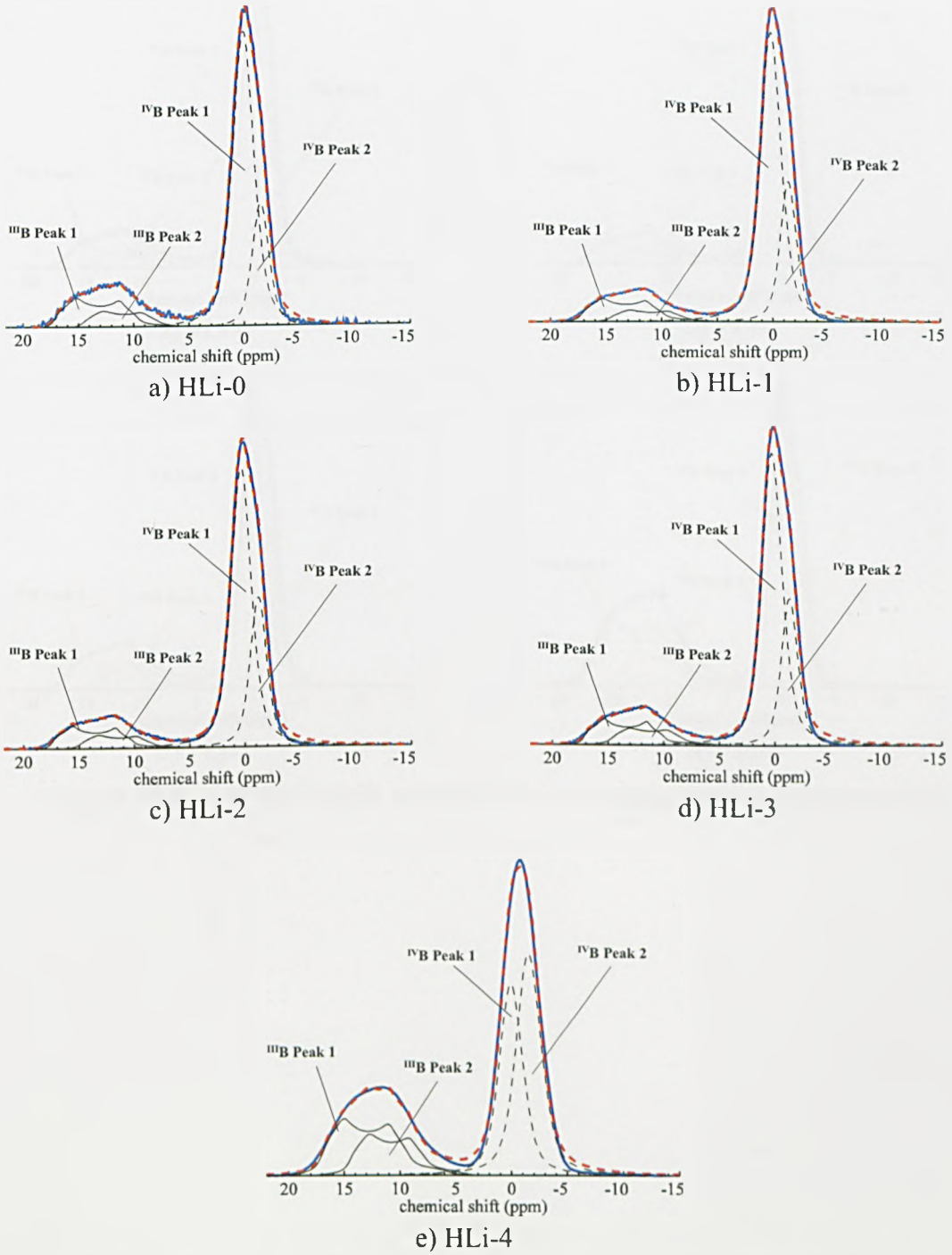

Figure 10.3: ^{11}B MAS-NMR spectra of ZrO_2 bearing glasses and example fits.

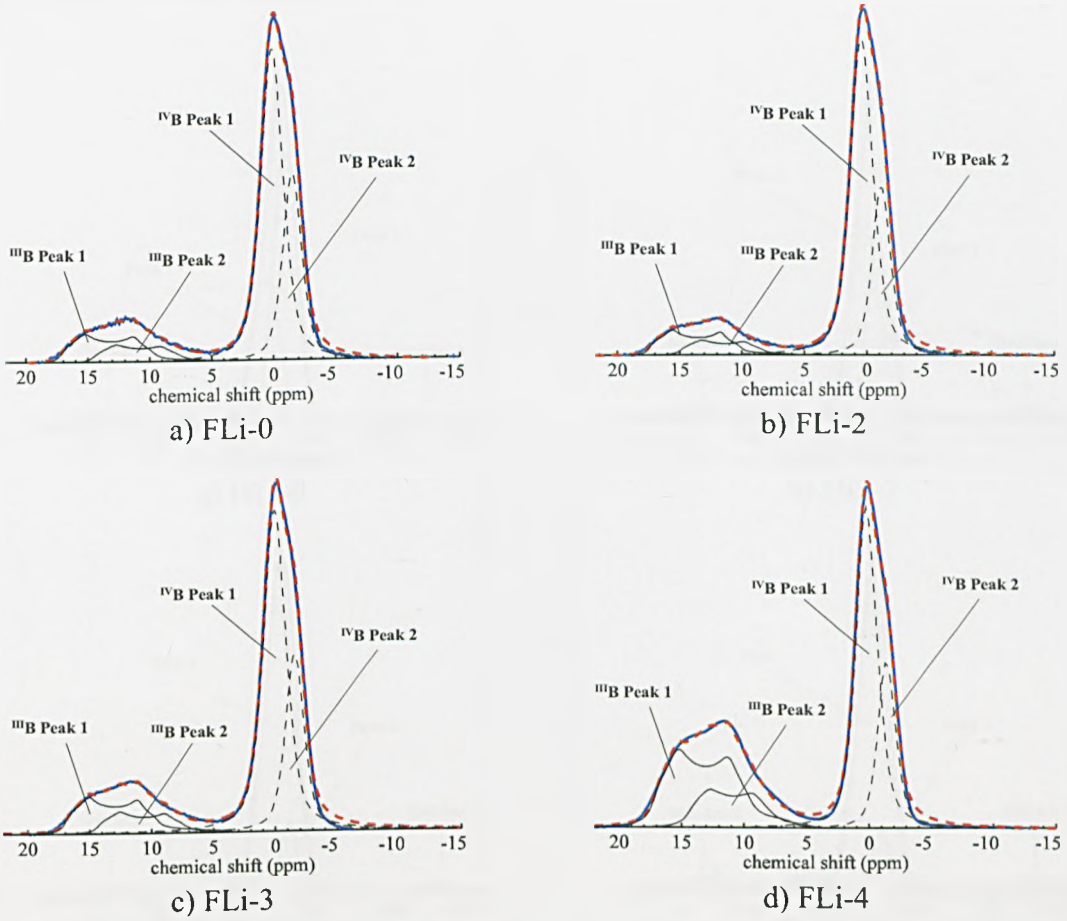

Figure 10.4: ^{11}B MAS-NMR spectra of ZrO_2 bearing glasses and example fits.

10.4.2 ^{29}Si MAS-NMR spectra

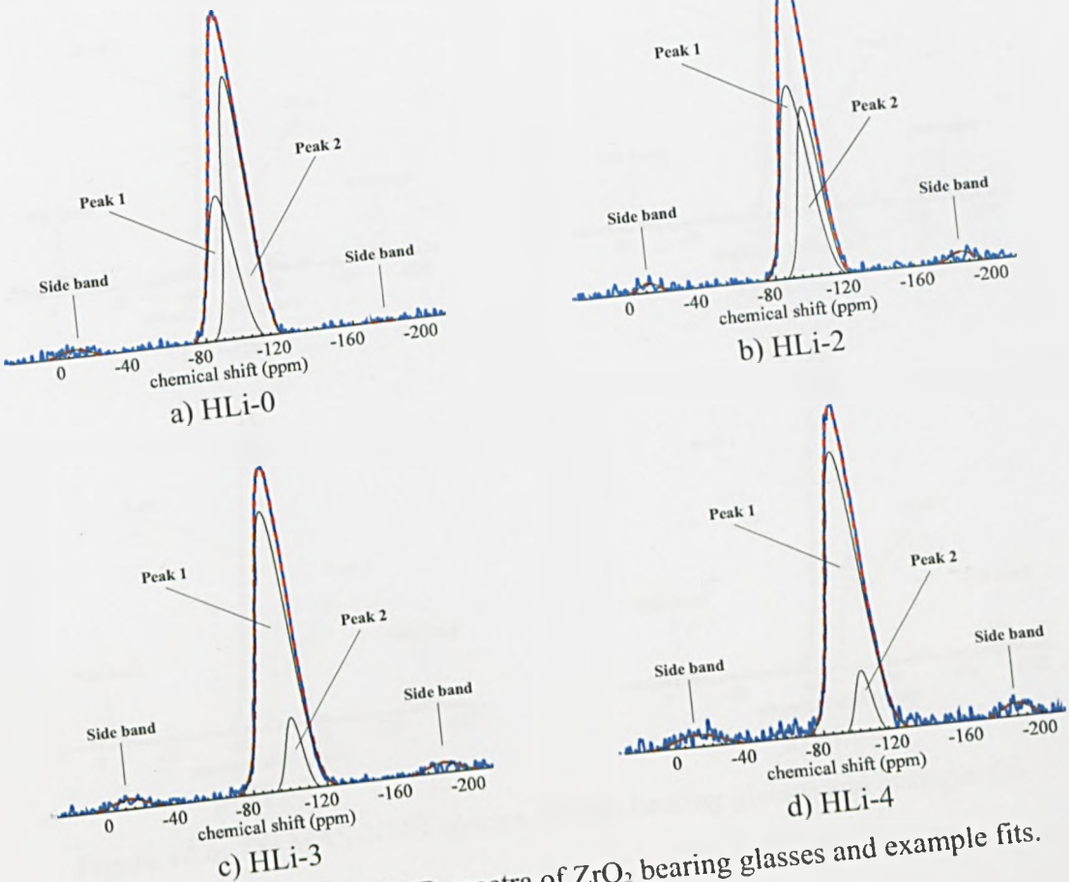

Figure 10.5: ^{29}Si MAS-NMR spectra of ZrO_2 bearing glasses and example fits.

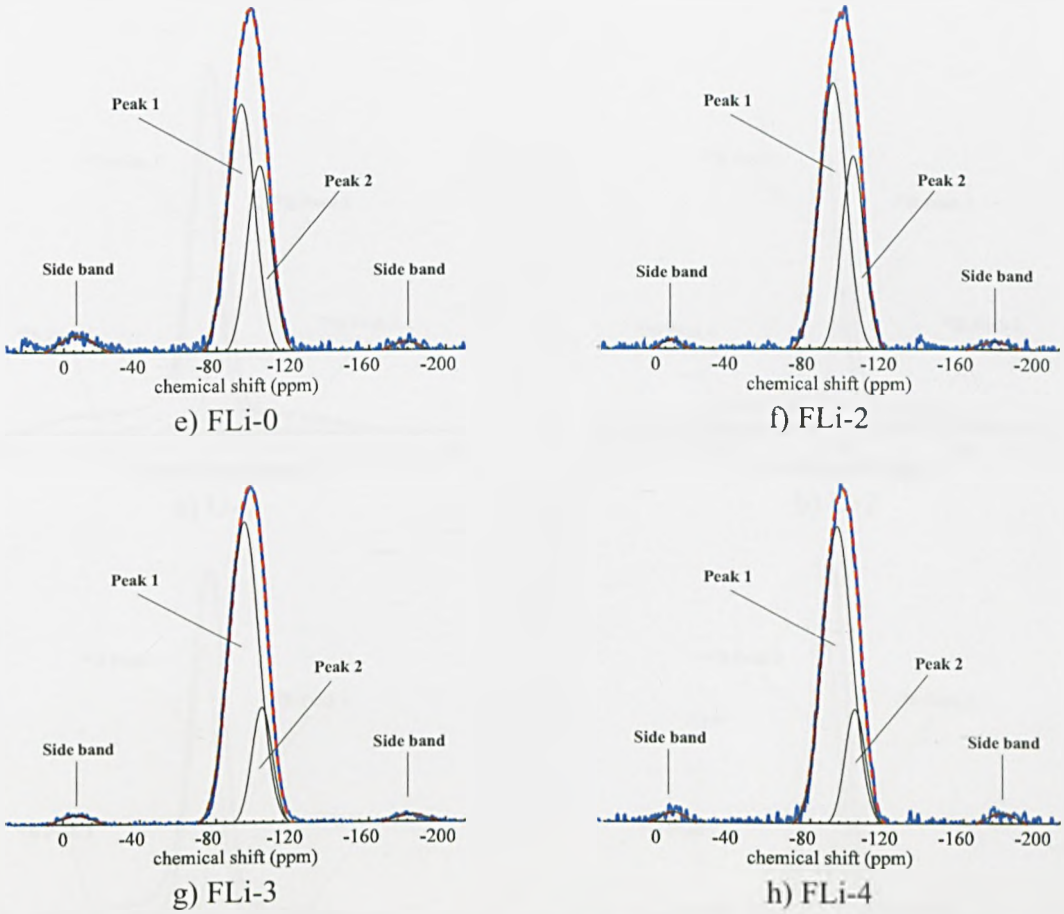

Figure 10.6: ^{29}Si MAS-NMR spectra of ZrO_2 bearing glasses and example fits.

10.5 Appendix E – Chapter 7- MAS-NMR analysis

Presented below are MAS-NMR spectra for all samples and isotopes used in this study. Each spectra has the fitted peaks shown and labelled. For a discussion of these results see **Chapter 7**.

10.5.1 ^{11}B MAS-NMR

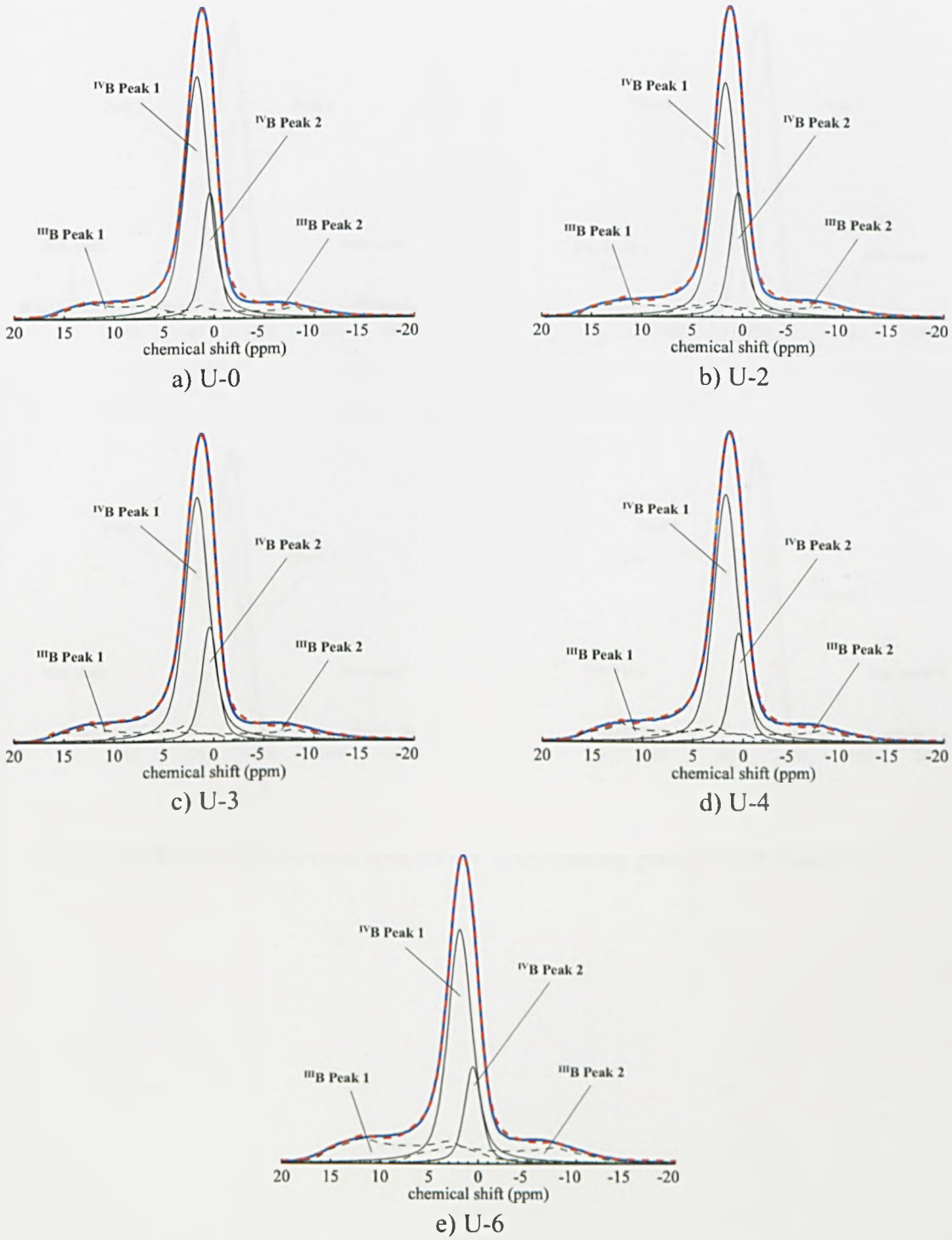

Figure 10.7: ^{11}B MAS-NMR spectra for UO_3 bearing glasses with example fits.

10.5.2 ^{29}Si MAS-NMR

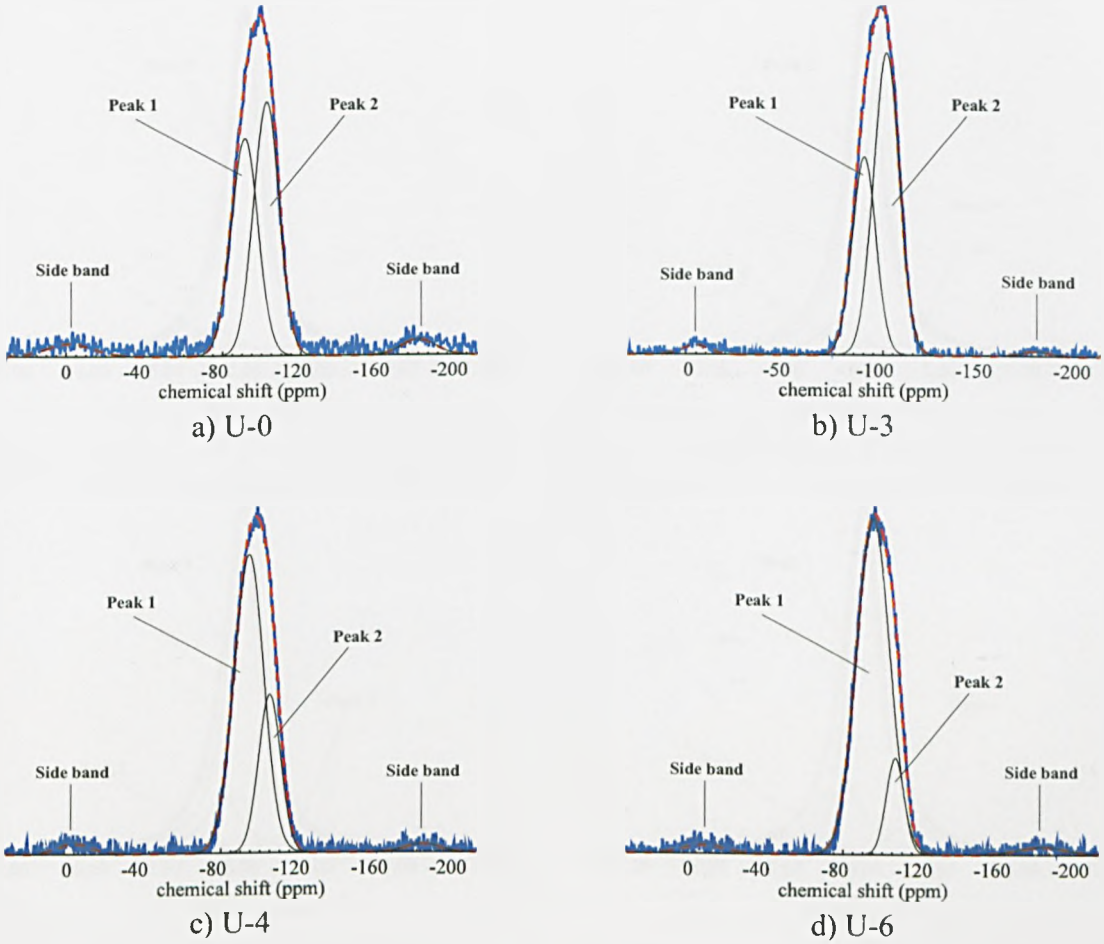

Figure 10.8 : ^{29}Si MAS-NMR spectra for UO_3 bearing glasses with example fits.

10.5.3 ^{7}Li MAS-NMR

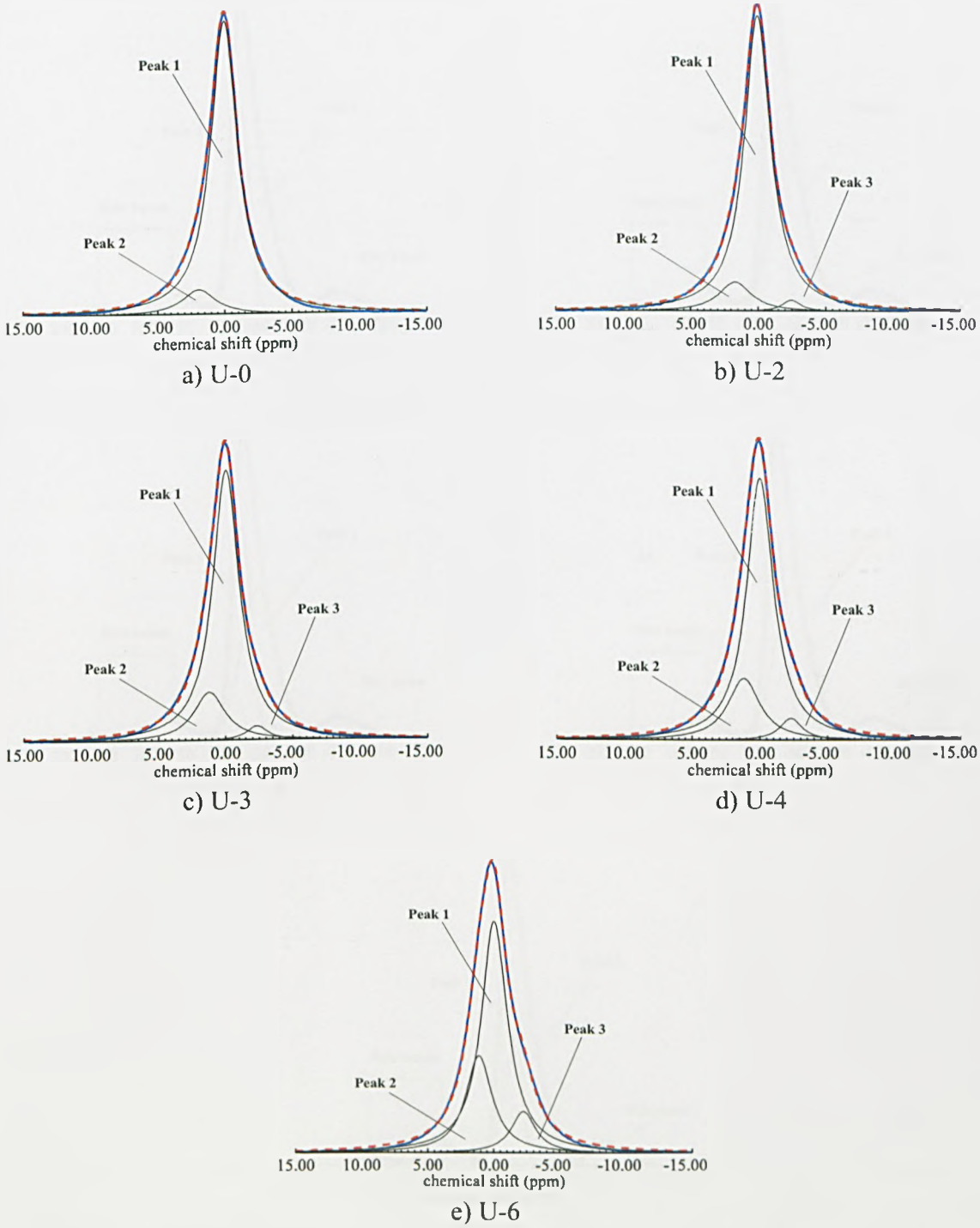

Figure 10.9: ^{7}Li MAS-NMR spectra for UO_3 bearing glasses with example fits.

10.5.4 ^{23}Na MAS-NMR

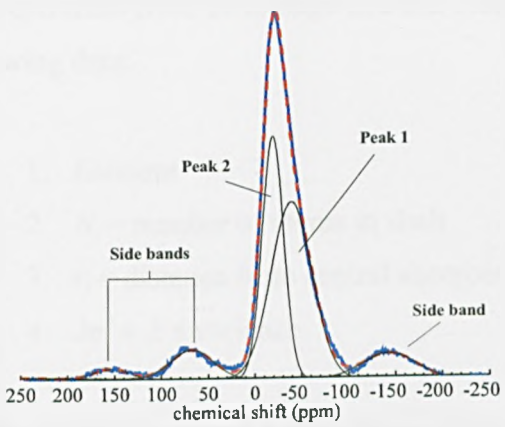

a) U-0

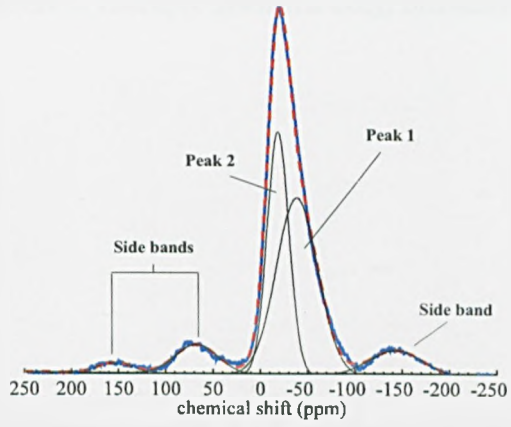

b) U-2

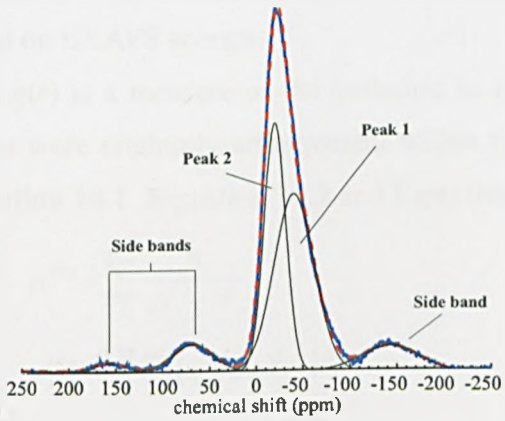

c) U-3

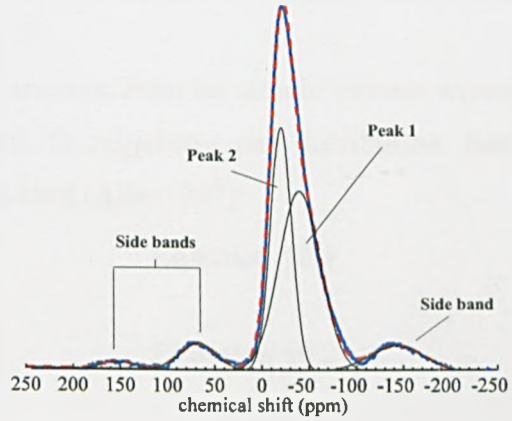

d) U-4

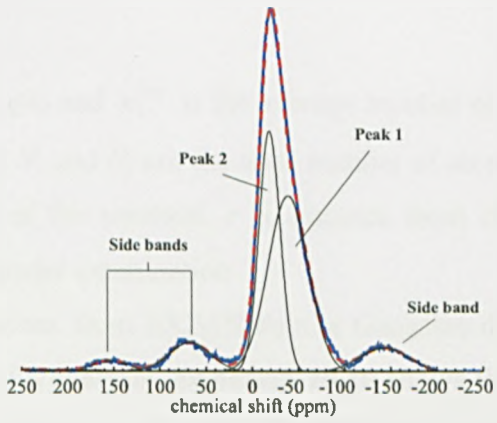

e) U-6

Figure 10.10: ^{23}Na MAS-NMR spectra for UO_3 bearing glasses with example fits.

10.6 Appendix F - Turning EXAFS data into a $g(r)$

Data extracted from Zr K-edge EXAFS results is in form of multiple shell fits each including the following data:

1. Element
2. N_i = number of atoms in shell
3. r_i = distance from central absorber
4. $2\sigma^2 \approx 2$ x variance

The method outlined below allows these EXAFS analysis results to be adapted and directly compared to $g(r)$ data take from MD simulations. It does not require the use complex analysis based on EXAFS spectra.

A $g(r)$ is a measure of the variation in atomistic structure from an atomic volume average if atoms were randomly arrangement within the material. To calculate a pair distribution function **Equation 10.1**, **Equation 10.2** and **Equation 10.3** are used (Allen1987):

$$n_i^{avg} = \sum_j \frac{n_i}{N_i + N_j} \qquad \textbf{Equation 10.1}$$

$$n_i^{id} = \frac{4\pi\rho}{3}[(r+\delta r)^3 - r^3] \qquad \textbf{Equation 10.2}$$

$$g(r+\frac{1}{2}\delta r) = \frac{n_i^{avg}}{n_i^{id}} \qquad \textbf{Equation 10.3}$$

where n_i is the number of i atoms and n_i^{avg} is the average number of i atoms within some interval $(r, r + \delta r)$ from an atom j and N_i and N_j are the total number of atoms i and j respectively within the system. ρ is the density of the material, r is distance from central atom, j, and δr is the thickness of a spherical shell under examination.

To extract similar distributions from EXAFS data, a Gaussian distribution is assumed taking the parameters from the EXAFS analysis. **Equation 10.10** shows this assumed distribution. This distribution can then be normalised in such a way to allow direct comparison between the EXAFS deduced structure and that found from MD ($g(r)$).

$$f_i = N_j e^{-\frac{1}{2}\left(\frac{(r-r_i)^2}{2\sigma^2}\right)} \qquad \textbf{Equation 10.10}$$

Where f_i can be considered equivalent to n_i in **Equation 10.7** and so:

$$n_i^{avg} = \frac{f_i}{N_i + N_j} \qquad \textbf{Equation 10.11}$$

$$n_i^{id} = \frac{4\pi d^3}{3}[(r+\delta r)^3 - r^3] \qquad \textbf{Equation 10.12}$$

$$g(r+\frac{1}{2}\delta r)\frac{n_i^{avg}}{n_i^{id}} \qquad \textbf{Equation 10.13}$$

the significant difference here being that within the EXAFS experimental data the concept of a volume over which the analysis was done is difficult to assign. However, an assumption can be made that it is equal to distance over which analysis was carried out. This can be considered equivalent to the point at which the Gaussian distributions extracted from the EXAFS data becomes very close to zero, here labelled *d*. For example: if $N_i = 2$, $r = 3.5$ and $2\sigma^2 = 0.01$ then $d \approx 4$.

10.7 Appendix G – Codes and programs used in data analysis

10.7.1 Off the shelf

No.	Program	Ref	Source	Use
1	DL_POLY 2.14	(Smith1996)	DL Laboratory	For MD calculation
2	DMFit	(Massiot2002)	CNRS	For MAS-NMR spectra analysis
3	EXCURV98	(Binsted1998)	DL Laboratory	EXAFS data analysis
4	EXCALIB	(EXC)	DL Laboratory	Analysis of XAS data
5	EXBROOK		DL Laboratory	Analysis of XANES data (background subtraction)
6	EXSPLINE		DL Laboratory	Analysis of EXAFS data (background subtraction)
7	WinXpow		Stoe	Analysis of powder XRD data
8	Atomeye 3	(Li2003)		Visualisation of MD configurations
9	Excel		Microsoft	General purpose data analysis and plotting
10	MATLAB		Mathworks	Used for plotting and data analysis (see **Table 10.10**)

Table 10.9: Showing details for programs used in this project for data analysis that were 'off the shelf'

10.7.2 In house (written by the author)

No.	Program	Language	Use
1	co-ord.f90	f90	Calculation of co-ordination numbers
2[a]	gofr.f90	f90	Calculation of g(r)
3	Lincom.m	MATLAB	Linear combination of standard spectra to fit a sample spectra (least squares fitting)
4	qcalc.f90	f90	Calculation of Si Q-numbers for comparision to MAS-NMR data
5[a]	fcc.f90	f90	For creation of an FCC lattice with random atom positioning on the lattice
6	bang.f90	f90	Calculation of bond angles for triplets of atoms (e.g. Si-O-Si)
7	EXAFS_gofr.f90	f90	For conversion of EXAFS analysis results to a g(r) for comparison to MD results.
8	peakfit.m	MATLAB	For fitting a pseudo-voigt peaks to Raman spectra (least squares fitting)
9[b]	msd.f90	f90	For calculating mean square displacement for MD simulations. Adapted from similar code written by W. Smith.

Table 10.10: Showing details for programs used in this project for data analysis that were written in house. Contributions also from [a] Karl Travis and [b] Bill Smith.

10.8 Appendix H – Graphical representation of MD cut-offs

Follows are a series of Figures showing $g(r)$s with the cut-offs used for calculating co-ordination numbers and bond angle distributions shown in the insets (see **Figure 10.11**). Values were chosen as set out in **Section 3.7.9**.

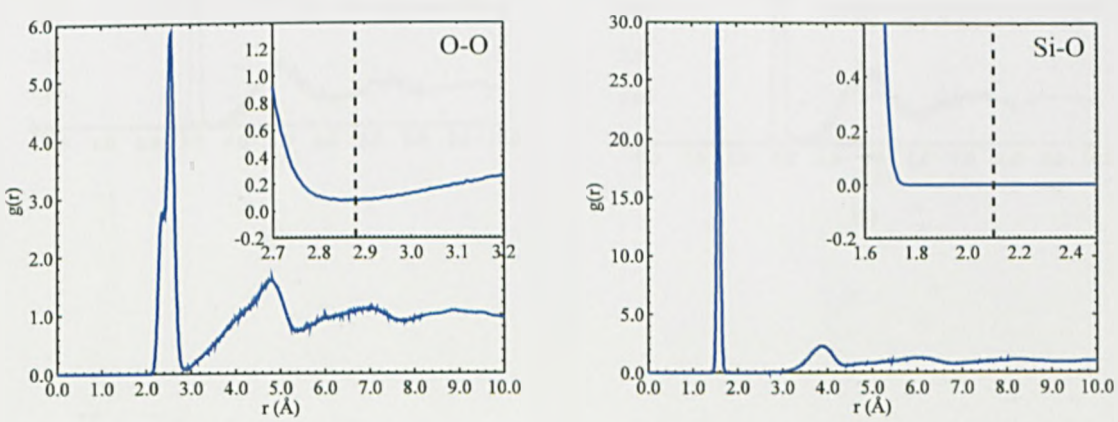

a) b)

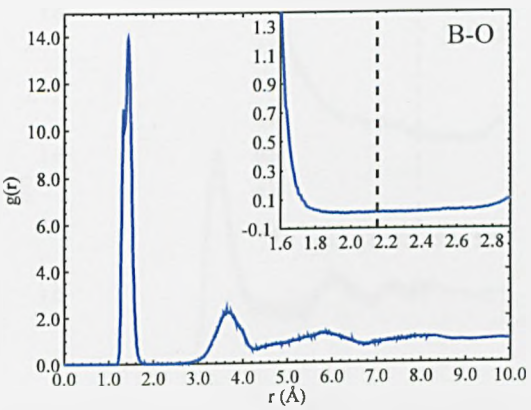

c)

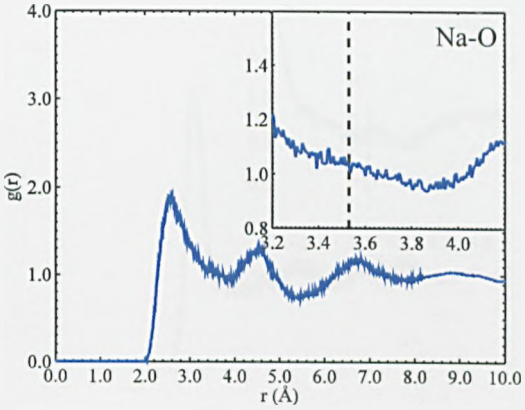

d)

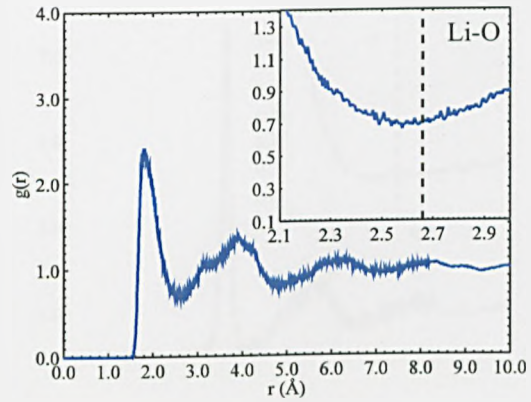

e)

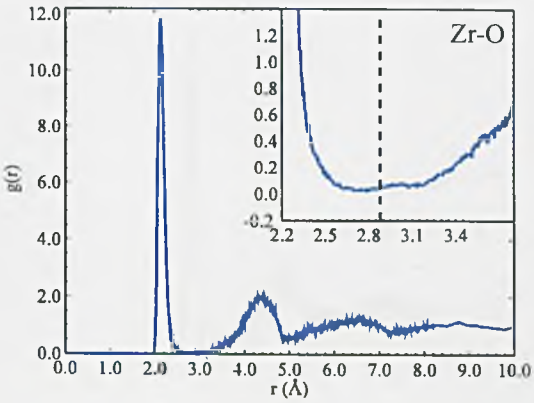

f)

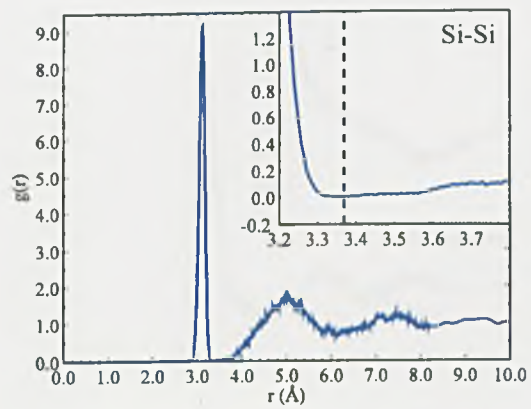

g)

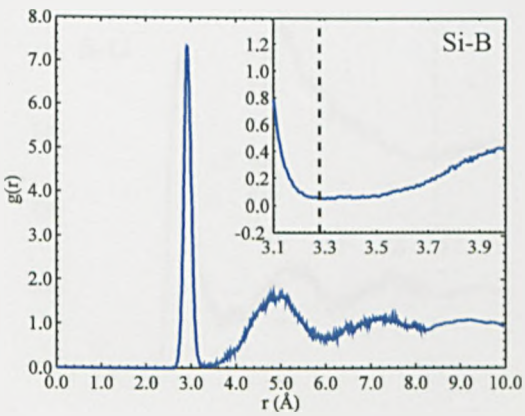

h)

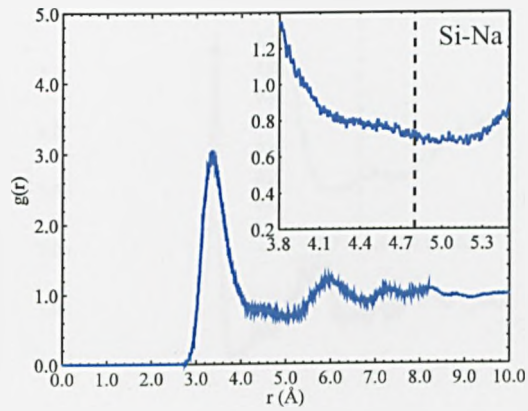

i)

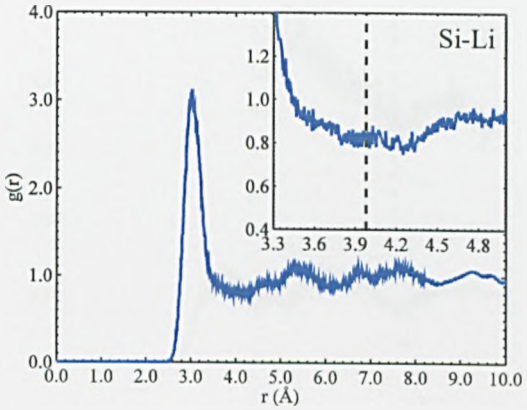

j)

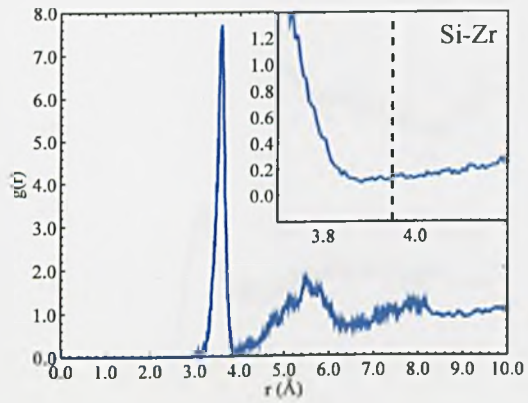

k)

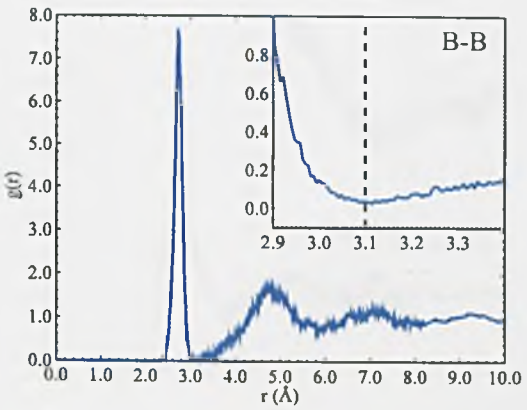

l)

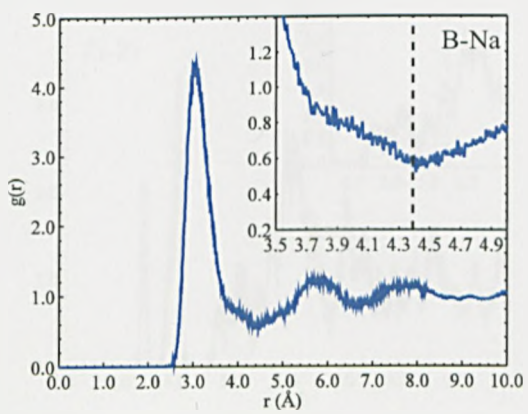

m)

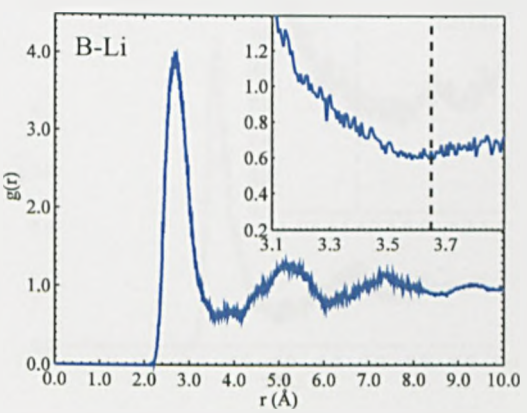

n)

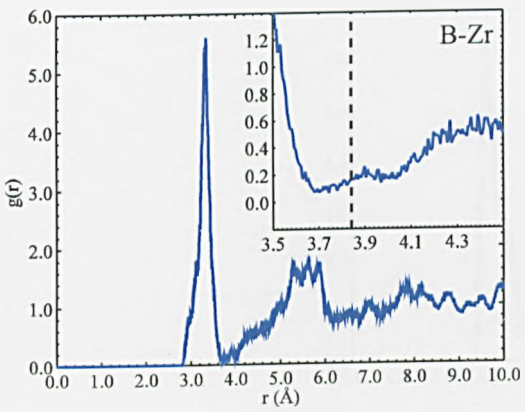

o)

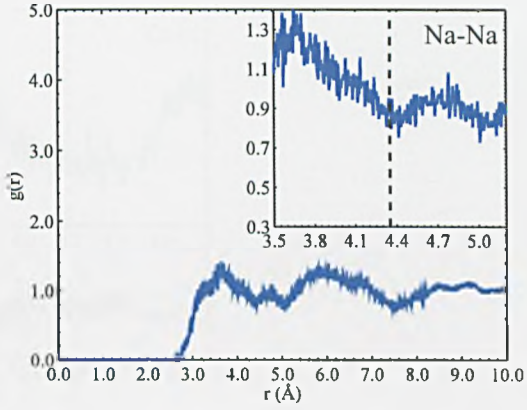

p)

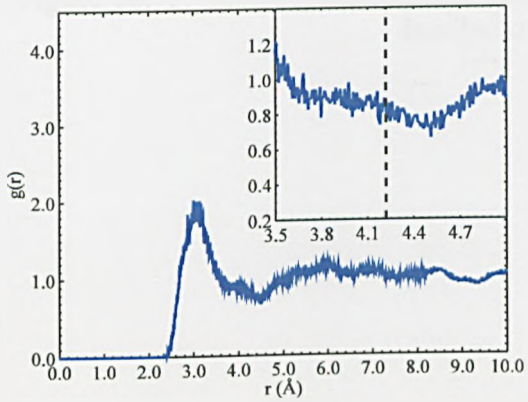

q)

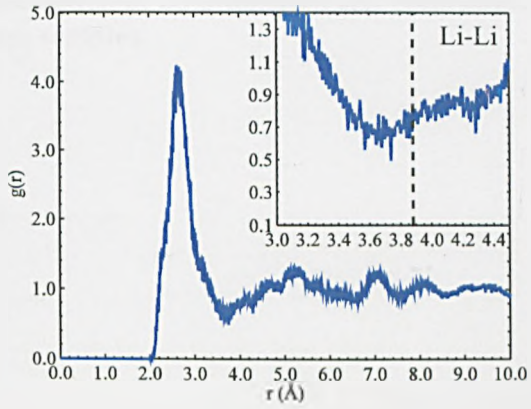

r)

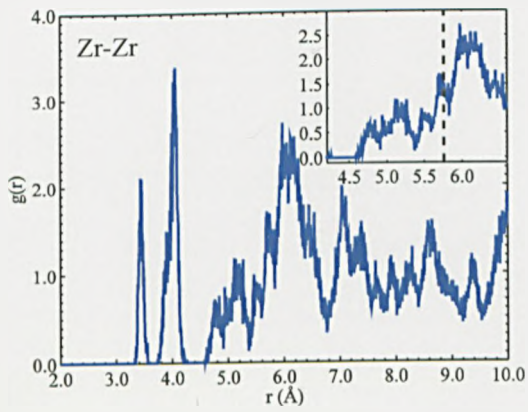

s)

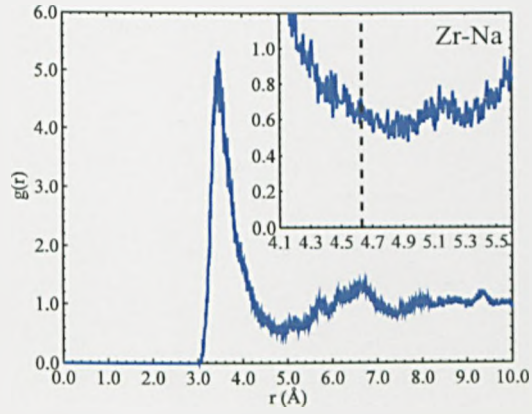

t)

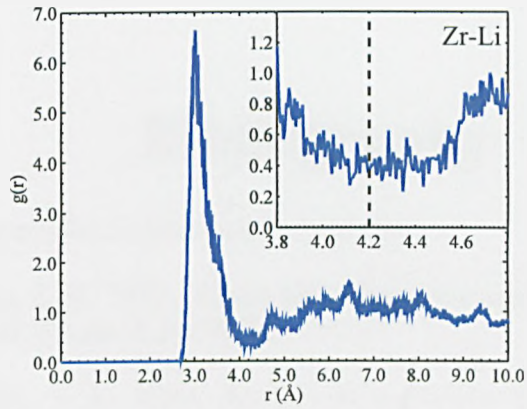

u)

Figure 10.11: Showing the cut-offs used in calculation of co-ordination and bond angle distributions from samples.

Bibliography

Accelrys 2005, http://www.accelrys.com/products/mstudio/.

Alder, B. J. & Wainwright, T. E. 1957, 'Phase transition for a hard sphere system', *Journal Of Chemical Physics*, vol. 27, no. 5, pp. 1208.

Alder, B. J. & Wainwright, T. E. 1959, 'Studies in molecular dynamics.1. General method', *Journal Of Chemical Physics*, vol. 31, no. 2, pp. 459.

Allen, M. P. & Tildesley, D. J. 1987, *Computer Simulation of Liquids*, Oxford Science Publications.

Andrews, A. I. & Gates, R. W. 1940, 'Solubility of a zirconium oxide opacifier in enamel glasses', *Journal Of The American Ceramic Society*, vol. **23**, no. 10, pp. 288.

Angeli, F., Delaye, J. M., Charpentier, T., Petit, J. C., Ghaleb, D. & Faucon, P. 2000, 'Influence of glass chemical composition on the Na-O bond distance:a Na-23 3Q-MAS NMR and molecular dynamics study', *Journal Of Non-Crystalline Solids*, vol. 276, no. 1-3, pp.132.

ASTM 2004, *Standard test method for static leaching of monolithic waste forms for disposal of radioactive waste*. pp. 1.

Atkins, P. W. 1999, *Physical chemistry*, Oxford university press.

Atkins, P. W., Overton, T., Rourke, J., Weller, M. & Armstrong, F. 2006, *Inorganic chemistry*, Oxford university press.

AUA 2007, Australian Uranium Association, *Nuclear Power in the United Kingdom*, Breifing paper #84, http://www.uic.com.au/nip84.htm.

Badyal, Y., Karabulut, M., Marasinghe, K., Saboungi, M-L., Haeffner, D., Shastri, S., Day, D. E., & Ray, C.S. 1999, 'The effects of uranium on the structure of iron phosphate glasses', *Materials Research Society Symposium Proceedings*, vol. 556, pp. 297.

Bamford, C. R. 1977, *Colour generation and control in glass*, Elsevier Scientific publishing company.

Barbieri, L., Cannillo, V., Leonelli, C., Montorsi, M., Siligardi, C. & Mustarelli, P. 2004, 'Characterisation of CaO-ZrO_2-SiO_2 glasses by MAS-NMR and molecular dynamics', *Physics and Chemistry of Glasses*, vol. 45, no. 2, pp.138.

BBC 2007, http://news.bbc.co.uk/1/shared/spl/hi/guides/456900/456932/html/nn2page1.stm.

Berry, A. J. & O'Neill, H. 2004, 'A XANES determination of the oxidation state of chromium in silicate glasses', *American Mineralogist*, vol. 89, pp.790.

Berendsen, H. J. C., Postma, J. P. M., Vangunsteren, W. F., Dinola, A. & Haak, J. R. 1984, 'Molecular-Dynamics With Coupling To An External Bath', *Journal Of Chemical Physics*, vol. 81, pp. 3684.

Bhasin, G., Bhatnagar, A., Bhowmik, S., Stehle, C., Affatigato, M., Feller, S., MacKenzie, J. & Martin, S. 1998, 'Short range order in sodium borosilicate glasses obtained via deconvolution of Si-29 MAS NMR spectra', *Physics And Chemistry Of Glasses*, vol. 39, no. 5, pp. 269.

Bingham, P. A., Parker, J. M., Searle, T., Williams, J. M. & Smith, I., 'Novel structural behaviour of iron in alkali-alkaline-earth-silica glasses', *Comptes Rendus Chimie*, vol. 5, no. 11, pp.797

Binsted, N. 1998, *EXCURV98: CCLRC Daresbury Laboratory computer program.*

Biscoe, J. & Warren, B. E. 1938, 'X-ray diffraction studies of soda-boric oxide glass', *Journal of the American Ceramics Society*, vol. 21, no. 8, pp.287.

BMSC 2005, http://www.bmsc.washington.edu/scatter/AS_periodic.html.

Brese, N. E. & O'Keeffe, M. 1991, 'Bond-Valence Parameters For Solids'. *Acta Crystallographica Section B-Structural Science*, vol. 47, pp. 192..

Brown, Jr., G. E., Farges, F. & Calas, G. 1995, 'X-ray scattering and X-ray spectroscopy studies of silicate melts', *Reviews in Mineralogy*, vol. 32.

Brown, I. D. 2002, *The chemical bond in inorganic chemistry: The bond valence model*, Oxford, Oxford university press.

Brown, I D. 2007, *http://www.ccp14.ac.uk/ccp/web-mirrors/i_d_brown/bond_valence_param/... bvparm2006.cif.*

Buck, E. C. & Bates, J. K. 1999, 'Microanalysis of colloids and suspended particles from nuclear waste glass alteration', *Applied Geochemistry*, vol. 14, no. 5, pp.635.

Bunker, B. C., Tallant, D. R., Kirkpatrick, R. J. & Turner, G. L. 1990, 'Multinuclear nuclear magnetic resonance and Raman investigation of sodium borosilicate glass structures', *Physics and Chemistry of Glasses*, vol. 31, no. 1, pp.30

Burakov, B. E., Strykanova, E. E. & Anderson, E. B., 'Secondary uranium minerals on the surface of Chernobyl `lava", *Materials Research Society Symposium – Proceedings*, vol. 465, pp. 1309.

Burns, R. G. 1993, *Mineralogical applications of crystal field theory*, Cambridge University Press.

Burns, P. C., Ewing, R. C. & Hawthorne, F. C. 1997, 'The crystal chemistry of hexavalent uranium: Polyhedron geometries, bond-valence parameters, and polymerization of polyhedra', *Canadian Mineralogist*, vol. 35, pp.1551.

Cachia, J. N., Deschanels, X., Den Auwer, C., Pinet, O., Phalippou, J., Hennig, C. & Scheinost, A. 2006, 'Enhancing cerium and plutonium solubility by reduction in borosilicate glass',

Journal of Nuclear Materials, vol. 352, no. 1-3, pp.182

Calestani, G., Montenero, A., Ferraguti, E., Ingletto, G., & Bettinelli, M. 1986, 'Influence of some oxide on the durability of a borosilicate glass', *Journal of Non-Crystalline Solids*, vol. 84, pp.452

Cormack, A. N. & Cao, Y. 1996, 'Molecular dynamics simulation of silicate glasses', *Molecular Engineering, vol.* 6, pp.183.

Cormier, L., Ghaleb, D., Delaye, J. M. & Calas, G. 2000, 'Competition for charge compensation in borosilicate glasses: Wide-angle x-ray scattering and molecular dynamics calculations', *Physical Review B - Condensed Matter and Materials Physics*, vol. 61, no. 21, pp. 14495.

Cotton, F. A., Wilkinson, G., Murillo, C. A. & Bochmann, M. 1999, *Advanced Inorganic Chemistry*, John Wiley & sons, inc.

Davis, L. L., Darab, J. G., Qian, M., Zhao, D., Palenik, C. S., Li, H., Strachan, D. M. & Li, L. 2003, 'Hafnium in peralkaline and peraluminous boroaluminosilicate glass and glass sub-components: A solubility study', *Journal of Non-Crystalline Solids*, vol. 328, no. 1-3, pp. 102.

DEFRA - Department for Environment FARA 2001, *Managing radioactive waste safely - Proposals for developing a policy for managing solid radioactive waste in the UK.*

Delaye, J. M. & Ghaleb, D. 1996, 'Molecular dynamics simulation of $SiO_2 + B_2O_3 + Na_2O + ZrO_2$ glass', *Journal of Non-Crystalline Solids*, vol. 195, no. 3, pp.239

Delaye, J. M. & Ghaleb, D. 1996b, 'Molecular dynamics simulation of a nuclear waste glass matrix', *Materials Science and Engineering B, vol.* 37, no. 1-3, pp.232.

Dell, W. J., Bray, P. J. & Xiao, S. Z. 1983, '^{11}B NMR studies and structural modelling of Na_2O-B_2O_3-SiO_2 glasses of high soda content', *Journal of Non-Crystalline Solids*, vol. 58, no. 1, pp.1

Dietzel, A. Z. 1942, 'Die KationenfeldstÃ¤rken und ihre Beziehungen zu EntglasungsvorgÃ¤ngen, zur Verbindungsbildung und zu den Schmelzpunkten von Silikaten', *Electrochemie*, vol. 48, pp.9.

Dimbleby, V. & Turner, W. E. S. 1925, 'The relationship between chemical composition and the resistance of glasses to the action of chemical reagents', *Journal of the Society of Glass Technology*, vol. 10, pp. 304.

Dimbleby, V., English, S., Firth, E. M., Hodkin, F. W. & Turner, W. E. S. 1927, 'Transparent zirconia-containing glasses', *Journal of the Society of Glass Technology*, vol. 11, pp. 52.

Dingwall, A. G. F. & Moore, H. J. 1953, Journal of the Society of Glass Technology, vol. 37, pp. 316.

Domine, F. & Velde, B. 1985, 'Preliminary investigation of processes governing the solubility of uranium in silicate melts', *Bulletin Mineralogy*, vol. 108, pp. 755.

Donald, I. W., Metcalfe, B. L. & Taylor, R. N. J. 1997, 'The immobilization of high level radioactive wastes using ceramics and glasses', *Journal of Materials Science*, vol. 32, no. 22, pp. 5851.

Douglas, R. W., Nath, P. & Paul, A. 1965, 'Oxygen ion activity and its influence on redox equilibrium in glasses', *Physics And Chemistry Of Glasses*, vol. 6, no. 6, pp. 216.

Du, W. F., Kuraoka, K., Akai, T. & Yazawa, T. 2001, 'Effect of additive ZrO_2 on spinodal phase separation and pore distribution of borosilicate glasses', *Journal of Physical Chemistry B*, vol. 105, no. 48, pp. 11949.

Du, L. S. & Stebbins, J. F. 2003a, 'Site preference and Si/B mixing in mixed-alkali borosilicate glasses: A high-resolution ^{11}B and ^{17}O NMR study', *Chemistry of Materials*, vol. 15, no. 20, pp. 3913.

Du, L. S. & Stebbins, J. F. 2003b, 'Solid-state NMR study of metastable immiscibility in alkali borosilicate glasses', *Journal of Non-Crystalline Solids*, vol. 315, no. 3, pp. 239.

Duffy, J. A. 1996, 'Redox equilibria in glass', *Journal of Non-Crystalline Solids*, vol. 196, pp. 45

Dunn, T. 1987, 'Uranium (VI) diffusion in a supercooled borosilicate melt', *Journal of Non-Crystalline Solids*, vol. 92, no. 1, pp. 1.

Eckert, H. 1992, 'Structural characterization of non-crystalline solids and glasses using solid state NMR', *Progress in Nuclear Magnetic Resonance Spectroscopy*, vol. 24, no. 3, pp. 159.

Ellison, A. J. & Hess, P. C. 1986, 'Solution behaviour of +4 cation in high silica melts: petrologic and geochemical implications', *Contributions to Mineralogy and Petrology*, vol. 94, pp. 343.

Ellison, A. J. G. & Hess, P. C. 1994a, 'Raman-study of potassium silicate-glasses containing Rb^+, Sr^{2+}, Y^{3+}, and Zr^{4+} - Implications for cation solution mechanisms in multicomponent liquids', *Geochimica Et Cosmochimica Acta*, vol. 58, no. 8, pp. 1877.

Ellison, A. J. G., Mazer, J. J. & Ebert, W. L. 1994b, 'Effect of glass composition on waste form durability: A critical review', Argonne National Laboratory.

Ewing, R. C., Weber, W. J. & Clinard, F. W. 1995, 'Radiation effects in nuclear waste forms for high-level radioactive waste', *Progress in Nuclear Energy*, vol. 29, no. 2, pp. 63.

EXSPLINE, 1995, A program for EXAFS background subtraction. 2000, Daresbury Laboratory. Based on an original program, SPLINE, P. Ellis, PhD Thesis, University of Sydney.

EXCALIB, Daresbury Laboratory.

Fábián, M., Sváb, E., Mészáros, G., Révay, Z. & Veress, E. 2007 'Neutron diffraction study of sodium borosilicate waste glasses containing uranium', *Journal of Non-Crystalline Solids*, vol. 353, pp. 1941.

Farges, F., Ponader, C. W. & Brown, Jr. G. E. 1991, 'Structural environments of incompatible elements in silicate glass/melt systems: I. Zirconium at trace levels', *Geochimica et Cosmochimica Acta*, vol. 55, no. 6, pp.1563.

Farges, F., Ponader, C. W., Calas, G. & Brown, Jr. G. E. 1992, 'Structural environments of incompatible elements in silicate glass/melt systems: II. UIV, UV, and UVI', *Geochimica et Cosmochimica Acta*, vol. 56, no. 12, pp.4205.

Farges, F. 1996, 'Does Zr-F "complexation" occur in magmas?', vol. 127, no. 4, pp.268.

Farges, F., Lefrere, Y., Rossano, S., Berthereua, A., Calas, G. & Brown Jr, G. E. 2004, 'The effect of redox state on the local structural environment of iron in silicate glasses: a combined XAFS spectroscopy, molecular dynamics, and bond valence study', *Journal of Non-Crystalline Solids*, vol. 344, pp.176

Feil, D. & Feller, S. 1990, 'The Density Of Sodium Borosilicate Glasses Related To Atomic Arrangements', *Journal Of Non-Crystalline Solids*, vol. 119, no. 1, pp. 103.

Feller, S. A., Kottke, J., Welter, J. & Nijhawan, S. 1997, 'Physical properties of alkali borosilicate glasses', *Proceedings of the 2nd International Conference On Borate Glasses, Crystals and Melts* p. 249.

Feuston, B. P. & Garofalini, S. H. 1988, 'Empirical 3-body potential for vitreous silica', *Journal Of Chemical Physics*, vol. 89, no. 9, pp. 5818.

Fletcher, D. A., McMeeking, R. F. & Parkin, D. 1996, 'The United Kingdom Chemical Database Service', *Journal Of Chemical Information And Computer Sciences*, vol. 36, no. 4, pp. 746.

Forland, T., Ostvold, T. & Krogh-Moe, J. 1968, 'Monte Carlo studies on fused salts I. Calculations for a two dimensional ionic model liquid', *Acta Chemica Scandinavica*, vol. 22, pp. 2415.

Frenkel, D. & Smit, B. 2002, *Understanding molecular simulation - From algorithms to applications*, Academic Press.

Galoisy, L., Pelegrin, E., Arrio, M. A., Ildefonse, P., Calas, G., Ghaleb, D., Fillet, C. & Pacaud, F. 1999, 'Evidence for 6-coordinated zirconium in inactive nuclear waste glasses', *Journal of the American Ceramic Society*, vol. 82, no. 8, pp. 2219.

Ghose, S. & Wan, C. 1978, 'Zektzerite, $NaLiZrSi_6O_{15}$ - Silicate with 6-tetrahedral-repeat double chains', *American Mineralogist*, vol. 63, no. 3-4, pp. 304.

Gibb, F. G. F. 2000, 'A new scheme for the very deep geological disposal of high-level radioactive waste', *Journal of the Geological Society*, vol. 157, no. 1, pp. 27.

Godon, N., Delaye, J. M., Deneele, D., Dussossoy, J. L., Fillet, C., Frugier, P. & Ganster, P. 2003, 'NF-PRO Part1: Reference report on the state of the art of glass properties and glass alteration during long term storage and under disposal conditions'

Goodhew, P. J., Humphreys, J. & Beanland, R. 2001, *Electron microscopy and analysis*, Taylor & Francis, London.

Gou, F., Greaves, G. N., Smith, W. & Winter, R. 2001, 'Molecular dynamics simulation of sodium borosilicate glasses', *Journal of Non-Cystalline Solids*, vol. 293-295, pp.539

Greaves, G. N., Fontaine, A., Lagarde, P., Raoux, D. & Gurman, S. J. 1981, 'Local-structure of

silicate-glasses', *Nature*, vol. 293, no. 5834, pp. 611.

Greaves, G. N. 1985, 'EXAFS and the structure of glass', *Journal Of Non-Crystalline Solids*, vol. 71, no. 1-3, pp. 203.

Greaves, G. N., Barrett, N. T., Antonini, G. M., Thornley, F. R., Willis, B. T. M. & Steel, A. 1989, 'Glancing-angle X-ray absorption spectroscopy of corroded borosilicate glass surfaces containing uranium', *Journal of the American Chemical Society*, vol. 111, no. 12, pp. 4313.

Greaves, G. N., Gurman, S. J., Catlow, C. R. A., Chadwick, A. V., Houde-Walter, S., Henderson, C. M. B. & Dobson, B. R. 1991, 'Structural basis for ionic diffusion in oxide glasses', *Philosophical Magazine A: Physics of Condensed Matter, Structure, Defects and Mechanical Properties*, vol. 64, no. 5, pp. 1059.

Greenwood, N. N. & Earnshaw, A. 1993, 'Chemistry of the elements', Butterworth-Heinemann.

Gurman, S. J., Binsted, N. & Ross, I. 1984, 'A rapid, exact curved-wave theory for EXAFS calculations', *Journal of Physical Chemistry*, vol. 17, no. 1, pp. 143.

Hand, R. J. & Seddon, A.B. 1997, 'An hypothesis on the nature of Griffith's crack in alkali silicate and silica glasses', *Physics and Chemistry of Glasses*, vol. 38, no. 1, pp. 11.

Harrison, T. M. & Watson, E. B. 1983, 'Kinetics of zircon dissolution and zirconium diffusion in granitic melts of variable water-content', *Contributions To Mineralogy And Petrology*, vol. 84, no. 1.

Hayward, P. J. 1988, 'The use of glass ceramics for immobilising high level wastes from nuclear fuel recycling', *Glass Technology*, vol. 29, no. 4, pp.122.

Hazen, R. M. & Finger, L. W. 1979, 'Crystal-structure and compressibility of zircon at high-pressure', *American Mineralogist*, vol. 64, no. 1-2, pp.196.

Heynes, M. S. R. & Rawson, H. 1961, 'An investigation into some high melting point glasss systems and their use as solvents for uranium dioxide', *Physics and Chemistry of Glass*, vol. 2, no. 1, pp. 1.

Holland, D., Parkinson, B. G., Islam, M. M., Duddridge, A. Roderick, J. M., Howes, A. P., & Scales, C. R. 2007, 'NMR investigation of cation distribution in HLW wasteform glass', *Materials Research Society*, In press.

Horak, W. & Sharp, D. E. 1935, 'Note on the effect of zirconia on the chemical durability of some borosilicate glasses', *Journal of the American Ceramic Society*, vol. 18, no. 1-12, pp. 281.

Hrma, P., Vienna, J. D., Wilson, B. K., Plaisted, T. J. & Heald, S. M. 2006, 'Chromium phase behaviour in a multi-component borosilicate glass melt', *Journal of Non-Crystalline Solids*, vol. 352, no. 21-22, pp. 2114.

Inoue, H., Aoki, N. & Yasui, I. 1987, 'Molecular-dynamics simulation of the structure of borate glasses', *Journal Of The American Ceramic Society*, vol. 70, no. 9, pp. 266.

IUPAC 2007, 'Gold book', *http://goldbook.iupac.org/index.html.*

Jantzen, C. M. 2005, 'The impacts of uranium and thorium on the defence waste processing facility (DWPF) viscosity model (U)', WSRC-TR-2004-00311.

Johnson, P. A. V., Wright, A. C. & Sinclair, R. N. 1983, 'Neutron scattering from vitreous silica', *Journal of Non-Crystalline Solids*, vol. 58, pp.109.

Jollivet, P., Auwer, C. D. & Simoni, E., 2002, 'Evolution of the uranium local environment during alteration of SON68 glass', *Journal of Nuclear Materials*, vol. 301, no. 2-3, pp.142.

Kalkowski, G., Kaindl, G., Brewer, W. D. & Krone, W. 1986, 'X-ray absorption on uranium systems at various thresholds', *Journal de Physique*, vol. 47, no. 12, pp. 943.

Kim, C. W., Choi, K., Park, J. K., Shin, S. W. & Song, M. J. 2001, 'Enthalpies of chromium oxide solution in soda lime borosilicate glass systems', *Journal of the American Ceramic Society*, vol. 84, no. 12, pp. 2987.

King, B. W. & Andrews, A. I. 1941, 'Solubility of zirconia in soda-borosilicate glasses', *Journal Of The American Ceramic Society*, vol. 24, no. 11, pp. 367.

Kinzie, C. J. & Commons, C. H. 1934, 'The effect of zirconium oxide in glasses, glazes, and enamels', *Journal Of The American Ceramic Society*, vol. 17, pp. 283

Knapp, G. S., Veal, B. W., Paulikas, A. P., Mitchell, A. W., Lam, D. J. & Klippert, T. E. 1984, 'EXAFS studies of sodium silicate glasses containing dissolved actinides', *3rd International EXAFS conference.*

Koningsberger, D. C. & Prins, R. 1987, *X-ray Absorption - Principles, applications, techniques of EXAFS, SEXAFS and XANES,* Wiley-Interscience.

Kovba, L. M., Ippolitova, E. A., Simanov, Y. P., & Spitsyn, V. I. 1958, 'The X-ray investigation of uranates of alkali elements', *Doklady Akademii Nauk SSSR*, vol. 12, pp.1042

Li, P., Chen, I.-W. & Penner-Hahn, J. E. 1993, 'X-ray-absorption studies of zirconia polymorphs. I. Characteristic local structure', *Physical Review B*, vol. 48, no. 1410, pp. 63.

Lippmaa, E., Magi, M., Samoson, A., Engelhardt, G. & Grimmer, A. R. 1980, 'Structural studies of silicates by solid-state high-resolution ^{29}Si NMR', *Journal of the American Chemical Society*, vol. 102, no. 15, pp. 4889.

Liu, G. K., Vikhnin, V. S., Zhuang, H. Z., Hong, K. S., Beitz, J. V., Antonio, M. R. & Soderholm, L. 2001, 'Formation of $UO_2(BO_3)_{(4)}$ clusters in B_2O_3 glass due to charge transfer and vibronic effects', *Journal Of Luminescence*, vol. 94, pp. 677.

Lobanova, M., Ledieu, A., Barboux, P., Devreux, F., Spalla, O. & Lambard, J. 2002, 'Effect of ZrO_2 on the glass durability', *Materials Research Society Symposium – Proceedings*, 571

Lutze, W. & Ewing, R. C. 1988, *Radioactive waste forms for the future*, North-Holland.

Lytle, T. L., Sayers, D. E. & Stern, E. A. 1989, 'Report of the international workshop on standards and criteria in X-ray Absorption Spectroscopy', *Physica B*, vol. 158, no. 1-3, pp. 701

Mackenzie, K. & Smith, M. 2002, *Multinuclear solid-state NMR of inorganic materials*, Pergamon Materials Series, Pergamon.

Maddrell, E. R. 2001, 'Generalized titanate ceramic waste form for advanced purex reprocessing', *Journal of the American Ceramic Society*, vol. 84, no. 5, pp. 1187.

Maeda, T., Banba, T., Sonoda, K., Inagaki, Y. & Furuya, H. 2001, 'Release and retention of uranium during glass corrosion', *Journal Of Nuclear Materials*, vol. 298, no. 1-2, pp.163.

Magrabi, C. 1988, 'Reference wastes for the Thorp and Thorp/Magnox blended vitrification development', BNFL internal report, RM 456.

Marples, J. A. C. 1988, 'The preparation, properties, and disposal of vitrified high-level waste from nuclear-fuel reprocessing', *Glass Technology*, vol. 29, no. 6, pp.230

Massiot, D., Fayon, F., Capron, M., King, I., Le Calve, S., Alonso, B., Durand, J. O., Bujoli, B., Gan, Z. & Hoatson, G. 2002, 'Modelling one- and two-dimensional solid-state NMR spectra', Magnetic Resonance in Chemistry, vol. 40, no. 1, pp.70

Matlack, K. S., Muller, I. S. & Hojaji, H. 1999, 'High-temperature melter tests for vitrification of BNFL high-level nuclear wastes', *Materials Research Society Symposium Proceedings*, 556, pp. 274.

McKeown, D. A., Muller, I. S., Buechele, A. C. & Pegg, I. L. 1999, 'X-ray absorption studies of the local environment of Zr in high-zirconia borosilicate glasses', *Journal of Non-Crystalline Solids*, vol. 258, no. 1, pp. 98.

McKeown, D. A., Muller, I. S., Buechele, A. C., Pegg, I. L. & Kendziora, C. A. 2000, 'Structural characterization of high-zirconia borosilicate glasses using Raman spectroscopy', *Journal of Non-Crystalline Solids*, vol. 262, no. 1, pp. 126.

McMillan, P. W. 1979, *Glass-ceramics*, London, Academic Press.

McMillan, P. F. & Wolf, G. H. 1995, 'Computer simulations of silicate melts', *Reviews in Mineralogy*, vol. 32, pp. 563.

Meneghini, C., Mobilio, S., Lusvarghi, L., Bondioli, F., Ferrari, A. M., Manfredini, T. & Siligardi, C. 2004, 'The structure of ZrO_2 phases and devitrification processes in a Ca-Zr-Si-O-based glass ceramic: a combined a-XRD and XAS study', *Journal Of Applied Crystallography*, vol. 37, pp.890.

Metropolis, N., Rosenbluth, A. W., Rosenbluth, M. N., Teller, A. H. & Teller, E. 1953, 'Equation of state calculations by fast computing machines', *Journal Of Chemical Physics*, vol. 21, no. 6, pp. 1087.

Montorsi, M., Leonelli, C., Menziani, M. C., Du, J. & Cormack, A. N. 2002, 'Molecular dynamics study of zirconia containing glasses', *Physics and Chemistry of Glasses*, vol. 43, no. 3, pp. 137.

Mozzi, R. L. & Warren, B. E. 1969, 'Structure of vitreous silica', *Journal Of Applied Crystallography*, vol. 2, pp. 164.

Ojovan, M., Pankov, A. & Lee, W. 2006, 'The ion exchange phase in corrosion of nuclear waste glasses', *Journal of Nuclear Materials*, vol. 358, no. 1, pp. 57.

Parkinson, B. G., Holland, D., Smith, M. E., Howes, A. P. & Scales, C. R. 2005, 'The effect of Cs_2O additions on HLW wasteform glasses', *Journal Of Non-Crystalline Solids*, vol. 351, no. 30-32, pp. 2425.

Parkinson, B. G. 2007, Thesis, 'Influence of Composition on Structure and Caesium Volatilisation from Glasses for HLW Confinement', University of Warwick.

Paul, A. 1974, 'Optical absorption of chromium (II) in glasses', *Physics and Chemistry of Glasses*, vol. 15, no. 4, pp. 91.

Paul, A. 1990, *Chemistry of glass*, Chapman and Hall.

Pauling, L. 1929, 'The principles determining the structure of complex ionic crystals', *Journal Of The American Chemical Society*, vol. 51, pp. 1010.

Pegg, I. L. & Joseph, I. 2001, 'Vitrification', *Hazardous and radioactive Waste treatment technologies handbook*, CRC Press.

Penner-Hahn, J. E. 1999, 'X-ray absorption spectroscopy in coordination chemistry', *Coordination Chemistry Reviews*, vol. 190-192, pp.1101.

Pennycook, S. J. 1992, 'Z-contrast transmission electron microscopy: Direct atomic imaging of materials', *Annual Review of Materials Science*, vol. 22, no. 1, pp. 171.

Peterson, M. L., Brown Jr, G. E., Parks, G. A. & Stein, C. L. 1997, 'Differential redox and sorption of Cr(III/VI) on natural silicate and oxide minerals:EXAFS and XANES results', *Geochimica et Cosmochimica Acta*, vol 61, no. 16, pp. 3399.

Petiau, J., Calas, G., Petit-Maire, D., Bianconi, A., Benfatto, M. & Marcelli, A. 1986, 'Delocalized verus localized unoccupied 5f states and the uranium site structure in uranium oxide and glasses probed by X-ray absorption near-edge structure', *Physical Review B*, vol. 34, no. 10, pp.7350.

P-NG 2007, http://www.p-ng.si/~arcon/xas/xas/xas2.htm 2007.

Rahman, A. 1964, 'Correlations in motion of atoms in liquid argon', *Physical Review A-General Physics*, vol. 136, no. 2A, pp. 405.

Rance, P. J. W. 1998, 'The development of advanced head-end process', *5th international nuclear conference on recycling, conditioning and disposal*, Nice, pp. 156.

Rodderick, J. M., Holland, D., Howes, A. P. & Scales, C.R. 2007, 'Density-structure relations in mixed-alkali borosilicate glases by ^{29}Si and ^{11}B MAS-NMR', *Journal of Non-Crystalline Solids*, vol. 293-295, no. 745-751, pp.746.

Rose, P. B., Ojovan, M. I., Hyatt, N. C. & Lee, W. E. 2004, 'Crystallisation within simulated high level waste borosilicate glass', *Materials research Society Symposium Proceedings*, 824, pp. 1.

Rossano, S., Farges, F., Ramos, A., Delaye, J. M. & Brown, Jr. G. E. 2002, 'Bond valence in silicate glasses', *Journal of Non-Crystalline Solids*, vol. 304, pp. 167.

Sayers, D. E., Stern, E. A. & Lytle, F. W. 1971, 'New technique for investigating noncrystalline structures - Fourier analysis of extended X-ray - absorption fine structure', *Physical Review Letters*, vol. 27, no.18, pp.1204.

Schmidt, A. J. & Elmore, M. R. (2002), 'Settling test using simulants to evaluate uranium metal distribution in K basin sludge', Technical Report, US Department of Energy, PNNL-13854.

Schreiber, H. D. & Balazs, G. B. 1982, 'The chemistry of uranium in borosilicate glasses. Part1. Simple base compositions relevant to the immobilisation of nuclear waste', *Physics And Chemistry Of Glasses*, vol. 23, no. 5, pp. 139.

Schreiber, H. D., Balazs, G. B., Jamison, P. L. & Shaffer, A. P. 1982, 'The chemistry of uranium in borosilicate glasses.2. Base compositions containing titanium relevant to the immobilization of nuclear waste', *Physics And Chemistry Of Glasses*, vol. 23, no. 5, pp. 147.

Schreiber, H. D. & Balazs, G. B. 1984a, 'Electromotive force series for redox couples in a borosilicate melt: The basis for electron exchange interactions of the redox couples, *Journal of Non-Crystalline Solids*, vol. 71, no. 1-3, pp. 59.

Schreiber, H. D., Minnix, L. M., Balazs, G. B. & Carpenter, B. E. 1984b, 'Chemistry of uranium in borosilicate glasses. Part 4. The ferric-ferrous couple as a potential redox buffer for the uranium redox state distribution against oxidising agents in a borosilicate melt', *Physics and Chemistry of Glasses*, vol. 25, no. 1, p.1

Schreiber, H. D., Balazs, G. B. & Solberg, T. N. 1985, 'Chemistry of uranium in borosilicate glasses. Part 6. The leaching of uranium for glass', *Physics and Chemistry of Glasses*, vol. 26, no. 2, pp. 35.

Siegel, S., Hoekstra, H. R., & Sherry, E. 1966, 'The Crystal Structure of High-Pressure UO_3', *Acta Crystallographica*, vol. 20, pp. 292.

Sen, S., Xu, Z. & Stebbins, J. F. 1998, 'Temperature dependent structural changes in borate, borosilicate and boroaluminate liquids: high-resolution B-11, Si-29 and Al-27 NMR studies', *Journal Of Non-Crystalline Solids*, vol. 226, no. 1-2, pp. 29.

Shannon, R. D. 1976, 'Revised effective ionic-radii and systematic studies of interatomic distances in halides and chalcogenides', Acta Crystallographica Section A, vol. 32, pp. 751.

Shelby, J. 2005, *Introduction to glass science and technology*, 2nd Edition, Royal Society of Chemistry.

Sherriff, B. L. & Grundy, H. D. 1988, 'Calculations of Si-29 MAS NMR chemical-shift from silicate mineral structure', *Nature*, vol. 332, no. 6167, pp. 819.

Sicard, L., Spalla, O. & Barboux, P. 2004, 'Study of the kinetics of glass alteration by small-angle X-ray scattering', *Journal of Physical Chemistry B*, vol. 108, no. 23, pp. 7702.

Slayter, G. 1952, 'Strength of glass', *American Ceramic Society Bulletin*, vol. 31, pp.276.

Smith, W. & Forester, T. R. 1996, 'DL-POLY-2.0: A general-purpose parallel molecular dynamics simulation package', *Journal of Molecular Graphics*, vol. 14, no. 3, pp. 136.

Soper, P. D., Walker, D. D. & Plodinec, M. J. 1983, 'Optimization of glass composition for the vitrification of nuclear waste at the Savannah River Plant', *American Ceramic Society Bulletin*, vol. 62, no. 9, pp. 1013.

Soules, T. F. 1979, 'Molecular dynamic calculation of the structure of sodium-silicate glasses', Journal Of Chemical Physics, vol. 71, no. 11, pp. 4570.

Soules, T. F. & Varshneya, A. K. 1981, 'Molecular dynamic calculations of a sodium borosilicate glass structure', *Journal Of The American Ceramic Society*, vol. 64, no. 3, pp. 145.

Stebbins, J. F. 1991, 'NMR evidence for five-coordinated silicon in a silicate glass at atmospheric pressure', *Nature*, vol. 351, no. 6328, pp. 638.

Stebbins, J. F., McMillan, P. F. & Dingwell, D. B. 1995, 'Structure, Dynamics and Properties of Silicate Melts', *Reviews in Mineralogy*, vol. 32.

Stevens, R. 1983, *An introduction to zirconia, Magnesium Elektron.*

Stillinger, F. H. & Weber, T. A. 1985, 'Computer-simulation of local order in condensed phases of silicon', *Physical Review B*, vol. 31, no. 8, pp. 5262.

Strachan, D. M. 2001, 'Glass dissolution: testing and modelling for long-term behaviour', *Journal Of Nuclear Materials*, vol. 298, no. 1-2, pp. 69.

Takada, C. R., Catlow, R. A. & Price, G. D. 1995, 'Computer modelling of B_2O_3: part 1. New interatomic potentials, crystalline phases, and predicted polymorphs', *Journal of Physics: Condensed Matter*, vol. 7, pp. 8659.

Tatsumi, K. & Hoffmann, R. 1980, 'Bent *cis* d^0 MoO_2^{2+} vs. linear trans d^0f^0 UO_2^{2+}: A significant role for nonvalence 6*p* orbitals in uranyl', *Inorganic Chemistry*, vol. 19, no. 9, pp. 2656.

Teo, B. K. 1981, 'Novel method for angle determination by EXAFS via a new multiple scattering formalism', *Journal of American Chemical Society*, vol. 103, pp. 3990.

Uwasterloo 2007, http://www.science.uwaterloo.ca/~cchieh/cact/nuctek/fissionyield.html.

Varshneya, A. K. 2006, *Fundamentals of inorganic glasses*, 2nd edition, Academic Press .

Vashita, P., Kalia, R. K. & Nakano, A. 1999, 'Multimillion atom molecular dynamics simulations of glasses and ceramic materials', *AIP Conference Proceedings*, vol. 489, pp. 149.

Vogel, H. 1921, 'Das Tempcratur-ahhangigkeitsgeaetz der ViskositHt von Fliisrigkeiten', *Zeitschriff fur Physik*, vol. 22, pp. 645.

Voigt, U., Lammert, H., Eckert, H. & Heuer, A. 2005, 'Cation clustering in lithium silicate glasses: Quantitative description by solid-state NMR and molecular dynamics simulations', *Physical Review B - Condensed Matter and Materials Physics*, vol. 72, no. 6, pp.064207.

Volf, M. B. 1984, *Chemical approach to glass*, Elsevier Science Ltd.

Volf, M. B. 1988, *Mathematical approach to glass*, Elsevier Science Ltd.

Volkovich, V. A., Griffiths, T. R. 1998, Fray, D. J. & Fields, M., 'Vibrational spectra of alkali metal (Li, Na and K) uranates and consequent assignment of uranate ion site symmetry', *Vibrational Spectroscopy*, vol. 17, no. 1-3, pp. 83.

Walsh, A., 'The application of atomic absorption spectra to chemical analysis', *Journal Of Analytical Chemistry*, vol. 60, no. 4, pp. 382.

Wang, T., Hand, R., James, P., & Scales, C. R. 2002, 'Glasses for vitrification of zirconia rich wastes', *Glass Technology*, vol. 43C, pp. 162.

Warren, B. E. 1941, 'Summary of work on atomic arrangement in glass', *Journal Of The American Ceramic Society*, vol. 24, no. 8, pp. 256.

Watson, E. B. 1979, 'Zircon saturation in felsic liquids - Experimental results and applications to trace-element geochemistry', *Contributions To Mineralogy And Petrology*, vol. 70, no. 4, pp. 407.

Webelements 2007, *http://www.webelements.com/*

West, A.R. 1999, *Basic solid state chemistry*, 2nd edition, Wiley.

Weyl, W. A. 1951, *Coloured glasses*, Society of Glass Technology.

Wilson, P. D. 1996, *The nuclear fuel cycle - from ore to wastes*, Oxford University Press.

Winterer, M., Delaplane, R. & McGreevy, R. 2002, 'X-ray diffraction, neutron scattering and EXAFS spectroscopy of monoclinic zirconia: Analysis by rietveld refinement and reverse Monte Carlo simulations', *Journal of Applied Crystallography*, vol. 35, no. 4, pp. 434.

Wirkus, C. D. & Wilder, D. R. 1962, 'Uranium-bearing glasses in the silicate and phosphate systems', *Journal Of Nuclear Materials*, vol. 5, no. 1, pp.18

Woodcock, L. V. 1971, 'Isothermal molecular dynamics calculations for liquid salts', *Chemical Physics Letters*, vol. 10, no. 3, pp. 257.

Woodcock, L. V. & Singer, K. 1971, 'Thermodynamic and structural properties of liquid ionic salts obtained by Monte Carlo computation.1. Potassium chloride', *Transactions Of The Faraday Society*, vol. 67, no. 577, pp. 12.

Woodcock, L. V., Angell, C. A. & Cheeseman, P. 1976, 'Molecular-dynamics studies of vitreous state - Simple ionic systems and silica', *Journal Of Chemical Physics*, vol. 65, no. 4, pp. 1565.

Yazawa, T., Tanaka, H., Eguchi, K. & Yokoyama, S. 1994, 'Novel alkali-resistant porous glass prepared from a mother glass based on the SiO_2-B_2O_3-RO-ZrO_2 (R = Mg, Ca, Sr, Ba and Zn) system', *Journal of Materials Science*, vol. 29, no. 13, pp. 3433.

Yun, Y. H., & Bray, P. J. 1978, 'Nuclear Magnetic Resonance Studies of the Glasses in the System Na_2O-B_2O_3-SiO_2', *Journal Of Non-Crystalline Solids*, vol. 27, no. 3, pp. 363.

Zachariasen, W. H. 1932, 'The atomic arrangement in glass', *Journal Of The American Chemical Society*, vol. 54, pp. 3841.

Zarzycki, J. 1991, *Glasses and the vitreous state*, Cambridge University Press.

Zhong, J. & Bray, P. J., 1989, 'Change in boron coordination in alkali borate glasses, and mixed alkali effects, as elucidated by NMR', *Journal of Non-Crystalline Solids*, vol. 111, no. 1, pp. 67.